Measurement of Charm Production in Deep Inelastic ep Scattering at HERA

by

Kirstin Hebbel

Measurement of Charm Production in Deep Inelastic *ep* Scattering at HERA

DISSERTATION

zur Erlangung des Doktorgrades
des Fachbereichs Physik
der Universität Hamburg

vorgelegt von

Kirstin Hebbel
aus Hamburg

Hamburg
März 2000

Gutachter der Dissertation:	Prof. Dr. V. Blobel
	Prof. Dr. R. Klanner
Gutachter der Disputation:	Prof. Dr. E. Lohrmann
	Prof. Dr. B. Naroska
Datum der Disputation:	11.4.2000
Dekan des Fachbereichs Physik und Vorsitzender des Promotionsausschusses:	Prof. Dr. Fr.-W. Büßer

Abstract

Open charm production in neutral current deep-inelastic scattering of 27.5 GeV positrons and 820 GeV protons has been studied at HERA. The integrated luminosity of the data sample, taken with the ZEUS detector in 1996/97, is 34 pb^{-1}. The semileptonic decay of charmed hadrons into electrons, $c \rightarrow e\nu X$, has been used to measure charm production. An inclusive electron signal has been obtained by combining information about the particle energy loss due to ionization in the central tracking detector (CTD) with energy deposits in the uranium calorimeter. The electron acceptance is limited by the method to $1.2 < p_{electron} < 5.0$ GeV and $0.65 < \theta_{electron} < 2.5$ rad. Statistical subtraction of the background due to electrons from non-charm decays, such as photon conversions, beauty and π^0 decays has been performed. Cross sections for charm production with semileptonic decays of the charm quarks have been measured in the two kinematic ranges $1 < Q^2 < 1000\,\mathrm{GeV}^2$ and $10 < Q^2 < 200\,\mathrm{GeV}^2$ with $0.03 < y < 0.7$ for both regions. The measured values $\sigma = 532 \pm 27^{+40}_{-96}$ pb and $226 \pm 12^{+14}_{-34}$ pb respectively agree within errors with theoretical predictions from NLO calculations. Differential cross sections as functions of W, Q^2, x, $p_{t\ electron}$ and $\eta_{electron}$ show reasonable agreement with theoretical predictions from NLO calculations. In order to determine the charm contribution to the proton structure function $F_2^{c\bar{c}}$, the observed cross section is extrapolated to the full kinematic region in $p_{electron}$ and $\theta_{electron}$. The measured $F_2^{c\bar{c}}$ agrees within errors with theoretical predictions and with the measurement made by ZEUS using the D meson decay channel. The ratio of $F_2^{c\bar{c}}$ to F_2 is shown to rise towards low x and high Q^2, and can be as high as 30 %.

Zusammenfassung

Die Produktion von Charm-Quarks in tiefunelastischen Streuprozessen wurde am HERA-Speicherring, wo Elektronen einer Energie von 27.5 GeV und Protonen einer Energie von 820 GeV zur Kollision gebracht werden, untersucht. Für die Analyse wurden die Datensätze des ZEUS Experiments aus den Jahren 1996 und 1997 verwendet, welche einer integrierten Luminosität von 34 pb^{-1} entsprechen. Als Nachweismethode für Charm-Produktion wurde der semileptonische Zerfall charmanter Hadronen in Elektronen verwendet. Ein inklusives Elektronen Signal wurde mit Hilfe der Information über den spezifischen Energieverlust der Teilchen im Füllgas der zentralen Spurkammer (CTD) und ihrer Energiedeposition im Uran Kalorimeter gemessen. Auf Grund der gewählten Methode ist die Akzeptanz der Elektronen auf $1.2 < p_{electron} < 5.0$ GeV und $0.65 < \theta_{electron} < 2.5$ rad beschränkt. Der Untergrund von Elektronen aus Photonkonversionen und Zerfällen anderer Teilchen in Elektronen wurde abgeschätzt und statistisch subtrahiert. Die Wirkungsquerschnitte für Charm-Produktion mit semileptonischem Zerfall des Charm-Quarks wurden in den zwei kinematischen Bereichen $1 < Q^2 < 1000\,\mathrm{GeV}^2$ und $10 < Q^2 < 200\,\mathrm{GeV}^2$ mit $0.03 < y < 0.7$ für beide Bereiche zu $532 \pm 27^{+40}_{-96}$ pb und $226 \pm 12^{+14}_{-34}$ pb bestimmt. Die Ergebnisse stimmen gut mit den theoretischen Vorhersagen aus QCD Berechnungen in nächstführender Ordnung (NLO) überein. Außerdem wurden die differentiellen Wirkungsquerschnitte, als Funktionen von W, Q^2, x, $p_{t\ electron}$ und $\eta_{electron}$ bestimmt. Sie zeigen ebenfalls zufriedenstellende Übereinstimmung mit NLO Vorhersagen. Die gemessenen Wirkungsquerschnitte wurden auf den gesamten $p_{electron}$ und $\theta_{electron}$ Bereich extrapoliert, um den Charm-Beitrag $F_2^{c\bar{c}}$ zur Strukturfunktion F_2 des Protons zu bestimmen. Die gemessene Strukturfunktion $F_2^{c\bar{c}}$ stimmt sowohl mit den theoretischen Vorhersagen als auch mit den Ergebnissen aus der Messung der D Mesonen Zerfälle bei ZEUS überein. Die Messung ergab, daß der Beitrag von $F_2^{c\bar{c}}$ zu F_2 zu kleinen x und großen Q^2 Werten bis zu 30 % ansteigt.

Contents

List of Figures

Chapter 1

Introduction

Electron scattering experiments have for many years played a central part in the endeavour to understand the structure of matter. In 1967 the first deep-inelastic electron proton scattering experiments were performed at the Stanford Linear Accelerator (SLAC). The experimental results indicated that the proton consists of point-like constituents, called partons [Blo69, Pan68]. The partons were identified with the quarks, which had been proposed in 1964 by Gell-Mann and Zweig [Gel64, Zwe64]. They developed a successful scheme, which explained how the then known hadrons consisted out of three types of fermions, the quarks. The quarks were distinguished by their different flavours, up (u), down (d) and strange (s). All hadrons known at that point could be built from these three quark types. However, to explain the existence of the Δ^{++} baryon which has spin 3/2 and consists of three identical spin-1/2 u quarks, the model had to be extended. A hadron consisting of identical quarks in the same quantum state would violate the Pauli principle. An additional quantum number, called colour, was introduced.

The existence of another heavier fourth quark flavour - charm (c) - was predicted by Glashow, Iliopulus and Maiani in 1970 [Gla70]. Only a few years later, in November 1974, the J/Ψ meson, which is the $c\bar{c}$ bound state, was discovered independently by two groups. At SLAC a very narrow resonance at 3.1 GeV was observed in e^+e^- collisions [Aug74], and at Brookhaven the same resonance was found colliding protons with a Be-target [Aub74]. A similar narrow resonance, the Υ at $9.5 - 10.5$ GeV was discovered in 1977 [Her77]. It was attributed to the bound state of an even heavier fifth quark, the beauty (b) quark. This discovery was followed by the prediction of the sixth quark, the top (t) quark. The observation of the top quark in $p\bar{p}$ collisions at Fermilab in 1995 was a great success for the Standard Model of elementary particle physics [Aba95, Abe95].

Today the Standard Model is the most successful and widely accepted theory to describe the interaction between quarks and leptons. The three forces of the weak, electromagnetic and strong interactions are combined in this model. Deep-inelastic lepton-nucleon scattering experiments play a crucial rôle in understanding the fundamental interactions. At DESY in Hamburg the HERA collider offers the possibility to study deep-inelastic ep scattering processes. The results from the two HERA experiments, ZEUS and H1, yield new insights into the substructure of the proton and provide a testing ground for quantum chromodynamics (QCD), the theory describing the strong interaction between quarks and gluons. A substantial fraction of the inclusive deep-inelastic ep scattering cross section was found to originate from charm production. Hence measurements of charm production in these events is of special interest in understanding the structure of the proton. The predominant production mechanism of charm in deep-inelastic ep scattering events is the boson-gluon-fusion process, $\gamma^* g \to c\bar{c}$, which means a measurement of charm production is sensitive to the gluon distribution of the proton. In addition, the high mass of the charm quark provides another hard scale apart from Q^2 (negative of the square of the four-momentum transfer from the scattered lepton to the proton) allowing perturbative QCD calculations to be performed more reliable.

The first measurement of the differential charm cross sections and the charm contribution, $F_2^{c\bar{c}}$ to the proton structure function F_2 was obtained by ZEUS and H1 using the data taken in 1994 [Adl96,Br97A]. Both experiments observed charm production via the detection of the decay products of charmed D mesons. Recently ZEUS published new results obtained from the data taken in 1996/97 in the same decay channel [Br00A]. The luminosity exceeds that for the 1994 analysis by more than a factor ten.

The topic of this thesis is the measurement of charm production in deep-inelastic scattering events using the semileptonic decay channel of charmed hadrons into electrons. This decay has a higher branching ratio than the decay channel of the D mesons, and therefore provides better statistics. The data set from 1996/97 with an integrated luminosity of $34\,\mathrm{pb}^{-1}$ is used. An inclusive measurement of all electrons in the selected deep-inelastic scattering events is performed. After estimation of the contribution from electrons from non-charm decays, a charm cross section, as well as differential cross sections and $F_2^{c\bar{c}}$ are determined. For the identification of the electrons the central tracking detector is used. The measurement of the energy loss due to ionization of the particles allows electrons to be distinguished from hadrons on a statistical basis.

This thesis starts with a theoretical description of deep-inelastic scattering processes. The proton structure function F_2 is introduced and its interpretation in terms of QCD is discussed. An overview of the charm production mechanism, the process of fragmentation and the semileptonic decay of charmed hadrons is given. The third chapter describes the HERA collider and the ZEUS detector. Emphasis is put on those detector components used for the analysis. Chapter 4 gives a brief overview over the Monte Carlo generators used and the theoretical calculations used in the physics simulations. The reconstruction and selection of the deep-inelastic ep scattering events is explained in Chapter 5. The further selection of events with semileptonic charm decays is described in Chapter 6. The use of the energy loss dE/dx to identify electrons is explained in more detail in the first part. The second part of this chapter demonstrates how the electron background from non-charm decays is estimated. The calculation of cross sections and the structure function $F_2^{c\bar{c}}$ is presented in Chapter 7. The results are compared with theoretical predictions as well as with the results obtained via the D meson decay channel. In Chapter 8 the analysis is summarized and some conclusions are drawn.

Chapter 2

Theoretical Overview

For the theoretical understanding of high energy ep scattering three out of the four fundamental forces of nature are relevant. These are the electromagnetic, weak and strong interactions. They are all believed to be accurately described by a quantum field theory possessing local gauge symmetries. Quantum electrodynamic (QED) describes the electromagnetic interaction with the massless photon as the intermediary gauge boson. QED is unified with the weak interaction in the standard electroweak model. The heavy $W^{\pm}$ and Z^0 particles are the gauge bosons of the weak interaction. In the 1970s quantum chromodynamics (QCD) was developed as the theory of strong interactions, describing quark and gluon interactions. QCD is based on a non-abelian local SU(3) colour symmetry. Each quark appears in one of three colour states. The strong force is mediated by massless gluons, which themselves carry colour.
This chapter gives a brief overview of the theory describing the physics of the analysis presented in this thesis. The first section explains the kinematics of deep-inelastic ep scattering (DIS) events in general and their interpretation in the framework of QCD. The production mechanism of heavy quarks in DIS events, the subsequent fragmentation into hadrons and their semileptonic decays are discussed in the second section. Further information can be found in textbooks [Ell96, Hal84].

2.1 Deep-Inelastic Scattering

A lepton-nucleon scattering process is defined as a deep-inelastic scattering (DIS) event, if the exchanged boson in the lepton-nucleon scattering process is highly virtual, i.e. $Q^2 \gg \mathcal{O}(1\,\mathrm{GeV}^2)$, where Q^2 is the negative of the square of the four-momentum transfer from the scattered lepton to the proton. Measuring the final state of deep-inelastic ep scattering events allows to determine the structure of the proton. Within the picture of the quark parton model, the proton consists of quarks and gluons. The highly-energetic incoming electron then probes the structure of the proton by coupling through the electroweak current to one of the partons inside the proton. For neutral current (NC) events, $e+p \longrightarrow e+X$, the exchanged boson is either a virtual photon γ^* or a Z^0 boson. For charged current (CC) events, $e+p \longrightarrow \nu_e + X$, the exchanged boson is the charged W boson, and the final state lepton is a neutrino, which escapes the detector undetected.

2.1.1 Kinematic Variables

In 1996/97 the center of mass energy $\sqrt{s}$ of the ep scattering process at HERA was 300 GeV due to the beam energies of $E_e = 27.5\,\mathrm{GeV}$ for the electrons and $E_p = 820\,\mathrm{GeV}$ for the protons.

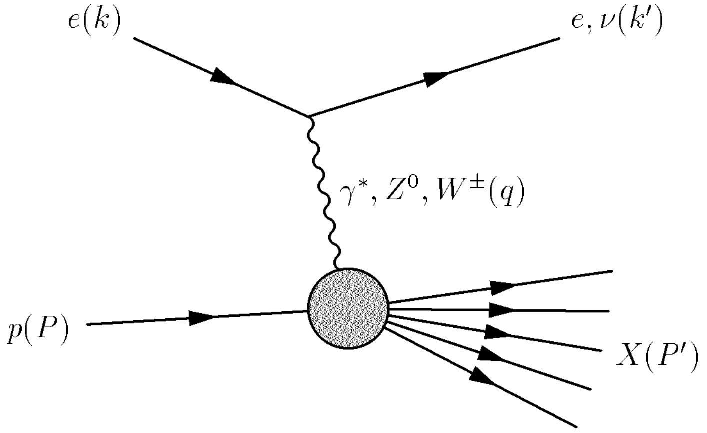

Figure 2.1: *Schematic diagram of a deep-inelastic ep scattering event. The four vectors of the particles are given in parentheses.*

Figure 2.1 shows a DIS event schematically. The symbols of the four-vectors of the incoming and outgoing particles are given in parentheses. Only two variables are needed to fully determine the kinematics of DIS events. Usually two out of the following three are chosen:

$$\begin{aligned} Q^2 &= -q^2 = -(k-k')^2 , \\ x &= \frac{Q^2}{2P\cdot q} \text{ and} \\ y &= \frac{q\cdot P}{k\cdot P} , \end{aligned} \tag{2.1}$$

where Q^2 is the negative squared four momentum transfer from the incoming electron to the proton. In the quark parton model, x can be interpreted as the momentum fraction of the proton carried by the struck parton and is called Bjorken x. The variable y represents the fractional energy transfered to the proton in its rest frame.
Neglecting the electron and proton masses, m_e and m_p, the three variables are related to each other by

$$Q^2 = x\cdot y\cdot s\,. \tag{2.2}$$

The square of the invariant mass of the hadronic final state system X is given by

$$W^2 = (P+q)^2 = Q^2(\frac{1}{x}-1)+m_p^2\,. \tag{2.3}$$

2.1.2 Cross Sections for DIS Events

The main subject of this thesis is the measurement of the cross section for heavy quark production in neutral current DIS events. Hence the following discussions will focus on neutral current events only. The theoretical description of the cross section for deep-inelastic scattering events consists of a leptonic and a hadronic part

$$d\sigma \sim L_{\mu\nu}\cdot W^{\mu\nu}\ . \tag{2.4}$$

The leptonic tensor $L_{\mu\nu}$ describes the interaction of the electron with the exchanged boson. $L_{\mu\nu}$ is calculable within the electroweak theory. For $Q^2 \ll M^2_{Z^0}$ photon exchange dominates and the leptonic tensor is described by QED alone. At higher energies, $Q^2 \sim M^2_{Z^0}$ the contribution from

Z^0 boson exchange must be taken into account. The interaction of the exchanged boson with the proton is described by the hadronic tensor $W^{\mu\nu}$. The hadronic tensor is not fully calculable but it can be parametrized. Assuming Lorentz invariance and four-vector current conservation, the double differential Born cross section of DIS events may be expressed in terms of structure functions F_1, F_2 and F_3 of the proton

$$\left(\frac{d^2\sigma^{NC}(e^{\pm}p)}{dx\ dQ^2}\right)_{Born} = \frac{4\pi\alpha^2}{xQ^4}[y^2 xF_1^{NC}(x,Q^2)+(1-y)F_2^{NC}(x,Q^2)\mp(y-\frac{y^2}{2})xF_3^{NC}(x,Q^2)] \quad (2.5)$$

where α is the electromagnetic coupling constant.
The structure functions express the non-calculable part of the hadronic tensor. The structure function F_3^{NC} represents the parity-violating contribution to the differential cross section due to Z^0 exchange, and thus only becomes noticeable at very high Q^2. For the analysis which is the subject of this thesis, the important regime is $Q^2 \ll M_{Z^0}^2$. Hence in the following discussions only γ^* exchange is considered. The structure function F_1 is related to F_2 and the longitudinal proton structure function F_L by the relation $F_L = F_2 - 2xF_1$. The contribution of F_L to the cross section is small, and only becomes significant at high y.
The structure functions in Equation 2.5 are defined with respect to the Born cross section, thus no electroweak radiative effects are taken into account. The measured cross section however also includes contributions from radiative processes, such as initial and final state radiation, where a photon is emitted from the electron before or after interacting with the proton. The measured double differential cross section is related to the Born cross section by

$$\left(\frac{d^2\sigma^{NC}(e^{\pm}p)}{dx\ dQ^2}\right)_{meas} = \left(\frac{d^2\sigma^{NC}(e^{\pm}p)}{dx\ dQ^2}\right)_{Born}[1+\delta_r(x,Q^2)] \quad . \quad (2.6)$$

The term $\delta_r(x,Q^2)$ contains the electroweak radiative corrections.

2.1.3 The Naive Quark Parton Model

The naive quark parton model describes the proton as consisting of point-like non-interacting constituents, the quarks. The deep-inelastic ep scattering process is then simply the scattering of a point-like particle inside the proton, as depicted in Figure 2.2. Thus for large enough Q^2 the point-like constituents of the proton can be resolved. Consequently for even higher Q^2 the structure functions, which describe the photon-proton scattering process, should no longer depend on some length scale $1/Q$, characterizing the size of the constituents of the proton. Therefore, in this model, the structure functions are expected to be independent of Q^2 because no further detailed structure can be resolved. Hence it follows that the structure functions only depend on one parameter, i.e. on x. This scaling behaviour of the structure functions

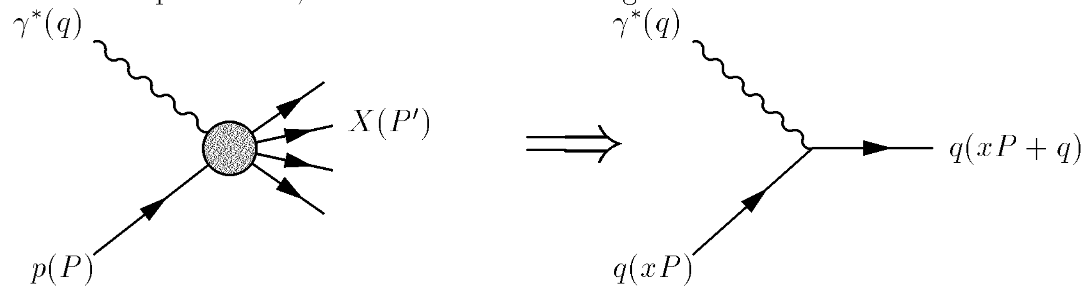

Figure 2.2: *For high Q^2 the ep scattering process (left picture) becomes an eq scattering process (right picture).*

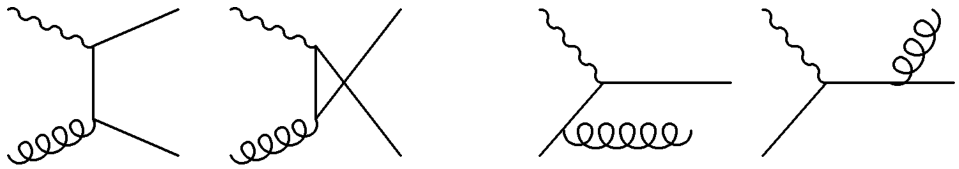

Figure 2.3: *The boson-gluon-fusion (BGF) processes (left two diagrams) and the QCD Compton processes (right two diagrams), $\mathcal{O}(\alpha_s)$ contributions to $ep \longrightarrow eX$.*

was predicted by Bjorken, and was observed in DIS experiments at SLAC a short time later [Bjo69].
In the picture of the quark parton model, the structure function F_2 for photon exchange only can be simply expressed in terms of quark densities $f_a(x)$ in the proton,

$$F_2(x) = \sum_a e_a^2 x f_a(x) \tag{2.7}$$

where the index a runs over all quark flavours and e_a is the charge of quark a. The structure functions F_1 and F_2 are related by the Callan-Gross relation, $2xF_1(x) = F_2(x)$. This is a consequence of the quarks being point-like spin $\frac{1}{2}$ particles. Hence it follows that the longitudinal structure function $F_L = F_2 - 2xF_1$ is zero in the picture of the naive quark parton model.
Another prediction from the naive quark parton model is that the integrated momentum fraction $\varepsilon_q = \sum_a \int_0^1 dx x f_a(x)$ carried by all quarks inside the proton should be equal to unity. However measurements showed that only about 50 % of the protons momentum is carried by the quarks. Hence the remaining 50 % must be carried by electrically neutral particles, the gluons described by QCD.

2.1.4 Quantum Chromodynamics

The gluons are the gauge bosons of the strong force. The strong interaction between quarks and gluons is described by QCD, a non-abelian gauge theory based on the SU(3) colour symmetry group. Quarks carry colour, the charge of the strong interaction. They appear in one of the three colours, red, green or blue. Colour is exchanged between the quarks via gluons. As a consequence of the non-abelian structure of QCD, the gluons themselves carry colour (forming a colour octet) and therefore interact with each other. The coupling constant of the strong force, α_s, is scale-dependent[1] . Towards high Q^2, and hence small distances, the coupling decreases. The dependence on the scale is given by the renormalization group equation. To leading order the strong coupling constant is given by

$$\alpha_s(Q^2) = \frac{12\pi}{(33 - 2N_f)\ln\left(\frac{Q^2}{\Lambda^2}\right)} \tag{2.8}$$

where N_f is the number of quark flavours. The parameter Λ describes the scale at which the coupling becomes large. For $Q^2 \gg \Lambda^2$, α_s decreases logarithmically and a perturbative description of the interaction is possible. This means due to the small coupling at high energies, the quarks inside the proton may be regarded as free at high Q^2 (asymptotic freedom). For low Q^2, i.e. $Q^2 \leq \mathcal{O}(\Lambda^2)$, the coupling becomes large and a perturbative description is no longer valid. Due to the large coupling at low Q^2, and hence at long distances, quarks cannot be observed as free particles but only as bound states in colourless hadrons. This behaviour is

[1] α, the electromagnetic coupling constant is also scale dependent, but to a lesser extent.

called confinement. Λ is not predicted by theory and so it must be determined by experiment. It is found to have a value of (100-300) MeV.

Since we have to take gluon radiation into account, the naive quark parton model, described in Section 2.1.3, which ignores any colour interactions is incomplete. In addition to $q\gamma^* \longrightarrow q$, processes like $q\gamma^* \longrightarrow qg$ (QCD Compton scattering) and $g\gamma^* \longrightarrow q\bar{q}$ (boson-gluon-fusion, BGF) also contribute to the cross section for deep-inelastic ep scattering. In the case of QCD Compton scattering, the quark radiates a gluon either before or after interacting with the virtual photon. If a gluon splits into a quark antiquark pair, and one of the quarks interacts with the virtual photon, the process is called boson-gluon-fusion. These two additional processes are shown schematically in Figure 2.3. In terms of perturbative QCD, the QCD Compton and BGF processes are leading order (LO) α_s contributions to the deep-inelastic cross section.

In the perturbative calculation of cross sections, divergences occur. The divergences can be interpreted in terms of virtual fluctuations, such as a gluon fluctuating into a $q\bar{q}$ or gg pair. The divergences can be absorbed into changes of the strong coupling constant α_s. Therefore a cut-off parameter, μ_R, is introduced and all fluctuations that occur at time scales $\Delta t < 1/\mu_R$ are absorbed into $\alpha_s(\mu_R)$.

2.1.5 Factorization for the Structure Functions

Perturbative QCD permits the calculation of the cross sections for scattering processes like $q\gamma^* \longrightarrow q$, $q\gamma^* \longrightarrow qg$ or $g\gamma^* \longrightarrow q\bar{q}$ at high Q^2 (hard scattering processes) because α_s becomes small. For calculations of ep scattering processes, the distributions of the quarks and gluons in the proton must be known. These parton densities are not calculable in perturbative QCD since α_s is large (confinement). The 'factorization theorem' defines the structure functions as a convolution of the hard scattering process, $\hat{F}_i^a$ calculable in perturbative QCD, with the parton densities $f_a(x)$ inside the proton [Col85]. The structure functions F_i of the proton may be written as follows:

$$F_i(x, Q^2) = \sum_a f_a(x, \mu_F) \otimes \hat{F}_i^a\left(x, \frac{Q}{\mu_F}, \alpha_s(\mu_R)\right) \tag{2.9}$$

where the sum runs over gluons and all quark and antiquark flavours. The factorization of the structure functions requires the introduction of the factorization scale μ_F. It divides the soft physics, namely the parton densities, from the hard physics, which is calculable in perturbative QCD. The partonic structure function $\hat{F}_i^a$ describes the hard scattering process between the virtual photon and the parton. Consequently both quantities, $f_a(x, \mu_F)$ and $\hat{F}_i^a(x, \frac{Q}{\mu_F}, \alpha_s(\mu_R))$, depend on the factorization scale μ_F. The measured quantities are independent of any arbitrary scale introduced by theory. In principle the factorization scale μ_F and the renormalization scale μ_R can take any values. A straightforward and common choice however is to set $\mu_F = \mu_R = Q = \mu$.

Different schemes exist to define the parton densities and the factorization and renormalization scale μ. Two schemes are used frequently, the $\overline{MS}$ (minimal subtraction) scheme and the DIS (deep-inelastic scattering) scheme. In the DIS scheme the corrections to all orders in α_s are absorbed into the parton density functions, such that the structure function F_2 is simply defined as $F_2(x, Q^2) = x\sum_a e_a^2 f_a(x, Q^2)$.

In Section 2.1.3 the structure function F_2 was already expressed in terms of quark densities of the proton within the picture of the naive quark parton model. In terms of QCD, Equation 2.7 is the lowest order, $\mathcal{O}(\alpha_s^0)$, calculation of the structure function F_2 using the factorization theorem as in Equation 2.9.

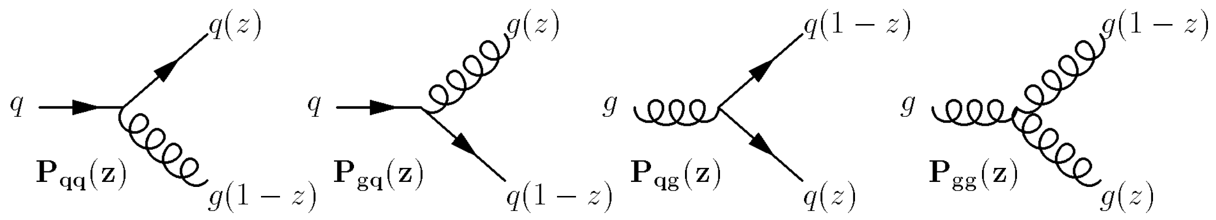

Figure 2.4: *The splitting functions.*

The concept of factorization also holds for the fragmentation of the struck partons into hadrons, where the process of a quark fragmenting into a hadron is also not calculable using perturbative QCD (see Section 2.2.3).

2.1.6 DGLAP Evolution Equations for Partons

Although the initial parton densities cannot be calculated perturbatively, QCD predicts their evolution with Q^2 if the density at a certain initial $Q^2 = Q_0^2$ value is given. The evolution is described by a set of integro-differential equations known as the DGLAP evolution equations after Dokshitzer, Gribov, Lipatov, Altarelli and Parisi [Alt77, Dok77, Gri72]. The evolution of the quark density is given by

$$\frac{dq_i(x,Q^2)}{d\ln(Q^2)} = \frac{\alpha_s(Q^2)}{2\pi}\int_x^1 \frac{dy}{y}\left(q_i(y,Q^2)P_{qq}\left(\frac{x}{y}\right) + g(y,Q^2)P_{qg}\left(\frac{x}{y}\right)\right) \tag{2.10}$$

and the evolution of the gluon density is given by

$$\frac{dg(x,Q^2)}{d\ln(Q^2)} = \frac{\alpha_s(Q^2)}{2\pi}\int_x^1 \frac{dy}{y}\left(\sum_i q_i(y,Q^2)P_{gq}\left(\frac{x}{y}\right) + g(y,Q^2)P_{gg}\left(\frac{x}{y}\right)\right)$$

where i denotes the quark flavour, and the sum runs over all quarks and antiquarks of all flavours. P_{pp} are the splitting functions

$$\begin{aligned}
P_{qq}(z) &= \frac{4}{3}\,\frac{1+z^2}{1-z} \\
P_{gq}(z) &= \frac{4}{3}\,\frac{1+(1-z)^2}{z} \\
P_{qg}(z) &= \frac{1}{2}\left(z^2+(1-z)^2\right) = P_{qg}(1-z) \\
P_{gg}(z) &= 6\left(\frac{1-z}{z} + \frac{z}{1-z} + z(1-z)\right)
\end{aligned} \tag{2.11}$$

They represent the probability for a quark to radiate a gluon or for a gluon to split into a quark-antiquark pair. The different processes are shown schematically in Figure 2.4.

The DGLAP equations express the fact that a quark (gluon) with momentum fraction x can come from a quark or gluon with momentum fraction $y > x$ which either radiated a gluon or split into a quark-antiquark or gluon-gluon pair. The probability for such a splitting or radiation is proportional to the respective splitting function. The integral runs over all possible momentum fractions $y > x$. Having a starting value for the parton density at fixed Q_0^2 the parton densities can then be evolved to any Q^2 value.

Due to the quarks radiating gluons as described by QCD and the gluons splitting into $q\bar{q}$ pairs, the picture of the naive quark parton model is only a first order approximation. One of the consequences is the scaling violation of the proton structure functions. Figure 2.5 shows the

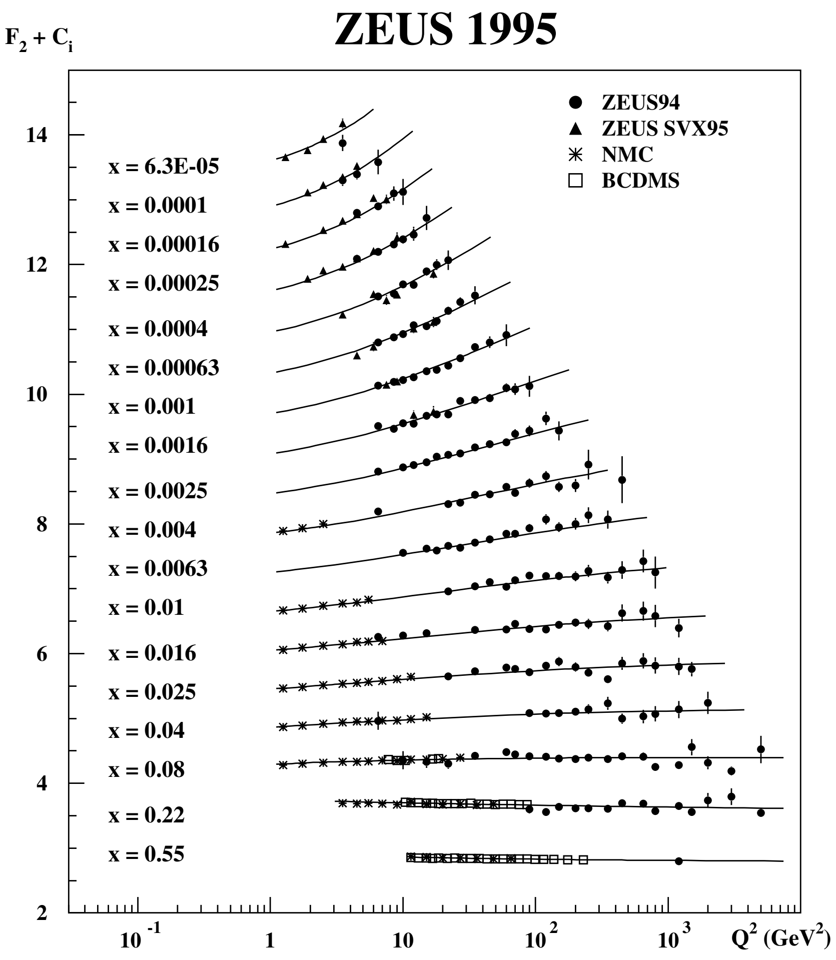

Figure 2.5: *The scaling violation of the proton structure function F_2 versus Q^2 for different values of x [Br99A].*

proton structure function F_2 versus Q^2 for different values of x. It can be seen, that only for $x \sim 0.22$ the structure function is independent of Q^2, but for lower x, F_2 increases significantly with increasing Q^2. The quarks inside the proton produced by gluon splitting are called sea quarks. Their number increases towards lower x. For increasing Q^2 more and more sea quarks at low x can be resolved. As a consequence the structure function rises with Q^2 in this low x region. Towards higher x the valence quarks carry the proton's momentum and the quark density decreases. Thus no more detailed structure can be resolved with higher Q^2 and the structure function decreases.

For a fixed value of α_s the scaling violation of the structure functions is calculable via perturbative QCD. Thus, its measurement allows the extraction of the gluon density in the proton (see Figure 2.6). It should be noted that QCD predicts that the parton densities are universal. They do not depend on the probe, and should therefore be independent of the measuring experiment.

QCD also predicts the emission of partons with a non-zero p_t with respect to the virtual photon due to gluon radiation of the quarks. The parton direction can be measured by measuring the jet of particles produced. A comparison of this measurement with QCD predictions is thus another important cross-check of the validity of QCD.

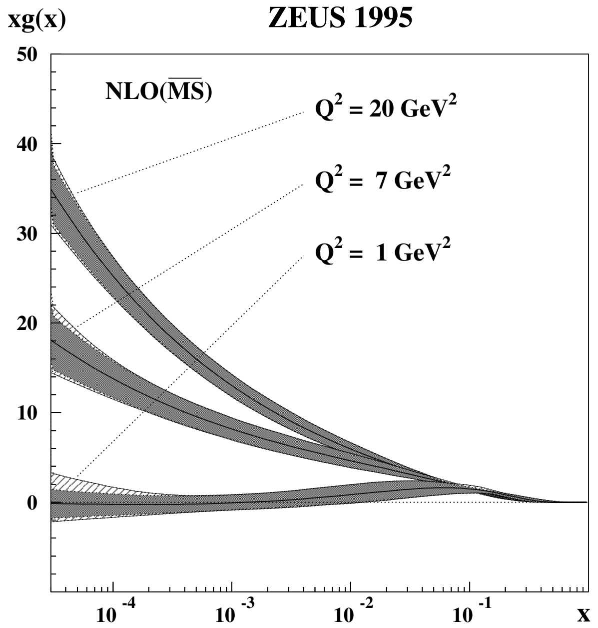

Figure 2.6: *The gluon momentum distribution $xg(x)$ as a function of x for different Q^2 values. The distribution is obtained from a ZEUS QCD fit to ZEUS and fixed target data as described in [Br99A].*

2.1.7 Parton Parametrizations

In order to extract the parton densities from measured proton structure functions, a parametrization of the densities, with a number of tunable parameters, is fitted to the experimental data. Once the parameters are tuned at a given Q_0^2, the obtained parametrization can be evolved to any Q^2 using the DGLAP evolution equations. Due to the universality of the parton densities the data used for the fit need not be restricted to ep scattering only, and data from other experiments, for instance $p\bar{p}$ scattering, may be used as well. This approach is used by the CTEQ collaboration and by Martin, Roberts and Stirling (MRS) [Lai97, Mar94]. They choose a starting scale Q_0^2 of a few GeV^2 to fit their parametrization and then evolve to higher Q^2 using the DGLAP equations.

In this analysis a model developed by Glück, Reya and Vogt (GRV) is used [Glü92]. They assume that at a very low scale $Q_0^2 \simeq 0.34\,\text{GeV}^2$ the proton consists only of valence-like quarks and gluons, which are parametrized. The sea quarks and gluons are then produced from the valence partons via DGLAP evolution.

2.2 Heavy Quarks in DIS

Quarks with masses which are considerably higher than the value of Λ, for instance $m_{c/b} \gg \Lambda$, with $m_c = 1.1$ to $1.4\,\text{GeV}$ and $m_b = 4.1$ to $4.4\,\text{GeV}$ [Cas99], are regarded as so-called "heavy" quarks. Therefore, in addition to Q^2, representing the hard scale for deep-inelastic ep scattering, another hard scale appears if we consider heavy quark production in such events ($\alpha_s(\mu = m_c) = 0.39$, $\alpha_s(\mu = m_b) = 0.22$ [Cas99]). This makes the measurement of heavy quark production in DIS an interesting test of perturbative QCD.

2.2.1 Charm Quark Production Mechanism

In this section the heavy quark production mechanisms and their description in theory are discussed. The focus is on open charm production only, since this is the subject of this thesis. Two theoretical approaches exist to describe the production of charm in deep-inelastic ep scattering. In the first approach no charm inside the proton is present, and it is only produced extrinsically. Hence, regarding only leading-order processes, charm is produced exclusively via the boson-gluon-fusion process, $\gamma^* g \longrightarrow c\bar{c}$, as illustrated in Figure 2.7. In this picture the charm production cross section is directly correlated with the gluon density in the proton and is therefore expected to increase towards low x. Comparisons of experimental results with theoretical predictions indeed show that the BGF process is the predominant production mechanism for charm quarks in deep-inelastic ep scattering at HERA [Br97A, Br00A, Adl96, Ad99A].
The second approach is intrinsic charm production, where a $c\bar{c}$ is assumed to exist in the proton bound state. These charm quarks are not produced by gluon splitting and are hence not described by perturbative QCD. Unlike in extrinsic production, the charm quarks from intrinsic production carry a larger momentum fraction x of the proton than the light quarks. Results from EMC fixed target experiments gave indications for this intrinsic charm component at high x [Har96, Ing91, Ing96]. The flavour excitation process assumes charm quarks to be existent in the proton sea. Here the virtual photon excites a heavy parton inside the proton, which means the process depends on the virtuality of the photon and is kinematically only possible for $Q^2 \gg m_c^2$.

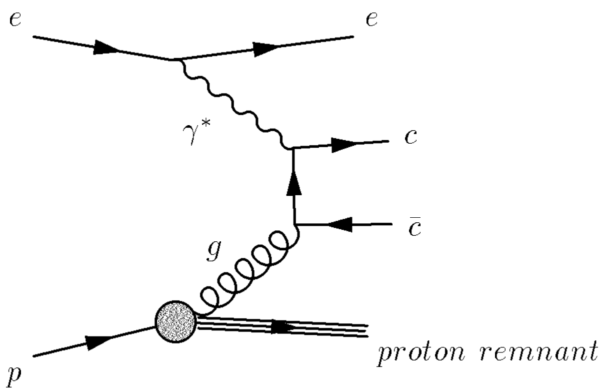

Figure 2.7: *The boson-gluon-fusion process is the dominant production mechanism for charm quarks in DIS.*

Several schemes exist to perform the calculation of heavy quark production, where the main difference between them is the treatment of the mass of the charm quark.
The zero-mass variable-flavour-number scheme (ZM-VFN) treats the charm quark as a massless parton. Depending on the scale Q^2 of the process, the number of active partons is either four or five. In Equation 2.9 the sum in this scheme runs over $a = u, d, s, g$ for $Q^2 < m_c^2$ and $a = u, d, s, c, g$ for $Q^2 > m_c^2$. The partonic structure function describes the hard scattering for all active partons, assigning them zero mass. For charm production this scheme is only a reasonable approximation for $Q^2 \gg m_c^2$, and clearly becomes unreliable in a region where $Q^2 \sim \mathcal{O}(m_c^2)$.
On the other hand, in the fixed-flavour-number scheme (FFN), a fixed number of flavours, where all quarks are regarded as massless, are assumed to contribute to the proton sea at all values of Q^2. In the FFN3 scheme only the light partons, $a = u, d, s, g$, are included in the proton parton densities f_a. The production of the heavy charm quark is calculated via the hard scattering process, using the exact, thus non-zero charm mass. The perturbative calculation

contains logarithmic factors, $\ln(Q^2/m_c^2)$, which become large if Q^2 becomes large. Hence the FFN scheme is most reliable in a region where $Q^2 \sim m_c^2$, and becomes inappropriate in the higher Q^2 region. The FFN4 scheme also treats charm as a massless active flavour at all values of Q^2 and therefore is only reliable at very high Q^2.

Other schemes exist which try to cover the problematic region between $Q^2 \sim m_c^2$ and $Q^2 \gg m_c^2$ where none of the above schemes is appropriate [Buz97]. One of them is the ACOT (Aivaziz-Collins- Olness-Tung, [Tun97]) scheme, which matches the FFN scheme with the ZM-VFN scheme with non-zero-mass charm quarks. The problematic terms in the FFN scheme, $\ln(Q^2/m_c^2)$, can be resummed and become a parton distribution f_c without taking the limit $m_c^2 \longrightarrow 0$ as done in the ZM-VFN scheme.

2.2.2 Charm Contribution $F_2^{c\bar{c}}$ to the Proton Structure Function

The double differential cross section for charm production in deep-inelastic scattering events, $e + p \longrightarrow e + c + \bar{c} + X$, where one of the charm quarks is tagged, can be expressed in terms of charm structure functions $F_i^{c\bar{c}}$, in analogy to Equation 2.5 in Section 2.1.2. Considering only virtual photon exchange, and thus neglecting F_3, and substituting F_1 by $(\frac{1}{2x}(F_2 - F_L))$, the following expression is obtained:

$$\frac{d^2\sigma_{c\bar{c}}^{NC}}{dx\ dQ^2} = \frac{2\pi\alpha^2}{xQ^4}[(1 + (1-y)^2)F_2^{c\bar{c}}(x, Q^2) - y^2 F_L^{c\bar{c}}(x, Q^2)] \ . \tag{2.12}$$

In the y range covered by this analysis the contribution to the cross section from the longitudinal structure function $F_L^{c\bar{c}}$ is small and therefore neglected. The charm contribution to the inclusive proton structure function F_2 is up to 20% at small x.

A precise measurement of $F_2^{c\bar{c}}$ and its comparison with theoretical predictions is therefore interesting for the understanding of the sea quark and gluon distribution of the proton. As discussed above, charm production is dominated in leading order by BGF, $\gamma^* g \longrightarrow c\bar{c}$. Considering Equation 2.9 the measurable quantity $F_2^{c\bar{c}}$ can therefore directly be related to the gluon density g of the proton by

$$F_2^{c\bar{c}}(x, Q^2) = g(x, \mu_F) \otimes \hat{F}_2^g(x, \frac{Q}{\mu_F}) \ . \tag{2.13}$$

$\hat{F}_2^g$ describes the BGF part, which is calculable in perturbative QCD. The extraction of $g(x)$ from charm measurements and its comparison with the result from the scaling violation of F_2 thus provides another consistency check of QCD.

In addition to the LO BGF process, next-to-leading order processes (NLO), in $\mathcal{O}(\alpha_s^2)$, contribute to the charm cross section. These are the gluon-bremsstrahlung process, $\gamma^* g \longrightarrow c\bar{c}g$, and processes of the type $\gamma^* q(\bar{q}) \longrightarrow c\bar{c}q(\bar{q})$. The $q(\bar{q})$ is a massless quark, radiating a gluon which then interacts with the virtual photon. A NLO calculation for the charm cross sections exists [Ha98A].

2.2.3 Fragmentation of Heavy Quarks

The particles observed experimentally are the decay products of the hadrons resulting from fragmentation of the charm quarks. Measurements of the charm cross section and the charm structure function $F_2^{c\bar{c}}$ therefore require assumptions about the fragmentation process and the branching of the subsequent decay into the observed particles.

To calculate the cross section for processes like $ep \longrightarrow eHX$, where H means a heavy hadron, the process of fragmentation needs to be described theoretically. The hadronization of charm

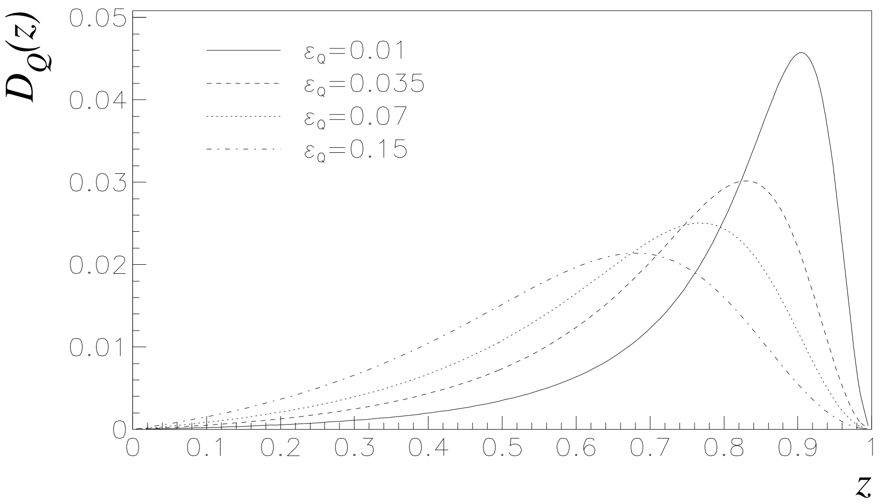

Figure 2.8: *The Peterson fragmentation function for different values of* ε_Q.

quarks into hadrons (confinement) is not calculable perturbatively in QCD, but is assumed to be independent of the hard scattering process. Hence the calculation of the cross section can be factorized in a way similar to the factorization of the proton structure function, which is described in Section 2.1.5. To extend the calculation for charm production to the production of heavy hadrons, the cross section for charm production has to be convoluted with a fragmentation function.

Several models exist to describe the process of fragmentation of heavy quarks Q into hadrons. Commonly used is the Peterson fragmentation function [Pet83] describing the transition $Q \longrightarrow H(Q\bar{q}) + q$.

$$D_Q^H(z) = \frac{N_H}{z}(1 - \frac{1}{z} - \frac{\varepsilon_Q}{1-z})^{-2} \tag{2.14}$$

The heavy quark Q with momentum P is marginally slowed down by picking up a light antiquark $\bar{q}$. The resulting hadron then carries the momentum zP, with a probability proportional to $D_Q^H(z)$. N_H is the normalization factor constrained by the sum over all hadrons containing the heavy quark, $\sum_H \int dz D_Q^H(z) = 1$. The only free parameter is ε_Q of $\mathcal{O}(m_q^2/m_Q^2)$, which can be determined from fits to experimental data from e^+e^- colliders.

Figure 2.8 shows the Peterson fragmentation function for different values of ε_Q. The function peaks at $z = (1 - 2\varepsilon_Q)$ and its width is $\sim \varepsilon_Q$. Thus the higher ε_Q the softer the spectrum of the fragmented heavy hadrons.

The variable z in Equation 2.14 is not directly accessible by experiments, and so other scaling variables which are close approximations to z must be used. Figure 2.9 shows the inclusive cross section for D^0 and D^{*+} production versus the variable $x_P = p/p_{max}$. The measurements were performed by the ARGUS [Alb91] and CLEO [Bor88] collaborations in e^+e^- collisions at $\sqrt{s} \sim 10\,\mathrm{GeV}$. A fit to the data using only the Peterson fragmentation function yields $\varepsilon_Q(D^0) = 0.135 \pm 0.010$ and $\varepsilon_Q(D^*) = 0.078 \pm 0.008$ [Cas99]. In order to obtain results which are comparable to other experiments, radiative effects such as parton shower evolution must be taken into account. This has been done by the OPAL collaboration. They studied the production of $D^{*\pm}$ mesons in Z^0 decays. The JETSET Monte Carlo generator ([Sjö94], see Section 4.1.1) was used for the simulation of parton showers. A fit of the Peterson function in conjunction with JETSET gives a softer fragmentation spectrum, with $\varepsilon_Q(D^*) = 0.035 \pm 0.009$ [Ake95]. This is the value used as input for predictions for D^* production at HERA. However,

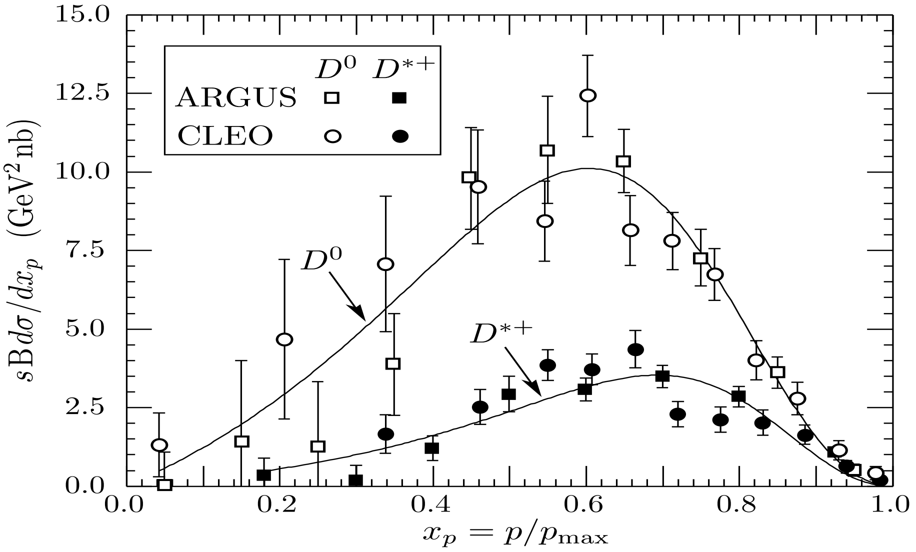

Figure 2.9: *The inclusive cross section for D^0 and D^{*+} production versus $x_P = p/p_{max}$ [Cas99]. The solid line shows the result of a fit to the data using the Peterson fragmentation function.*

since the kinematics at HERA differ from those at e^+e^- colliders it is not yet clear whether this value is applicable to HERA physics. Moreover recent calculations for photoproduction processes showed, that the value also depends on the treatment of the perturbative part of the cross sections. NLO calculations require a different value than LO calculations [Ca97A, Ca97B]. Which value to choose for NLO DIS calculation is not clear [Ha98A].

2.2.4 Semileptonic Decay of Heavy Hadrons

The semileptonic decay of the charm quark is an electroweak process, describable within the Standard Model. The decay width is proportional to squared elements of the Cabibbo-Kobayashi-Maskawa (CKM) matrix and for the most probable decay into a strange quark is given by

$$\Gamma^c_{sl} \sim |V_{cs}|^2 m_c^5 \tag{2.15}$$

depicted in Figure 2.10.
To calculate the decay width of hadrons an assumption has to be made about the influence of the accompanying light quark. In the spectator model any influence from the light quark is neglected. In the hadronic decay of the charm quark the W^+ decays into a $u\bar{d}$. The decay of the W^+ into quarks is three times more likely than the semileptonic one into electrons or muons because of the three colours of the quark. Thus the naive semileptonic branching ratio in the spectator model, ignoring any effects from strong interactions is,

$$BR(c \longrightarrow e\nu X) = \frac{1}{1+1+3} \ . \tag{2.16}$$

The semileptonic branching ratio determined from measurements is only about 9.5% [Alb92], in contradiction to the spectator model result. Moreover the spectator model predicts the lifetimes for all charmed hadrons to be equal, only dependent on the lifetime of the heavy quark

$$\tau = \frac{\hbar}{\Gamma_{leptonic} + \Gamma_{SL} + \Gamma_{nonleptonic}} \ . \tag{2.17}$$

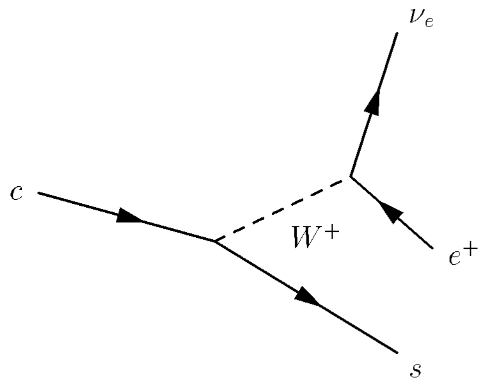

Figure 2.10: *Schematic drawing of the semileptonic charm quark decay.*

This is also inconsistent with experimental results, for instance

$$\frac{\tau(D^+)}{\tau(D^0)} \simeq 2.5 \tag{2.18}$$

The naive spectator model is not applicable to describe all decay channels of charmed hadrons. Diagrams involving the spectator quarks must be taken into account. Since the leptonic widths are negligible and the semileptonic ones are comparable, e.g.

$$\frac{\Gamma(D^0 \to e^+X)}{\Gamma(D^+ \to e^+X)} = \frac{BR(D^0 \to e^+X)\tau(D^+)}{BR(D^+ \to e^+X)\tau(D^0)} = 1.03 \pm 0.12 \tag{2.19}$$

the failure of the spectator model is due to the different hadronic decay widths of the charmed hadrons [Bia96]. Strong radiative corrections have to be taken into account as well as non-spectator diagrams. There is not yet a reliable description of non-leptonic charm decays.

Chapter 3

The ZEUS Detector at HERA

This chapter gives a brief overview of the HERA accelerator complex and the ZEUS detector. The detector components used for the analysis will be described in some detail. An extensive description of the whole detector can be found in [Der93].

3.1 The HERA Collider

The construction of the Hadron-Elektron-Ring-Anlage (HERA) was started in 1984 and finished in 1990 at the Deutsches Elektronen-Synchrotron (DESY) in Hamburg, Germany. It is the first electron proton collider and is designed to collide 820 GeV protons with 30 GeV electrons.

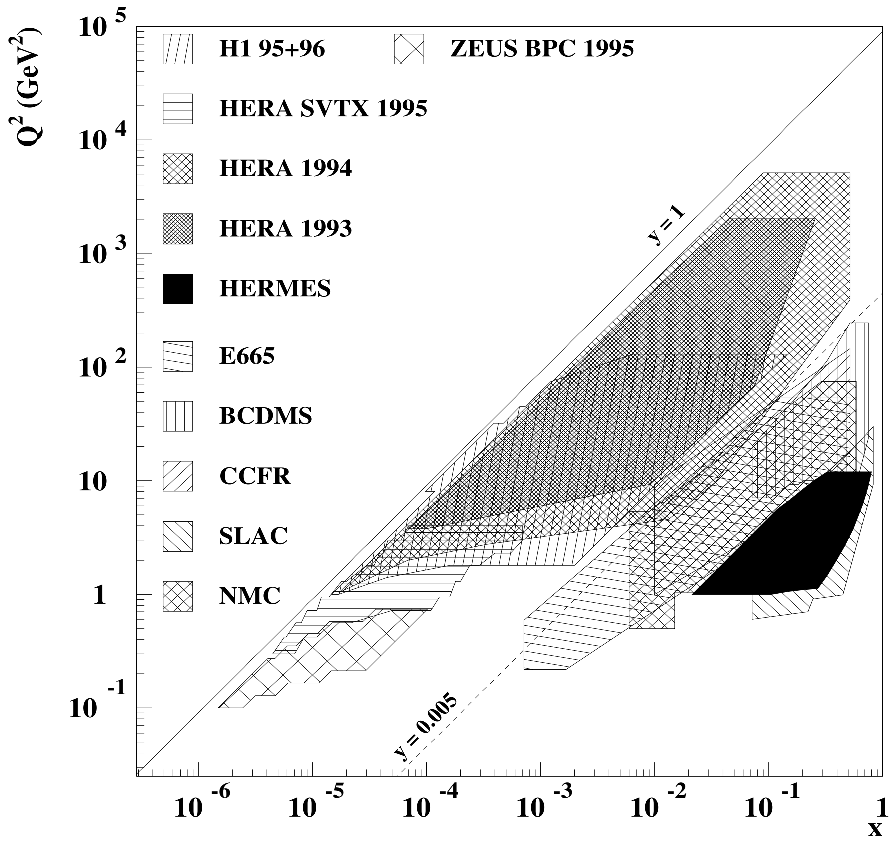

Figure 3.1: *The kinematic region covered by HERA experiments in comparison to that of fixed target experiments.*

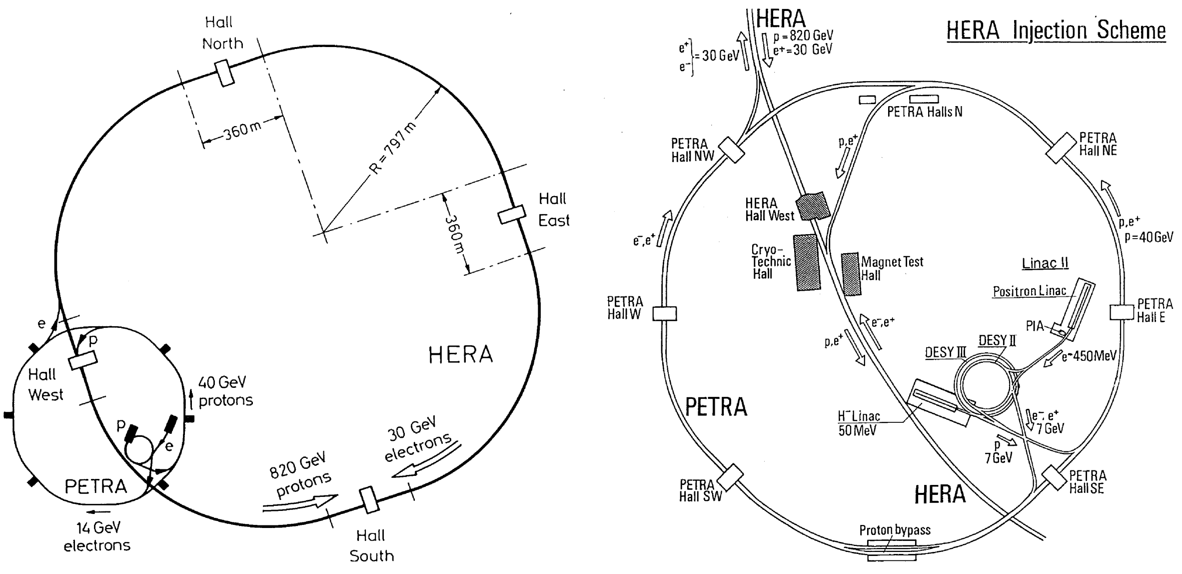

Figure 3.2: *The HERA storage ring (left) and its pre-accelerator complex (right).*

Compared to fixed target experiments the center of mass energy at HERA is an order of magnitude higher and therefore a new kinematic region is accessible. Figure 3.2 shows the (x, Q^2) plane covered by HERA experiments compared to several fixed target experiments at SLAC, Fermilab and CERN using different beams (electrons, muons, neutrinos) and targets. There is an overlap region between the fixed target and HERA experiments which gives the possibility to compare results from HERA with those obtained at the fixed target experiments. The HERA tunnel is 6.3 km long and is located 10 – 20 m underground. There are four experiments located at the HERA ring. ZEUS and H1, which reside in the South and North Halls, make use of head-on electron-proton collisions. The HERMES experiment in the East Hall uses polarized electrons to study the nucleon spin structure with an internal polarized gas target. HERA-B is located in the West Hall and is designed to study $\mathcal{CP}$ violation in the $B\bar{B}$ system. It uses a wire target in the proton beam halo for the production of B-mesons.

The HERA collider and its pre-accelerator system is shown in the left hand diagram of Figure 3.2. The right hand diagram shows the injection scheme in more detail. The proton acceleration starts with negative hydrogen ions (H^-) from the 50 MeV proton linac. After stripping the electrons off the H^- ions the remaining protons are injected into the proton synchrotron DESY III where they are accelerated up to 7.5 GeV. They are further accelerated in PETRA and at 40 GeV injected into the HERA proton storage ring. A similar acceleration scheme is performed for the electrons. The pre-acceleration starts in a linear accelerator (LINAC) up to 450 MeV, followed by an acceleration in DESY II up to 7 GeV. The electrons are then injected into PETRA, and when they have achieved an energy of 14 GeV they are injected into the HERA electron storage ring. Electrons and protons are grouped into bunches of $\mathcal{O}(10^{10})$ particles each. 210 bunches of each electrons and protons spaced by 96 ns can be filled into HERA. To study beam related background some of the 210 bunches are left empty. These are called 'pilot-bunches'. The length of the bunches is about 0.8 cm for the electrons and 11 cm for the protons. At the interaction point the transverse dimensions of the beams are made as small as possible. The electron beam width is designed to be 0.3 mm and its height 0.04 mm. For protons the width is designed to be 0.32 mm and the height 0.1 mm.

The first electron proton collisions at HERA occurred in October 1991 and ZEUS took first physics data in spring 1992. From 1994 onwards positrons were used instead of electrons, because of the longer lifetime of the positron beam. The beam energies in 1996/1997 were

Parameter	**Design Value**	**Average in 1996/1997**
proton beam energy	820 GeV	820 GeV
electron beam energy	30 GeV	27.58 GeV
proton current	160 mA	76 mA
electron current	60 mA	36 mA
number of bunches	210	180
maximal instantaneous luminosity	$1.5 \cdot 10^{31}\mathrm{cm}^{-2}s^{-1}$	$1.4 \cdot 10^{31}\mathrm{cm}^{-2}s^{-1}$

Table 3.1: *HERA beam parameters for the 1996/1997 running period compared to the design values.*

27.5 GeV and 820 GeV for positrons and protons respectively, resulting in a center of mass energy ($\sqrt{s}$) of 300 GeV. Beam parameters, such as lifetimes and currents, are listed in Table 3.1 for the 96/97 running period and are compared to their design values. Since HERA started operating in 1992, the integrated luminosity gathered each year continuously increased. The left plot in Figure 3.3 shows the delivered luminosity by HERA for the different years versus the days of running. The right plot shows the luminosity which was actually taken by the ZEUS detector. During the 1996 and 1997 running period 38 pb^{-1} of data were taken by the ZEUS detector which can be used for physics analysis. As can be seen in Figure 3.3, during 1998 and the beginning of 1999, HERA was running again with electrons. During the 1997/1998 shutdown new pumps were installed in the electron ring to improve the lifetime of the electrons. In 1998 the proton energy was raised to 920 GeV. During the shutdown in the year 2000 the HERA luminosity upgrade is planned, with the aim to increase the luminosity by a factor five.

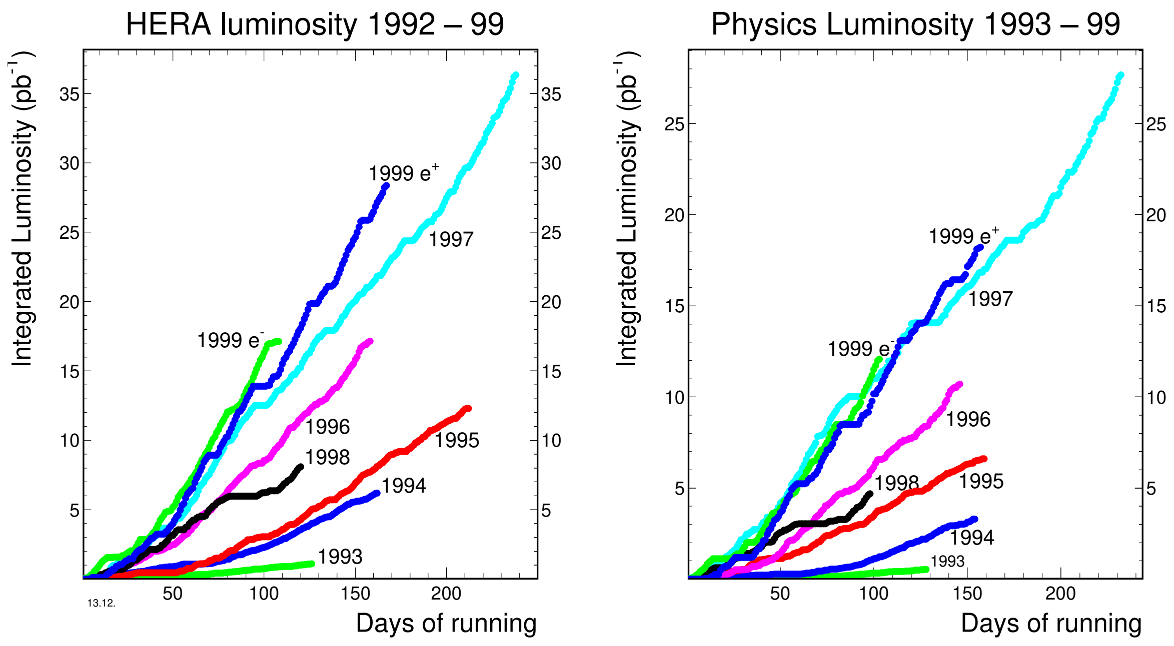

Figure 3.3: *The left plot shows the integrated luminosity delivered by HERA in the 1993-1999 running periods. The luminosity which was taken by the ZEUS detector and which is useful for physics analysis is shown in the right plot.*

3.2 The ZEUS Detector

The ZEUS detector is a multi-purpose detector, built by the ZEUS collaboration in the late 1980s. In spring 1992 it was installed in the South Hall and since then new detector components have been added continuously. The dimensions of the main ZEUS detector are $12\,\mathrm{m} \times 10\,\mathrm{m} \times 19\,\mathrm{m}$ and its weight is about 3600 tons. Figure 3.4 shows an overview of the detector. The main components are labeled. The picture shows a view of the detector in a direction perpendicular to the beam. The directions of the proton and electron beams are indicated. In the ZEUS coordinate system the direction of the outgoing protons defines the positive Z direction, also referred to as the forward direction. The right-handed ZEUS coordinate system has its origin at the nominal interaction point. In this frame the X-axis points towards the center of the HERA storage ring, the Y-axis upwards. The polar angle θ is defined with respect to the positive Z direction. The polar angle is often expressed in terms of pseudorapidity η, defined as $\eta = -\ln(\tan(\theta/2))$. The difference in pseudorapidity, $\Delta\eta$, is relativistic invariant under translation along the Z direction. The azimuthal angle ϕ is measured with respect to the positive X direction. The ZEUS detector covers most of the 4π solid angle, except for the regions around the beampipe. As can be seen in Figure 3.4, it has an asymmetric shape. Due to the large momentum difference between the electron and the proton beam, the final state particles are boosted to the forward direction.
The inner part of the ZEUS detector around the interaction point is covered by the central tracking detector (CTD), complemented by forward and rear tracking detectors (FDET, RTD). The tracking detectors are surrounded by a super-conducting solenoid producing a magnetic field of 1.43 T. Still shown in Figure 3.4 is the vertex detector (VXD) which was removed during the 1995/1996 shutdown. A new silicon microvertex detector (MVD) is under construction and will be installed during the shutdown in 2000, [Br97B]. The forward tracking will also be improved by a straw-tube tracker (STT), [Br98A]. The tracking detectors are surrounded by the the uranium-scintillator calorimeter, which is split into forward, barrel and rear parts (FCAL, BCAL and RCAL). Presampler detectors are installed in front of the calorimeter modules. To improve the discrimination between electromagnetic and hadronic showers for low energy

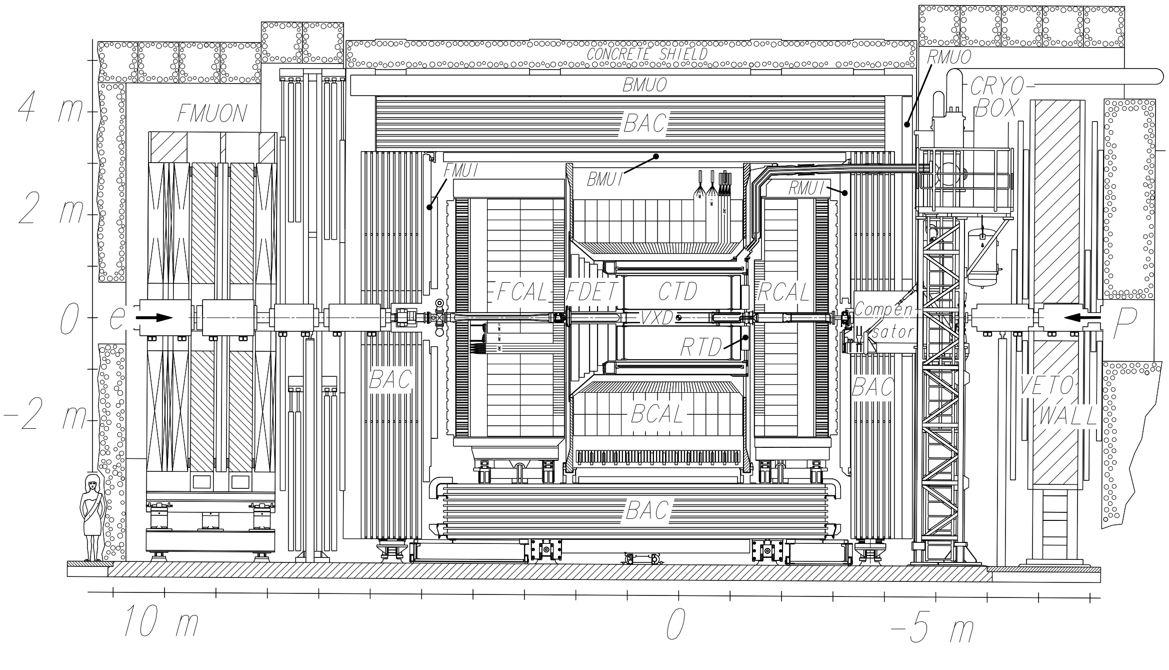

Figure 3.4: *The main ZEUS detector viewed perpendicular to the beam direction.*

particles (< 5 GeV), silicon diodes have been added in the FCAL and RCAL (hadron-electron-separator, HES). The small angle rear tracking detector (SRTD) is situated between the RTD and the RCAL, covering the region around the beampipe. To cover even smaller electron scattering angles a small electromagnetic beam pipe calorimeter (BPC) was installed in 1995 in the beam hole of the RCAL. In 1997 the position resolution of the BPC was improved by the installation of a silicon tracker in front of the BPC, the beam pipe tracker (BPT). The forward plug calorimeter (FPC) was installed in 1998 increasing the acceptance of the FCAL by one unit in pseudorapidity. The whole uranium calorimeter is enclosed by an iron yoke which provides the return path for the solenoid magnetic field flux. The yoke is instrumented to measure energy leakage of the main calorimeter (BAC). Inside and outside the iron yoke are installed the muon identification chambers, (FMUI,BMUI,RMUI and FMUO, BMUO, RMUO). Additional detectors are installed outside the main detector along the beam pipe. A scintillator counter, the proton remnant tagger (PRT), is installed around the beam pipe, at $Z = 5.1$ m. Further downstream are located the six components of the leading proton spectrometer (LPS), at distances from 24 m to 90 m from the interaction point. A forward neutron calorimeter (FNC) is installed at $Z = 105.6$ m to measure forward neutrons. In the rear direction at $Z = -7.3$ m a scintillator hodoscope with iron wall (VETO) is used to reject beam-related background. The C5 beam monitor located around the beam pipe at $Z = -3.15$ m monitors the beam condition. The LUMI detectors, consisting of two small electromagnetic calorimeters at $Z = -34$ m and $Z = -107$ m, measure bremsstrahlung events for the luminosity determination. The LUMI detectors are also used to tag photoproduction events, as well as the two additional calorimeters at $Z = -8$ m and $Z = -44$ m.

3.2.1 The Central Tracking Detector

The central tracking detector (CTD) is a cylindrical gas-filled wire chamber. The gas is a mixture of 83% argon, 5% CO_2 and 12% ethane bubbled through alcohol. Charged particles traversing the CTD ionize the gas along their trajectory, which amounts to about 10-20 ionized atoms per centimetre for minimum ionizing particles. The freed electrons drift towards the positive sense wires, while the positive ions are repelled and drift towards the negative field wires. The freed electrons drift with a velocity of approximately 50 μm/ns. In the field of the sense wire, avalanche-like multiplication of the electrons occurs, where the amplification factor is about 10^4.

The CTD consists of 72 radial layers of sense wires which are arranged into groups of eight layers forming nine superlayers (SL). A group of eight wires in the $r - \phi$ plane of each superlayer is called a cell. An octant of the CTD is shown in Figure 3.5. The large dots represent the sense wires, the smaller dots the field wires. The chamber consists of 576 drift cells in total, giving 4608 sense wires and 19584 field wires. The orientation of the wires of each cell is tilted by 45^o with respect to the radius. The tilt compensates the Lorentz angle of 45^o from the combined electric and magnetic field such that the electrons drift azimuthally towards the the sense wires. The superlayers are numbered from 1 (innermost) to 9 (outermost). The five odd-numbered superlayers have wires parallel to the chamber axis, and are called axial superlayers. The three inner axial superlayers are equipped with a z-by-timing system, which measures the time difference between the arrival times of the signal from the opposite ends of the chamber. It thereby provides fast information about the Z position of a track which is used in trigger decisions by the first level trigger (FLT). The resolution in Z obtained by the z-by-timing method is of the order of a few centimetres. The four even-numbered superlayers are called stereo layers, because they are tilted at small angles ($\sim 5^o$) with respect to the chamber axis.

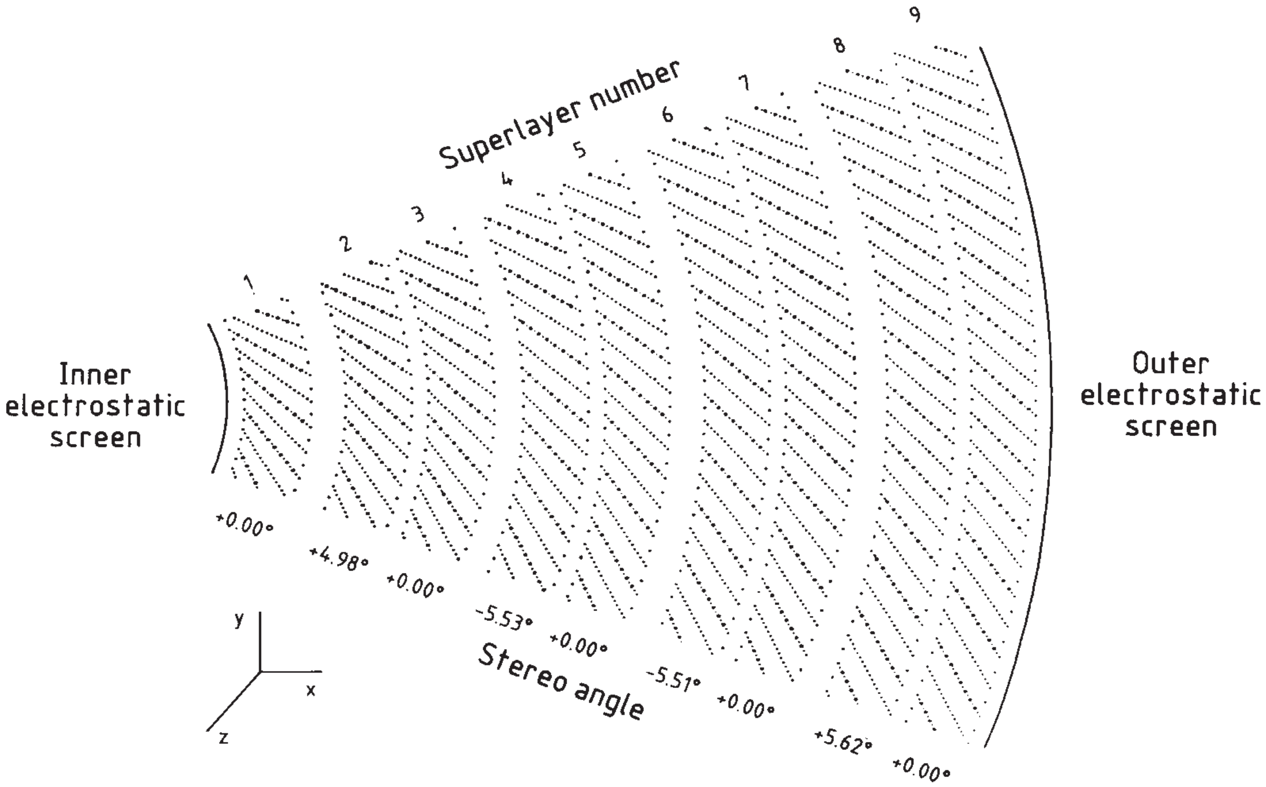

Figure 3.5: *$X - Y$ cross section through one octant of the CTD. Sense wires are indicated by the large dots.*

The tilt is zero at $Z = 0$ and largest at the ends of the chamber. The stereo layers improve the Z position resolution to $1.0 - 1.4$ mm.

The overall coverage of the polar angle by the CTD ranges from 11^o to 168^o. To have appropriate tracking quality, usually hits in at least the three innermost superlayer are demanded, giving a coverage in θ of $18 - 160^o$. The dimensions of the CTD and its angular coverage are summarized in Table 3.2.

The resolution per hit, which is θ-dependent, is approximately $200\,\mu$m. The position of the hits is calculated from the information of the arrival time of the pulses on the sense wires, assuming constant drift velocity and a straight path towards the closest wire. The resolution for the measurement of the transverse momentum p_t of a track depends on the single hit resolution as well as on multiple scattering effects inside and before the CTD. For tracks coming from the main vertex, passing at least three superlayers and with $p_t > 150\,\mathrm{MeV}$, the resolution can be parametrized as $\sigma(p_t)/p_t = 0.0058\,p_t \oplus 0.0065 \oplus 0.0014/p_t$, with p_t in GeV. The track finding efficiency for scattered DIS positrons, which have high momentum and are well isolated, is close

radius of active volume	$18.2 - 79.4$ cm
Z of active volume	$-100 \ - \ +105$ cm
overall coverage of θ	$11.3 < \theta < 168.2^o$
SL3 coverage of θ	$18.4 < \theta < 160.7^o$
SL5 coverage of θ	$24.9 < \theta < 154.0^o$
SL9 coverage of θ	$36.1 < \theta < 142.6^o$

Table 3.2: *Parameters of the CTD.*

to 100 %. For hadrons, the finding efficiency is roughly 95 %. The CTD is also used to measure the event vertex. Using stereo layer information it is determined with a resolution of 0.4 cm in Z direction and with 0.1 cm resolution transverse to the beam.

Measuring dE/dx with the CTD

Apart from position and momentum measurement, the CTD also provides information about the particle type via the energy loss due to ionization (see Section 6.3). The energy loss of a particle is approximately proportional to the number of ions produced in the gas, and thus proportional to the amount of charge measured as a signal on the sense wires.
All sense wires are read out with an 8-bit flash analogue-to-digital converter (FADC). The signals from the sense wires are digitised by sampling the signal every 9.6 ns. Thus for a given wire the data is packed into an array of digitised signals in FADC counts in time bins of 9.6 ns. These are called pulse trains. The FADC output is further analysed by digital signal processors (DSPs) which search the pulse train for groups of time bins having a characteristic pulse shape. The DSPs then determine the height of the pulse and its arrival time in bins of 2.4 ns using a constant fraction discriminator. The height of the pulse is stored as the relevant information about the energy loss of the particle rather than the area of the pulse. This is done, because the height is less affected by noise, and overlapping hits can be more easily disentangled. Studies with 1992 data showed that the height of the pulse is proportional to its area [Cat95]. The arrival time of the pulse relative to the trigger then gives the drift time. After track reconstruction the pulse heights can be associated with one trajectory through the detector and the total energy loss is given by the FADC pulse heights. The shape of the FADC signal follows a Landau-like distribution, as can be seen in Figure 3.6. Due to the limited eight bit readout, saturation occurs at 235 FADC counts for very high energy losses.
The energy loss, and thus the pulse height in FADC counts is influenced by the trajectory of the track and detector effects. First the correction for the path length dx has to be applied, which depends on the the polar angle θ of the track. In addition the different gain of the sense wires, the Z position of the hit, the drift distance, differences between positive and negative tracks and the Lorentz angle are taken into account. Finally pulses are not used for the dE/dx measurement at all if the track is parallel to the drift direction, if the drift distance is near a cell boundary or if the pulse height is distorted by an earlier hit (within 100 ns) on the same sense wire.
After these corrections, a certain number of hits form the Landau-like FADC distribution, which contains the information about the energy loss due to ionization of the particle. It is assumed to be independent of detector effects and the θ and ϕ of the track. To avoid the large asymmetric tail of the distribution a truncated mean is performed, where the 10 % lowest and 30 % highest pulses are discarded. If at least four hits remain, the mean energy loss is then defined as the sum over the remaining pulse heights divided by the remaining number of hits. If the remaining 60 % of the pulse heights still contains saturated hits they are removed in addition, thus resulting in a number of hits below 60 %. Saturated FADC pulses occur predominantly at shallow angles with respect to the beam axis where the path length of the tracks is long, but the number of hits is low. If the number of saturated hits is higher than 30 % they pull the mean dE/dx towards higher values and degrade the resolution. To recover the normalization of the remaining hits after discarding all saturated hits, a fitted polynomial correction is applied to the calculation for the mean energy loss [Ha98B,Ver98].
The value of dE/dx for a given particle type in a certain momentum and angular range changes as a function of time, due to changes in the composition of the gas and the pressure, which is equal to the atmospheric pressure. A variation in the pressure changes the density of the

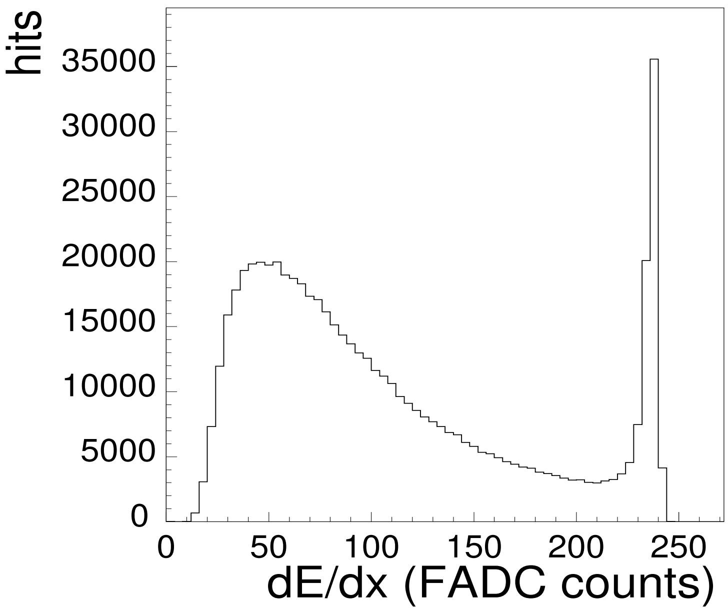

Figure 3.6: *The FADC signal for low momentum pions [Wi99A].*

gas and thus directly influences the number of ions produced. To account for any variation of dE/dx between different runs[1], all measured dE/dx values in one run are normalised to the energy loss of positive pions with a momentum of $0.3 < p < 0.4$ GeV in that run. To account also for pressure variation within a run, the pressure is monitored every 10-20 minutes and a correction factor is applied to each measured dE/dx value. The longterm variation of dE/dx with the pressure during a year are large, up to 20 %, whereas the variations within a run are at most 2 %.

3.2.2 The Uranium Calorimeter

The ZEUS calorimeter is a sandwich uranium-scintillator calorimeter. It consists of a number of layers of 3.3 mm thick depleted uranium ($98.1\%\ U^{238}, 1.7\%\ Nb, 0.2\%\ U^{235}$) plates wrapped in stainless steel foils and 2.6 mm thick sheets of plastic scintillators. The uranium plates act as the absorber material in a sense that the energy of particles traversing the material is reduced due to shower developement. The scintillators are the actual detectors, measuring the produced shower particles. The scintillators are read out via plastic wavelength shifters by photomultipliers. The thicknesses of the absorber and detector plates were chosen such that the response for hadrons and electrons is equal. Hence it is a compensating calorimeter. Due to its high atomic number (Z) uranium has a small radiation length X_0, which thus allows the detector to be more compact. The purpose of the stainless steel foils is to reduce the signal from the natural radioactivity of the uranium. It has to be reduced to a level at which it does not interfere with the measurements of real physics particles but is still high enough to be able to use the uranium noise signal for calibration purposes.
At 99.6 % of the solid angle, the interaction point is covered almost hermetically by the calorimeter. The calorimeter is constructed in three parts, the forward (FCAL), barrel (BCAL) and rear (RCAL) calorimeter. The FCAL covers polar angles from 2.2^o to 39.9^o, the BCAL from 36.7^o to 129.1^o and the RCAL from 128.1^o to 178.4^o. As can be seen in Figure 3.4 the FCAL is

[1] A period of data taking, which usually lasts a few hours.

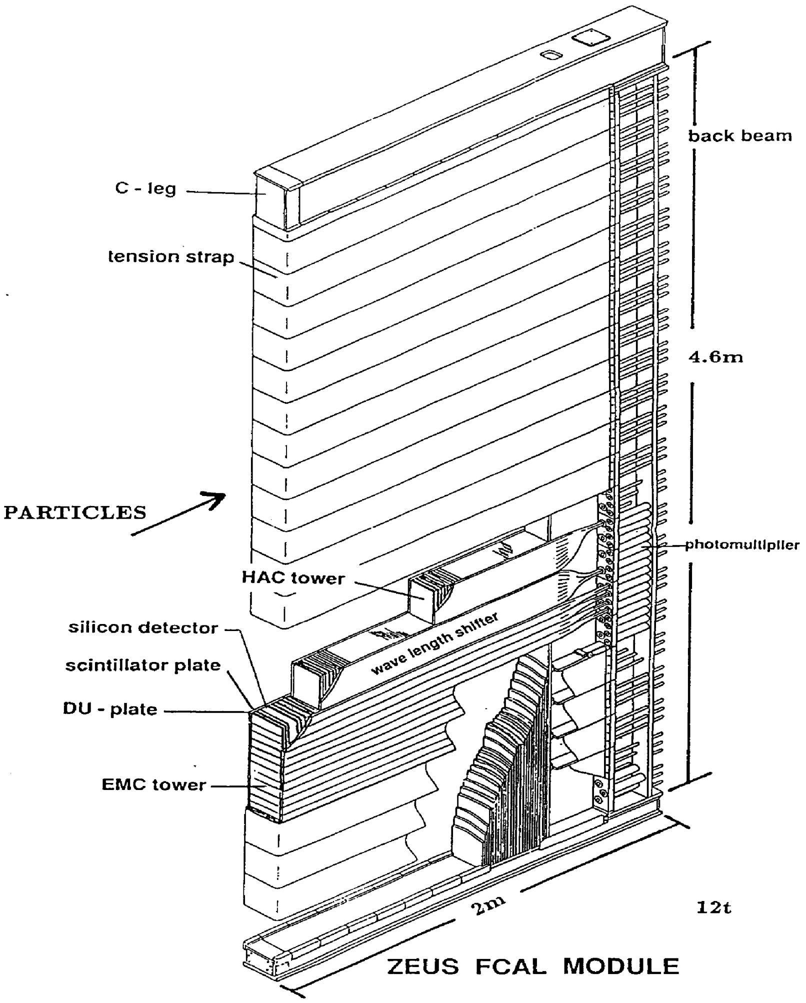

Figure 3.7: *The structure of a FCAL module.*

deeper (151 cm) than the RCAL (86 cm), to account for the asymmetry of the event topology, due to the difference in electron and proton beam energies. Each of the calorimeter parts is subdivided into modules, which are segmented into towers. As an example a module of the FCAL is shown in Figure 3.7. The towers of all modules are further segmented into hadronic (HAC) and electromagnetic (EMC) cells. The size of the front face of the EMC cells is $5 \times 20\,\mathrm{cm}^2$ (FCAL, BCAL) or $10 \times 20\,\mathrm{cm}^2$ (RCAL). The hadronic cells are larger: the cross-section at the front face is $20 \times 20\,\mathrm{cm}^2$. The depth of the EMC cells in terms of radiation length X_0 and interaction length λ is $\sim 25X_0 \sim 1\lambda$, with $X_0 = 0.74\,\mathrm{cm}$ and $\lambda = 21\,\mathrm{cm}$. The depth of the HAC cells varies between $\sim 2\lambda$ in the BCAL and $\sim 3\lambda$ in FCAL and RCAL. Each tower consists of four (FCAL, BCAL) or two (RCAL) EMC cells and one (RCAL) or two (FCAL, BCAL) HAC cells. The towers are constructed such that the EMC cells are on the inner side of the detector, pointing to the interaction point. In total there are nearly 6000 cells in the calorimeter which are read out on both sides by photomultipliers, thus resulting in about 12000 channels.

The energy resolution of the calorimeter determined from test beam measurements with some of the modules is $\sigma_h/E = 35\%/\sqrt{E}$ for hadrons and $\sigma_e/E = 18\%/\sqrt{E}$ for electrons, with E measured in GeV. The calorimeter is calibrated on a daily basis using the uranium noise signal and test pulses to an accuracy of 1 %. The timing resolution for energy deposits greater than 4 GeV is better than one nanosecond. The energy resolution of the calorimeter suffers from showering effects in the inactive material in front of the calorimeter, which amounts to up

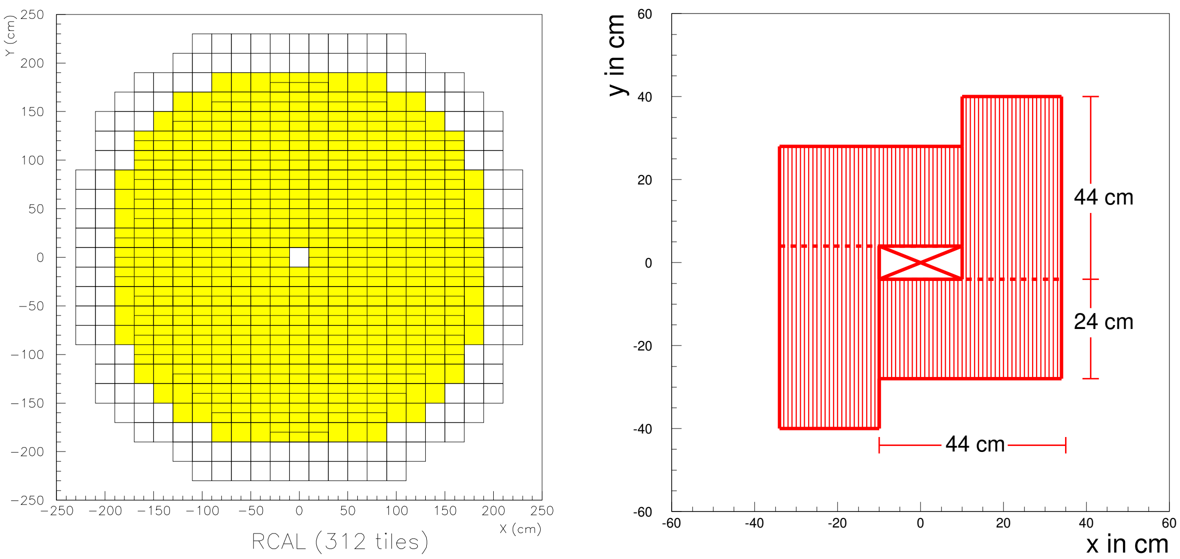

Figure 3.8: *The coverage of the front face of the RCAL by the presampler (left picture). Schematic drawing of the SRTD showing the orientation of the scintillator strips in one of the two planes (right picture).*

to four radiation lengths, depending on the angle. To improve the energy measurement the presamplers can be used, which consist of segmented scintillator arrays positioned directly in front of the calorimeter sections. The coverage of the RCAL front face by the presampler is shown in the left-hand diagram of Figure 3.8.

3.2.3 The Small Angle Rear Tracking Detector

The small angle rear tracking detector (SRTD) was installed in 1994 to improve the angle and energy measurement of the scattered electron in low Q^2 DIS events. It is located on the face of the RCAL covering the region around the RCAL beam pipe hole. The SRTD is positioned at $Z = -148\,\mathrm{cm}$ and its outer dimensions are $68 \times 68\,\mathrm{cm}^2$, which correspond to coverage of the polar angle θ from 162^o to 176^o. The upper angular limit is given by the $20 \times 8\,\mathrm{cm}^2$ hole for the beampipe. The right-hand diagram in Figure 3.8 shows the SRTD geometry.
The detector consists of two orthogonal layers of scintillator strips, each strip 10 mm wide and 5 mm thick. The pulse height information is obtained via an optical fibre-photomultiplier readout. Apart from a precise position measurement, the SRTD is also used to correct for energy losses in the inactive material in front of the detector, and thus improves the energy resolution of the calorimeter in the same way as the presamplers. In addition, the SRTD also provides fast timing information for the first level trigger (FLT) to reject beam-gas background.

3.2.4 The Luminosity Monitor

Precise knowledge of the time-integrated luminosity $\mathcal{L}_{int} = \int \mathcal{L} dt$ is required for all cross section and therefore all structure function measurements. The time-integrated luminosity enters the calculation of a cross section σ directly, via

$$\sigma = \frac{N}{\mathcal{L}_{int}} \tag{3.1}$$

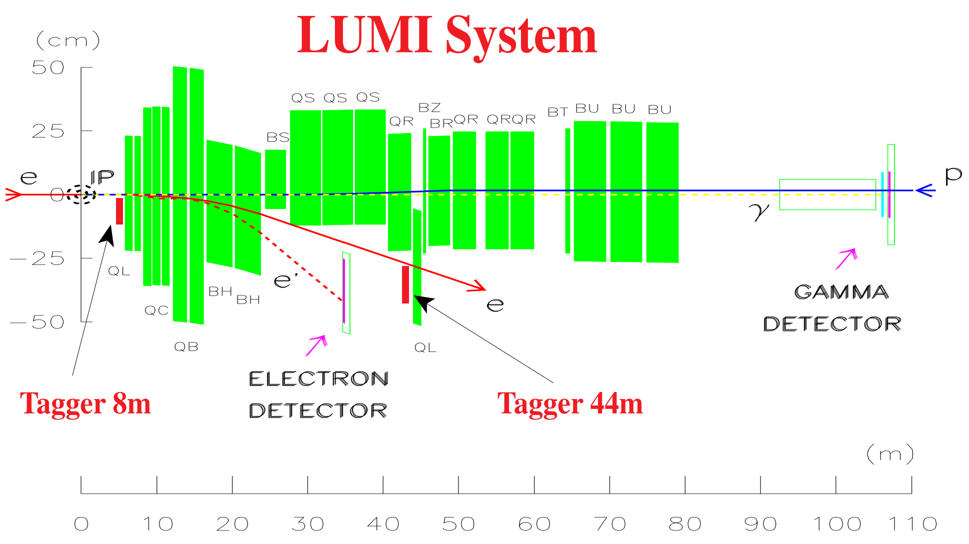

Figure 3.9: *The luminosity monitor system and the 8 and 44 m taggers.*

where N is the total number of events for a specific process measured during a certain time interval. The integrated luminosity can be obtained by measuring the number of events N for processes with a well-known cross section σ. At ZEUS the number of Bethe-Heitler bremsstrahlung events, $ep \longrightarrow ep\gamma$, is counted. The cross section for this process is high and can be calculated in QED with an accuracy of 0.5%.
Figure 3.9 shows the luminosity monitor system (LUMI) which was constructed to measure this process. Photons which are radiated at angles smaller than 0.5 mrad exit the beam pipe through a Cu-Be window at $Z = -92$ m and are then detected in the photon detector. It consists of a lead-scintillator calorimeter with a position detector made out of scintillator fingers and is positioned at $Z = -107$ m. The measured photon rate has to be corrected for background events originating from bremsstrahlung processes with residual gas molecules. The empty proton bunches paired with electron bunches are used to determine this background. The accuracy of the luminosity measurement, which depends on the beam conditions, is about 1.5%.

3.2.5 The ZEUS Trigger System

The layout of the ZEUS trigger system is dictated by the HERA bunch crossing time of 96 ns, corresponding to a collision rate of $\sim$ 10 MHz. The effective total interaction rate, which is dominated by the proton beam interacting with residual gas molecules amounts to about 10 – 100 kHz. To select the interesting physics events, ZEUS uses a three-level trigger system, shown schematically in Figure 3.10.
The first level trigger (FLT), which is pipelined, is designed to reduce the rate to a few 100 Hz. Each of the detector components possesses its own FLT and passes its trigger information on to the global first level trigger (GFLT). The decision is based on properties such as energy sums, thresholds or timing information. The data is stored in local pipelines awaiting the decision of the GFLT, which returns its decision to the components after 46 bunch crossings $\sim 4.4\,\mu$s. If the GFLT decides to keep the event the data is passed on to the second level trigger (SLT).
The SLT is based on software running on a network of transputers. The SLT is designed to reduce the rate to below 100 Hz. It is organised in a similar way to the FLT, with the global second level trigger (GSLT) taking the decision to reject or accept the event within 7 ms. At the SLT level, information about the vertex, limited tracking information and calorimeter timing

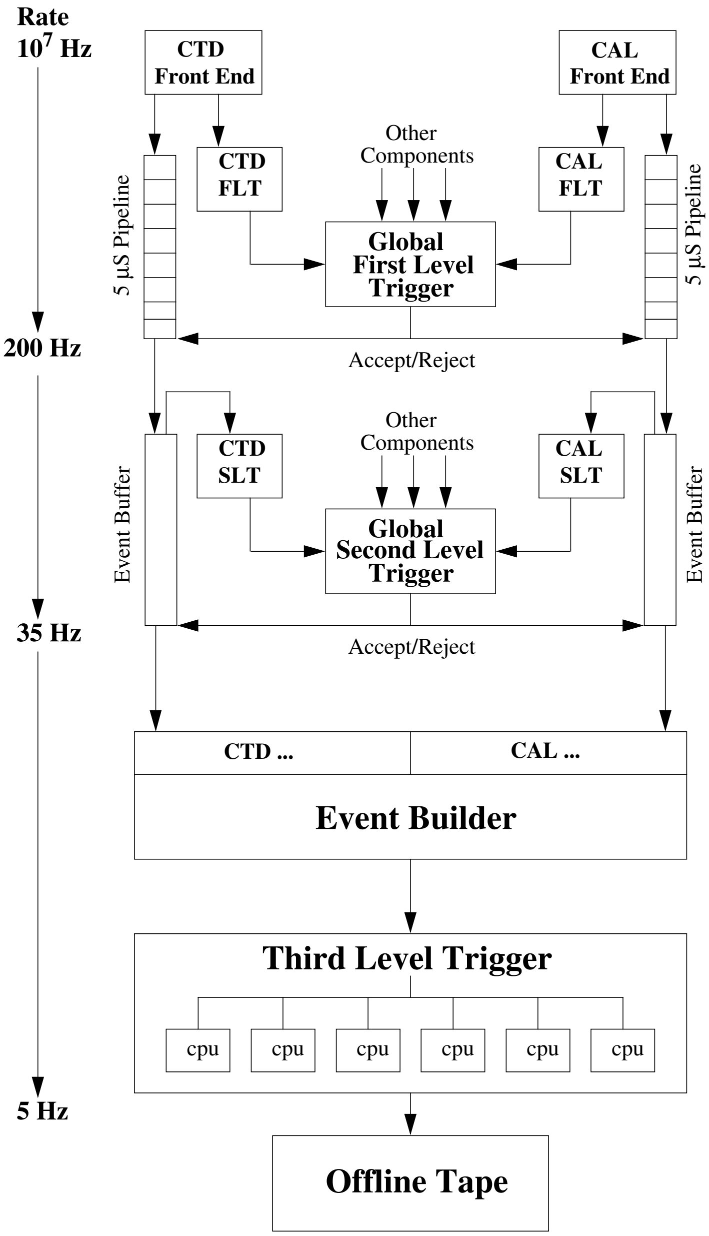

Figure 3.10: *Schematic diagram of the ZEUS trigger system.*

are available for the decision making. If the GSLT decision is positive all components send their data to the event builder, which combines the data of different components and makes it accessible to the third level trigger (TLT). The software-based TLT runs part of the offline reconstruction on a computer farm. Detailed tracking is performed, as well as jet finding and tagging of the scattered DIS electron. After the final TLT decision the rate is reduced to few Hz. The accepted events are written to tape, with the typical event size of $\sim 100\,$kBytes, to be processed by the full ZEUS reconstruction software.

3.2.6 Monte Carlo Simulation of the ZEUS Detector

To correct the measured data for detector effects, a Monte Carlo (MC) simulation of all detector components is available. The initial physics processes are generated by event generators (see Section 4.1). The path of the produced particles through the ZEUS detector, including particle decays, multiple scattering or energy loss is then described by the ZEUS MC program MOZART. MOZART is based on the GEANT detector simulation package [Bru89]. It contains subprograms for the simulation of the trigger (ZGANA) and the offline reconstruction (ZEPHYR). The detector simulation is based on the current understanding of the detector from physics studies and test beam measurements, taking care of the different materials and the exact geometry. The aim of the detector simulation is to produce signals as close as possible to real raw data signals, so that the same offline reconstruction software can be used for both MC and data.

In the CTD simulation a hit on a sense wire is produced when a charged particle crosses the corresponding drift plane. The drift time is obtained assuming constant drift velocity in the same way as in data. The pulse height is determined from GEANT, which gives a conversion factor for the energy loss of the particular particle in the gas of the CTD. Thus no information of the pulse shape is available. The MC does not simulate the avalanches nor the drift of the ionization to the sense wire. Therefore, effects caused by the ionization behaviour which then show up in the shape of the pulses are not described by the MC. The MC provides the information of the signals after digitization, i.e. the output of the DSPs. The signals are then further modified to account for effects such as double hits on a wire and chamber geometry in the same way as it is done in data. Due to the lack of a proper simulation of the ionization effects, the dE/dx information in simulations has to be used with care.

Chapter 4

Physics Simulation

In order to study the detector response for certain physics events, it is necessary to obtain an event sample in which the deep-inelastic ep scattering process is simulated (event generator) followed by a full detector simulation. The basis for these simulations are Monte Carlo (MC) techniques.
The event generator used for this analysis will be described in the first section. The second section describes a NLO calculation for charm production in DIS events, which will be used for the acceptance correction of the final physics results.

4.1 Event Generators

The ZEUS detector is a complex system, and its efficiency and resolution for determining particle momenta and positions must be accurately determined. The measured data must be corrected for these detector effects in such a way that the results are detector-independent and can be compared with other experiments and with theoretical predictions.
The initial physics scattering process is simulated by event generators. They use as theoretical input the perturbatively calculable QCD for the hard part of the scattering process and phenomenological models to describe the soft physics , such as the parton density functions and the fragmentation process. In the next step the produced collection of particles, namely hadrons and leptons, are propagated through the ZEUS detector taking account of decays, multiple scattering or ionization as described in Section 3.2.6.

4.1.1 RAPGAP

The Monte Carlo event generator used in this analysis is RAPGAP [Jun95]. The generator starts the physics simulation by generating the four-momenta of the particles involved in the ep scattering process according to theoretical predictions. The hard scattering process is calculated using perturbative QCD. The parametrization of the parton densities of the proton can be selected. For the MC data produced for this analysis the GRV model was chosen, using the GRVHO94 [Glü95] parametrization from the PDFLIB software package [Plo93] (see Section 2.1.7). The generator takes care of radiative processes before or after the actual ep scattering process, i.e. initial and final state radiation. For the QED radiative process along the electron line, RAPGAP uses the HERACLES event generator [Kiw92] to generate the ($e\ \gamma^*\ e$) vertex including initial and final state radiation as well as virtual corrections. QCD radiative processes are simulated in QCD parton showers based on the DGLAP evolution equations to leading order in α_s. For a more detailed simulation of the LO processes the exact matrix elements for the

specific process can be included. This is done in case of heavy quark production via the BGF process. In RAPGAP the BGF process is the only production mechanism for heavy quarks if the GRV parton density is chosen. Parton showers are used to approximate higher order QCD corrections in case of BGF heavy quark production.
For the fragmentation of the generated partons into hadrons RAPGAP uses the Lund-string model as implemented in JETSET [Sjö94]. In this model a colour string connects the proton remnant with the produced coloured partons. The further the parton moves away from the proton remnant, the more energy is stored in the colour string and it breaks up by the production of $q\bar{q}$ pairs. By this method light $q\bar{q}$ pairs are produced between the outgoing partons and the proton remnant. The production of heavy quarks in this process is heavily suppressed due to their large mass and hence they are not expected to be produced via fragmentation but only in the hard scattering process. The treatment of the proton remnant is done by the program LEPTO [Ing97]. In the case of BGF a colour octet gluon is removed from the proton producing a $q\bar{q}$ pair. Two colour strings are produced connecting each of the quarks with parts of the proton remnant.
To describe the fraction of the charm quark's momentum carried by the charm hadron, RAPGAP offers a choice between different fragmentation functions. The fragmentation function taken by default is a modification of the 'Lund symmetric fragmentation function' [Sjö94] for heavy quarks. It is of the form

$$f(z) \propto \frac{1}{z^{1+r_Q b m_Q^2}} z^{a_\alpha} \left(\frac{1-z}{z}\right)^{a_\beta} \exp\left(-\frac{b m_\perp^2}{z}\right) , \tag{4.1}$$

where a_α and a_β are separate parameters for the different flavours participating, b is a universal parameter, r_Q can be set to different values for charmed or beauty hadrons and $m_\perp = m^2 + p_x^2 + p_y^2$ is the hadron's transverse mass. Due to the different parameters for different flavours, the momentum spectra of the different charmed hadrons are allowed to be different. Another possible choice is the Peterson fragmentation function (Equation 2.14). Here the ε_Q is the only free parameter specific for the different charmed hadrons. However only one value for ε_Q can be chosen if the Peterson fragmentation is used for the fragmentation of heavy quarks. Although ε_Q is expected to vary with the mass of the picked up light quark (see Section 2.2.3), recent NLO fits yield an ε_{D_s} equal within errors to ε_{D^*} [Br00B].
The MC data used in this analysis was produced using the default RAPGAP fragmentation function. For comparison a small MC sample using the Peterson fragmentation function with $\varepsilon_Q = 0.035$ was also generated (see Section 2.2.3). The distribution of interest is the momentum distribution of the charmed hadrons which decay semileptonically. The left plot in Figure 4.1 shows the momentum distribution of different charmed hadrons in the laboratory frame produced by RAPGAP with the default fragmentation function. No significant difference between the distributions is seen. The middle and right plot show a comparison between the Peterson fragmentation function and the default Lund fragmentation function. In case of the charmed hadrons (middle plot) as well as of the electrons from semileptonic charm decays (right plot) the momentum distributions produced with the two different fragmentation functions agree well.
Assumptions have to be made about the multiplicity distributions of the different charmed hadrons. Exclusive fragmentation fractions have been measured by e^+e^- collider experiments. This is also true for the branching ratios of the decays for many charmed hadrons. In particular the decays of the D^0 and the $D^\pm$ have been well studied. If the explicit branching ratios for the decay is known, RAPGAP uses the value as given by the PDG. For those not yet measured the values are estimated. The branching ratios are tuned such that the inclusive branching ratios

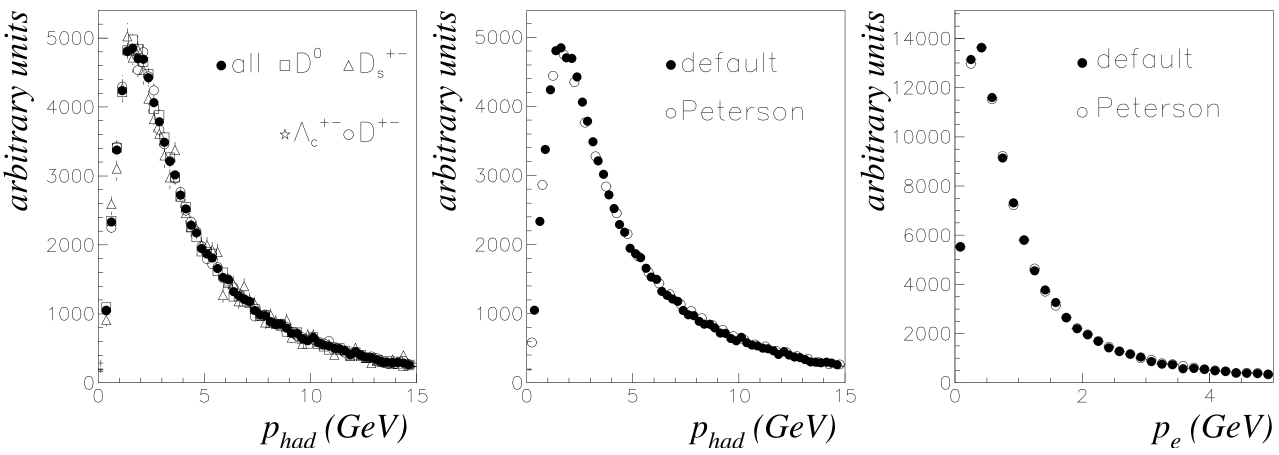

Figure 4.1: *The left plot shows the momentum distribution in the laboratory frame for different charmed hadrons as produced by RAPGAP using the default fragmentation function. The middle plot shows the momentum distribution of all charmed hadrons as in the left plot compared to the distribution obtained using the Peterson fragmentation function. The right plot shows the comparison between the two fragmentation function for the momentum distribution of the electrons that stem from the semileptonic decays of the charmed hadrons.*

in the end again agree with the measured ones. The branching ratio for the semileptonic charm decay into electrons in RAPGAP is 9.5 %, in agreement with the measurement [Alb92].
This procedure also fixes the branching fraction of the charm quarks into hadrons. The majority of produced charmed hadrons in RAPGAP are $D^{*\pm}$ and D^{*0} mesons, each contributing about 30 % to the total amount of charmed hadrons. In addition $D_s^{*\pm}$, D^0 and $D^\pm$ mesons amount to about 10 % each. A small fraction of about 4 % of $\Lambda_c^\pm$ baryons is produced and 3 % of other charmed hadrons. The masses of the charmed hadrons are taken according to the Particle Data Group (PDG) [Cas99]. The charm mass is set to $m_c = 1.5\,\mathrm{GeV}$.
In order to select events with semileptonic decays of charm quarks into electrons, a filter program was written. The event generator produces all kinds of charmed hadrons of which only those having a semileptonically decaying charmed hadron were passed on through the ZEUS detector simulation. The composition of charmed hadrons decaying semileptonically is a consequence of the decay rates of the D^* mesons described above, and of the fragmentation process itself. The majority of the electrons stem from semileptonic decays of D^0 (48 %) and $D^\pm$ (37 %) mesons. The remaining electrons are produced by $D_s^\pm$ decays (10 %), $\Lambda_c^\pm$ decays (4 %) and other decaying charmed hadrons (1 %).

4.2 NLO Calculation

The RAPGAP MC event generator performs an integration of the LO matrix elements. To reduce scale dependencies of the calculation of the hard scattering process, calculations that also include higher order corrections are desirable. For heavy quark production, a NLO Monte Carlo program exists, the HVQDIS program [Ha98A].

4.2.1 HVQDIS

The HVQDIS program provides kinematic distributions calculated in NLO for heavy quark production in DIS events. But the program does not generate single events like an event

generator. Therefore no full MC simulation including the detector and trigger simulation of the NLO predictions is possible. The measured data has to be corrected for detector effects with LO MC such as RAPGAP and the obtained distributions can then be compared to the NLO predictions from the HVQDIS program.
The calculation is performed in a three-flavour-number scheme (FFN3, Section 2.2.1) assuming charm production only to occur via BGF and higher order QCD processes. The calculation starts with the differential cross section for charm production in terms of charm structure functions of the proton as in Equation 2.12. The higher order corrections, including gluon-bremsstrahlung $\gamma^* g \longrightarrow c\bar{c}g$, higher order production processes $\gamma^* q(\bar{q}) \longrightarrow c\bar{c}q(\bar{q})$ and virtual corrections are calculated and added as NLO corrections to the charm structure functions. For the parton density parametrization only those using the same renormalization scheme as used in the calculation should be used, which is the case for the GRV94 set [Glü95]. Due to the use of the FFN3 scheme the results are expected to be most accurate at $Q^2 \sim m_c^2$ and to become less reliable for $Q^2 \gg m_c^2$. The choice of the value for the charm quark mass is left to the user and will be changed for systematic checks.

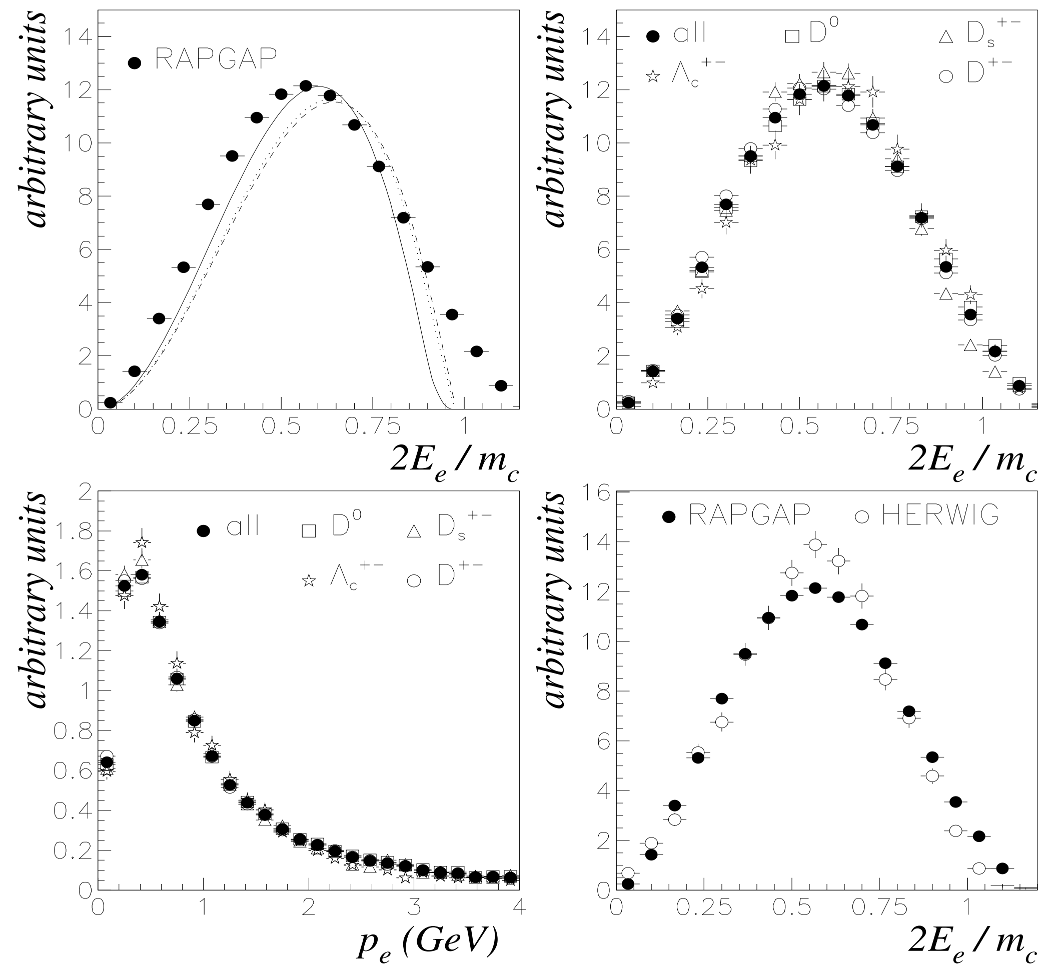

Figure 4.2: *Energy distribution of electrons from semileptonic charm decays in the hadron rest frame as obtained from RAPGAP in comparison with predictions from the spectator model (upper left plot). The energy distribution of electrons coming from different charmed hadrons(upper right plot). The momentum distribution of the electrons in the laboratory frame (lower left plot). Comparison of the distribution obtained from RAPGAP with that from the HERWIG event generator (lower right plot).*

The program returns the differential distributions for parton kinematics accurate to $\mathcal{O}(\alpha, \alpha_s^2)$. For the hadronization into heavy hadrons the Peterson fragmentation function is used. The parameter ε_Q has to be given as an input. For the normalization of the cross section the branching fraction (e.g. $BR(c \to D^*) = 0.222$[Ack98] for D^* production) is used. To be able to compare results from charm production measurements via the semileptonic decay channel, $c \to e\nu X$, with NLO calculations, the HVQDIS program was extended to compute this decay channel [Har99]. In the rest frame of the decaying hadron the electrons are distributed isotropically. The momentum distribution of the electrons in the rest frame of the decaying hadrons is obtained from a Monte Carlo event generator, where RAPGAP was chosen. The fragmentation was performed using the Peterson fragmentation function with $\varepsilon_Q = 0.035$ [Ver98].
The histogram in the upper left plot of Figure 4.2 shows the energy distribution of electrons from semileptonic charm decays in the rest frame of the decaying hadron. The distribution was obtained from MC data generated with RAPGAP using the default fragmentation function. Also shown are the theoretical predictions obtained assuming the simple spectator model (see section 2.2.4). Within the picture of the spectator model the electron spectrum can be calculated using [Ell96]

$$\frac{d\Gamma_{sl}^c}{dx} \sim |V_{cs}|^2 m_c^5 \ \frac{12x^2(x_m - x)^2}{1-x} , \tag{4.2}$$

where only the predominant decay mode into an s quark is taken into account. The variable x is the rescaled energy of the electron, ($x = 2E_e/m_c$), and x_m gives the kinematic limit of the spectrum, ($x_m = 1 - (m_s/m_c)^2$). The shape of the distribution depends on the masses chosen for m_s and m_c. The dotted line shows the prediction using $m_s = 0.115\,\text{GeV}$ and $m_c = 1.25\,\text{GeV}$ as given by the Particle Data Group [Cas99]. The dashed line is calculated with the quark masses, $m_s = 0.199\,\text{GeV}$ and $m_c = 1.5\,\text{GeV}$ as used in RAPGAP. To obtain the solid line the strange quark mass was increased to $m_s = 0.35\,\text{GeV}$ whereas the charm mass was kept at $m_c = 1.5\,\text{GeV}$. The agreement between the histogram obtained from RAPGAP and the spectator model prediction is reasonable, but obviously depends on the masses chosen. The upper right plot shows the same energy distribution separately for the different charmed hadrons in RAPGAP. The shape of the energy distribution agrees well for the different hadrons. Thus the influence of the composition of the different hadrons contributing electrons from semileptonic charm decay on the momentum

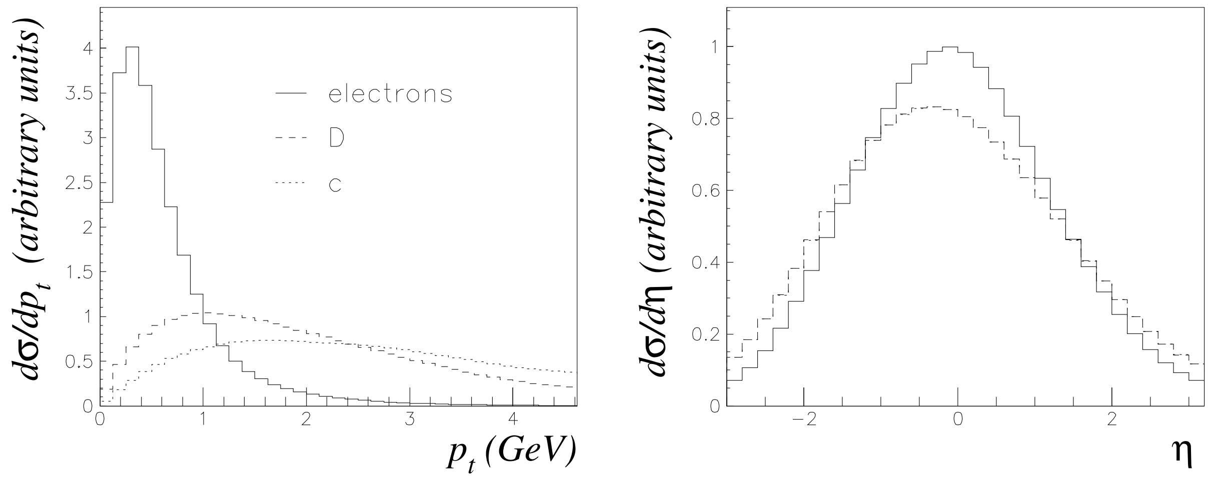

Figure 4.3: *The p_t (left plot) and the η (right plot) distribution of charm quarks, D^* mesons and electrons from semileptonic decays of charmed mesons. The distributions are obtained from NLO calculations with the HVQDIS program for $0.04 < y < 0.7$ and $0 < Q^2 < 100\,GeV^2$.*

of the electrons is negligible. The lower left plot shows the momentum distribution of electrons from different charmed hadron decays in the laboratory frame. They are also in good agreement. For comparison the electron spectrum was also obtained using another MC generator, HERWIG [Mar92]. HERWIG is a general purpose event generator using the cluster hadronization model to simulate the process of fragmentation. The composition of hadrons is slightly different for HERWIG. The agreement between RAPGAP and HERWIG is reasonable.
Figure 4.3 shows the p_t and η distribution of charm quarks, D^* mesons and electrons from semileptonic charm decays as calculated in NLO with the HVQDIS program. The kinematic range for the calculation was $0.04 < y < 0.7$ and $10 < Q^2 < 100\,\mathrm{GeV}^2$. For the fragmentation of the charm quark into the D^* meson the Peterson fragmentation function was used with $\varepsilon_Q = 0.035$. Due to the soft fragmentation, the p_t of the charmed meson is only slightly lower than that of the charm quark and the η distributions agree very closely. Since the electrons only get a small fraction of the hadron's energy (see Figure 4.2) the transverse momentum clearly is shifted towards lower values compared to the D^* meson resulting also in a more central η distribution.
The overall cross section for the process $c \to e\mu X$ is fixed by the branching ratio. The differential cross sections also depend on the value chosen for the Peterson parameter, ε_Q. The HVQDIS program allows one to compute kinematic distributions for electrons from the semileptonic decay of single charmed hadrons. The used input momentum distribution for the electrons from the semileptonic decay is always the same as obtained from RAPGAP. Thus for a correct calculation of the kinematics, the program would have to be run for all kinds of charmed hadrons, with the corresponding parameter ε_Q for the fragmentation. It was shown in the last section that the momentum distributions of the different charmed hadrons agree well.
The effect of a variation of the Peterson parameter, ε_Q, on the electron distributions is demonstrated in Figure 4.4. The p_t and η distribution of electrons from semileptonic charm decays are shown for D^* production using $\varepsilon_Q = 0.035$ and $\varepsilon_Q = 0.085$. A higher ε_Q value chosen for the fragmentation corresponds to a lower momentum fraction of the charmed meson and hence results in a lower momentum of the electron as can be seen in the left plot. Although the parameter ε_Q was varied rather drastically the effect on the resulting momentum and polar angular distributions of the electron is small. As mentioned in the last section, recent NLO fits resulted in the same parameter $\varepsilon_Q = 0.035$ for D^* and D_s production. Hence this theoretical uncertainty is neglected in the following.

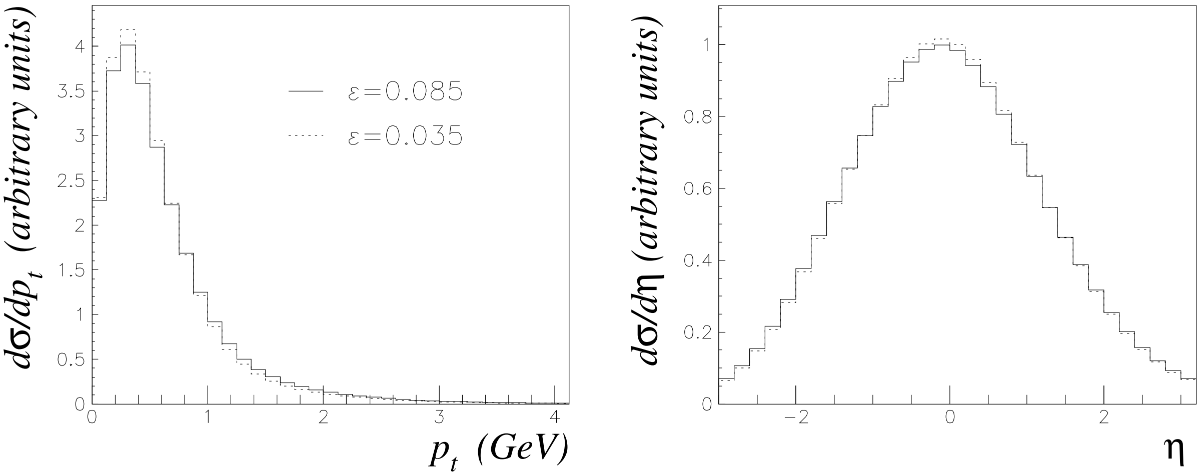

Figure 4.4: *The p_t (left plot) and η (right plot) distribution of electrons for different values for ε_Q. The distributions are calculated in NLO with the HVQDIS program in the kinematic range,* $0.04 < y < 0.7$ *and* $10 < Q^2 < 100\,GeV^2$.

Chapter 5

Reconstruction and Selection of the Inclusive DIS Sample

In this chapter the selection of the inclusive DIS data sample is discussed. First the reconstruction of DIS events is explained. In the second section the trigger selection and offline cuts used for this analysis are discussed. In the final section the agreement between the selected data sample and a Monte Carlo sample is investigated.

5.1 Reconstruction of DIS Events

To measure the proton structure function F_2 in NC DIS events, precise determination of the kinematic variables x, y and Q^2 is necessary. Therefore the measurable quantities, such as energy and angle of the scattered DIS positron and the hadronic energy flow, must be reconstructed with high accuracy.

5.1.1 The Final State of DIS Events

Figure 5.1 shows schematically a neutral current deep-inelastic scattering event in the ZEUS coordinate system. The positron is coming from the negative z direction having four-momentum k before, and k' after emitting the virtual photon. The polar scattering angle of the positron θ_e is measured with respect to the positive z direction. The proton is moving in the positive z direction with four-momentum P. The struck quark fragments into a jet of particles referred to as current jet. The four momentum of the entire hadronic system in the final state, thus including the current jet and the proton remnant is P'. γ_h is the polar angle between the current jet and the positive z direction. Neglecting masses of positron and proton, the four momenta of the particles can be written as

$$k = \begin{pmatrix} E_e \\ 0 \\ 0 \\ -E_e \end{pmatrix}, k' = \begin{pmatrix} E'_e \\ E'_e \cos(\phi_e) \sin(\theta_e) \\ E'_e \sin(\phi_e) \sin(\theta_e) \\ E'_e \cos(\theta_e) \end{pmatrix}, P = \begin{pmatrix} E_p \\ 0 \\ 0 \\ E_p \end{pmatrix}, P' = \begin{pmatrix} \sum_h E_h \\ \sum_h p_{x,h} \\ \sum_h p_{y,h} \\ \sum_h p_{z,h} \end{pmatrix}. \tag{5.1}$$

The sum $\sum_h$ runs over all hadronic particles in the final state.
In the naive quark parton model the two body final state of the e^+p scattering process is completely constrained using two variables, for example the polar angle and energy of the scattered positron. In this picture the angle γ_h is simply the polar angle of the struck quark. Similarly the kinematics of DIS events can be reconstructed using two measurable quantities.

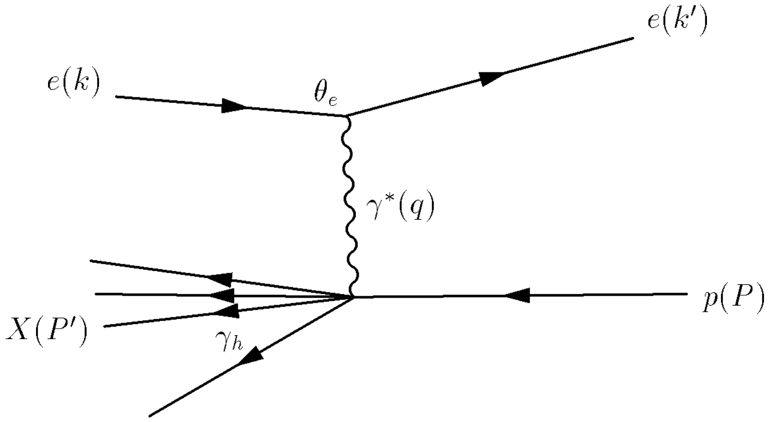

Figure 5.1: *Schematic drawing of a deep-inelastic ep scattering event.*

Which quantities to choose and how to measure them with high accuracy will be discussed in the next two sections. The determination of x, y and Q^2 from the measured quantities will then be discussed in section 5.1.4.

The appearance of the final state of a typical NC DIS event in the detector can be seen in an event display. Figure 5.2 shows the ZEUS event display for a high Q^2, $Q^2 \sim 800\,\mathrm{GeV}^2$, neutral current event. The typical signature is the well-isolated positron scattered opposite to the current jet. Both are in this case detected in the BCAL. Some energy deposit from the proton remnant around the FCAL beampipe region can also be seen.

5.1.2 Identification of the DIS Positron

The measurement of the positron's kinematic variables requires first of all the identification of the scattered DIS positron using electron finders. The electron finder used in this analysis is based on a neural network trained with MC data (named SINISTRA, [Abr95,Sin97]). The finder is based on the different shower development of electromagnetic and hadronic particles in the calorimeter. The cells in the calorimeter are combined to form islands. Starting from a local energy maximum as a seed point, neighbouring cells above a certain energy threshold are added. The geometry of the calorimeter, including the gaps between the BCAL and F- and RCAL is taken into account. Electromagnetic showers are shorter than hadronic showers. Thus they are concentrated on the EMC part of the calorimeter, whilst energy deposits from hadronic particles occur also in the HAC part. The different shower depths of the positron and the hadronic particles can be seen in Figure 5.2.

The output of the neural network is the probability that the island was produced by the scattered positron. If the probability is above 90 % the found island is defined to be a positron candidate. Among the candidates the most probable one is chosen to be the scattered DIS positron. Figure 5.3 shows the positron finding efficiency of the electron finder versus the true energy of the scattered positron obtained from a DIS MC sample with $Q^2 > 1\,\mathrm{GeV}^2$. Above positron energies of 10 GeV the efficiency is above 80 % and reaches almost 100 % for even higher energies. Low energy positrons produce hadron-like showers, complicating the electron finding. Also preshowering of the positron due to inactive material in front of the calorimeter or non-isolated positrons worsen the identification of the positron. In addition photons or low-energetic hadrons may fake an electromagnetic cluster, which is then misidentified as the positron.

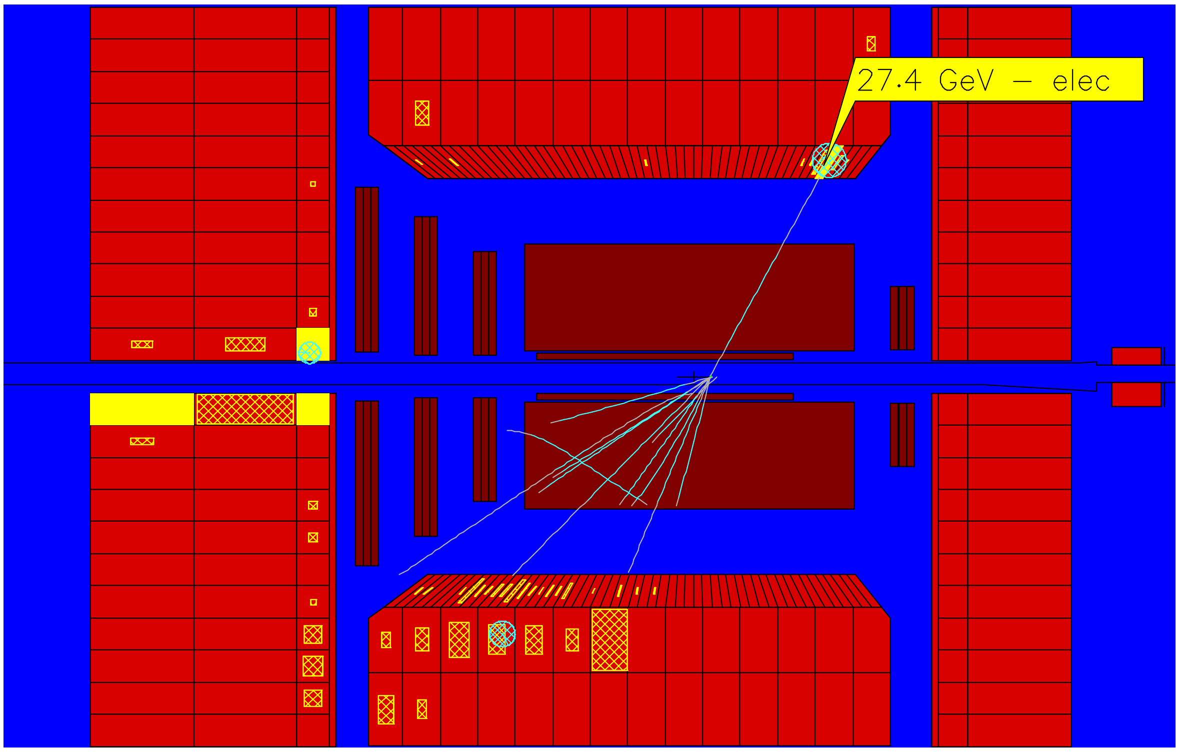

Figure 5.2: *Event display of a neutral current DIS event.*

Measurement of the Scattering Angle of the Positron

Once the scattered positron has been identified by the electron finder, its position and energy must be determined as precisely as possible. The position measurement is used to reconstruct the polar positron scattering angle θ_e, which enters directly into the calculation of x and Q^2. Therefore, especially at small scattering angles, a precise determination of the positron position is required. In the rear direction the SRTD is used for position measurement (see Section 3.2.3). The SRTD position resolution is better than 3.0 mm. Outside the SRTD region the energy share between the left and right photomultiplier of a calorimeter cell is used. The overall angular resolution varies between 0.1 to 0.2°.

Energy Measurement of the Scattered Positron

The energy of the scattered positron is determined using the calorimeter. To improve the energy resolution the RCAL presampler is used if there is some energy deposit produced by the positron in this detector component. In addition the SRTD is used as a presampler, whenever there is a hit from the positron in the detector.
The basic principle of a presampler is the measurement of the multiplicity of the particle shower. If the particle showers in inactive material in front of the detector, then the multiplicity increases. Thus the measured multiplicity contains information about the energy loss in inactive material, and thereby improves the energy measurement of the calorimeter. The applied energy correction is a simple linear ansatz,

$$E_{cor} = E_{cal} + \alpha_{pres/SRTD} \cdot E_{pres/SRTD} \tag{5.2}$$

where E_{cal} is the energy measured with the calorimeter and $E_{pres/SRTD}$ is the energy measured with the presampler and SRTD respectively. The parameter α is obtained from data using over-constrained events where the positron energy is known or could be obtained without using

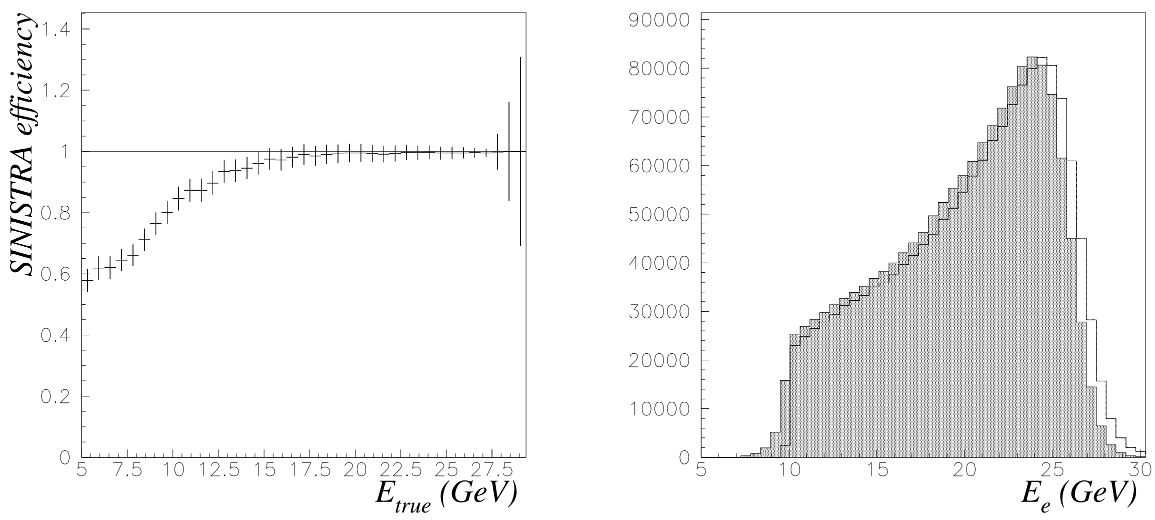

Figure 5.3: *The efficiency of the electron finder SINISTRA (left plot) versus the true energy of the scattered positrons. The positron energy (right plot) in a DIS data sample before (shaded histogram) and after SRTD and RCAL presampler energy corrections (empty histogram).*

the calorimeter. These are for instance kinematic peak events, which are constrained to the very low-y region, where the scattered electron energy is close to the electron beam energy and can be accurately determined from the scattering angle. Also used are QED Compton events ($ep \rightarrow ep\gamma$), where the electron and the photon are contained in the calorimeter and are fully determined by the measured scattering angles. The achieved accuracy for the corrected positron energy is 2 %. This linear ansatz does not take into account any variation of the thickness of the inactive material. The right plot in Figure 5.3 shows the effect of the energy correction.

5.1.3 The Hadronic Energy Flow

The measurement of the hadronic particles in the final state is fully based on the calorimeter. All calorimeter cells which are not assigned to the scattered positron are considered to belong to the hadronic final state. Therefore the suppression of noise originating from the uranium and from the electronics is important.

Noise Suppression

To study the noise behaviour of the calorimeter random trigger events have been selected which contain no particles thus only noise contributes to the signals in the calorimeter. The predominant noise contribution originates from the uranium radioactivity. The uranium signals amount to a few tens of MeV per cell, where the energy is the sum of the energy measured by the two photomultipliers of each cell. The uranium noise signals are distributed equally over the whole calorimeter. A lower energy cut of 60 MeV for every EMC cell and 110 MeV for every HAC cell is applied, to avoid any contribution from uranium noise to the real physics signals. For isolated cells the minimum energy is required to be even higher, 100 MeV for the EMC cells and 160 MeV for the HAC cells. In case only one of the photomultiplier fired or large differences between the two signals of one cell occurred the imbalance, $(E_1 - E_2)/(E_1 + E_2)$, of any cell has to be lower than 50 %, and the cell is removed otherwise. Finally the behaviour of the cells over a long run range is monitored. Those cells, which show a significantly higher signal than the others, are not used for the reconstruction of the hadronic variables.

Reconstruction of Hadronic Quantities

The determination of the hadronic parameters suffers from the limited acceptance of the calorimeter, where particles can escape undetected in the direction of the beampipe. In addition the reconstruction of angle and energy becomes complicated for events which do not show the typical structure as in Figure 5.2, for instance multiple-jet events. To minimize the effect of energy losses along the beampipe the difference between the energy and the momentum in z direction, $\delta_h = \sum_h (E_h - p_{z,h})$ is used as a measurable quantity for the reconstruction of the event kinematics. As a second variable the transverse momentum $P_{T,h} = \sqrt{(\sum_h p_{x,h}^2) + (\sum_h p_{y,h}^2)}$ is chosen. The angle γ_h can be determined from these quantities by

$$\cos\gamma_h = \frac{P_{T,h}^2 - \delta_h^2}{P_{T,h}^2 + \delta_h^2} \ . \tag{5.3}$$

5.1.4 Reconstruction of the Kinematic Variables

In Section 2.1.1, Equation 2.1 the commonly used kinematic variables x, y and Q^2 were defined. They are dependent on the four momenta of the incoming and outgoing particles, which are fully determined by measurable quantities. At a fixed center of mass energy, the final state is determined by only two variables. This is no longer true if the center-of-mass energy changes due to the positron radiating off a photon before interacting with the proton. This process is called initial state radiation.
Assuming the initial beam energies are known, measuring the positron and hadron quantities leads to an overconstrained system. Therefore different methods are possible to reconstruct x, y and Q^2, of which the three most accurate and commonly used methods will be explained in more detail. The accuracy of the different reconstruction methods varies strongly over the phase space depending on the detector qualities for the different measurements.

Electron Method

The electron method only uses the measured quantities of the scattered positron, its polar angle θ_e and its energy E'_e. The formula for x, y and Q^2 can be derived from Equation 2.1 substituting the four vectors as defined in Equation 5.1.

$$x_e = \frac{E_e}{E_p}\,\frac{E'_e(1+\cos(\theta_e))}{2E_e - E'_e(1-\cos(\theta_e))} \ , \tag{5.4}$$

$$y_e = 1 - \frac{E'_e}{2E_e}(1-\cos(\theta_e)) \ , \tag{5.5}$$

$$Q_e^2 = 2E_e E'_e(1+\cos(\theta_e)) \ . \tag{5.6}$$

Jacquet-Blondel Method

Another possibility is to use only the hadronic quantities to determine the event kinematics. This method was developed by Jacquet and Blondel (JB) [Jac79]. Using $q = k - k' = P' - P$ and transverse momentum conservation, $p_{T,e} = p_{T,h}$, the kinematic variables are given by

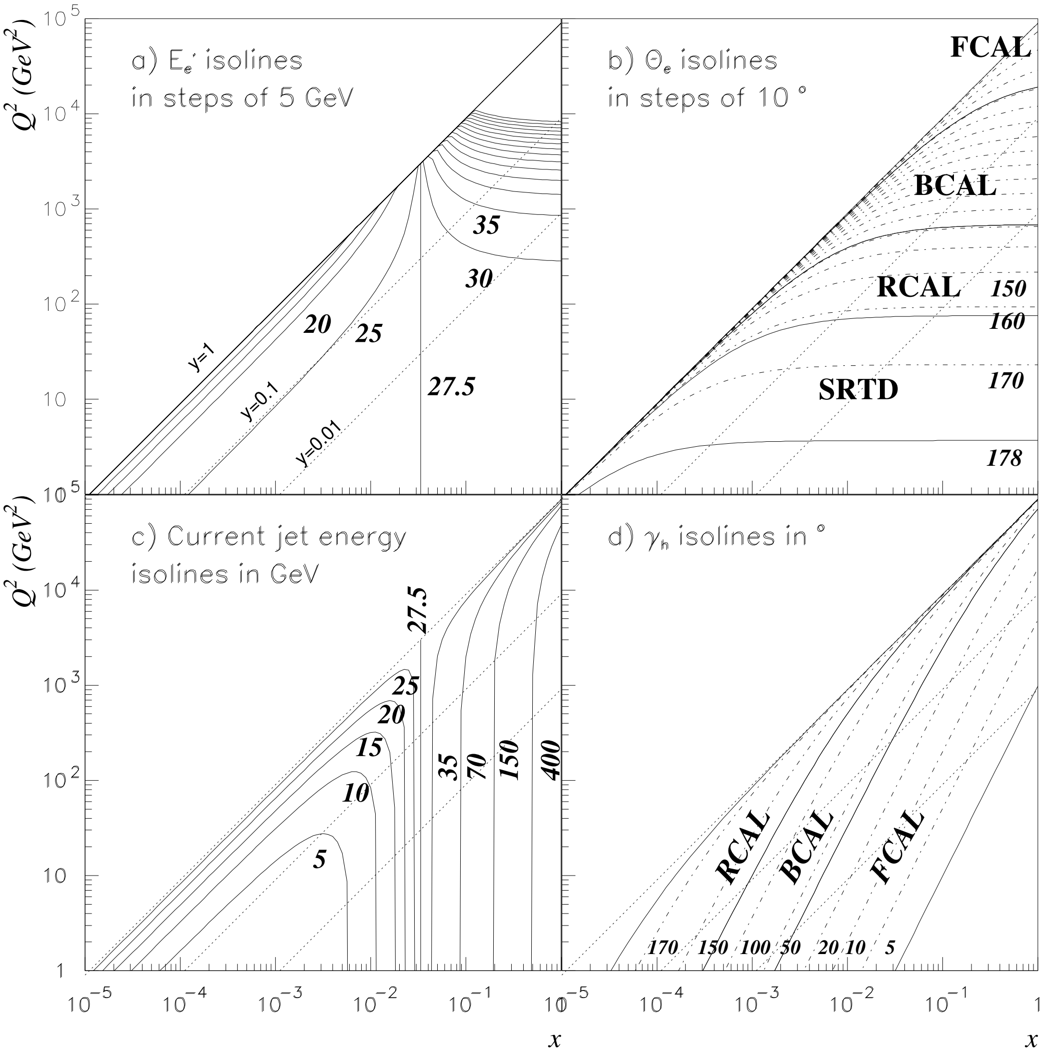

Figure 5.4: *Isolines of* a) *constant positron energy* E_e', b) *constant positron scattering angle* θ_e, c) *constant current jet energy and* d) *constant hadronic angle* γ_h *in the* (x, Q^2) *plane. See text for further explanation.*

$$y_{JB} = \frac{\delta_h}{2E_e} , \tag{5.7}$$

$$Q^2_{JB} = \frac{p^2_{T,h}}{1 - y_{JB}} , \tag{5.8}$$

$$x_{JB} = \frac{Q^2_{JB}}{s \cdot y_{JB}} . \tag{5.9}$$

Double Angle Method

A third reconstruction method only uses the measured angles, θ_{DA} and γ, and therefore is independent of any energy scale. The method is called double angle method (DA), and yields the following expressions for x, y and Q^2:

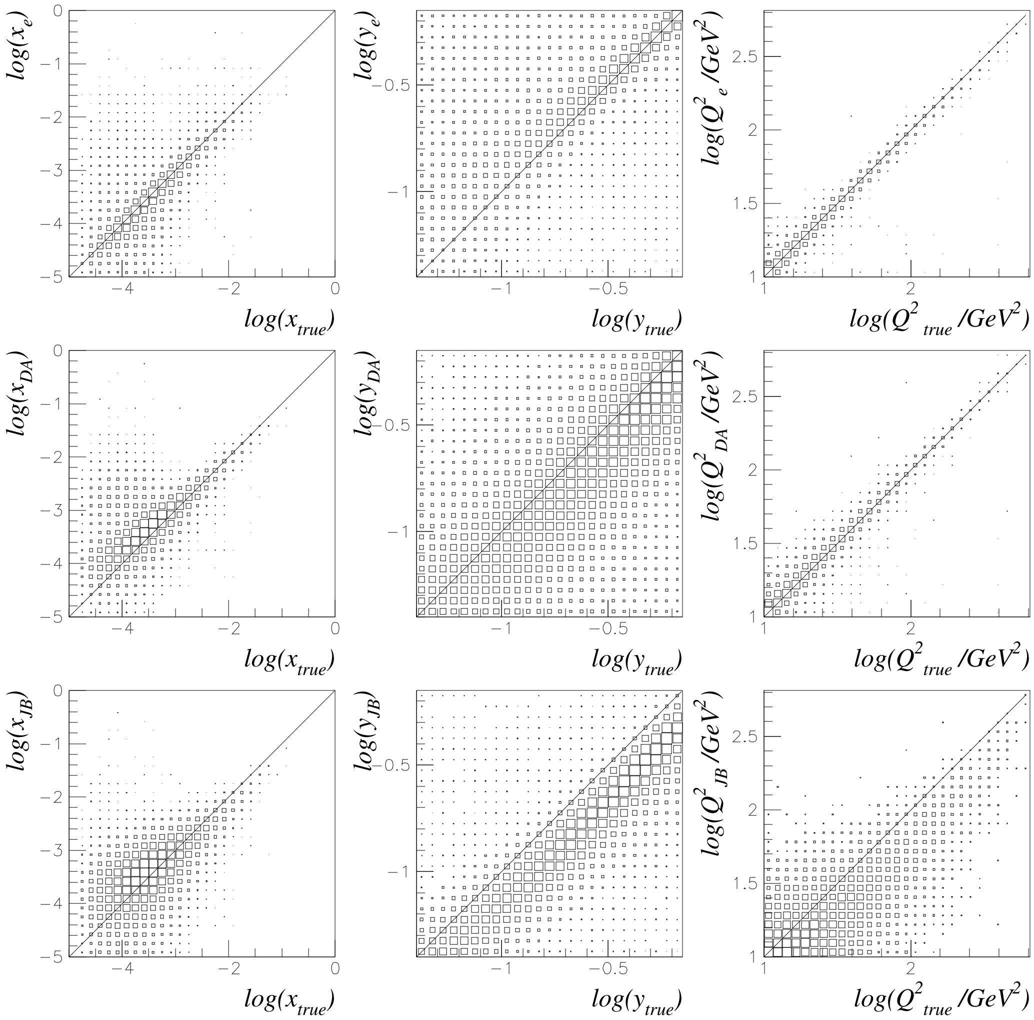

Figure 5.5: *Comparison of the different reconstruction methods. The true variables are plotted versus the reconstructed ones. The first row shows the resolution of the electron method, the second row the resolution of the double angle method and the third row the resolution of the Jacquet-Blondel method.*

$$x_{DA} = \frac{E_e}{E_p}\,\frac{\sin\gamma_h + \sin\theta_e + \sin(\theta_e+\gamma_h)}{\sin\gamma_h + \sin\theta_e - \sin(\theta_e+\gamma_h)}\ , \tag{5.10}$$

$$y_{DA} = \frac{\sin\theta_e(1-\cos\gamma_h)}{\sin\gamma_h + \sin\theta_e - \sin(\theta_e+\gamma_h)}\ , \tag{5.11}$$

$$Q^2_{DA} = 4E_e^2\,\frac{\sin\gamma_h(1+\cos\theta_e)}{\sin\gamma_h + \sin\theta_e - \sin(\theta_e+\gamma_h)}\ . \tag{5.12}$$

Comparison of the Reconstruction Methods

The quality of the different reconstruction methods depends on the accuracy of the measured quantities used for the reconstruction. To understand the resolution in different regions of the phase space Figure 5.4 shows isolines of the measured quantities in the (x, Q^2) plane. In general a variable can be measured with high resolution if the isoline density is high, because then shifts in the measured quantity due to detector effects give only small changes of the variable. This is true only if the isolines run almost perpendicular to the variable. If the isoline is running parallel to the kinematic variable a change of the measured quantity does not effect the variable at all.

Figure 5.4 *a*) shows lines of constant energy E'_e of the scattered positron. The dotted diagonal lines indicate different y ranges and the kinematic limit at $y = 1$. Low positron energies correspond to high y values, whereas high energies populate the high-Q^2 region. In the region of low Q^2 and high y the isolines are dense and parallel to y. Thus the resolution of the electron method in this region is good, but deteriorates towards low y values, where E'_e is almost constant. Plot *b*) shows the positron scattering angle isolines as dashed lines. The solid lines indicate the coverage of the different detector components. The SRTD covers the low-Q^2 region where the isolines are further apart towards lower Q^2. Thus the precision of the θ_e measurement dominates the resolution of Q^2_e.

Figure 5.4 *c*) and *d*) show the hadronic quantities. The current jet energy is defined as the total hadronic energy, which is a good approximation since the proton remnant disappears through the forward beampipe in most events. The coverage of γ_h by the different calorimeter sections is indicated by the solid lines.

The Jacquet-Blondel method is very sensitive to noise effects in the calorimeter. Especially in the region of low y and low Q^2 small uncertainties in the energy scale can lead to large migrations of the reconstructed variables.

The resolution of the different methods is shown in Figure 5.5. The true variables are plotted versus the reconstructed ones for a sample of DIS MC events. The poor resolution of y_e in the low-y region can be seen, as well as good resolution of y_{JB} in this region. Overall the values of y_{JB} are shifted towards lower values, leading to large migration effects. In addition compared to the other methods, the Jacquet-Blondel method has a poor resolution in x and Q^2. The double angle and electron methods show a comparable resolution in Q^2. In x and y the electron method yields slightly better resolution, whereas overall the resolution of the double angle method is more stable. Since the double angle method is to first order independent of the energy scale and less sensitive to initial state radiation, this method was chosen for the reconstruction of the event kinematics.

The three reconstruction methods introduced above can also be combined to the so-called 'mixed methods'. Additional reconstruction methods exist, e.g. the 'Σ method' or the 'P_T method'. The 'Σ method' uses the energy and the angle of the scattered positron, E'_e and θ_e, and the hadronic quantity $\delta_h = \Sigma = \sum_h (E_h - p_{z,h})$. This method often is combined with the electron method, using Q^2_e and $y_\Sigma = \Sigma/(\Sigma + E'_e(1 - \cos\theta_e))$, called '$e\Sigma$ method'. The 'P_T method' combines all information of the scattered positron and the hadronic final state. The reconstruction of x, y and Q^2 then follows from energy and momentum conservation (for further information about the reconstruction methods see e.g. [Def99, Fri99, Qua96]).

5.2 Selection of the DIS Data Sample

In this section the selection of the DIS events used for this analysis is outlined. First the trigger selection will be discussed, followed by a description of the offline cuts. Both are based on the identification of the scattered DIS positron. In addition, several cuts are applied to reject non-physics or non-DIS background events.

The detector performance was monitored during the whole running period. All runs which were affected by detector problems, such as a large number of bad cells in the calorimeter or very low statistic runs, which makes the dE/dx corrections worse, were discarded. The total integrated luminosity taken during the 1996 and 1997 running period and used for the analysis is $\mathcal{L}_{int} = 34.0\,\mathrm{pb}^{-1}$.

5.2.1 Trigger Selection

In Section 3.2.5 the ZEUS trigger system was introduced. Different physics filters are used at each trigger level. Each of the physics filters is designed to trigger events from a certain process. During the 1996/1997 running period no special trigger existed to trigger DIS events with a semileptonic decay. Thus for this analysis the inclusive DIS trigger were used to select the events. The DIS filters are based on tagging the scattered positron.
In addition at all three trigger levels background events can be rejected using timing information. All ZEUS detector components are gated by the HERA clock. They are calibrated in such a way that for collisions at the nominal interaction point their time is zero. Thus interactions outside the interaction region produce positive or negative time shifts. Requiring the time to be within a certain time window is an effective way to reject beam gas events, occuring outside the interaction region.

First Level Trigger (FLT)

At the FLT level, information about energy deposits in calorimeter sections is available. In addition the calorimeter cells are searched for isolated energy deposits. The CTD provides information about the existence of tracks pointing to the interaction region. Timing information from the C5 counter or the VETO wall is used to reject background from beam gas events.
For this analysis three of the DIS filters were used to select events. Two of them require an isolated electromagnetic energy deposit in the RCAL of more than $\sim 2\,\mathrm{GeV}$ as a crude electron finding algorithm. In addition the two filters ask for different combinations of energy in the different calorimeter sections above a threshold of a few GeV, a track found in the CTD or a hit in the SRTD. The third filter requires some energy thresholds in connection with a found track in the CTD. All filters require certain timing conditions as measured by the VETO counters to reject background events. The selection efficiency for DIS events with this filter combination is close to 100 % in the kinematic region of this analysis.

Second Level Trigger (SLT)

At the SLT level the calorimeter timing information is used to reject non-physics events. The time is calculated separately in each of the calorimeter sections as a mean of the time measured by each photomultiplier. If any of the quantities $|t_{RCAL}|$, $|t_{FCAL}|$ or $|t_{FCAL} - t_{RCAL}|$ is larger than 8 ns, or the mean of the entire calorimeter time is larger than 10 ns the event is not accepted by the SLT. This cut removes beam-gas events. To reject cosmic events a cut on the time difference between the upper and lower BCAL halves is applied, ($|t_{up} - t_{down}| < -10\,\mathrm{ns}$). Empty events, where none of the calorimeter cells has a signal above some threshold, are also removed. Additional events are rejected, which have low overall activity in the calorimeter, but one high and isolated energy deposit. This is likely to be due to a noisy cell and not due to a physics event.
To select DIS events at the SLT level, energy cuts on the different calorimeter sections similar to those of the FLT are applied. In addition, a logical OR out of the FLT DIS filters is required. The specific SLT filter used for this analysis requires ($E - p_z + 2E_\gamma^{Lumi} > 29\,\mathrm{GeV}$). The quantity

$(E - p_z)$ is obtained by summing up all calorimeter cells, $(E - p_z) = \sum_i (E_i - p_{i,z})$. E_γ^{Lumi} is the energy measured with the photon detector of the luminosity system. For an event fully contained in the detector, momentum conservation requires $(E-p_z)$ to be the same in the initial and in the final state. Hence it follows that it is expected to be twice the incoming positron energy ($(E-p_z) = (E-p_z)_{proton} + (E-p_z)_{electron} \simeq (E_p - E_p) + (E_e - (-E_e)) = 2E_e = 55\,\mathrm{GeV}$). For DIS events, where the scattered positron is measured somewhere in the detector the $(E - p_z)$ is indeed around 55 GeV (see Section 5.2.2 Figure 5.7). Photoproduction events, where the positron escapes down the beampipe, or beam gas events initiated inside the detector both show lower values for $(E - p_z)$. Cutting away the lower $(E - p_z)$ region therefore effectively reduces background events. Due to initial state radiation the initial positron energy is lower than 27.5 GeV. To recover the measured $(E - p_z)$ for some of these events the photon energy is added if it is measured with the luminosity calorimeter. An upper cut on $(E - p_z)$ of 100 GeV is also applied to further reduce background like beam gas events or events with noisy cells.

Third Level Trigger (TLT)

At the TLT, combined information from different detector components is available. Different electron finders are used to identify the scattered DIS positron. Timing cuts to reject background events are applied, which are similar to the SLT but slightly tighter. The TLT DIS filters require the logical OR out of the FLT DIS filters, $(E - p_z + 2E_\gamma^{Lumi}) > 30\,\mathrm{GeV}$ and $(E - p_z < 100\,\mathrm{GeV})$.
To select the DIS events for this analysis at the TLT level, two different filters were used. Both require that at least one out of four electron finders found a candidate for the scattered positron with $E'_e > 4\,\mathrm{GeV}$. The electron finder used for the offline selection is one of the four finders. The difference between the two filters is the cut on the position of the scattered positron. If the scattering angle θ_e is large, the positron hits the SRTD close to the beampipe. In order to avoid energy leakage at the detector edges, it is necessary to reject hits which are inside a box of $(|X| = 12\,\mathrm{cm}, |Y| = 6\,\mathrm{cm})$ around the beampipe (box cut). High θ_e corresponds to low Q^2 events. Since the cross section for DIS events increases rapidly towards low Q^2 values the cut on the positron position around the beampipe can be increased to reduce the trigger rate. One of the TLT filters only requires the minimal cut at $|X| = 12\,\mathrm{cm}$ and $|Y| = 6\,\mathrm{cm}$, but was prescaled by a factor of 100 for most of the running period during 1997 to reduce the

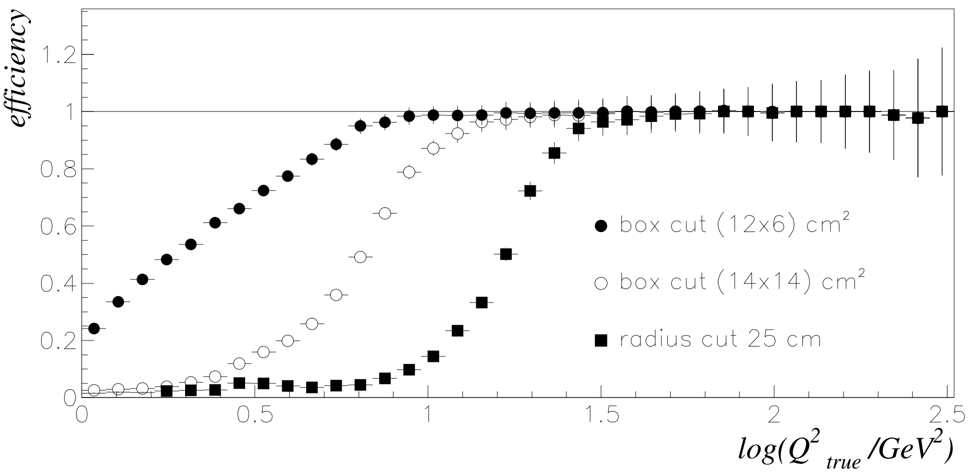

Figure 5.6: *Efficiency for the different TLT filters versus the true Q^2 of the event, determined from a sample of DIS MC* $(0.04 < y_{true} < 0.7)$.

high rate of low Q^2 events. The second filter used changed during the running period 1996. Initially events were only taken if the positron position was outside a box of $|X| = 14\,\mathrm{cm}$ and $|Y| = 14\,\mathrm{cm}$ around the beampipe. This cut was increased to a radial cut of $r_{positron} > 25\,\mathrm{cm}$ for the remaining running period. The events are selected with a logical OR of the two filters. Due to the prescale of the filter with the minimal cut on the positron position, the statistics of the final sample are reduced in the low Q^2 region. Figure 5.6 shows the efficiency of the three different TLT filters. The different cuts on the positron position directly correspond to cuts on Q^2. The TLT filter using only the radial cut of 25 cm is reasonably efficient above Q^2 values of $\sim 20\,\mathrm{GeV}^2$. About 70 % of the integrated luminosity was taken with the TLT filter with the radial cut and a prescale of 100 on the low-Q^2 trigger with the $(6 \times 12)\,\mathrm{cm}^2$ box cut.

Offline Bits

The ZEUS physics groups define filter bits which are calculated during reconstruction. These bits can be used offline for a fast access to the desired data. To select the DIS event sample, the general neutral current DIS bit was used, which requires the neutral current TLT filters to have taken the event.

5.2.2 Offline Cuts

For the offline selection of the DIS event sample the fully reconstructed data was available. Thus the kinematic variables were calculated using corrections, such as energy or noise corrections, wherever possible. Some of the cuts applied are similar to those used at the trigger level, but more stringent.

Cut on the Vertex Z-position

The Z vertex distributions for selected DIS events after the trigger selection are shown in the left plot of Figure 5.7 for data and MC. The distribution of the data, represented by the stars, shows a peak around $Z = 0\,\mathrm{cm}$. The width of 10 cm is caused by the proton bunch length. A second peak at $Z = 70\,\mathrm{cm}$ can be seen, as well as another smaller one at $Z = -70\,\mathrm{cm}$. They are called satellite peaks. They are produced by events where the positrons interact with protons which were trapped in a neighbouring RF bucket and are therefore ahead or behind the main proton bunch, by 4.8 ns. A cut on the Z-position of the event vertex of $\pm 40\,\mathrm{cm}$ is applied mainly to avoid any contribution from beamgas events. Thereby also the satellite peak events are cut away. The events from positrons scattering off the satellite protons are however good physics events which contribute to the total integrated luminosity. Therefore a good description of the Z vertex by MC data is necessary to calculate the correct detector acceptance using the MC events. The black dots in Figure 5.7 show the vertex distribution given by MC. It does not accurately describe the satellite peaks in the data distribution. For this reason a vertex reweighting routine was developed, which uses a minimum bias sample from data to reweight the MC according to the data vertex distribution [Qua98]. The open dots show the reweighted MC distribution, which gives a better description of the data. The agreement is not perfect because the data shown is only a small subsample of the 1996 data and not the whole data set from which the minimum bias sample was extracted.

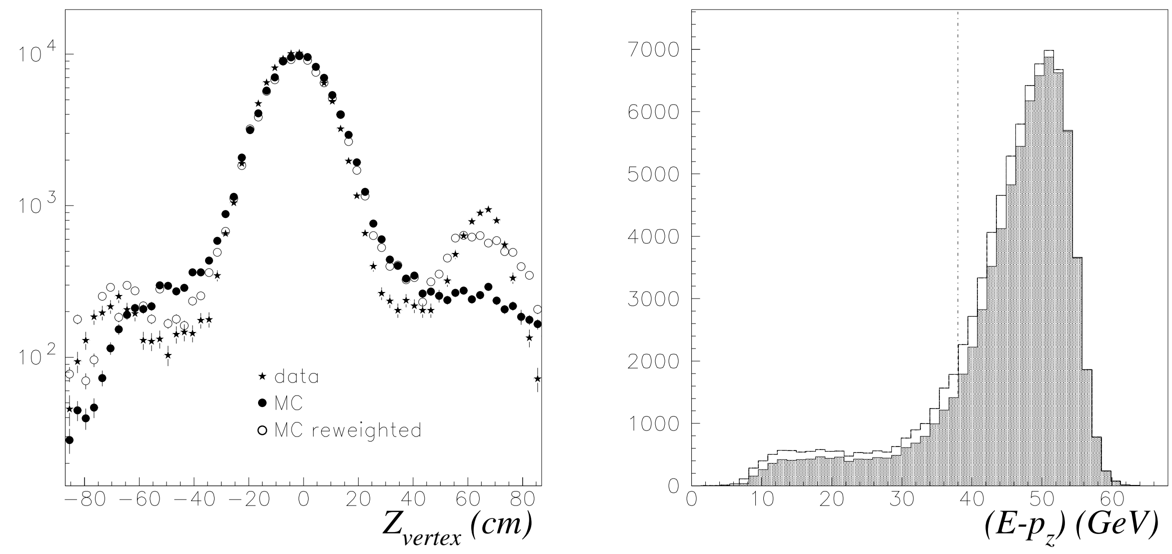

Figure 5.7: *The left plot shows the Z position of the event vertex for a data sample (stars), a MC sample (dots) and a reweighted MC DIS sample (open dots). The right plot shows the $(E-p_z)$ distribution of MC DIS events ($Q^2 > 1\,GeV^2$). The hatched histogram is the subset of events with a found DIS positron candidate. The dashed line indicates the cut applied offline.*

The $(E - p_z)$ Cut

A lower $(E-p_z)$ cut of 38 GeV is applied to reduce background from photoproduction events as well as events with initial state radiation. The right plot in Figure 5.7 shows the $(E-p_z)$ distribution for a sample of DIS MC events ($Q^2 < 1\,\mathrm{GeV}^2$). The hatched histogram shows the subset of those events where a positron candidate inside the detector was found by the electron finder. Both distributions show a peak at 55 GeV and a long tail towards low $(E-p_z)$ from events with initial state radiation. The events missing in the hatched histogram are those in which the positron left the detector undetected through the beam pipe. To avoid these inefficiencies, and to remove the events with initial state radiation as well as background from photoproduction events, a cut at 38 GeV is applied.

Positron Candidate

The electron finder SINISTRA described in Section 5.1.2 is used to identify the scattered DIS positron. To have high finding efficiencies (see Figure 5.3) and avoid large impurities due to misidentified positrons at low energies, the corrected energy of the found candidate is required to be $E_e^{SINISTRA} > 10\,\mathrm{GeV}$. A cut on the positron position of ($|x| = 12.5\,\mathrm{cm}$, $|y| = 6.5\,\mathrm{cm}$) around the RCAL beampipe is applied, which is slightly tighter than the one applied on TLT level for the low Q^2 configuration.

Cut on y_e

The phase space for the scattered positron with $E_e' < 27.5\,\mathrm{GeV}$ to reach the FCAL is limited (see Figure 5.4). For small positron energies this refers to the region of high y. In this low energy region the probability is high that the electron finder falsely identifies a π^0 as the scattered positron. To avoid contamination of the sample by photoproduction events which have a misidentified positron candidate, an upper cut of $y_e < 0.95$ is applied.

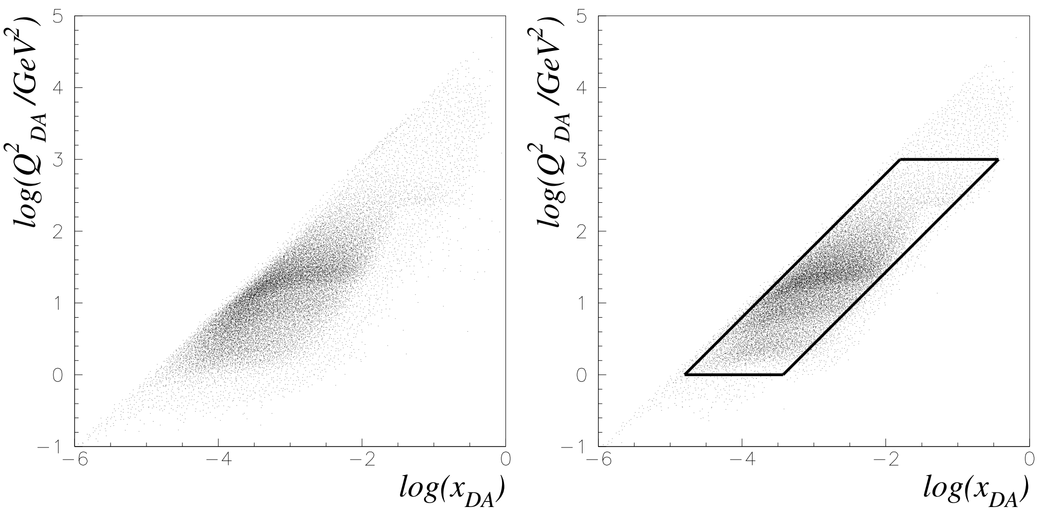

Figure 5.8: *Left plot: The preselected DIS data sample after trigger selection and some soft cuts (see text), right plot: The final DIS sample after all offline cuts and with at least one track coming from the main vertex with $p_t > 0.5\,\mathrm{GeV}$. The selected kinematic region, $0.03 < y_{DA} < 0.7$ and $1 < Q^2_{DA} < 1000\,\mathrm{GeV}^2$, is indicated by the solid line.*

Cut on y_{JB}

Although the Jacquet-Blondel method is not useful for the kinematic reconstruction due to the large migrations and poor resolution, a lower cut on y_{JB} is used to control noise effects in the calorimeter. y_{JB} only depends on the difference between the total hadronic energy and longitudinal hadronic momentum (see Equation 5.7). Thus in the low-y region, contributions from noise can effectively distort the y measurement. Since the hadronic angle γ_h, which enters the calculation of the double angle variables, depends also on the hadronic quantities, a lower cut on y_{JB} of $y_{JB} > 0.02$ improves the resolution for the reconstruction of γ_h.

Kinematic Region

Figure 5.8 shows in the (x, Q^2) plane the preselected data sample (left plot) and the final sample (right plot). For the preselected sample, only the trigger selection and some loose cuts, namely ($E'_e > 8\,\mathrm{GeV}$), $(E - p_z) > 32\,\mathrm{GeV}$ and $|z_{vertex}| < 45\,\mathrm{cm}$, were applied. The final sample is selected with all offline cuts and the requirement of at least one track coming from the vertex with $p_t > 0.5\,\mathrm{GeV}$. This preselects the charm candidate events (see next chapter). The low-Q^2 region is restricted by the acceptance of the RCAL and the SRTD. The statistics in the low-Q^2 region inside the detector acceptance are further reduced due to the 25 cm radial cut and the $(14\times 14)\,\mathrm{cm}^2$ box cut at the TLT level. At high Q^2 the effect of the cross section decreasing with increasing Q^2 restricts the kinematic regime. Close to the kinematic limit at high y, the cut on the positron energy results in an effective y_e cut of about 0.64. The low-y region is restricted by the lower cut on y_{JB}. The selection of DIS events for the determination of the cross section and $F_2^{c\bar{c}}$ is restricted to the kinematic region, $0.03 < y_{DA} < 0.7$ and $1 < Q^2_{DA} < 1000\,\mathrm{GeV}^2$, indicated by the solid line in the right plot of Figure 5.8.

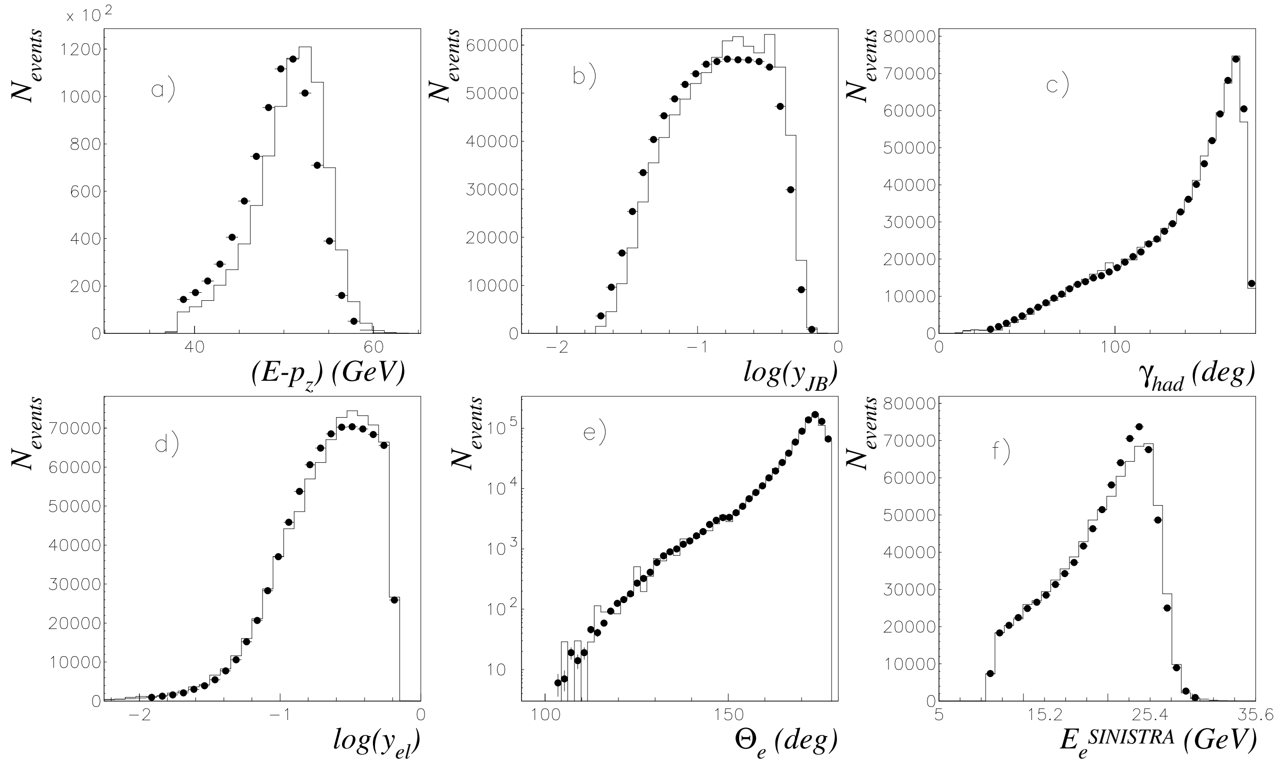

Figure 5.9: *The $(E - p_z)$ (a), y_{JB} (b), γ_{had} (c), y_e (d), θ_e (e) and the corrected positron energy (f) of the selected data sample (dots) in comparison with an inclusive DIS MC sample (solid line).*

5.3 Comparison of Data and MC

In this section a comparison is made between data and an inclusive DIS MC sample for some of the relevant variables. DJANGO [Sch91] was used for the generation of the DIS events, which is an interface between HERACLES [Kiw92] and LEPTO [Ing97] (see Section 4.1.1). The events are selected with the same criteria in data and MC. The cuts are applied according to the above discussion in the kinematic region $0.03 < y_{DA} < 0.7$ and $1 < Q^2_{DA} < 1000\,\mathrm{GeV}^2$. Only the 1996 subsample, corresponding to about $\mathcal{L}_{96} = 9.5\,\mathrm{pb}^{-1}$ out of $\mathcal{L}_{96/97} = 34.0\,\mathrm{pb}^{-1}$, is shown in the following figures. The MC is normalized to the data.

Figure 5.9 a) shows a discrepancy of the $(E - p_z)$ distribution between data and MC. The data is shifted towards lower values. The corrected positron energy in Figure 5.9 f) also shows some disagreement. The data overshoots the MC in the kinematic peak region around $E_e^{SINISTR} = 27.5\,\mathrm{GeV}$. A possible explanation for this disagreement could be the SRTD and presampler energy corrections which are different for data and MC. This is also likely to be the reason for the shift in the $(E - p_z)$ distribution. Figures 5.9 b) and d) show the variables $\log(y_{JB})$ and $\log(y_e)$. Both show similar disagreements. The data is below the MC in the high-y region but overshoots it towards lower y values.

The hadronic angle γ_{had} and the polar angle of the scattered positron θ_e are shown in Figures 5.9 c) and e) respectively. Good agreement between data and MC is found for these two quantities. The kinematic variables $\log(x_{DA})$, $\log(y_{DA})$ and Q^2_{DA} are shown in Figures 5.10 a), b) and c) respectively. The agreement between the data (dots) and the DIS sample (solid line) is good. Also shown are the distribution for the charm MC sample (dashed line), exhibiting the different kinematics of charm production in DIS events. Figures 5.10 d) and e) show p_{track} and θ_{track} for all tracks coming from the main event vertex. The agreement between data and the DIS

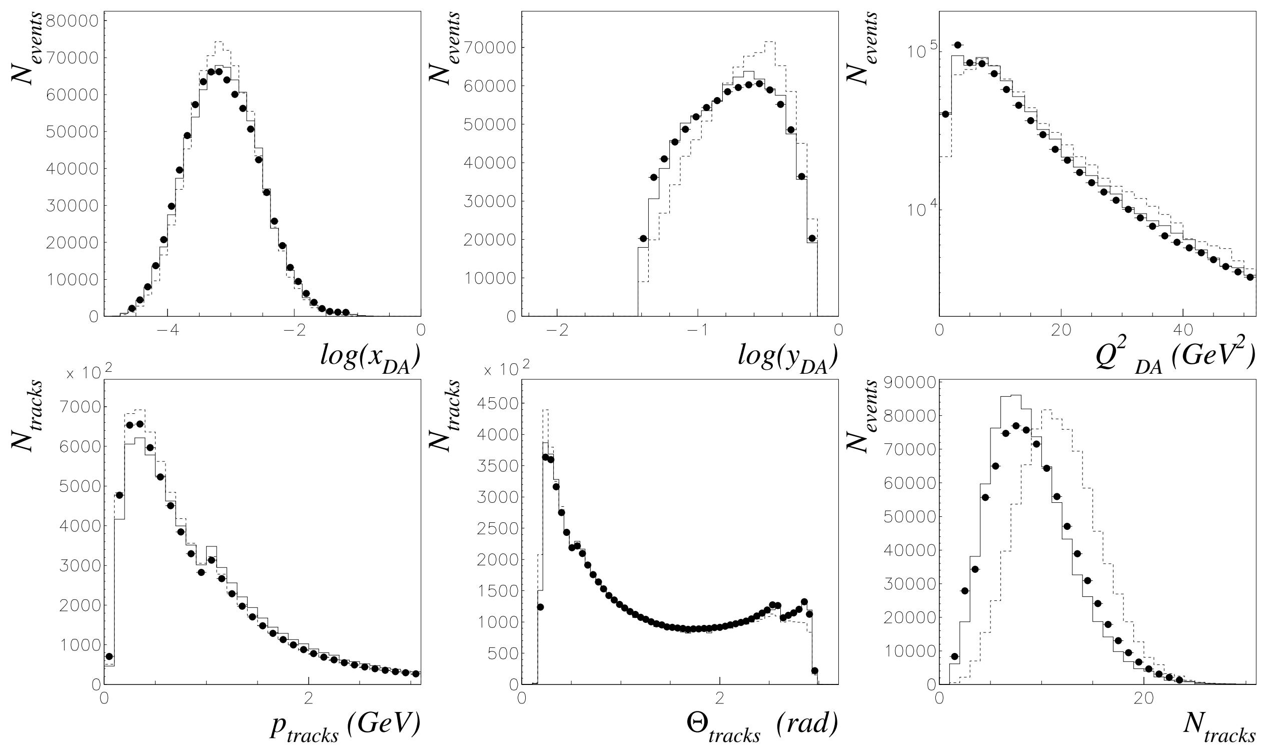

Figure 5.10: *The kinematic variables $log(x_{DA})$ (a), $log(y_{DA})$ (b) and Q^2_{DA} (c) of the selected data sample (dots) compared to an inclusive DIS MC sample (solid line) and the charm MC sample (dashed line) are shown. The lower three plots show the momentum (d) and the polar angle (e) of all tracks coming from the event vertex, and the number of tracks itself (f).*

and charm MC samples is reasonable. To enhance the number of candidate events for the later semileptonic charm analysis, only events with at least one track with $p_{track} > 1.0$ GeV and $0.55 < \theta_{track} < 2.6$ rad were selected. This results in small peaks at 1 GeV in the momentum distribution and at 0.55 and 2.6 rad in the polar angle distribution. The total number of tracks coming from the event vertex is shown in Figure 5.10 f). The number of tracks in the DIS MC events is shifted towards slightly lower values compared to the data. Due to the decaying charmed hadrons the average track multiplicity of the charm events peaks at higher values than for the inclusive DIS events.

The efficiency corrections to the data are done with the exclusive charm MC sample as described in Section 4.1.1. Hence the above discussion served only to demonstrate the general shape of the different variables of the selected DIS sample. The disagreement between the data and the inclusive DIS MC for the quantity $(E-p_z)$ and the positron energy $E_e^{SINISTRA}$ are accounted for by varying the cuts on these quantities as a systematic check. However, the kinematic variables x, y and Q^2, which directly enter into the calculation of the cross sections are sufficiently well described for the measurement.

Chapter 6

Charm Selection

In this chapter the selection of charm candidate events from the inclusive DIS sample will be discussed. In the first two sections a general overview is given about charm tagging at ZEUS. In the third section the use of the CTD for particle identification by the measurement of the particle's energy loss (dE/dx) due to ionization is explained. The necessary corrections that have to be applied to use dE/dx in this analysis are presented. In the fourth section, the method used to identify electrons and the estimation of background electrons from non-charm decays is explained.

6.1 Identification of Charm with the ZEUS Detector

The identification of charm production in DIS events proceeds via the measurement of the decay products of charmed hadrons. In the case of open charm production the predominantly produced hadrons are D mesons. Only a small fraction of the produced charm quarks form baryons, e.g. Λ_c, Σ_c, Ξ_c or Ω_c. To form a D meson, the charm quark most likely picks up a u or a d quark forming a $D^0(\bar{D^0})$ or a $D^{\pm}$ either in the ground state or in one of the short-lived excited states such as D^{*0} or $D^{*\pm}$. A smaller fraction of the charm quarks fragments into a D_s meson by picking up an s quark. The produced $c\bar{c}$ pair may also form a bound state, such as the J/Ψ. The contribution of these processes to the inclusive charm cross section in deep-inelastic ep scattering events is small, between 2.5 % and 4.5 % [Br99B,Br00A].
Charmed hadrons, which have charged decay products, can be observed in the central tracking chamber (CTD). At HERA the production mechanisms of D^0, $D^{*\pm}$,D_s or J/Ψ have been investigated [Adl96, Ad99A, Ad99B, Br97A, Br99B, Br99C, Br00A, Br00B]. Measurements of exclusive decay channels such as $J/\Psi \to e^+e^-(\mu^+\mu^-)$ or $D^0 \to K^-\pi^+$ provide clean signals, but suffer, especially in the case of D meson production, from small branching ratios for the specific decays. The statistics of the charm signal can be improved using inclusive channels such as the semileptonic decay of charm quarks, requiring either a muon or an electron in the final state.
Since the lifetimes of the ground states of the charmed hadrons are large, $\mathcal{O}(10^{-12})$ s, their decay vertices are well separated from the primary interaction vertex. A method commonly used by other experiments to improve charm tagging is to identify these secondary vertices. At HERA the separation of the decay vertex from the primary vertex is $\sim 100\mu$m. The resolution of the ZEUS detector is currently not adequate to resolve the secondary vertices. With the installation of the microvertex detector (MVD) [Br97B] and the straw-tube tracker (STT) [BR98A] in the year 2000, the general tracking, especially in the forward region, will be substantially improved, allowing secondary vertices to be tagged.
The results from the analysis of semileptonic charm decays in this thesis will be compared to

those obtained from the ZEUS measurement of D^* production in DIS events using the same 1996/97 data set [Br00A]. The D^* method is therefore explained in more detail below.

The D^* Decay Channel

Charm production in DIS, as well as in photoproduction, was observed at ZEUS via the measurement of $D^{*\pm}$ production [Br00A,Br99C] in the following two decay channels,

$$\begin{array}{rlllll} D^{*+} \longrightarrow & D^0 & + \pi_s^+ & & & \\ & \hookrightarrow & K^- & + \pi^+ & & \\ & \hookrightarrow & K^- & + \pi^- + & \pi^+ + & \pi^+ \quad , \end{array} \tag{6.1}$$

and in their charge-conjugate channels[1]. Due to the small mass difference between the D^{*+} and the D^0 meson, $\Delta M = M(D^{*+}) - M(D^0) = (2010 - 1865)\,\mathrm{MeV} = 145\,\mathrm{MeV}$, the momentum of the pion in the D^{*+} rest frame is very low, hence the subscript "slow" π_s^+. The mass difference ΔM can therefore be measured more accurately than the mass of the D^{*+} or D^0 meson itself. The decay $D^{*+} \to D^0\pi_s^+$ has a branching ratio of $\sim 68\,\%$. The probabilities for the subsequent decay of the D^0 into charged particles is low, $3.85\,\%$ for the $D^0 \to K^-\pi^+$ decay and $7.6\,\%$ for the $D^0 \to K^-\pi^-\pi^+\pi^+$ decay. Compared to the $(K\pi\pi_s)$ channel, the $(K\pi\pi\pi\pi_s)$ channel has the advantage of the higher branching ratio but suffers from larger background due the larger number of tracks to be combined.

The selection of the desired events starts with the forming of a D^0 candidate. In case of the $D^0 \to K^- + \pi^+$ channel, pairs of oppositely-charged tracks are alternately assigned the masses of a charged kaon and a charged pion. An additional slow track with opposite charge to that of the kaon track and an assigned pion mass is combined with the D^0 to form the D^* candidate. For the selection of the $D^0 \to K^-\pi^-\pi^+\pi^+$ channel the same procedure is followed but two negative and two positive tracks are combined to form the D^0 candidate.

Cuts on the p_T and η of the different tracks are applied to achieve good tracking resolution and to reduce the combinatorial background. The kinematic region of the measured D^* candidate is then $1.5 < p_T(D^*) < 15\,\mathrm{GeV}$ and $|\eta(D^*)| < 1.5$ for the $(K\pi\pi_s)$ channel, and $2.5 < p_T(D^*) < 15\,\mathrm{GeV}$ and $|\eta(D^*)| < 1.5$ for the $(K\pi\pi\pi\pi_s)$ channel.

The $M(D^0)$ signals are obtained by selecting events with $143 < \Delta M < 148\,\mathrm{MeV}$. To pick out the ΔM signal, a cut on $M(D^0)$ is applied: $1.80 < M(D^0) < 1.92\,\mathrm{GeV}$ for the $(K\pi\pi_s)$ channel and $1.81 < M(D^0) < 1.91\,\mathrm{GeV}$ for the $(K\pi\pi\pi\pi_s)$ channel. The obtained $M(D^0)$ distributions are shown in Figures 6.1 a) and c) for the $(K\pi\pi_s)$ and $(K\pi\pi\pi\pi_s)$ channels respectively and Figures 6.1 b) and d) shows the ΔM distribution for the two channels. The distribution of $M(D^0)$ for the $(K\pi\pi_s)$ channel exhibits a second peak around 1.6 GeV. These are events originating from $D^0 \to K^-\pi^-\pi^0$ decays where the neutral pion is not reconstructed.

The dashed lines in Figures 6.1 c) and d) represent the background events of the $(K\pi\pi\pi\pi_s)$ channel. The background events are obtained using events from side-bands in the ΔM distribution outside the signal region to form the D^0 background and vice versa for the ΔM background distribution. The distributions are fitted and the measured values for the mass of the D^0 and the mass difference ΔM agree well with the PDG values [Cas99]. $M(D^0)_{K\pi\pi_s} = 1863.2 \pm 0.8\,\mathrm{MeV}$, $M(D^0)_{K\pi\pi\pi\pi_s} = 1862.7 \pm 1.5\,\mathrm{MeV}$, $M(D^0)_{PDG} = 1864.6 \pm 0.5\,\mathrm{MeV}$ and $\Delta M_{K\pi\pi_s} = 145.44 \pm 0.05\,\mathrm{MeV}$, $\Delta M_{K\pi\pi\pi\pi_s} = 145.61 \pm 0.05\,\mathrm{MeV}$, $\Delta M_{PDG} = 145.397 \pm 0.030\,\mathrm{MeV}$. The number of selected $D^{*\pm}$ events for the $(K\pi\pi_s)$ channel is 2064 ± 72, determined from a fit to the ΔM distribution. For the $(K\pi\pi\pi\pi_s)$ channel a signal of 1277 ± 124 $D^{*\pm}$ events was obtained by subtracting the background events estimated from the side-bands.

[1] In the following the charge-conjugate is always implied.

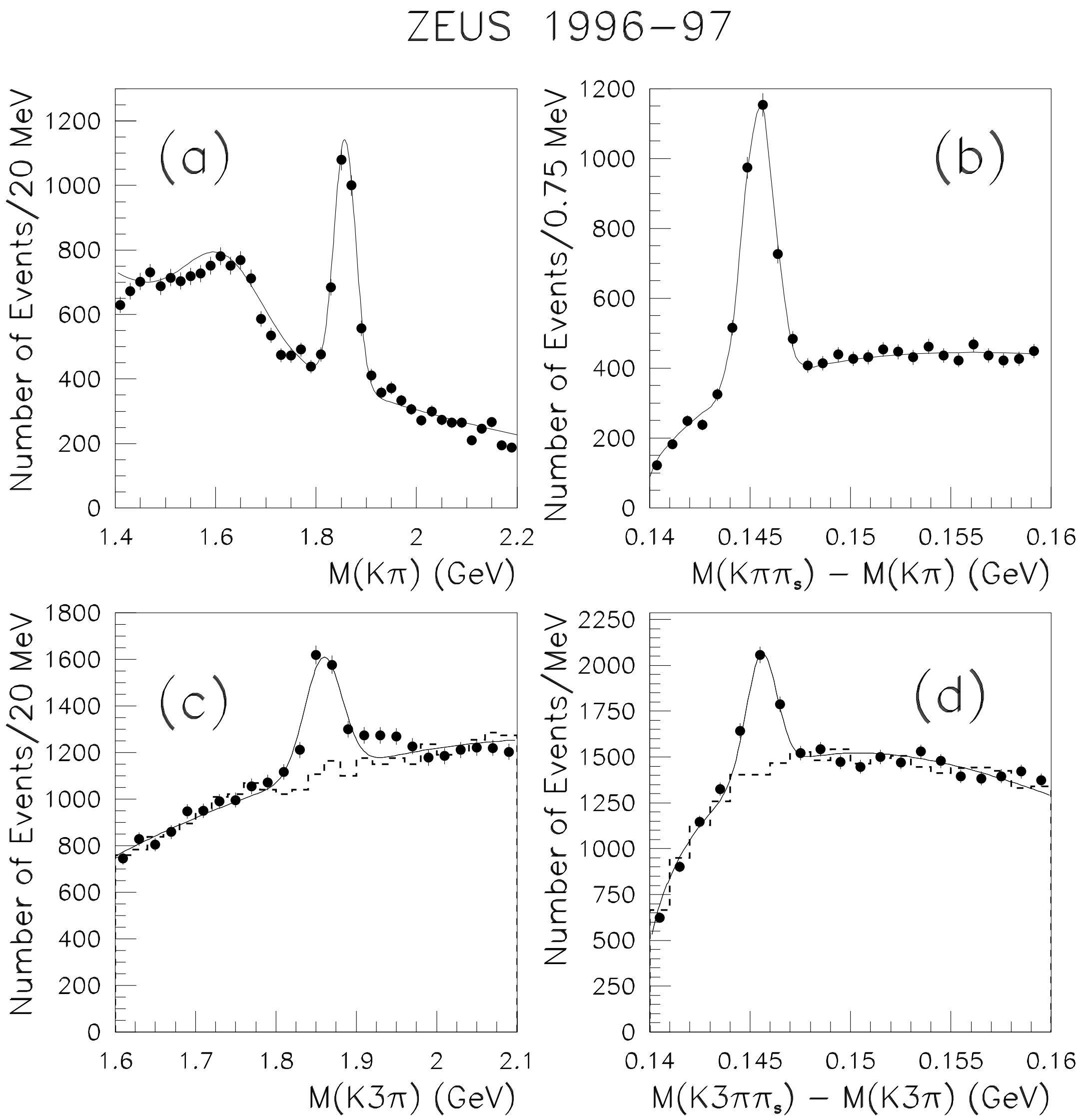

Figure 6.1: *a) and c) show the mass distributions $M(D^0)$ for the $(K\pi\pi_s)$ and $(K\pi\pi\pi\pi_s)$ channels respectively. b) and d) show the ΔM signals for the $(K\pi\pi_s)$ and $(K\pi\pi\pi\pi_s)$ channels respectively [Br00A].*

For the extraction of the charm contribution to the proton structure function $F_2^{c\bar{c}}$, the measured $D^{*\pm}$ cross section has to be extrapolated to the full phase space in $p_T(D^*)$ and $\eta(D^*)$. The acceptance of the $D^{*\pm}$ candidates varies between 25 % and 65 % for the $(K\pi\pi_s)$ channel and between 10 % and 25 % for the $(K\pi\pi\pi\pi_s)$ channel. To convert the measured cross section for $D^{*\pm}$ production into a charm cross section, the hadronization fraction $f(c \to D^{*\pm}) = 0.222 \pm 0.014 \pm 0.014$, as measured by the OPAL collaboration, is used [Ack98].

The Semileptonic Decay

The D^* channel provides a clean charm signal, but due to the low overall branching ratio of $BR(c \to D^* \to D^0\pi_s \to K\pi\pi_s(K\pi\pi\pi\pi_s)) = 0.6\,\%$ (1.2 %) the statistics are very limited. The semileptonic decay of charm quarks into electrons or muons yields better statistics due to the higher branching ratio of $BR(c \to e\nu X(\mu\nu X)) \sim 10\,\%$. However, since it is an inclusive measurement, the background of electrons or muons that do not stem from semileptonic charm

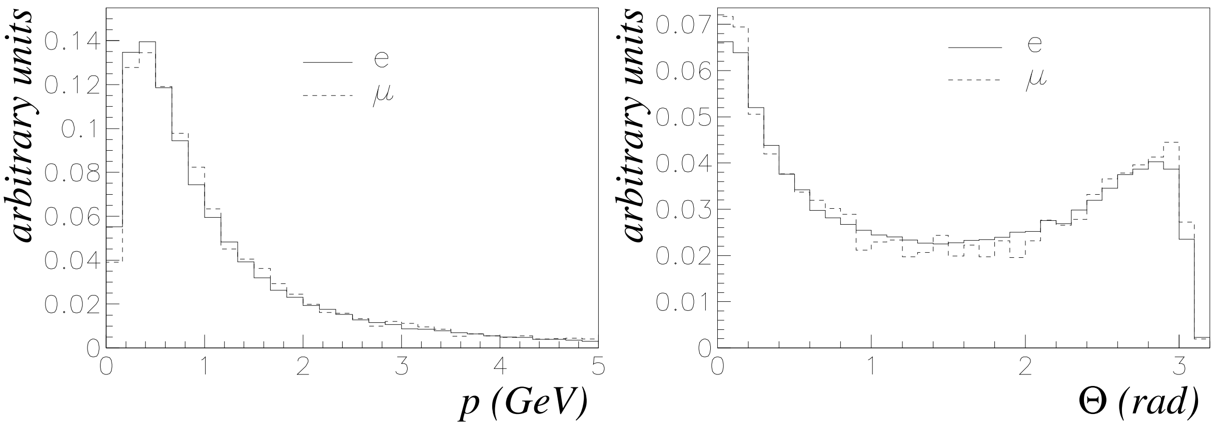

Figure 6.2: *Momentum (left plot) and theta (right plot) distributions of* $e^{\pm}$ *(solid line) and* $\mu^{\pm}$ *(dashed line) from semileptonic charm decays obtained from a RAPGAP DIS MC sample of charm events.*

decays must be estimated.
Figure 6.2 shows the momentum and theta distributions of leptons from semileptonic charm decays in the laboratory frame. The distributions are obtained using a DIS MC sample ($Q^2 > 0.6\,\mathrm{GeV}^2$) of charm events generated with RAPGAP. The momentum distributions for both the electrons and the muons peak at low momenta between 0.2 to 0.6 GeV. The muon spectrum is shifted to slightly higher momenta compared to the electrons.
To tag the muons from semileptonic decays at ZEUS the muon chambers are generally used (see Section 3.2). However, in order to reach the inner muon chambers the muon has to traverse the calorimeter, and to reach also the outer chambers the backing calorimeter also has to be passed. Hence the muon momentum distribution measured with the muon chambers has an implied lower momentum cut of about 2 GeV, cutting away most of the signal (see Figure 6.2). Using only the CTD and the calorimeter to tag muons is not feasible, but they are used in combination with the muon chambers to improve the tracking resolution.
The detection of electrons does not entail such a severe momentum cut. They can be identified using for instance the calorimeter and the HES or the presampler detectors. The method used in this analysis makes use of the energy loss measured with the CTD combined with information about the energy deposit in the calorimeter.

6.2 Semileptonic Decays of Charm Quarks into Electrons

At ZEUS the possibility of measuring electrons from semileptonic charm decays using the measurement of the energy loss dE/dx with the CTD was first investigated with the 1993 data set [Wou95]. The results were limited by the small statistics and relatively poor understanding of dE/dx. Improved results were obtained with the 1995 data set due to larger statistics and a better understanding of dE/dx. Using this data set the charm contribution to the proton structure function, $F_2^{c\bar{c}}$, was extracted for the first time using the semileptonic decay channel [Heb99, Ver98]. The 1996/97 data set provides a factor of six more luminosity than the 1995 set. Due to the increased statistics further detailed studies concerning dE/dx and its application in

this analysis could be performed. A similar method was used to extract a beauty cross section in photoproduction with the 1996/97 data set [Wi99A, Wi99B].
Although the branching ratio of the semileptonic charm decay is about a factor of 10 higher than for the D^* channel the absolute gain in statistics by this method is lower, about a factor of 3 to 4. This is due to the limited electron acceptance and will be further discussed in Section 7.5.6, where the results of the two independent decay channels will be compared.
The use of dE/dx in combination with the calorimeter information as explained in Section 6.4 allows the measurement of an inclusive electron signal. Thus the background from electrons from non-charm decays must be estimated and subtracted (see Section 6.4.1).

6.3 Particle Identification using the CTD

Particles traversing the volume of the CTD lose energy by ionization of the gas molecules. The amount of the energy loss per unit length along the path (dE/dx) depends on the particle's velocity and therefore on its mass. This means that the measurement of the energy loss with the CTD offers the possibility of distinguishing between different particle types. The transformation of the raw pulse size into the quantity dE/dx and the corrections applied during reconstruction are described in Section 3.2.1. This section gives a brief overview of the expected energy loss from a theoretical point of view and a comparison with dE/dx measurements at ZEUS. Additional offline corrections which are applied to be able to use the dE/dx information for this analysis are also explained.
For charged particles other than electrons the energy loss whilst traversing matter proceeds predominantly via ionization. The mean energy loss dE per path-length dx for a particle with charge z and velocity $\beta = v/c$ is described theoretically by the Bethe-Bloch equation [Cas99]

$$-\frac{dE}{dx} = Kz^2\frac{Z}{A}\frac{1}{\beta^2}\left(\frac{1}{2}\ln\frac{2m_ec^2\beta^2\gamma^2T_{max}}{I^2} - \beta^2 - \frac{\delta}{2}\right) \quad , \tag{6.2}$$

where $K = 4\pi N_A r_e^2 m_e c^2$, A is the atomic mass of the material and Z is the atomic number. I is the mean excitation energy, which is difficult to calculate, but may be determined from measurements for different materials. For materials with $Z > 20$ it is given approximately by $I = Z\,10\,eV$. T_{max} is the maximum kinetic energy which can be transfered to an electron in one single collision allowed by the kinematics. A good approximation is $T_{max} = 2m_ec^2\beta^2\gamma^2$ for particles with mass M, where $M \gg m_e$ [Leo92]. δ is the density effect correction which is important at high energies. Polarization of the atoms along the path of the charged particle leads to a shielding effect for electrons far from the particle path. This leads to a reduced energy loss of particles at high energies. The size of the effect depends on the density of the material. The mean energy loss in one single collision is small, $\mathcal{O}(10^{-6} - 10^{-5}\,\mathrm{GeV/cm})$, when compared to the total energy of the particles. Therefore the assumption that the momentum of the particles stays constant on their way through the CTD, and hence the mean energy loss per path-length dE/dx is the same in each collision is justified.
The Bethe-Bloch equation describes the energy loss as a function of $\beta = v/c = \sqrt{1-1/\gamma^2} = c|\vec{p}|/E$, which dependends on the momentum and mass of the particle. The left plot in Figure 6.3 shows the predicted energy loss for pions, kaons and protons according to the Bethe-Bloch formula. The density correction is neglected. The energy loss is normalized to the energy loss of pions with 0.3 GeV momentum. At non-relativistic energies the energy loss, dominated by the $1/\beta^2$ factor, decreases until $p/(Mc) = \beta\gamma \simeq 3$ (minimum ionizing particles). For higher energies the energy loss rises logarithmically. Taking the density corrections into account cancels the

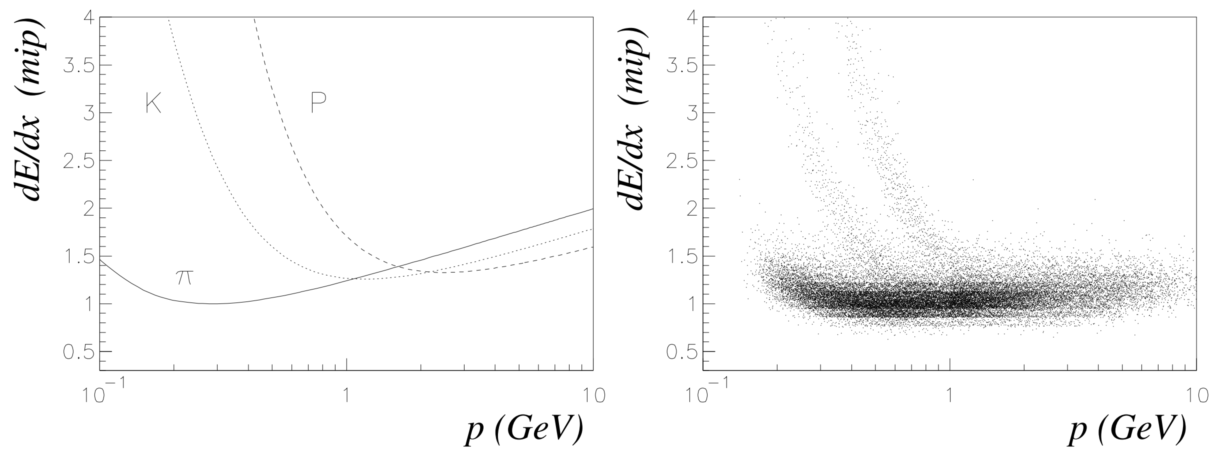

Figure 6.3: *The left plot shows the theoretical predictions for the energy loss of hadrons according to the Bethe-Bloch formula. No density correction is applied. The right plot shows the energy loss of negatively charged particles measured with the CTD. In both histograms the energy loss is normalized to that of pions with momenta between* 0.3 *and* 0.4 *GeV.*

logarithmic rise, so that the energy loss reaches a plateau at very high velocities. The right plot in Figure 6.3 shows the energy loss for negatively charged particles measured with the CTD (see Section 3.2.1). The proton, kaon and pion bands in the low-energy region are clearly distinguishable. For higher energies, the energy loss rises slower than the theoretical prediction in the left plot, exhibiting the missing density correction.

Due to their small mass, electrons lose a substantial amount of their energy by bremsstrahlung processes in the electric field of the nuclei in addition to ionization processes. Above a certain threshold, $\mathcal{O}(100\,\mathrm{MeV})$, depending on the material, the energy loss due to bremsstrahlung dominates. For a theoretical description of the energy loss for electrons due to ionization the Bethe-Bloch formula has to be modified. Due to their small mass electrons reach the rela-

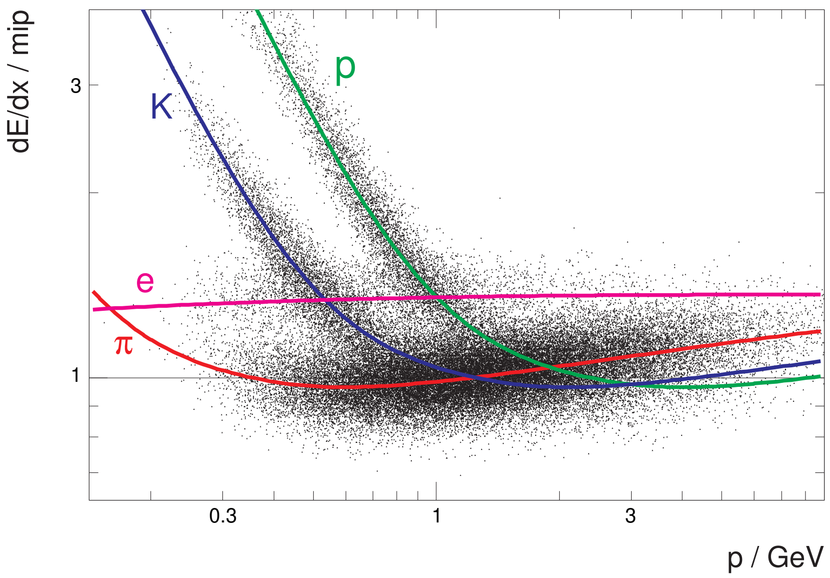

Figure 6.4: *The measured* dE/dx *distribution for negatively charged particles and the fitted* dE/dx *parametrization, adapted from [Dep99].*

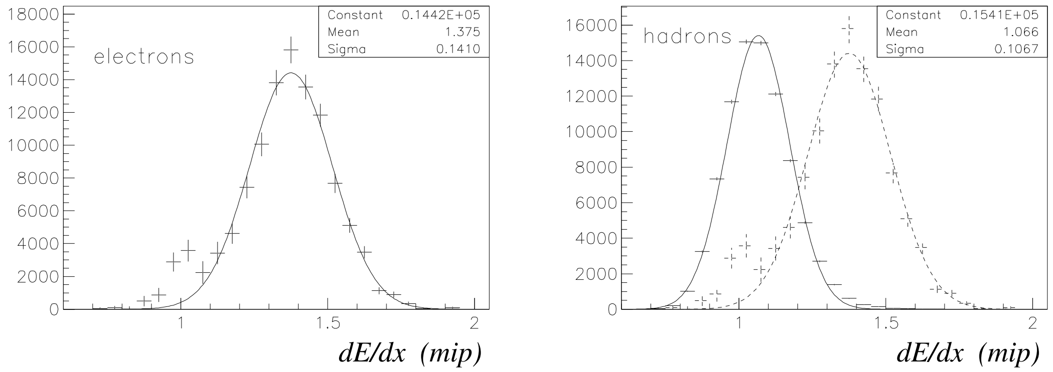

Figure 6.5: *The dE/dx distribution of electrons from photon conversions (left plot) and for negatively charged hadrons (right plot). The electron sample contains a small fraction of hadrons, which have dE/dx values around 1 mip (see Section 6.4.1). All tracks are required to have $p_{track} > 1.2\,GeV$ and $0.65 < \theta_{track} < 2.5\,rad$. The distribution for the electrons is also plotted in the right plot for comparison (dashed histogram).*

tivistic limit at lower momenta than hadrons. Therefore their energy loss does not exhibit the momentum dependence, and is expected to be constant in the momentum region under consideration.

At ZEUS a dE/dx parametrization and a dE/dx likelihood for particle identification was developed [Dep99]. The solid lines in Figure 6.4 show the fitted dE/dx parameterizations for the different particle types. Of interest for this analysis is the separation between electrons and hadrons. The dE/dx distribution for electrons is almost constant with momentum. At low momenta, below 1 GeV, the energy loss of hadrons varies strongly with momentum and thereby overlapping with the constant value of the electron energy loss. Thus a separation between electrons and hadrons in this region is not feasible. At high momenta however the dE/dx of hadrons forms a broad band which is separated from that for electrons. The dE/dx resolution and the separation between electrons and negatively charged hadrons in the high momentum region is demonstrated in Figure 6.5. All tracks have $p_{track} > 1.2\,\mathrm{GeV}$ and $0.65 < \theta_{track} < 2.5\,\mathrm{rad}$. The cut on the θ range ensures that the tracks pass through all nine superlayers of the CTD, thus producing the maximal number of hits. For tracks outside this angular region the dE/dx

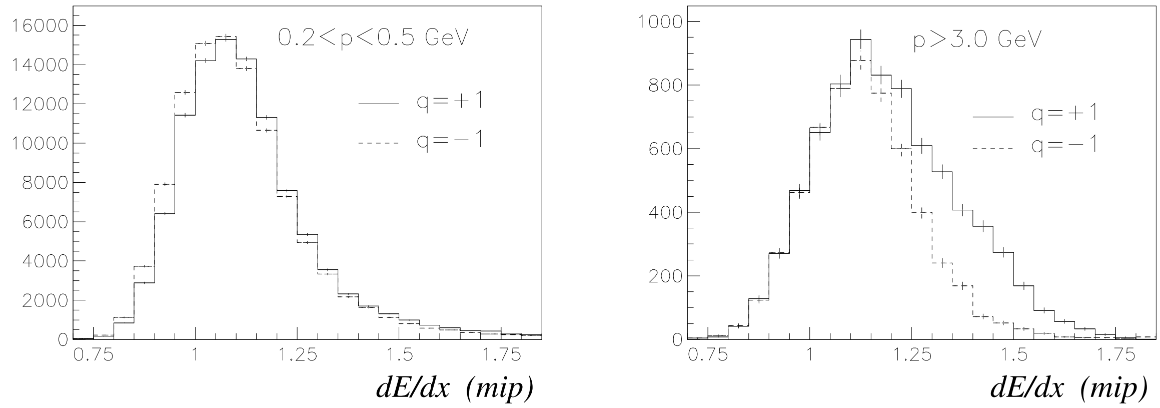

Figure 6.6: *Comparison of the dE/dx distribution of tracks from positively (solid histogram) and negatively (dashed histogram) charged particles for an inclusive sample of tracks with $0.2 < p < 0.5\,\mathrm{GeV}$ (left plot) and $p > 3.0\,\mathrm{GeV}$ (right plot). The shoulder at 1.5 mips in the distribution for positively charged particles in the right plot stems from the scattered DIS positrons.*

resolution decreases rapidly, because the number of hits which are used for the dE/dx measurement decreases. The dE/dx resolution in this central region of the CTD is about 10 %. The dE/dx distribution of the electrons in Figure 6.5 is broader than the hadron distribution. This is caused by the momentum and polar angular distribution of the electrons from photon conversions. The momenta of the electrons are lower compared to the hadrons, and they are predominantly produced at shallow angles with respect to the beam axis. Both aspects decrease the resolution of the dE/dx measurement.

All studies concerning dE/dx measurements must be performed separately for negatively and positively charged particles. Due to the CTD geometry there is a difference in tracking efficiency and FADC pulse shape between positive and negative particles, especially for low momentum tracks [Cat95,Dep99]. Due to the form of the magnetic field close to the sense wires of the CTD, the electrons from positive tracks arrive over a shorter time interval than those from negative tracks. This results in a different pulse shape for tracks from negatively and positively charged particles and a lower pulse height for negatively charged particles. The effect diminishes for increasing momenta. Figure 6.6 demonstrates the dE/dx difference for positively and negatively charged particles. The left plot shows the shift of dE/dx towards lower values for an inclusive sample of negatively-charged particles in the low momentum range, $0.2 < p < 0.5$ GeV. This shift vanishes at high momenta, as can be seen in the right plot. The tracks stem predominantly from pions and therefore peak around 1 mip. The shoulder at $dE/dx \sim 1.4$ mips in the dE/dx distribution for the high momentum positive tracks originates from the scattered DIS positrons.

6.3.1 Corrections to dE/dx

At ZEUS the measured energy loss is given as truncated mean of the FADC signal, normalized to the mean energy loss of minimum ionizing positive pions as described in Section 3.2.1. Several corrections for chamber effects and track geometry are applied in the reconstruction software, such that the value of dE/dx is only expected to depend on the particle type, its charge and its momentum. Nevertheless, a dependency of dE/dx on the polar angle of the track and on the event multiplicity was found. All studies described in the following were performed with the inclusive DIS sample (see Section 5.2) thus the obtained correction functions are optimized for this analysis. Considering the difference between positive and negative tracks all corrections have to be determined for each charge separately.

Dependence of dE/dx on the Polar Angle of the Track

In 1994 the dependence of the measured energy loss on the polar angle of the track was observed for the first time. The mean energy loss decreases towards steep angles with respect to the beam axis, and increases for shallow angles with respect to the beam axis. The dashed histogram in Figure 6.7 shows the mean energy loss versus the polar angle θ of the track for a clean sample of electrons from photon conversions measured with the 1996/97 data set (see Section 6.4.1). The distribution exhibits a clear dip around $\theta = 90^o$. For electrons the energy loss varies up to 7 % but it is less pronounced for particles with lower energy loss. The dotted histogram shows the mean energy loss for an inclusive sample of negatively charged hadrons with $p > 1.2$ GeV. No effect can be seen. However the hadron sample is a mixture out of different particles, mainly pions but also anti-protons and kaons.

The reason for this angular dependency is the so called “space-charge” effect. At polar angles around 90^o the amount of charge produced per centimetre along a wire due to the energy loss by ionization is larger than at shallower angles. Thus a saturation of the gas amplification occurs at the wire. This effect is even more pronounced for large energy losses. From 1995 onwards,

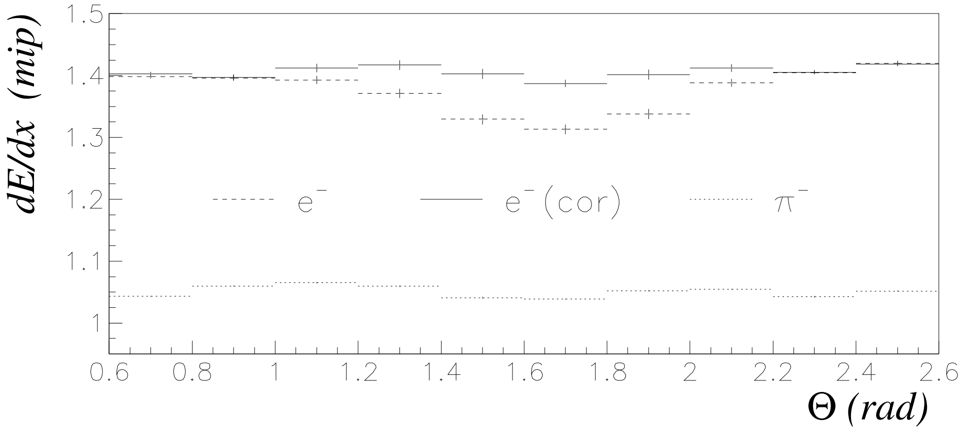

Figure 6.7: *Dependence of the energy loss dE/dx on the polar angle θ of the track for electrons from clean photon conversions and for hadrons ($p > 1.2\,GeV$). The solid line shows the angular behaviour of the dE/dx for electrons after applying the space charge correction. To obtain the mean energy loss, a Gaussian function was fitted to the dE/dx distribution in each θ bin. The error on the mean is the error on the peak position.*

the size of this effect was reduced by lowering the high voltage of the CTD, thus by reducing the gain. However to have reasonable tracking efficiency the high voltage cannot be lowered any further, and so a correction for this effect has to be applied.

To obtain the correction function the dE/dx distribution for electrons in Figure 6.7 was parameterized with respect to the polar angle. Since the energy loss of electrons does not depend on the momentum of the particles, all clean conversion electrons tagged in the 1996/97 data set with $p > 0.2\,\mathrm{GeV}$ were used. The corrected energy loss for electrons is shown in the same figure by the solid histogram. This correction function is only valid for electrons but is in fact applied

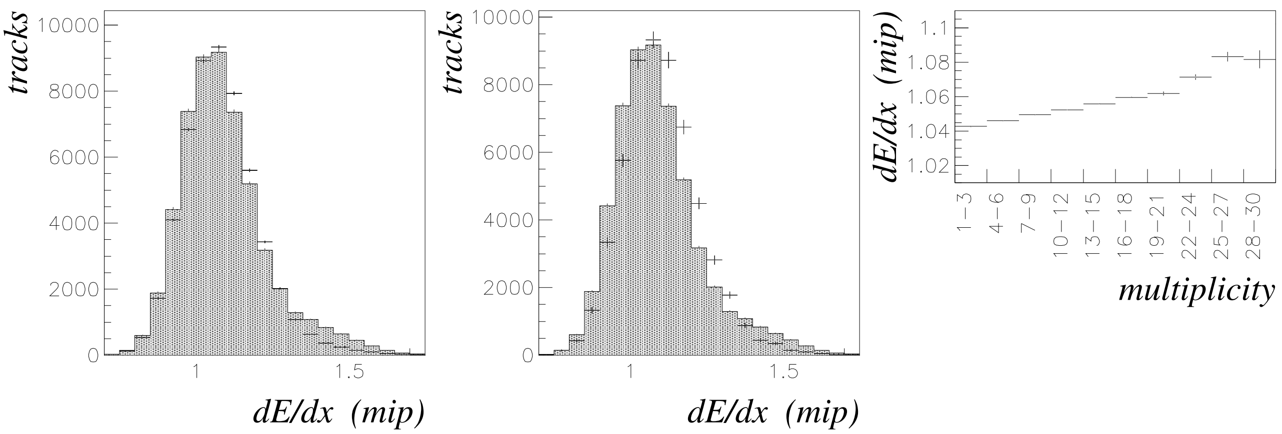

Figure 6.8: *The dependence of dE/dx on the track multiplicity of the event. The shaded histogram in the left two plots shows the dE/dx distribution for hadrons ($p > 1.2\,GeV, 0.65 < \theta < 2.5\,rad, q = -1$) in events with only 1-3 tracks, compared to the distribution for tracks from events with 10-12 (left plot) and 22-24 (middle plot) tracks. The right plot shows the mean energy loss versus the track multiplicity of the event. The error on the mean is the error on the peak position.*

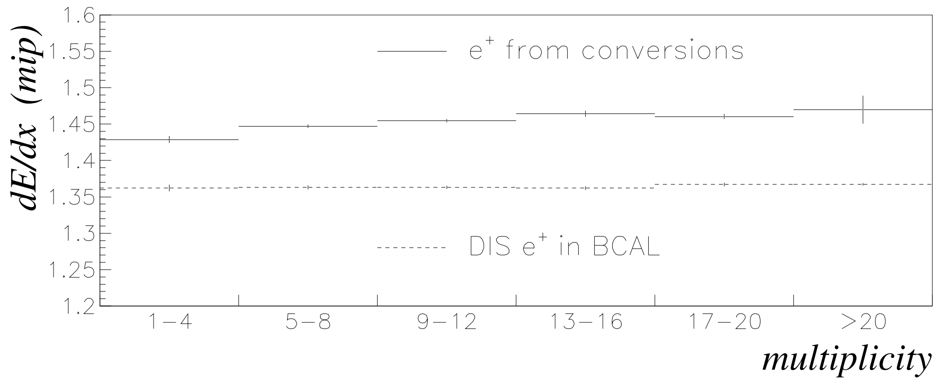

Figure 6.9: *The dependence of dE/dx on the track multiplicity of the event for DIS positrons measured in the BCAL (dashed histogram) compared to positrons from photon conversions (solid histogram).*

for all tracks, as will be discussed in the next section. Another possible correction function taking the different size of the effect for different values of dE/dx into account is also possible. The latter method will be used as a systematic check (see Section 7.2).

Dependence of dE/dx on the Track Multiplicity

The dependence of the measured energy loss on the track multiplicity of the event was first observed during the analysis of the 1995 data set [Heb99]. The effect is demonstrated in Figure 6.8. The mean energy loss increases if the number of tracks in the event increases. The left two plots show dE/dx distributions of negatively charged hadrons with $p_{track} > 1.2\,\mathrm{GeV}$ and $0.65 < \theta_{track} < 2.5\,\mathrm{rad}$. The shaded histogram represents tracks from events with only 1-3 tracks whereas the points show the distribution for the same kind of particles but out of events with 10-12 (left) and 22-24 (right) tracks. Only those tracks which are measured to come from the main interaction vertex are included. In addition to the vertex tracks, a large number of additional tracks exist which do not stem from the interaction vertex, for instance those from backscattering particles. About 50 % of all tracks are measured to originate in the event vertex, but this fraction varies strongly with the kinematic region (x, Q^2) of the event (see Figure C.2 in Appendix C).
The overall shift of dE/dx amounts to at most 4 %. Since most tracks are part of a jet of

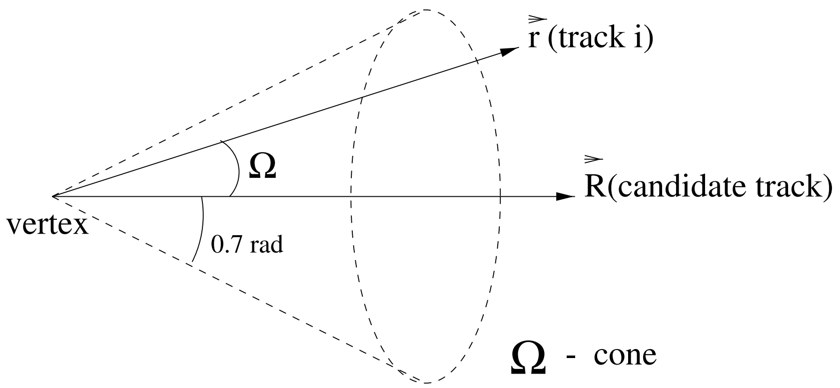

Figure 6.10: *Illustration of the Ω-cone, to define the isolation of a track.*

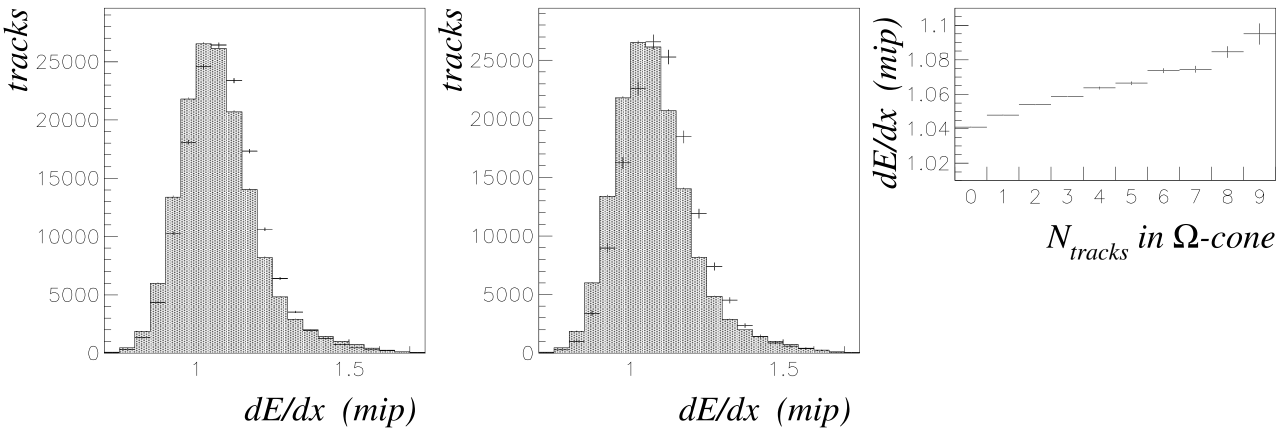

Figure 6.11: *The dependence of dE/dx on the isolation of the track. The shaded histogram in the left two plots shows the dE/dx distribution for well isolated tracks, with no other track inside a cone of 0.7 rad. In comparison the distribution for tracks with three (left) and six (middle) other tracks inside a cone of 0.7 rad is shown. The right plot shows the mean energy loss versus the number of tracks inside a cone of 0.7 rad.*

particles, the effect is more likely to depend on a local track multiplicity than on the overall event multiplicity. To test this idea the energy loss of DIS positrons detected in the BCAL was investigated. The scattered DIS positron is isolated (see Figure 5.2) balancing the p_T of the current jet. To have a reasonable dE/dx resolution the scattered positron is required to be found in the BCAL, equivalent to $0.64 < \theta_{DIS\ e^+} < 2.25\,\text{rad}$. About 15000 events were found in the 1995-97 data sets. The dE/dx dependence of these tracks on the event multiplicity is shown in Figure 6.9, compared to the dE/dx of positrons from photon conversions in these events. No effect can be seen for the isolated DIS positrons. The conversion positrons show a shift towards higher dE/dx for higher multiplicities, which is of the same order as the one for the hadron sample in Figure 6.8. However the mean dE/dx value for the scattered DIS positrons

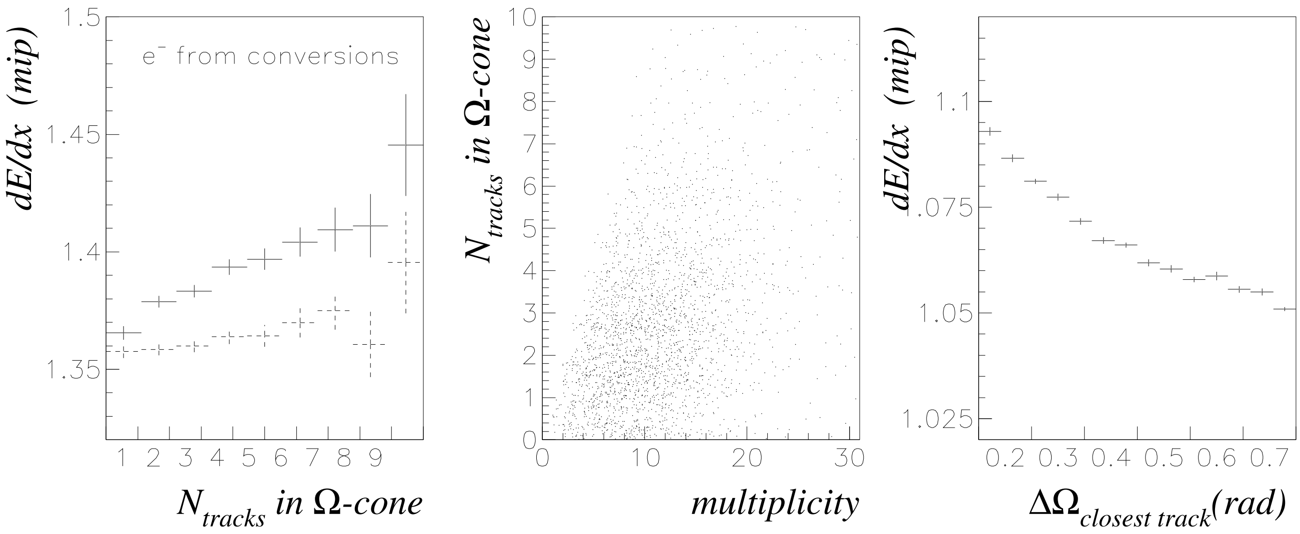

Figure 6.12: *dE/dx versus the number of tracks inside a cone of 0.7 rad for electrons (left), before correction (solid histogram) and after correction (dashed histogram). The isolation of the tracks versus the event multiplicity (middle). The dependence of dE/dx on the closest other track for the inclusive hadron sample tracks (right).*

differs from that of the conversion positrons even in the lowest multiplicity bin. This can be explained by the chamber geometry, similar to the difference between positively and negatively charged particles, as already mentioned above. A study of the momentum dependence of the energy loss of positrons and electrons from photon conversions has shown that for electrons dE/dx is constant with respect to the momentum as expected from theoretical predictions. Positrons however show a shift of dE/dx towards lower values for high momenta. This effect is also existent for hadrons in addition to the momentum dependence as predicted by the Bethe-Bloch formula. Therefore for the high momentum DIS positrons the dE/dx is shifted towards lower values compared to the low momentum conversion positrons even though both tracks are almost isolated in the lowest multiplicity bin.

To parameterize the isolation of tracks, the number of vertex tracks inside a cone around the candidate track is counted, as illustrated in Figure 6.10. The angle Ω is defined as $\cos\Omega = \vec{r}\cdot\vec{R}/(|\vec{r}||\vec{R}|)$. Tracks which do not stem from the interaction vertex cannot be taken into account in this procedure, since their polar and azimuthal angle is not precisely defined with respect to the ZEUS coordinate system. The dependence of the dE/dx of a track on the isolation can be seen in Figure 6.11 for a hadron sample selected in the same way as for the multiplicity dependence study shown in Figure 6.8. The shaded histograms in the left two plots show the dE/dx distribution for well isolated tracks where no other vertex track was found inside a cone of $\Omega = 0.7\,\mathrm{rad}$. The points show the shift of dE/dx towards higher values for three (left plot) and six (middle plot) other tracks inside a cone of 0.7 rad. The right plot shows the mean dE/dx versus the number of tracks inside a Ω-cone of 0.7 rad. A clear shift to higher dE/dx values for less isolated tracks can be seen. The overall shift amounts to up to 4 %. Thus it is of the same order as the shift with multiplicity.

Another indication that the effect depends on the isolation of the tracks and not on the overall track multiplicity of the event can be seen in in the rightmost plot of Figure 6.12. It shows the mean dE/dx of the hadron sample tracks versus the distance $\Delta\Omega$ in (ϕ, θ) to the closest other vertex track. The more separated the next track, the lower the dE/dx of the track. The middle plot in Figure 6.12 shows the track multiplicity of the event versus the isolation of the tracks. As expected a clear correlation is seen.

To correct for this effect, the Ω distribution in the right plot in Figure 6.11 is used. For each track the number of tracks, N_{track}, inside a cone of 0.7 rad is determined and its dE/dx value corrected to that of an isolated track:

$$\left(\frac{dE}{dx}\right)_{corrected} = \left(\frac{dE}{dx}\right)_{measured} - \left(\overline{\left(\frac{dE}{dx}\right)}(N_{track}) - \overline{\left(\frac{dE}{dx}\right)}(N_{track} = 0)\right) \ . \tag{6.3}$$

The shift of the dE/dx value with the number of tracks inside the cone is of the same order for electrons and for hadrons. This allows the use of the correction obtained from the inclusive hadron sample for any particle type. In the case of electrons, the left most plot in Figure 6.12 shows that the effect for conversion electrons (solid histogram) is sufficiently corrected (dashed histogram) by this method. To resolve the multiplicity problem, the chosen Ω-cone has to be at least 0.7 rad. Using a smaller cone for the correction does not correct entirely the multiplicity dependence. The same problem exists if the distribution of the closest other track (right plot in Figure 6.12) is used for the correction.

Figure 6.13 shows the mean dE/dx versus the track multiplicity of the event before (dashed histogram) and after (solid histogram) the applied Ω correction, for the inclusive hadron sample (left plot) and electrons from photon conversions (right plot). The correction seems to fail for the highest multiplicity bins. Since the statistics in those bins are low, the expected effect of this remaining multiplicity dependency is expected to be negligible.

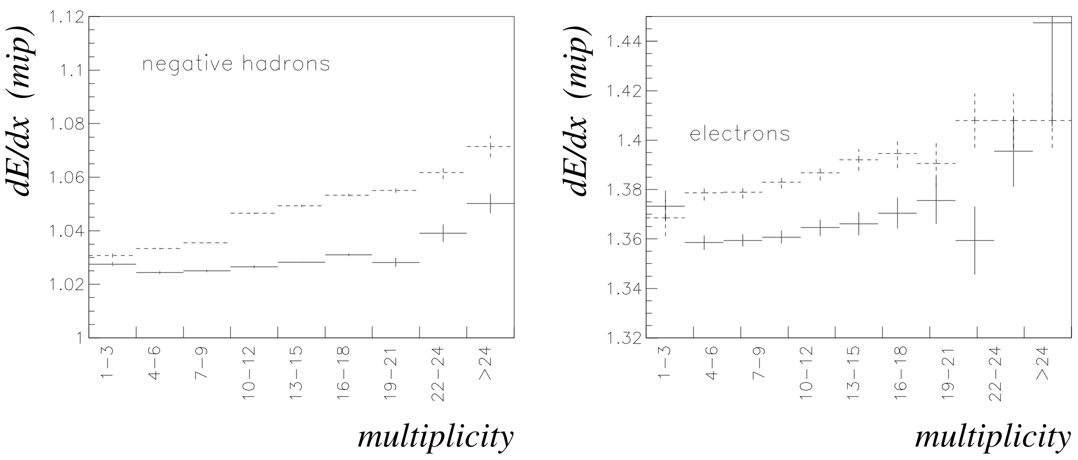

Figure 6.13: *The multiplicity dependence of dE/dx for negatively charged hadrons (left) and electrons (right) before (dashed histogram) and after (solid histogram) Ω correction.*

To study the effect of the multiplcity dependence of dE/dx on the cross section, the cross section was measured once with and once without the correction applied. The correction of this effect reduces the overall cross section by 7 % and is thus a non-negligible effect.
Although a correction for the multiplicity dependence has been found, the reason is not yet fully understood. The effect has been studied in polar angle and momentum bins to exclude any correlation for instance with the space charge effect. However the effect is the same for tracks in the different momentum or angular regions. To check whether double hits on a single wire in the inner superlayers of the CTD might cause this effect, the inner wires were excluded in a study of the raw 1995 data. The effect would be expected to be less pronounced since double hits are most likely to occur on the inner wires where the track density is highest. Nevertheless no reduction of the effect was observed.

6.4 Electron Finding using dE/dx and the Calorimeter

As discussed in the last section, for high particle momenta the hadrons form a broad band around dE/dx values of 1 mip, whereas the electrons have dE/dx values of 1.4 mip. To separate electrons from hadrons their momenta must be greater than at least 1.2 GeV. Below this limit the dE/dx of protons increases rapidly with decreasing momentum, merging with the energy loss measured for the electrons (see Figure 6.4). For very high momenta, the separation even improves, since for $p_{track} > 3.0$ GeV the energy loss difference between pions, kaons and protons stays constant and the $dE/dx_{hadrons}$ rises only slowly with increasing momentum. However, as shown in Figure 6.2 the acceptance for electrons from semileptonic charm decays decreases rapidly with a higher momentum cut. Hence the lowest possible momentum cut of 1.2 GeV is chosen to select tracks for this analysis.
Nevertheless, the information of the CTD alone does not provide a sufficient tool to select electrons. As can be seen in Figure 6.5, there is a broad overlap between the dE/dx distributions of electrons and hadrons. The majority of tracks in a DIS event is hadronic, thus the electron dE/dx signal is hidden under the hadron signal (see e.g. Figure 6.6). In addition to the dE/dx signal, the energy deposited by the particles in the calorimeter may be used for the identification of electrons via a statistical subtraction method.
In order to obtain information about the energy deposited by the particles in the calorimeter, each track must be matched to a so called calorimeter condensate [Jon92]. A condensate is a

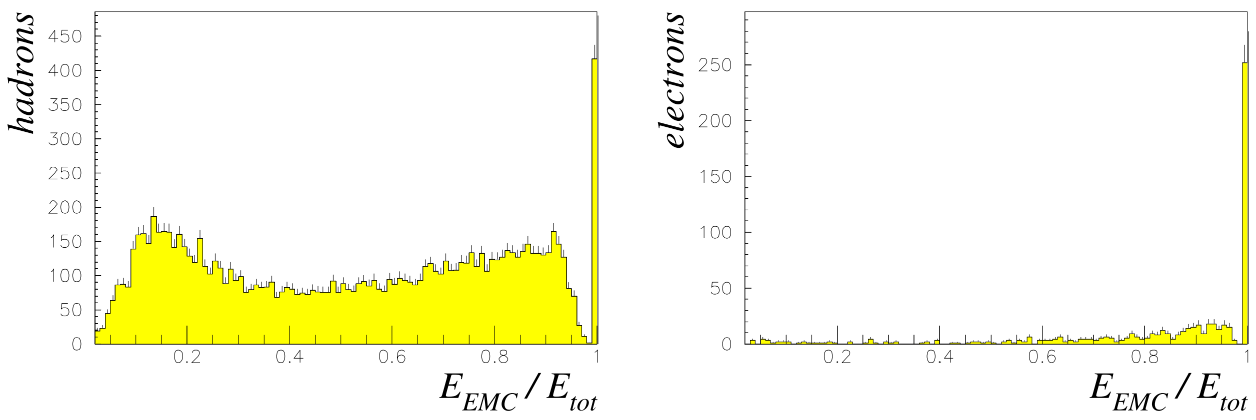

Figure 6.14: *The ratio E_{EMC}/E_{tot} of the matched condensates for hadrons (left plot) and electrons (right plot) obtained from MC data.*

local cluster of calorimeter cells. The aim is to gather together cells which belong to the energy deposit of one single particle. The condensates are built in a similar way as the islands in Section 5.1.2, but are generally smaller objects. To match the condensate with a particle, the track of the particle is extrapolated to the calorimeter surface. The condensate closest to the extrapolated track is taken as the matched one. Isolated tracks are usually found to belong to only one condensate, whereas nearby particles in dense jets may be merged into one condensate. Since electromagnetic showers are typically shorter than hadronic showers, electrons predominantly produce signals in the EMC part of the calorimeter. Hence the fraction of energy deposited in the EMC part (E_{EMC}) compared to the total energy deposit (E_{tot}) contains information about the particle type.
Figure 6.14 shows the ratio E_{EMC}/E_{tot} of condensates from hadron tracks (left plot) and electron tracks (right plot), obtained from an inclusive DIS Monte Carlo sample. For electrons the ratio, E_{EMC}/E_{tot}, of the matched condensate peaks at 1. The condensates with low E_{EMC}/E_{tot} values originate from mismatches, where the wrong condensate is matched to the electron track. Increasing the matching quality by lowering the distance between the extrapolated track and the condensate increases the fraction of condensates with $E_{EMC}/E_{tot} = 1$. Most of the condensates produced by hadrons also have major energy deposits in the EMC part. However a substantial amount of hadronic tracks leave energy in the HAC part, producing condensates with E_{EMC}/E_{tot} below 50 %. Hence a cut on the quantity E_{EMC}/E_{tot} allows one to obtain an almost purely hadronic sample of tracks. Selecting tracks with matched condensates having $E_{EMC}/E_{tot} > 0.9$ on the other hand results in a sample of predominantly hadronic tracks but also containing the tracks that stem from electrons. The quantity E_{EMC}/E_{tot} of the matched condensates is used in this way to produce two samples of tracks:

- the signal sample: all tracks that have a matched condensate with more than 90% of its energy in the EMC part of the calorimeter ($E_{EMC}/E_{tot} > 0.9$).

- the background sample: all tracks that have a matched condensate with less than 40% of its energy in the EMC part ($E_{EMC}/E_{tot} < 0.4$) and an energy of at least 300 MeV deposited in the HAC section to avoid noisy cells (in addition the the general noise cuts which are already applied to all calorimeter cells, see Section 5.1.3).

Statistically subtracting the dE/dx distribution of the appropriately normalized background sample from the signal sample should yield the dE/dx distribution of the electrons in the

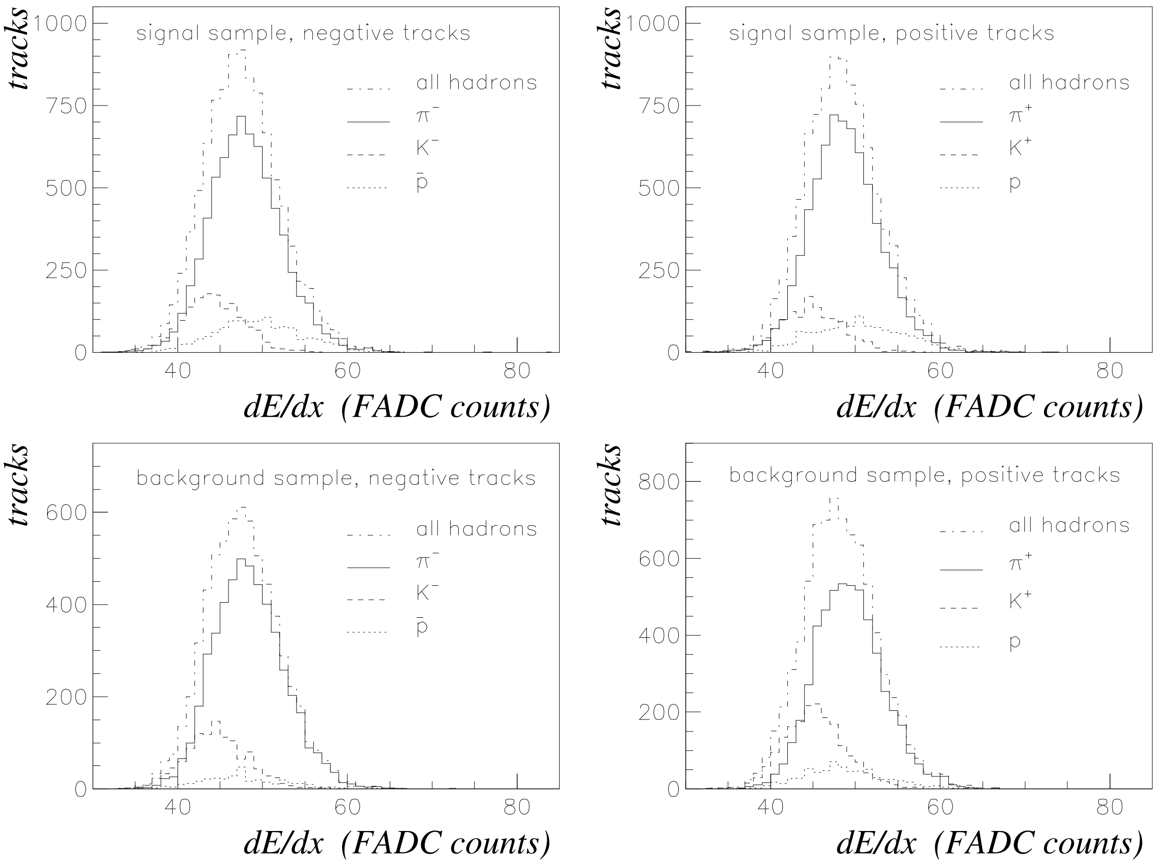

Figure 6.15: *The dE/dx distributions of the signal sample (upper plots) and the background sample (lower plots) for negatively (left plots) and positively (right plots) charged particles, as obtained from a DIS MC. The different particle types are plotted separately. All tracks have* $p_{track} > 1.2\,GeV$ *and* $0.65 < \theta_{track} < 2.5\,rad$.

selected events. Since the measured energy losses for positive and negative tracks for particles of the same type and momentum differ, the whole method has to be performed for positive and negative tracks separately. The subtraction method only works if the background sample describes the dE/dx distribution of the hadrons in the signal sample exactly. Several aspects influence the dE/dx of a track and therefore have to be taken into account.

- Although the hadrons form a broad dE/dx band at high momenta (see Figure 6.4) the mean dE/dx values are still different for kaons, protons and pions. The majority of hadronic tracks originate from pions. However the mixture of hadronic particles should be the same in the signal and in the background sample.

- The energy loss of hadrons rises with increasing momentum whereas the dE/dx of electrons stays constant. The background sample tracks have higher momenta than the signal sample tracks due to the requirement of at least 60 % energy deposit in the HAC part. Hence the background sample tracks have to be reweighted to match the momentum distribution of the signal sample.

- The measured energy loss of a track depends on the polar angle and on its isolation as discussed in the last section. The correction functions have to be optimized for the selected sample of tracks. The correction for the space charge effect is obtained for electrons only

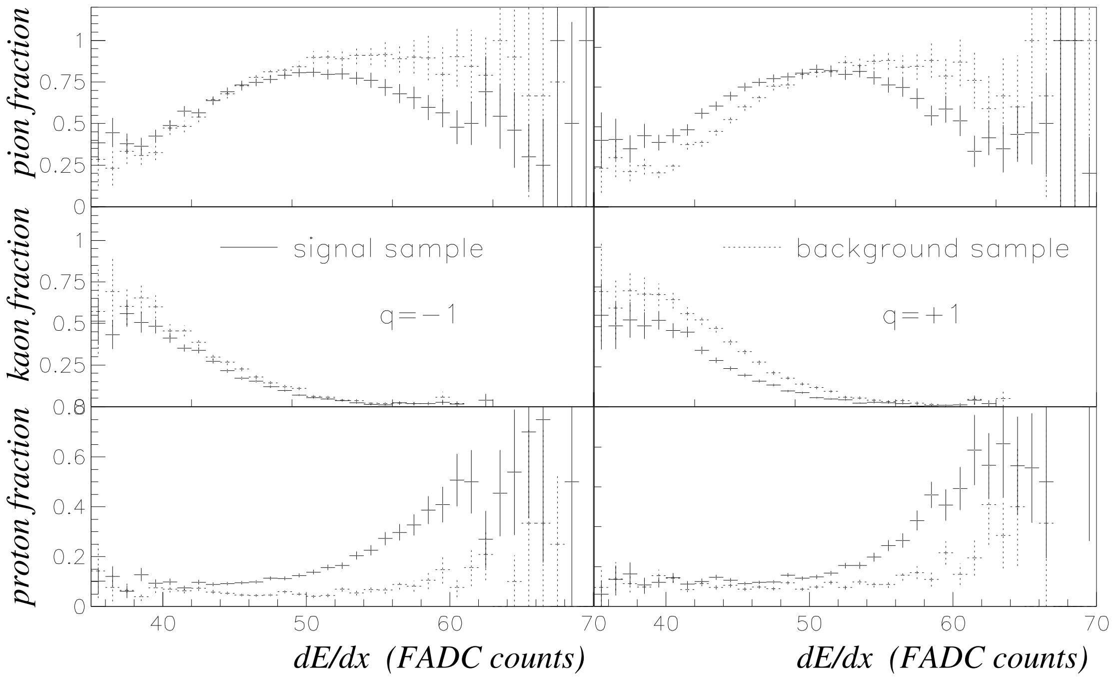

Figure 6.16: *The pion (upper plots), kaon (middle plots) and proton (lower plots) fraction of all hadrons for the signal (solid histogram) and background sample (dotted histogram). Negatively (left plots) and positively (right plots) charged particles are shown separately.*

but is applied to any track. Since the θ distributions of the signal and background samples are different, a reweighting of the background sample in θ has to be performed.

In order to study the hadron mixture in the two samples, a DIS MC sample is investigated. Figure 6.15 shows the dE/dx distributions for the signal and background samples for positively and negatively charged particles separately. It should be noted that the dE/dx distributions are only used to represent the hadron fractions. As already discussed in Section 3.2.6 the MC simulation of the energy loss in the CTD has to be used with care, and does not describe all effects correctly. The majority (about 70 %) of all tracks stems from pions, whereas the fraction of kaons and protons varies. Figure 6.16 shows the ratio of the different hadron types to all hadrons.

The Positron Channel

For positively charged particles a clear difference between the signal and the background samples is observed in the kaon fraction. The background sample consists of about 24 % kaons whereas the signal sample only contains about 13 % kaons. The fraction of signal sample protons is small, about 10 %, and slightly lower in the background sample. The particle ratios stay constant with momentum, so an increased momentum cut does not bring the kaon fraction of the two samples into agreement. Variation of the E_{EMC}/E_{tot} cut does not influence the ratios considerably either. The correct simulation of the hadron tracks in the signal sample by the background sample is the basis of the statistical subtraction method. Due to the large kaon difference the method is not directly applicable to the positive channel. Performing the method with positive tracks indeed gave no clear electron signal but a double peak structure. In addition a sizeable background from scattered DIS positrons is expected [Ver98]. This is possible if a photon from initial state radiation is misidentified as the scattered positron and the DIS positron is then selected as a signal sample track. Finally the whole analysis should be done separately for negative and positive tracks due to the different dE/dx systematics. The above considerations lead to the decision to analyse only the negative channel.

The Electron Channel

For negative tracks the fraction of kaons in the signal and background samples are the same within errors. The overall fraction of kaons amounts to about 17 %. The relative number of protons is small, but differs for the two samples. About 12 % of the tracks in the signal sample stem from protons whereas the background sample contains only 6 % protons. The fraction of protons does not vary with an increase of the momentum cut or a variation of the E_{EMC}/E_{tot} cut. The estimation of the systematic effect on the electron signal due to the different proton fraction will be discussed in Section 7.2.
The final track selection is optimized to achieve good tracking and dE/dx resolution and clean matching. The detailed track requirements are the following:

- Given the fact that the resolution of the ZEUS detector during 1996 and 1997 was not adequate to resolve secondary vertices, the track is required to come from the main event vertex.
- Track momentum: $1.2 < p_{track} < 5\,\mathrm{GeV}$, where the upper cut avoids contamination in the dE/dx region of electrons by highly relativistic hadrons. Since the momentum spectrum of the electrons from semileptonic charm decay drops rapidly, only a small fraction of the signal is being cut away.
- Track polar angle: $0.65 < \theta_{track} < 2.5\,\mathrm{rad}$, where the dE/dx resolution is best ($\sim 10\%$).
- Track charge: $q_{track} = -1$.
- Matching condensate: a condensate must be associated with the track. The distance of closest approach on the calorimeter surface has to be less than 20 cm.
- The condensate energy should roughly match the track momentum, $0.2 < E_{cond}/p_{track} < 3.0$. This cut removes accidental matches especially in the signal sample and thus improves the matching quality (see Figure 6.17).

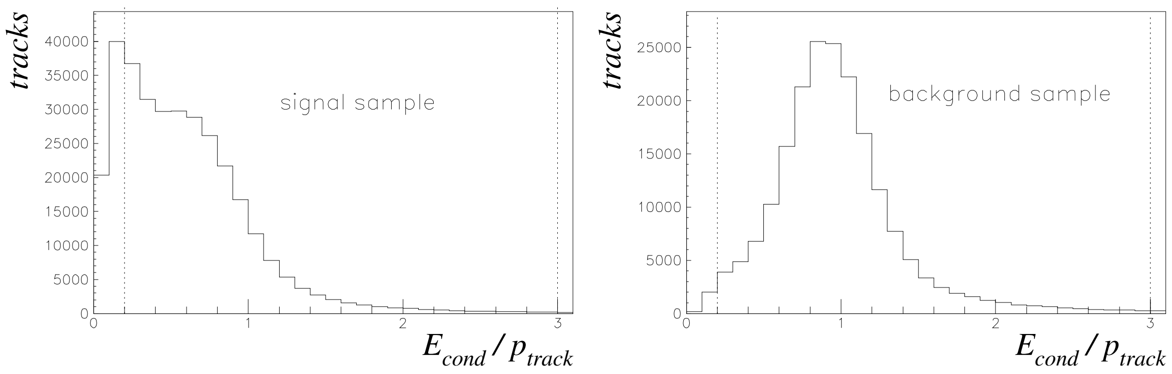

Figure 6.17: *The quantity E_{cond}/p_{track} for the selected tracks in the signal (left plot) and background sample (right plot). The applied cut is indicated by the dotted lines.*

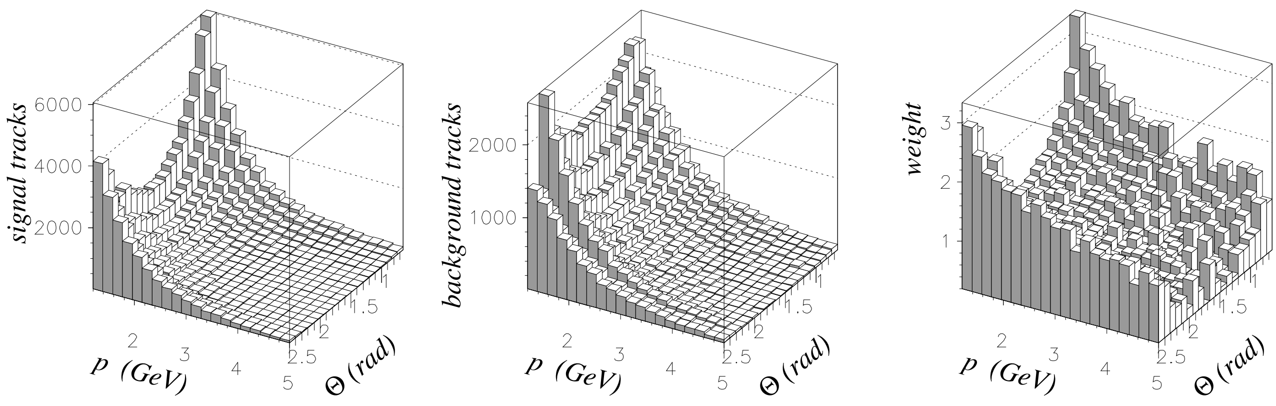

Figure 6.18: *p versus θ of the signal sample tracks (left plot) and background sample tracks (middle plot). The resulting reweighting function is shown in the right plot.*

- Isolated track on the calorimeter surface. Every track is extrapolated to the calorimeter surface. If any other track is closer than 20 cm to the candidate track it is removed. This cut improves the matching quality. In particular, mismatch of electrons to hadronic condensates is avoided, which would otherwise be subtracted from the actual electron signal. To avoid any influence on the dE/dx of the track due to this additional isolation cut, the same cut is applied to the signal and background samples. The drawback of this additional isolation cut is a decrease of the acceptance for the semileptonic tracks.

- The track should not point to the condensate of the found DIS positron or be identical to the track assigned to the DIS positron.

The dE/dx correction functions for the isolation effect and the θ dependence were obtained for tracks selected according to the above criteria. As a consequence of the $E_{EMC}/E_{tot} < 0.4$ cut, the number of tracks in the background sample is about 30 % smaller than in the signal sample. For the statistical subtraction method high statistics for the background sample are desired. Assuming that the corrected energy loss of a particle only depends on the momentum and polar angle of the track, the statistics of the background sample can be increased by adding tracks from any kinematic range. Hence in the following the background sample contains tracks from the whole preselected data, i.e. after trigger selection and some soft cuts (see Section 5.2.2).
in order to match the momentum and polar angle distributions of the background sample tracks with those of the signal sample, a two-dimensional reweighting in p and θ is performed. Figure 6.18 shows the the momentum versus the polar angle of the tracks for the signal sample (left plot) and the background sample (middle plot). The different momentum shape due to the cut on E_{EMC}/E_{tot} can be seen. The distribution in θ is also different. The signal sample has more tracks at shallow angles than the background sample. The electrons from tagged photon conversions (see next section) were subtracted from the signal sample to reduce the electron contribution to the sample. The right plot shows the signal sample (p, θ) distribution divided by that of the background sample. The resulting distribution is used as a reweighting function, where a weight is applied to each background sample track according to its momentum and polar angle.
After reweighting, the background sample must be normalized to the signal sample. This is done in the range $0.8 < dE/dx < 1.1$ where only hadronic tracks are expected in both samples. Due to the reweighting procedure, the normalization factor α is expected to have a value close to 1. Varying the lower bound of the normalization area from 0.8 to 0.0 has almost no impact on

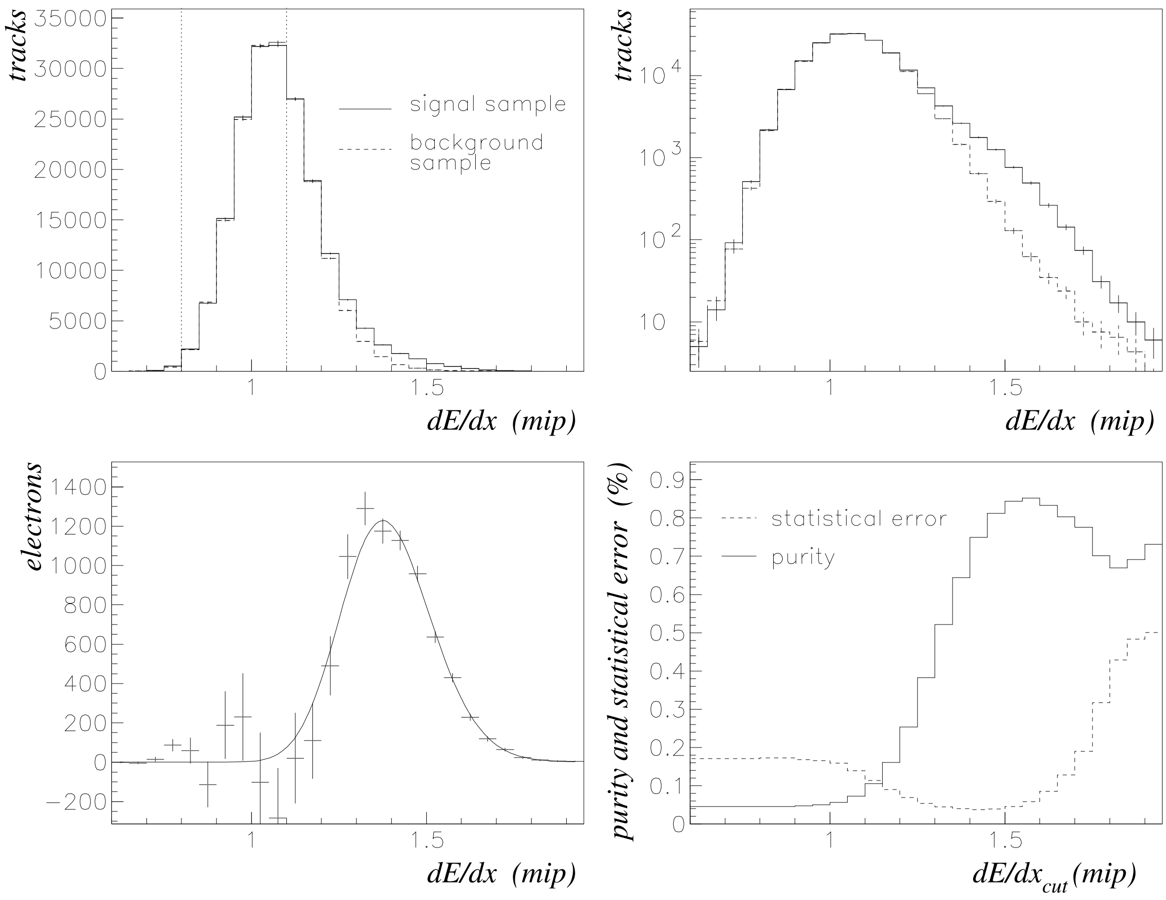

Figure 6.19: *The dE/dx distribution of the signal and background sample on a linear (upper left plot) and a logarithmic (upper right plot) scale. The dotted lines in the upper left plot indicate the normalization range. The dE/dx distribution of the electron signal resulting from the statistical subtraction (lower left plot). The relative statistical error and the purity of the electron signal versus dE/dx_{cut} (lower right plot).*

the resulting number of electrons after the subtraction. The effect is less than 0.5 %. However the upper value should not be greater than 1.1 because for higher dE/dx values the fraction of electrons entering the normalization region becomes significant.

The resulting dE/dx distributions of the signal and the reweighted and normalized background sample are shown in the upper two plots of Figure 6.19. The electrons in the signal sample are visible as a shoulder in the distribution around dE/dx values of 1.4 mips. The lower left plot shows the electron signal after statistical subtraction of the background sample from the signal sample. The shape of the dE/dx distributions of the two samples in the normalization area is not in perfect agreement. This results in an undershoot and overshoot of the electron signal after the subtraction in this region. Note however that the error bars are such that the value is consistent with zero. The electron signal is fitted with a constrained fit from a clean sample of electrons from photon conversions (see next section for further explanation).

At dE/dx values of around 1 mip, two very large and similar numbers are subtracted, and so the statistical errors are large. In order to optimize the statistical error, a dE/dx_{cut} value is defined and the number of tracks is only counted for dE/dx values greater than this cut value.

The number of electrons in the signal $n_{electron}$ is then given by,

$$\begin{aligned} n_{electron}(dE/dx > dE/dx_{cut}) &= n_{sg}(dE/dx > dE/dx_{cut}) - \alpha \cdot n_{bg}(dE/dx > dE/dx_{cut}) \\ \alpha = \frac{n_{sg}(0.8 < \frac{dE}{dx} < 1.1)}{n_{bg}(0.8 < \frac{dE}{dx} < 1.1)} & \qquad \text{(normalization factor)}, \end{aligned} \tag{6.4}$$

where n_{sg} and n_{bg} are the number of tracks in the signal and in the background sample respectively. The remaining part of the electron signal is estimated using the constrained fit from a clean photon conversion electron sample (see Section 7.3).
The most suitable dE/dx cut value is at the minimum of the relative statistical error, which is defined as the total statistical error $\sigma_{tot}(n_{electron})$ divided by the number of electrons $n_{electron}$ for $dE/dx > dE/dx_{cut}$ in each case. The behaviour of the relative statistical error is shown in the lower right plot of Figure 6.19. Also shown in this plot is the purity of the electron signal, defined as the number of tracks in the electron signal divided by the total number of tracks in the signal sample, $n_{electron}(dE/dx > dE/dx_{cut})/n_{sg}(dE/dx > dE/dx_{cut})$. At $dE/dx = 1.4$ mips the statistical error shows a minimum of $\approx 5\%$. The purity of the electron signal if one cuts at this dE/dx value is about 75 %.

6.4.1 Electron Background

The electron signal contains electrons from various sources, including photon conversions, b-quarks, c-quarks, pions and other decays. In order to obtain the number of electrons from semileptonic charm decays, the non-charm electron background must be estimated or measured. The major contribution to the electron background comes from photon conversions, Dalitz decays of π^0s and beauty decays. The additional background from other miscellaneous decays into electrons is small. It has been estimated from MC data to be less than 1 % in the acceptance region [Ver98] and is therefore neglected in the following.

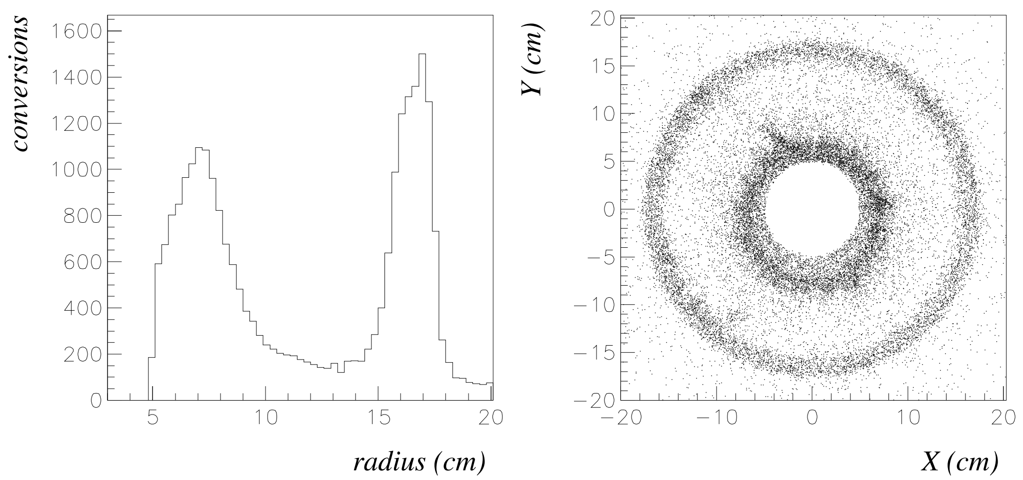

Figure 6.20: *The radius (left plot) and the XY position (right plot) of the origin of photon conversions found by the conversion finder in data. The beampipe and the inner CTD wall can be seen in both plots. The finder only considers tracks as coming from a photon conversion if the origin is further than 5 cm away from the interaction point.*

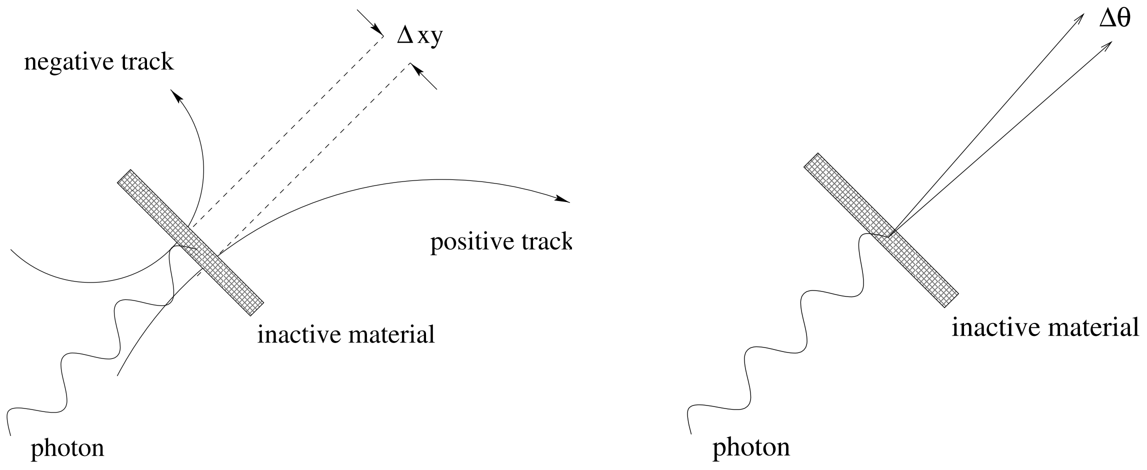

Figure 6.21: *A schematic diagram of a photon converting into an electron-positron pair in inactive material. The left figure shows the XY view, the right one the RZ view.*

Electrons from Photon Conversions

The major contribution to the electron background results from photons converting into electron-positron pairs either in the beampipe or within other inactive material in front of the tracking detector. Figure 6.20 shows the measured origin of photon conversion processes tagged with a conversion finder as described below. The beampipe and inner CTD wall are clearly visible. The probability for the process $\gamma \to e^+e^-$ is proportional to the thickness of inactive material traversed. Therefore the number of electrons produced by photon conversions increases towards shallow angles with respect to the beam axis (see Figure 6.24). In the central region of the ZEUS detector, the combined inactive material from the beampipe and the inner CTD wall amounts to about $0.03\,X_0$ [Hal99]. The converting photons are predominantly produced by π_0 decays. This leads to about one detectable photon conversion per 10 DIS events. The energy of the photons is relatively low, and the resulting momentum distribution of the electron-positron pairs peaks at $0.5\,\mathrm{GeV}$, similar to that of electrons from semileptonic charm decays (see Figure 6.24).

Since the photon conversion process has a relatively clean signature it can be tagged efficiently with a geometrically based conversion finder, [Köp94]. Figure 6.21 shows a schematic diagram

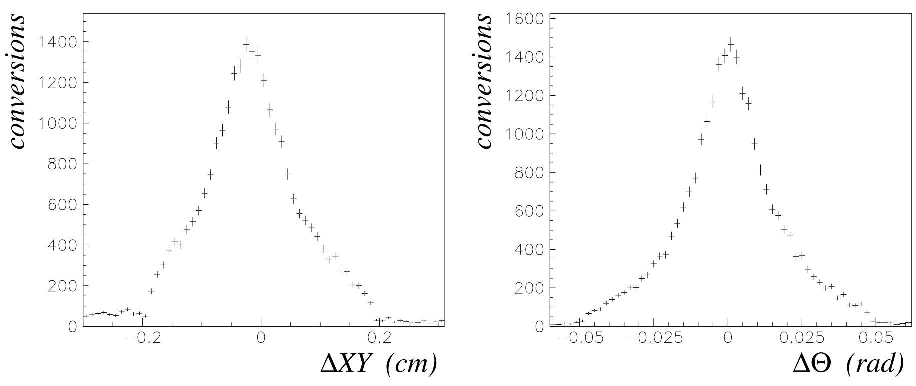

Figure 6.22: *The ΔXY (left plot) and $\Delta\theta$ (right plot) distribution of a clean conversion sample in data.*

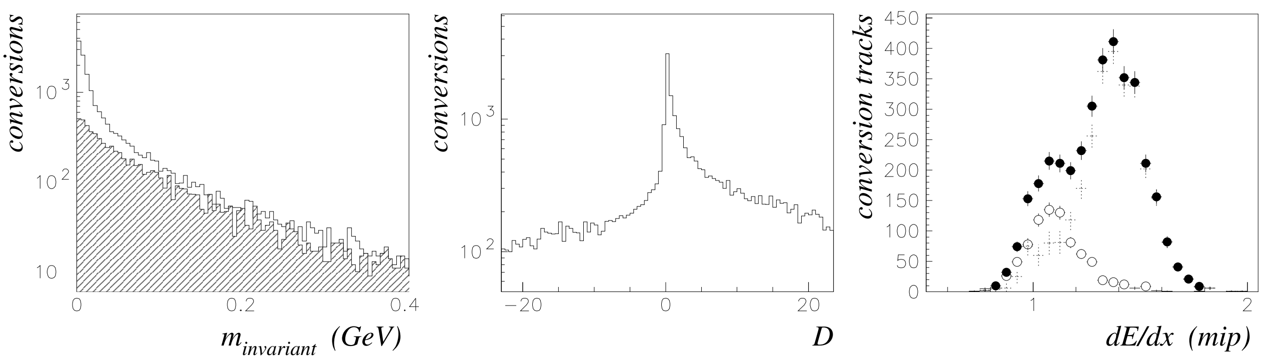

Figure 6.23: *The left plot shows the invariant mass of the e^-e^+ pair where the shaded histogram represents the background from equal-charge pairs. The middle plot shows the conversion quality quantity D. $D < 0$ indicates that a background pair was tagged. The right plot shows the dE/dx distributions of an inclusive conversion sample for opposite-charge (solid dots) and equal-charge (open dots) track pairs. Subtraction of the two yields the dashed crosses.*

of a photon converting into in a e^+e^- pair in the XY and RZ views, where R refers to the radius, $R = \sqrt{(X^2+Y^2)}$. The conversion finder looks for two tracks with zero opening angle originating somewhere in the detector material. Oppositely-charged track pairs are considered as originating from a photon conversion, whereas equal charge track pairs are kept for background studies. The polar angle difference $\Delta\theta$ of the two tracks (right figure) and the distance in the XY plane at the point of tangency of the two tracks ΔXY (left figure) are determined. The value of $\Delta\theta$ and ΔXY should be zero in case of a perfect conversion candidate, but they are smeared around zero due to the tracking resolution of the detector (see Figure 6.22). The conversion finder then calculates the quantity D,

$$D = \sqrt{\left(\frac{\Delta XY}{\sigma_{XY}}\right)^2 + \left(\frac{\Delta\theta}{\sigma_\theta}\right)^2}\,, \tag{6.5}$$

where σ_{XY} and σ_θ are the r.m.s. resolutions of the ΔXY and $\Delta\theta$ distributions, measured separately for data and MC. The finder tests all possible track combinations and defines the two tracks having the smallest D value as a conversion pair. The quantity D thus defines the quality of the conversion found by the finder. For equally-charged track pairs the assigned D values are negative. Varying the cut on D for the selection of conversion candidates affects both the efficiency and the purity of the tagged sample.

Ignoring the track charges, the probability to fake a conversion candidate is the same for opposite- and equal-charge track pairs. This can be seen by looking at the dE/dx distributions of the equal and opposite track pairs in the right plot of Figure 6.23. The hadronic background in the conversion electron sample shows up at dE/dx around 1 mip. The background can be simulated using the equal-charge track pairs (open dots). Statistical subtraction of the dE/dx distribution for equal-charge track pairs from that for opposite-charge track pairs yields the distribution for a pure conversion sample (dashed crosses). To obtain the number of background electrons from photon conversions, the same procedure is applied as was used to obtain the inclusive number of electrons. This means only those tracks with $dE/dx > dE/dx_{cut}$ are considered, and the rest is estimated using the constrained electron fit. Therefore hadronic backgrounds around dE/dx values of 1 mip in the conversion signal have no noticeable contribution to the final number after subtraction.

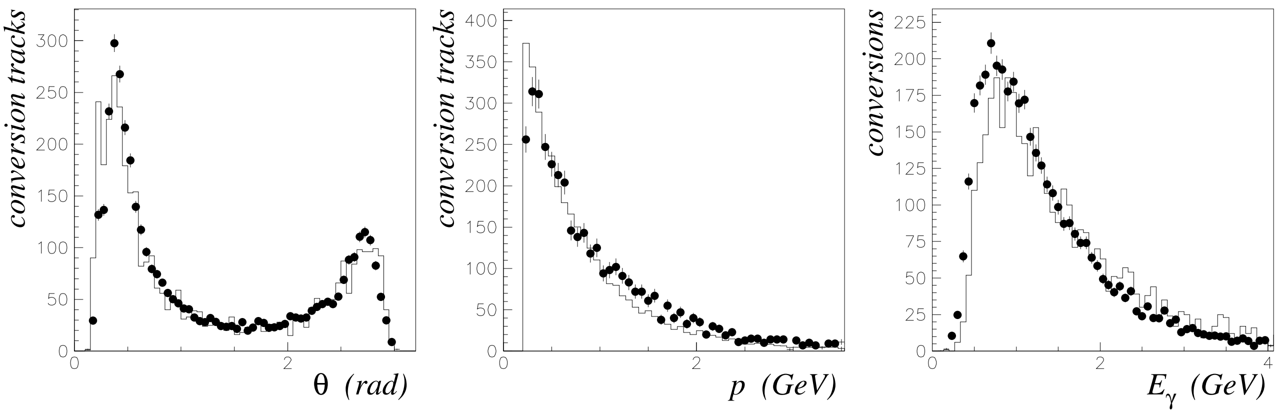

Figure 6.24: *Comparison of the theta (left plot) and momentum (middle plot) distributions of clean conversion tracks found in data (solid dots) with tracks found in MC (solid line) that stem from true conversions. The right plot shows the energy E_γ of the converting photon.*

The efficiency and purity of the conversion finder is dependent on the quality cut D chosen to tag the conversions. In addition a cut on the invariant mass $m_{invariant}$ of the electron-positron pair can be applied. Two samples for later use in this analysis are defined:

- clean conversion sample: $D < 5$ and $m_{invariant} < 0.025\,\mathrm{GeV}$

  This sample, which has a purity of about 90 %, can be used to investigate how real electrons behave in data.

- inclusive conversion sample: $D < 15$ and no cut on $m_{invariant}$

  This is the way the background electrons in the inclusive electron signal are tagged. The purity of this sample is about 80 %, but it has a higher efficiency than the clean conversion sample.

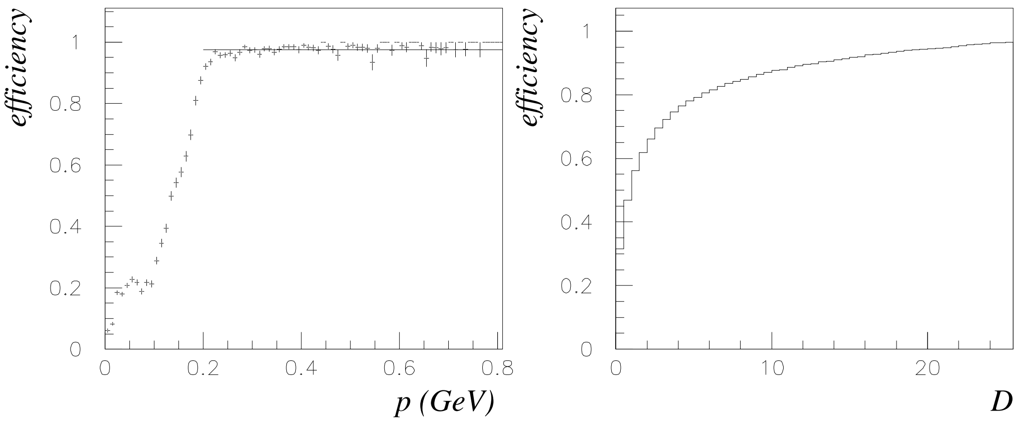

Figure 6.25: *Reconstruction efficiency for conversion electrons versus the true momentum (left plot) and the conversion finding efficiency of the finder as a function of D (right plot), both determined from MC.*

MC data is used to determine the efficiency of the conversion finding procedure. In order to verify that the MC simulation of conversions is similar to real data, the θ and p distributions of the conversion tracks and the photon energy E_γ are shown for data and MC conversions in Figure 6.24.

First the track reconstruction efficiency for electrons inside the required angular region, $0.65 < \theta < 2.5\,\mathrm{rad}$, must be determined. Since the opening angle between the e^-e^+ track pairs is close to zero (see right plot in Figure 6.22) it makes no difference whether only one or both tracks are required to be within this θ region.

The left plot in Figure 6.25 shows the reconstruction efficiency versus the true track momentum for e^+e^- tracks in the range $0.65 < \theta < 2.5\,\mathrm{rad}$. For track momenta above 200 MeV the tracks are reconstructed with an efficiency of $\epsilon_{reconstruction} = 97.5\,\%$. Below momenta of 200 MeV the reconstruction efficiency drops rapidly. To avoid missing tracks at very low momenta both tracks found by the conversion finder are required to have more than 200 MeV momentum.

The missing fraction of conversions due to the 200 MeV momentum cut can be estimated using QED calculations for pair production. The energy share distribution E_{e^-}/E_γ of the photon energy E_γ between the electron and the positron has been calculated by Tsai [Tsa74]. The calculation starts with the exact QED calculation for pair production and takes screening of the charged nucleus by the orbiting electrons into account. The exact formula for the differential cross section as a function of E_{e^-}/E_γ can be found in Appendix A. The magnitude of the cross section depends on the atomic number Z of the material, whereas the shape of the distribution is rather independent on the value chosen for Z. The calculations done for this analysis consist of cross section ratios and are therefore independent of the absolute value of the cross section. The material considered is aluminium, for which Z=13.

The left plot in Figure 6.26 shows the energy share distribution for different photon energies E_γ. In Figure 6.27 the same distributions are shown for three different photon energies, taking the cut on the electron momentum into account. The solid line represents the calculation with the 200 MeV momentum cut on each track. The dashed line is calculated without this momentum cut. The gap in the middle around 0.5 appears due to the $p > 1.2\,\mathrm{GeV}$ momentum cut of our analysis sample. The right plot in Figure 6.26 shows the energy share E_{e^-}/E_γ measured in the data, with the 200 MeV momentum cut, compared to the QED calculation.

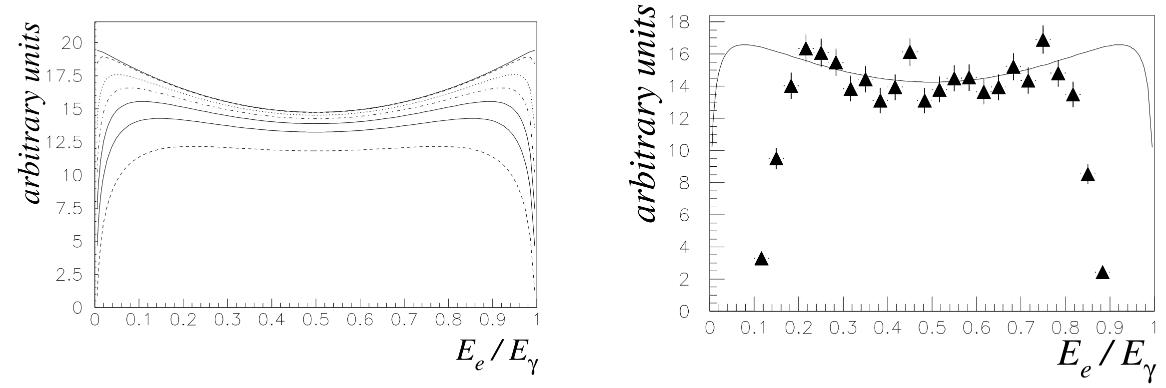

Figure 6.26: *The left plot shows the shared energy distribution E_{e^-}/E_γ according to the calculation by Tsai [Tsa74] for aluminium (Z=13) for different photon energies, E_γ = 0.2 (bottom curve), 0.5, 1.0, 2.0, 5.0, 50.0 and 500.0 (top curve) GeV. The right plot shows the comparison with data for photon energies between 1 and 2 GeV. The conversions in data were selected with the 200 MeV momentum cut.*

To obtain the missing fraction of conversions, the integrals of the E_{e^-}/E_γ distribution from 0.0 to 1.0 with and without the 200 MeV momentum cut are calculated for each photon energy E_γ. The ratio of the two integrals then gives the findable fraction of conversions as a function of E_γ. The result is plotted in the lower right plot of Figure 6.27. The inverse of this fraction is used as a correction factor $\kappa_{Tsai}(E_\gamma)$ for every conversion track found in the sample.
MC data is used to determine the conversion finding efficiency for a given D cut MC. The total efficiency to tag all photon conversions in an event is rather low and depends heavily on the Z position of the origin of the conversion [Köp94]. The selected tracks for this analysis are required to come from the main event vertex. Hence the conversion finding efficiency must be determined for track pairs of which at least one track comes from the vertex and is within the required momentum and polar angular ranges. Both tracks are required to have a momentum higher than 200 MeV. The right plot in Figure 6.25 shows the finding efficiency versus D. The efficiency to tag the inclusive conversion sample, $D < 15$, amounts to $\epsilon_{D-cut} = 91.6\%$.
The total number of conversions in the electron signal can now be calculated:

$$\begin{aligned} N_{conv}(E_\gamma) &= N_{tagged}\ \kappa_{Tsai}(E_\gamma)\ \epsilon_{reconstruction}\ \epsilon_{D-cut} \\ &= N_{tagged}\ \kappa_{Tsai}(E_\gamma) \cdot 0.975 \cdot 0.916\ , \end{aligned} \tag{6.6}$$

where N_{tagged} is the number of conversion electrons, after background subtraction.

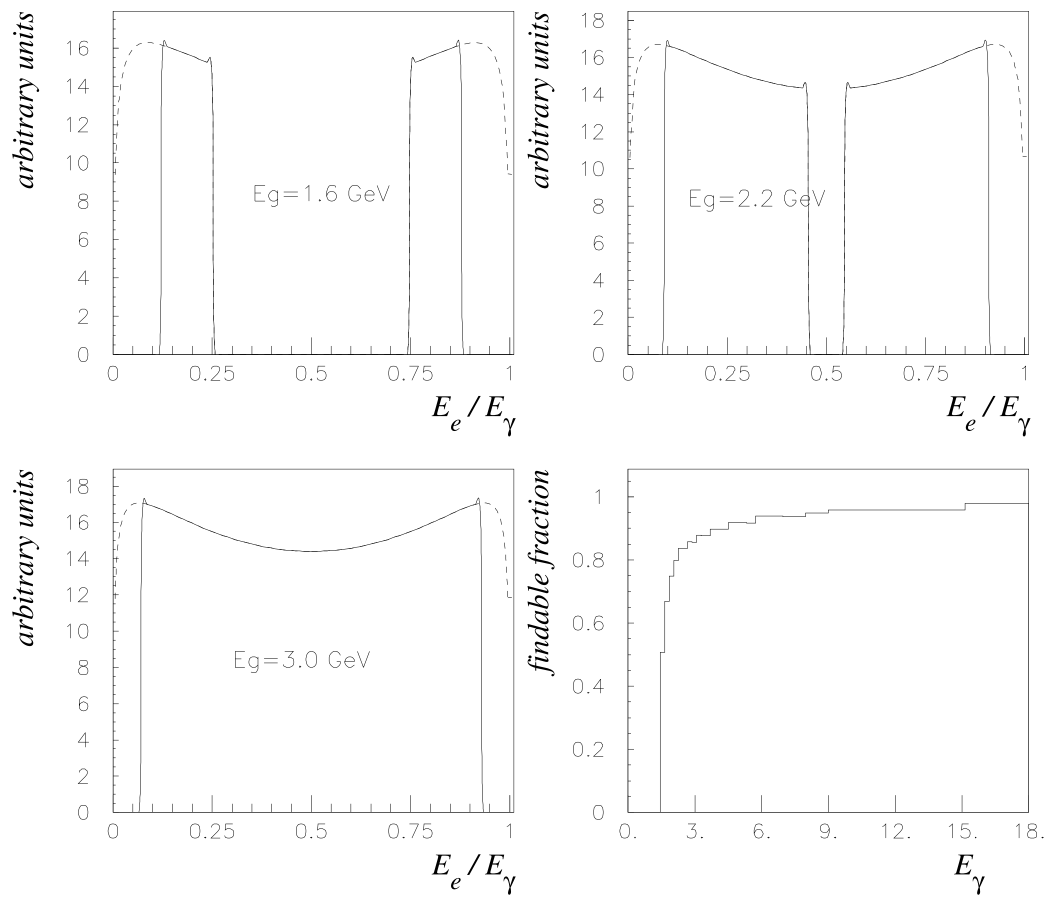

Figure 6.27: *Shared energy distribution E_{e-}/E_γ for tracks with (solid line) and without (dashed line) the 200 MeV momentum cut for different photon energies E_γ. The lower right plot shows the findable fraction of conversions due to the 200 MeV momentum cut.*

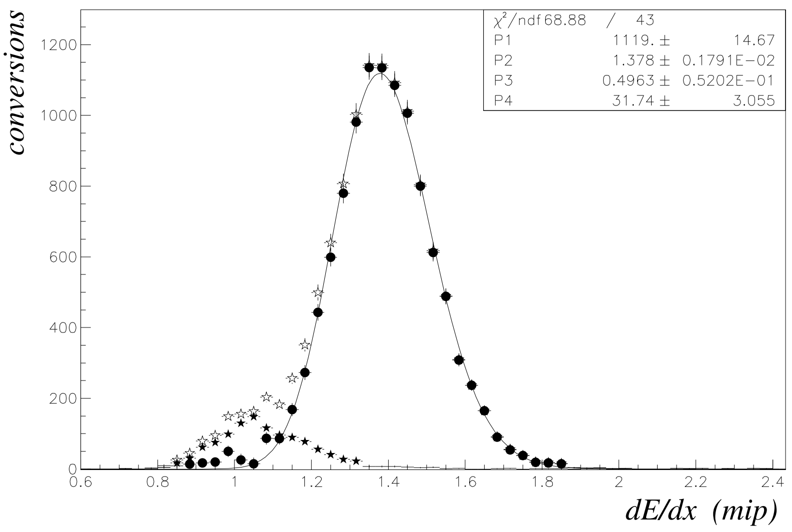

Figure 6.28: *Landau-like fit to a sample of clean conversion electrons. The open stars represent all electrons from opposite-charge pairs, the solid stars the background from equal-charge pairs and the solid dots the clean electron sample after background subtraction.*

Figure 6.28 shows the dE/dx distribution of a clean conversion sample. The selection criteria for the tracks are the same as those for the signal sample, and all dE/dx corrections are applied. The distribution is fitted with the following 'Landau-like' function:

$$L(x) = P_1\ e^{-P_4\ P_3\left(\frac{x-P_2}{P_3}+e^{-\frac{x-P_2}{P_3}}-1\right)}$$

where the first parameter defines the height of the peak, the second the peak position (most probable value), the third the symmetric width and the fourth the asymmetry of the Landau function. These parameters are used later on for the constrained fit to the inclusive electron signal, where only the height (P_1) of the distribution is a free parameter.

Electrons from Dalitz Decays of π_0

Another significant source of background electrons are π^0s decaying in the Dalitz mode into $e^+e^-\gamma$. As the branching ratio for this process is known, their contribution to the inclusive electron signal can be estimated from track multiplicities in the data.
Relying on the assumption that the number of π^0s is $N_{\pi^0} = (N_{\pi^+}+N_{\pi^-})/2$ (by isospin symmetry), it is only necessary to measure the number of charged pions in the data. The multiplicity distribution of π^+, π^- and π^0s in an inclusive DIS MC sample is shown in the left plot of Figure 6.29, confirming the assumption made above.
The charged pions cannot be measured directly, since they are not sufficienctly separated from other hadrons. However the fraction of pions out of all tracks, which predominantly stem from hadrons, can be determined from MC. The right two plots in Figure 6.29 show the measured fraction of charged pions out of all measured tracks versus the track momentum (upper plot) and versus the polar angle (lower plot). The ratios stay almost constant in the selected momentum and angular range (indicated by the dashed lines). A fit in the acceptance region yields a pion fraction of $70.0 \pm 0.4\,\%$. Hence the number of pions in the selected sample can be estimated in

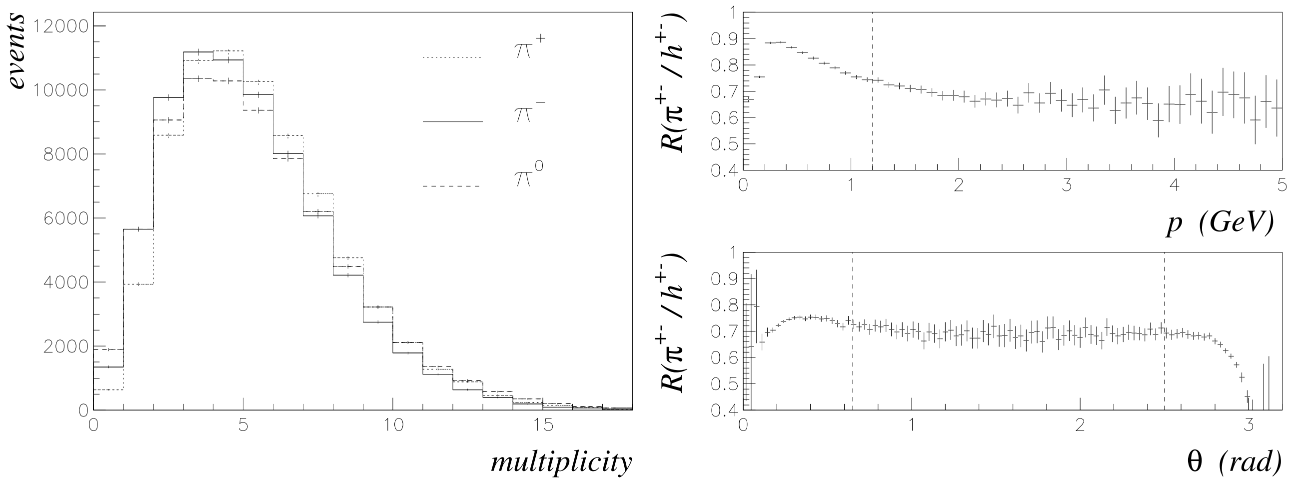

Figure 6.29: *The left plot shows the multiplicities of pions of different charges in MC DIS events. The right plots show the pion to hadron ratio versus momentum, for* $0.65 < \theta < 2.5\,rad$ *(upper plot), and versus the polar angle for* $1.2 < p < 5.0\,GeV$ *(lower plot). The selected momentum and angular range is indicated by the dashed lines.*

the following way:

$$N_{\pi^0}(p,\theta) \simeq 0.5 \cdot N_{\pi^\pm}(p,\theta) \simeq 0.5 \cdot 0.7 \cdot N_{h^\pm}(p,\theta)\ . \tag{6.7}$$

This distribution is used as an input to reweight a MC sample of exclusive $\pi^0 \to e^+e^-\gamma$ decays. The branching ratio for the Dalitz decay is $BR(\pi^0 \to e^+e^-\gamma) = 1.198\%$. Hence, counting the number of π^0s in the accepted momentum and angular region and multiplying by the branching ratio yields the expected number of measured electrons from Dalitz decays. The measured hadron distribution $N_{h^\pm}(p,\theta)$ is obtained for all tracks coming from the main vertex, without requiring a matched track or a cut on E_{EMC}/E_{tot}. Hence, the number of Dalitz electrons has to be multiplied by the matching and $E_{EMC}/E_{tot} > 0.9$ cut efficiency before being subtracted from the inclusive electron signal.
The number of background electrons from Dalitz decays in the inclusive electron signal is finally given by

$$N_{e^-\ from\ \pi^0\to e^+e^-\gamma}^{1.2<p<5.0\ GeV,\ 0.65<\theta<2.5\ rad} = N_{\pi^0,reweighted}^{1.2<p<5.0\ GeV,\ 0.65<\theta<2.5\ rad}\ BR\ \epsilon_{matching}\epsilon_{E_{EMC}/E_{tot}}\ . \tag{6.8}$$

Electrons from Beauty Decays

Another contribution to the background electrons comes from semileptonic beauty decays. Both the direct semileptonic decays $b \to e\nu X$ and two-stage semileptonic charm decays, e.g. $b \to DX \to e\nu X'$ have to be taken into account. The inclusive branching ratio for the semileptonic decay of B mesons totals to around 10 %. MC data generated with RAPGAP is used to estimate the background from these decays.
The cross section for beauty production depends on the kinematic region and is small in the range of this analysis. The solid dots in Figure 6.30 represent the cross section ratio $\sigma_b(b \to e\nu X)/\sigma_c(c \to e\nu X)$ versus Q^2, x and W for $Q^2 > 0.6\,\mathrm{GeV}^2$. The beauty cross section is well below 5 % of the charm cross section. Towards very high values of Q^2 the ratio increases up to 25 %, because $\sigma_b/\sigma_c \simeq e_b^2/e_c^2 = 1/4$. Due to the cuts on the momentum and polar angle of the electrons, the beauty fraction in the selected events is enhanced. The open dots in Figure 6.30

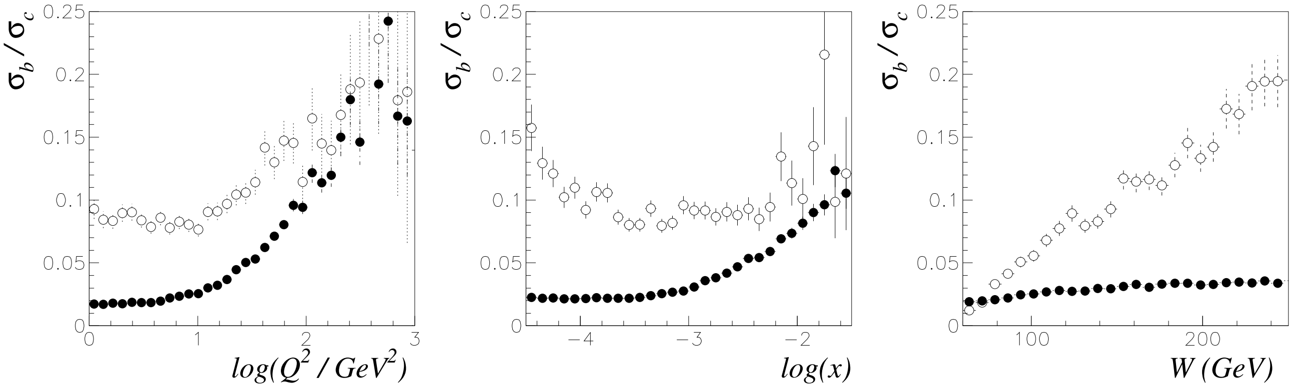

Figure 6.30: *$\sigma_b(b \to e\nu X)/\sigma_c(c \to e\nu X)$ versus Q^2, x and W as obtained from RAPGAP for $Q^2 > 0.6\,GeV^2$. The solid dots represent all electrons from semileptonic b and c decays, whereas the open dots represent those electrons in the acceptance region of this analysis, $1.2 < p < 5.0\,GeV$ and $0.65 < \theta < 2.5\,rad$.*

show the cross section ratio for electrons with $1.2 < p < 5.0\,\mathrm{GeV}$ and $0.65 < \theta < 2.5\,\mathrm{rad}$. The different acceptance of electrons from semileptonic charm and beauty decays can also be seen in Figure 6.31. The ratio of the background from beauty decays into electrons to the inclusive electron signal is around 4 %. This ratio depends on the kinematic region of the events and

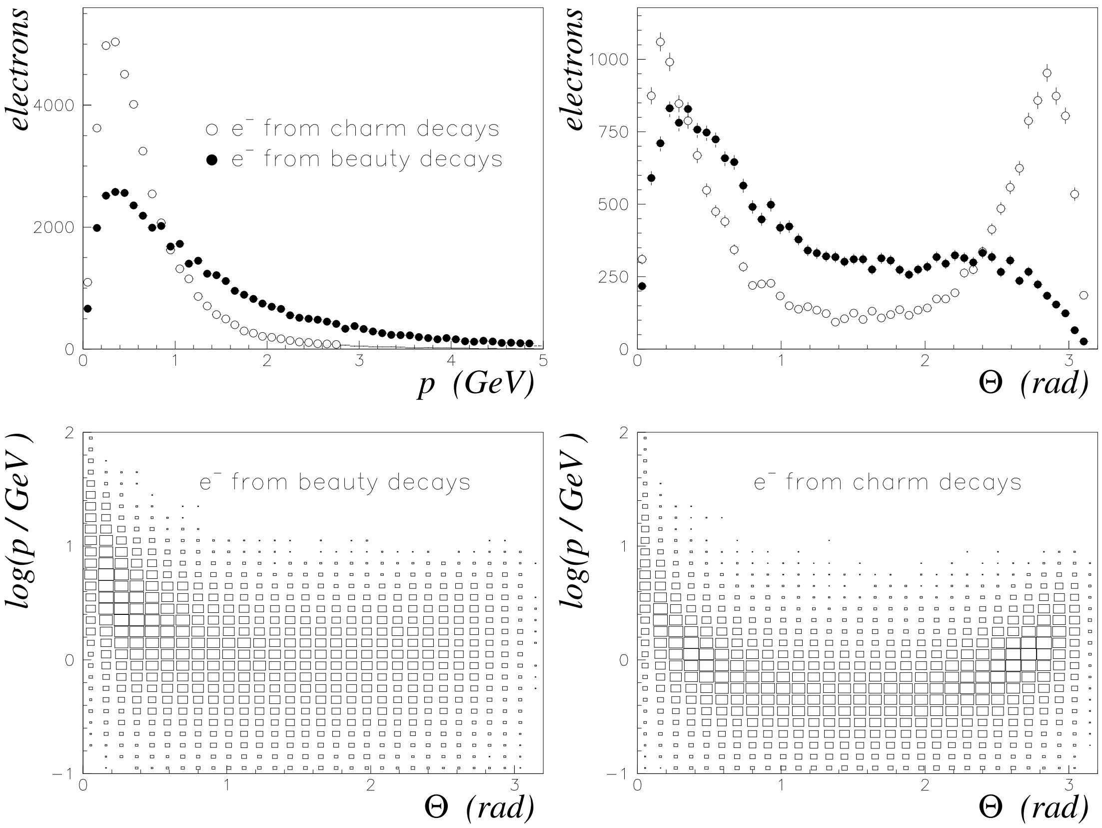

Figure 6.31: *The upper left plot shows the momentum distribution of electrons from semileptonic charm and beauty decays with $0.65 < \theta_{electron} < 2.5\,rad$. The upper right plot shows the θ distribution for $1.2 < p_{electron} < 5.0\,GeV$. The distributions for the beauty decays are normalized to one of the charm decays. The lower two plots show the polar angle versus the momentum of the electrons from beauty (left) and charm (right) decays.*

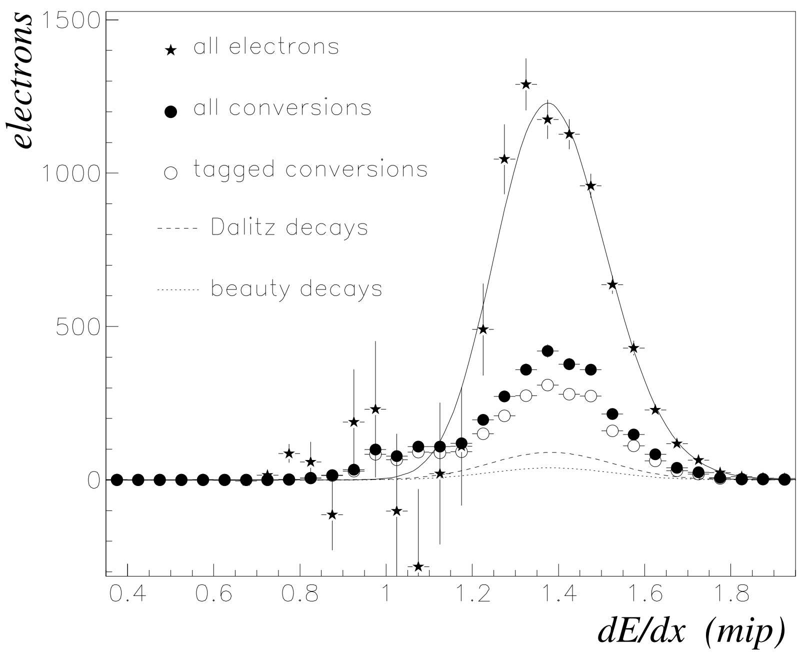

Figure 6.32: *The inclusive electron signal for the kinematic range $1 < Q^2 < 1000\,GeV^2$ and $0.03 < y < 0.7$. The contribution from the various non-charm background electrons is indicated. The fit to the electron sample is the constrained fit from the clean conversion sample obtained from data.*

increases in the high-Q^2 high-y region to up to 10 %.
In order to estimate the number of background electrons from MC, those electrons from beauty decays which satisfy the signal sample selection cuts are counted, and corrected for the different luminosities of data and MC.

Summary of Background Electrons

The contributions from the different background sources to the inclusive electron signal is shown in Figure 6.32. The total number of electrons in the inclusive signal is 7888, measured in the kinematic range $1 < Q^2 < 1000\,\mathrm{GeV}^2$ and $0.03 < y < 0.7$.
The number of tagged conversions is indicated by the open dots. The Tsai correction for the missing fraction of very asymmetric e^-e^+ pairs due to the 200 MeV momentum cut increases the number of conversions by about 20 %. After correction for the conversion finding efficiency the total number of electrons from photon conversions in the inclusive sample amounts to 40 %. The background from Dalitz decays and beauty decays is also indicated. They contribute about 8 % and 4 % respectively.
In order to obtain the signals for the calculation of differential cross sections and to measure $F_2^{c\bar{c}}$, it is necessary to repeat the whole electron finding method in each bin separately. In doing this, the background sample tracks are always taken from the overall sample and are reweighted in (p, θ) to match the (p, θ) distribution of the signal sample in each of the bins. The electron background must be estimated and subtracted in each kinematic bin.

6.4.2 Comparison of Data and MC

The selection of charm events described in the last section is an inclusive method, and hence no pure charm distribution can be measured to be compared with MC data. Nevertheless, a subsample consisting of approximately 50 % electrons from semileptonic charm decays can be selected in data. The lower right plot in Figure 6.19 shows the purity of the signal sample. Selecting signal sample tracks with $dE/dx > 1.4$ mips yields a highly enriched electron sample with about 20 % tracks produced by hadrons. Considering the background electrons from photon conversions, Dalitz and beauty decays, about 50 % of the signal sample tracks with $dE/dx > 1.4$ mip stem from semileptonic charm decays. Out of the selected DIS sample only those events having a charm candidate track are selected. Figure 6.33 shows the comparison for some kinematic variables and track quantities between the selected charm candidates and a charm MC generated with RAPGAP. In the MC data only events that have at least one true electron track from a semileptonic charm decay are selected, which matches the signal sample requirements.

Figures 6.33 a), b) and c) show the y_{DA}, Q^2_{DA} and x_{DA} of the event respectively. The y_{DA} in the MC is shifted towards higher values compared to the data. The Q^2_{DA} distribution also shows a disagreement, the charm MC having fewer events at low Q^2 values. Considering Figure 5.10, where the inclusive DIS sample was compared with an inclusive DIS MC and the charm MC sample, the differences in Figures 6.33 a), b) and c) can be attributed to the 50 % of non-charm events in the data. The number of vertex tracks is shown in Figure 6.33 d). Here the selected charm candidate events match the charm MC better than the inclusive DIS sample as shown in Figure 5.10 f). The momentum and polar angle of the tracks in Figures 6.33 e) and f) agree well within errors.

The MC sample is used to determine the matching and E_{EMC}/E_{tot} cut efficiency. Therefore a good description of the data by the MC is needed for the quantity E_{EMC}/E_{tot} and the distance of closest approach (DCA) between the extrapolated track at the calorimeter surface and the matched condensate. The agreement between data and MC for those two variables is reasonable as can be seen in Figures 6.33 g) and h). Figure 6.33 i) shows the isolation of the tracks at the calorimeter surface. Only tracks having no other track within 20 cm are selected as signal and background sample tracks. The tracks in the data are less well isolated than the tracks in MC, which is most likely due to the additional conversion electrons in the data.

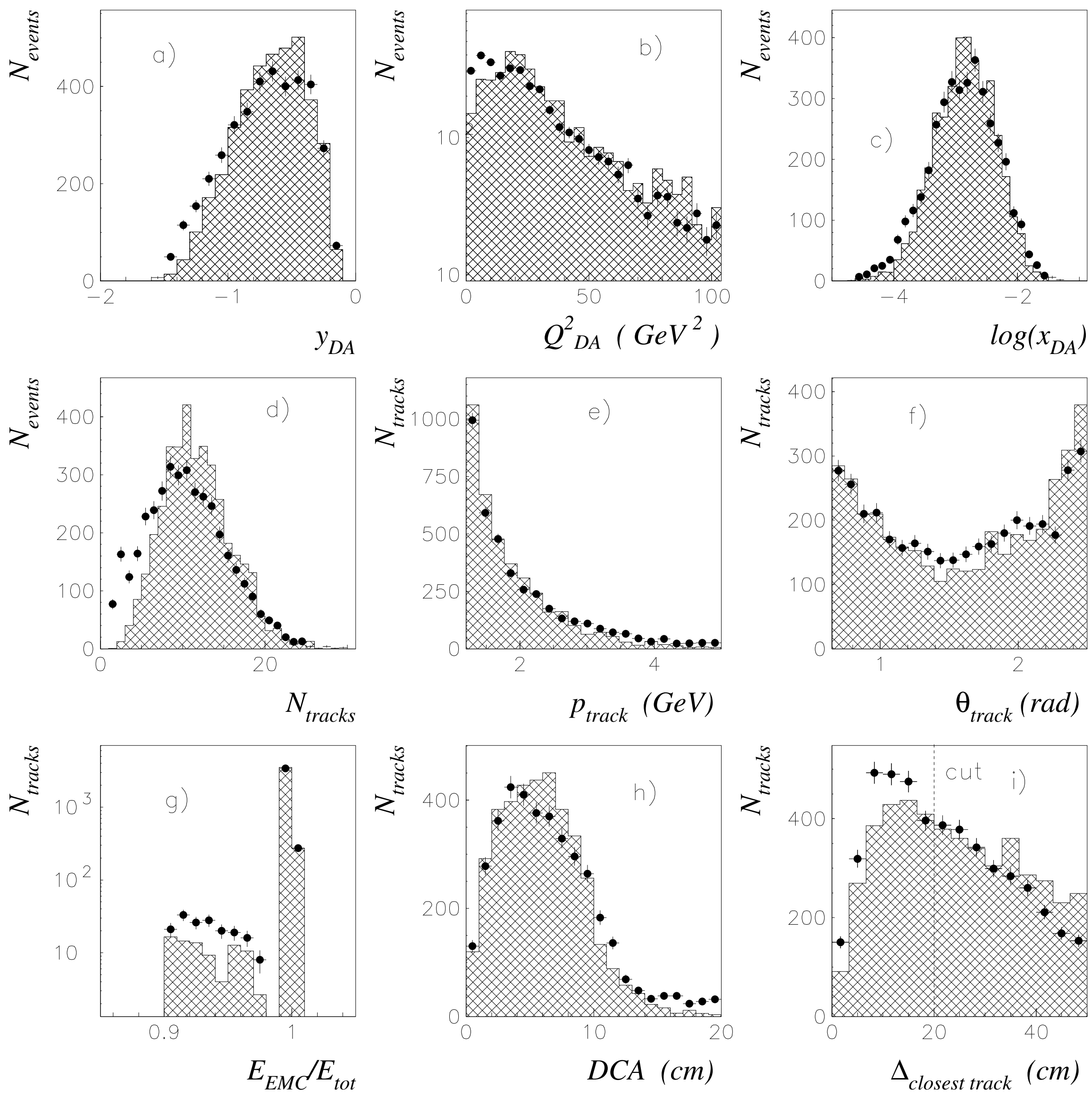

Figure 6.33: *Comparison between data (dots) and MC (shaded histogram). All selected events in data have at least one signal sample track with* $dE/dx > 1.4\,mips$*. The MC is generated with RAPGAP. Only charm events with at least one signal sample track that originates from a true electron from a semileptonic charm decay are selected. Shown is a)* y_{DA}*, b)* Q^2_{DA}*, c)* x_{DA} *and d) the number of vertex tracks in the event. Also shown are the track quantities e) momentum, f) polar angle, g)* E_{EMC}/E_{tot}*, h) distance of closest approach to matched condensate and i) the closest other track on the calorimeter surface. The MC is normalized to the data.*

Chapter 7

Cross Sections and $F_2^{c\bar{c}}$

In this chapter the results for the charm cross section and the $F_2^{c\bar{c}}$ will be presented. In the first section the calculation of the efficiencies, in particular the track finding efficiency will be explained. The second section gives an overview of the systematic checks that have been performed. The results for the integrated and differential cross sections are presented in sections three and four. The fifth section explains the unfolding procedure, which is used to obtain $F_2^{c\bar{c}}$, and presents the results. The last section contains a comparison between the results from the semileptonic analysis and the analysis using the D^* channel.

7.1 Determination of the Efficiencies

The determination of the efficiency to select charm events of the kind $\bar{c} \rightarrow e^- \bar{\nu} X$ is split into two steps. First the event selection efficiency is determined using the charm Monte Carlo sample generated with the RAPGAP program ($Q^2_{true} > 0.6\,\mathrm{GeV}^2$) (see Section 4.1.1).
In a second step the efficiency to find the electron tracks from the semileptonic charm decays within the selected events is determined, using the same Monte Carlo sample. The track finding efficiency refers to the efficiency to find a track from semileptonic charm decay in the signal sample. No simulated dE/dx distributions are used, and the statistical subtraction is not performed on the Monte Carlo data. Thereby any use of dE/dx from Monte Carlo data is avoided, which is desirable, since the energy loss does not model the data correctly.

7.1.1 Event Selection Efficiency

The event selection efficiency is calculated for each kinematic bin in (x, Q^2) for the cross sections and for $F_2^{c\bar{c}}$ as well as for each of the differential cross section bins,

$$\varepsilon_{event\ selection} = \frac{\text{selected events in reconstructed kinematic region}}{\text{all events in true kinematic region}} \,. \tag{7.1}$$

Only events which have a true electron track from a semileptonic charm decay with $1.2 < p_{electron} < 5.0\,\mathrm{GeV}$ and $0.65 < \theta_{electron} < 2.5\,\mathrm{rad}$ are considered. The kinematic region in the numerator is defined in terms of reconstructed variables, such as Q^2_{DA} or x_{DA}, whereas in the denominator it is defined in terms of true variables as they are generated in the Monte Carlo. Thereby migration effects resulting from the reconstruction of the event kinematics (see Section 5.1.4 Figure 5.5) are taken into account. Figure 7.1 shows the event selection efficiency versus the true Q^2 and y of the event, for the three different third level trigger (TLT) configurations (see Section 5.2.1). To obtain the final efficiency for the total data sample, the efficiencies for

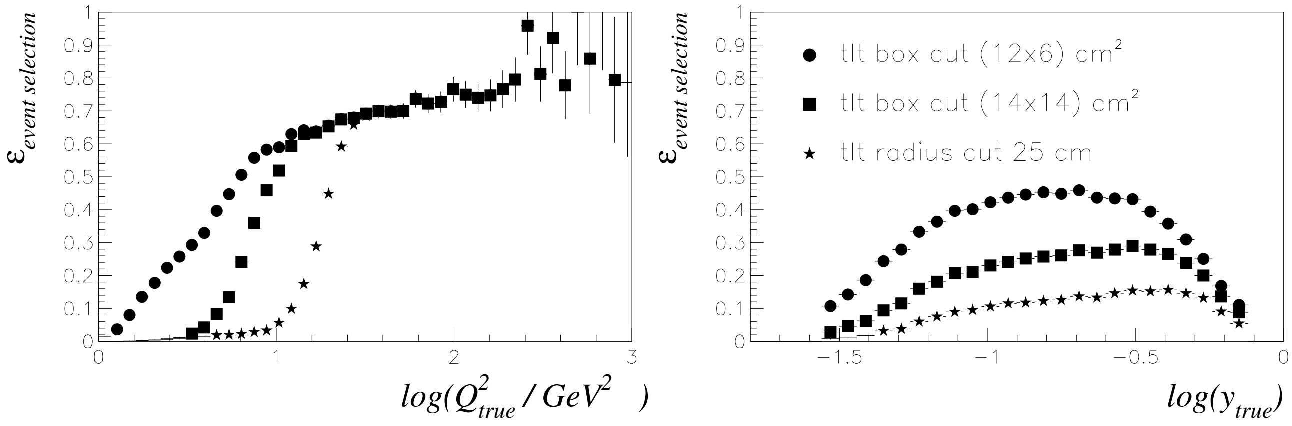

Figure 7.1: *Event selection efficiency versus Q^2 (left plot, $0.03 < y < 0.7$) and versus y (right plot, $1 < Q^2 < 1000\,\mathrm{GeV}^2$) as obtained from the charm Monte Carlo sample generated with RAPGAP. The efficiencies for the different TLT trigger configurations are shown.*

the different trigger configurations have to be determined separately and are then weighted with the luminosity of the corresponding running periods.

7.1.2 The Electron Track Finding Efficiency

The efficiency to find electrons from semileptonic charm decays depends on the selection criteria for the signal sample tracks. The resulting track finding efficiency $\varepsilon_{track\ finding}$ is the product of the efficiencies ε_i for each selection step, which are

- $\varepsilon_{vertex\ track}$: The track must be reconstructed as a track coming from the event vertex.
- $\varepsilon_{matching}$: The track must be matched to a calorimeter condensate, with the distance of closest approach less than 20 cm and $0.2 < E_{cond}/p_{track} < 3.0$.
- $\varepsilon_{E_{EMC}/E_{tot}>0.9}$: 90 % of the energy deposit has to be in the electromagnetic part of the calorimeter.
- $\varepsilon_{isolation}$: The track is isolated on the calorimeter surface within a circle of 20 cm radius.

The dependence of the different efficiencies on the momentum and the polar angle of the electron is demonstrated in Figure 7.2. Electron tracks from all selected DIS events have been used for this presentation. It can be seen that all efficiencies are almost constant within the momentum and polar angular range of the analysis (indicated by the dotted lines). The vertex finding, the matching and the E_{EMC}/E_{tot} cut efficiency is about 95 %. Around $\theta = 2.3$ rad a dip is observed for $\varepsilon_{E_{EMC}/E_{tot}>0.9}$ with respect to the polar angle (Figure 7.2 f). This corresponds to the overlap region between the BCAL and the RCAL. Since condensates are small objects and the detailed calorimeter geometry is not taken into account during their reconstruction, the matching quality is worsen in this region. The efficiency associated with the requirement of the track to be isolated on the calorimeter surface is only about 75 % as can be seen in Figure 7.2 g) and h). The efficiency of the isolation cut decreases in the central detector region (Figure 7.2 h), which is simply caused by geometry. The isolation cut is harder in the central region and less stringent towards shallow angles. The values for the efficiencies depend on the kinematic range of the event. Especially the matching and the isolation cut depend on the track multiplicity

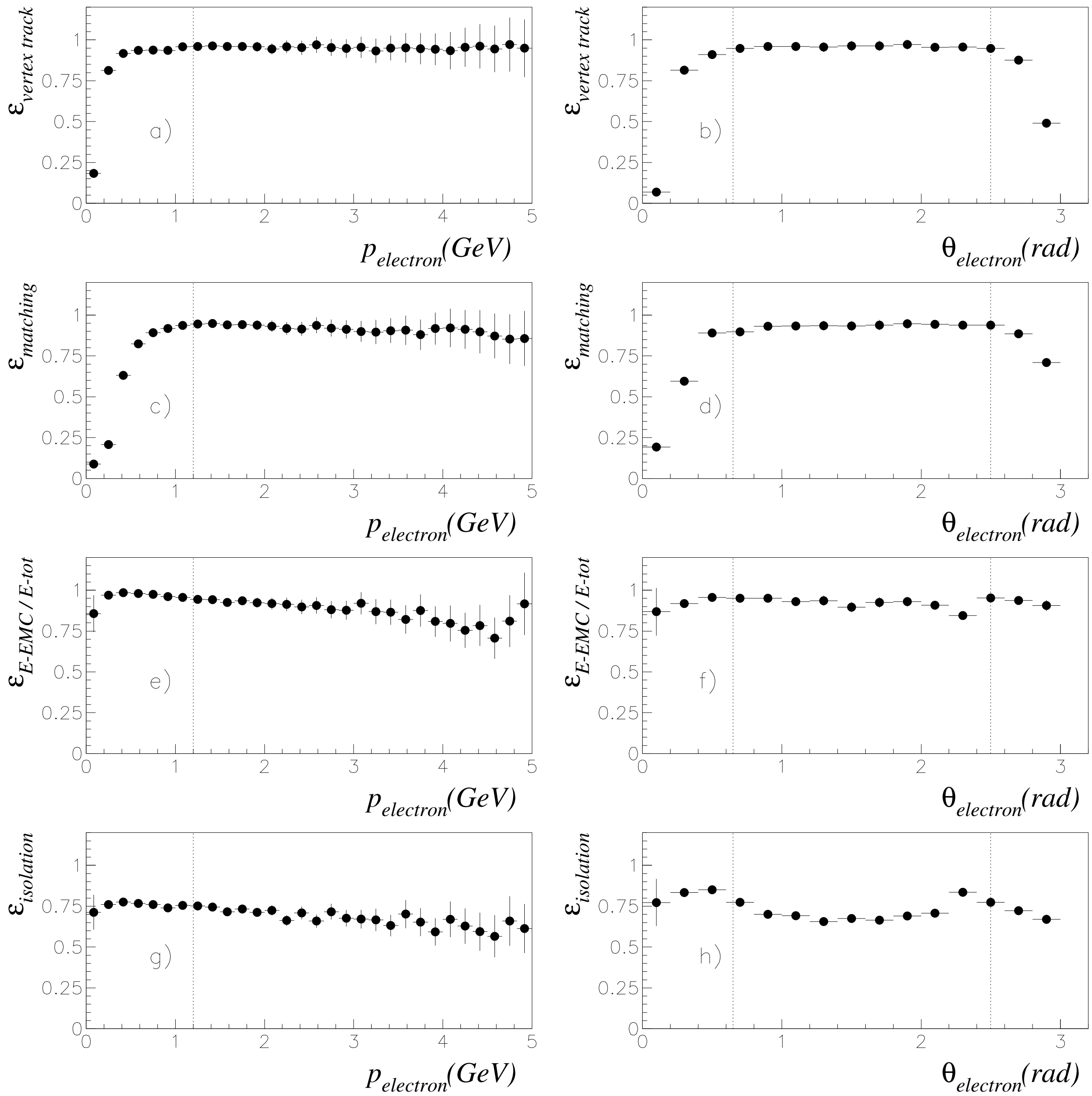

Figure 7.2: *Track finding efficiencies versus momentum and polar angle of the electron from semileptonic charm decays. The efficiencies are obtained from a charm Monte Carlo sample generated with RAPGAP. The efficiencies for each selection step are shown, a) and b) $\varepsilon_{vertex\ track}$, c) and d) $\varepsilon_{matching}$, e) and f) $\varepsilon_{E_{EMC}/E_{tot}>0.9}$ and g) and h) $\varepsilon_{isolation}$.*

and hence on the value of y of the event. Therefore the final track finding efficiencies have to be determined for each kinematic bin separately. This is done in a two-dimensional way in (p, θ),

$$\varepsilon_{track\ finding} = \frac{(\text{reconstructed electron tracks in signal sample})^{1.2<\mathrm{p_{reconstructed}}<5.0\,\mathrm{GeV}}_{0.65<\theta_{\mathrm{reconstructed}}<2.5\,\mathrm{rad}}}{(\text{true electrons})^{1.2<\mathrm{p_{true}}<5.0\,\mathrm{GeV}}_{0.65<\theta_{\mathrm{true}}<2.5\,\mathrm{rad}}} \,. \qquad (7.2)$$

Instead of relying on Monte Carlo to determine the track finding efficiency, a sample of clean photon conversion electrons from data could be used. Figure 7.3 shows the comparison for $\varepsilon_{matching}$ and $\varepsilon_{E_{EMC}/E_{tot}>0.9}$ between electrons from semileptonic decays in Monte Carlo (open dots) and electrons from clean photon conversions found in data (solid dots). The results were obtained with the 1995 data set. The efficiencies obtained with the electrons from photon

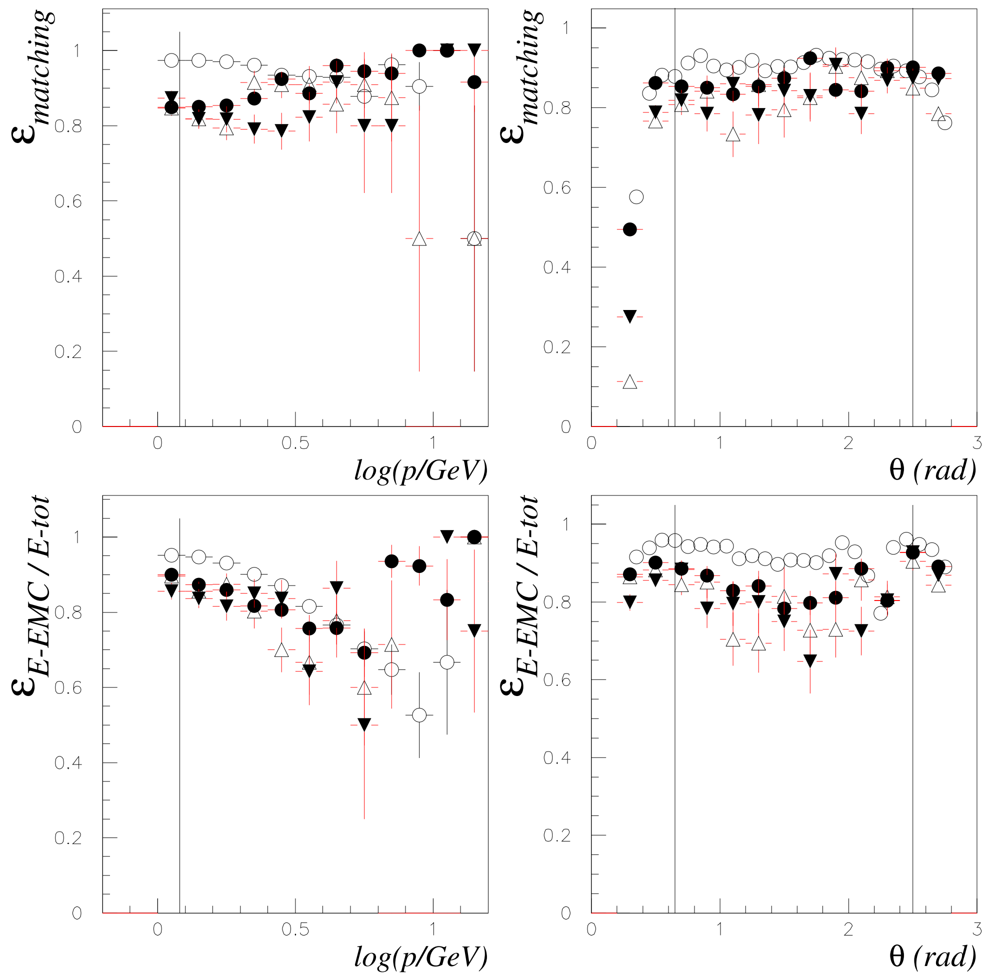

Figure 7.3: *Matching and E_{EMC}/E_{tot} cut efficiency versus momentum and polar angle of the electrons obtained with the 1995 data. Comparison between electrons from semileptonic decays in Monte Carlo (open dots), clean conversion electrons from data (solid dots), clean conversions found in Monte Carlo (solid triangles) and true conversion electrons in Monte Carlo (open triangles).*

conversions from data are clearly below the efficiencies obtained with the simulated electrons from charm decays in Monte Carlo. Also shown are the efficiencies obtained for tagged clean photon conversions in Monte Carlo (solid triangles) and for electrons from true Monte Carlo photon conversions (open triangles). The efficiencies for the Monte Carlo conversions agree very well with the ones for the clean conversions found in data. The reason for the difference between the conversion electrons and the electrons from semileptonic charm decays was found to be differences in the reconstruction quality. Electrons from photon conversions do not stem from the event vertex but originate somewhere in inactive material in the beampipe or the CTD wall. Nevertheless a large fraction of such tracks are reconstructed as coming from the vertex and thereby end up in the signal sample. An extrapolation of these poorly reconstructed tracks to the calorimeter surface deteriorates the matching efficiency compared to real vertex tracks, such as the electrons from charm decay. Furthermore, the quality of the matching decreases for the tracks from photon conversions, as can be seen in the lower E_{EMC}/E_{tot} cut efficiency, meaning that the number of mismatches is higher for these tracks than for the true electrons from charm decays (for further discussion see [Heb99]).

7.2 Systematic Uncertainties

In the following the systematic checks which were performed for this analysis are discussed. They are grouped into three subjects: checks performed on the charm selection method, checks performed on the DIS selection and theoretical uncertainties. In this discussion the resulting error from the uncertainty on the cross section is given. The different systematic uncertainties are added in quadrature to form the total systematic error. A more detailed study of the systematic uncertainties in the (x, Q^2) bins for the $F_2^{c\bar{c}}$ measurement will be presented in Section 7.5.5.

7.2.1 Systematic Checks Performed on the Charm Selection Method

Acceptance Variation of the Electrons from Semileptonic Decays

The acceptance region for the electrons is optimized to maximize the available statistics while still allowing the analysis to be performed.
The lower momentum cut is given by the dE/dx distribution. For track momenta lower than 1.2 GeV, the dE/dx distribution of anti-protons starts to overlap with the dE/dx distribution of electrons (see Figure 6.4 in Section 6.3). Hence a variation of the momentum cut affects the purity of the measured electron signal (see Figure 6.19). The cut on the polar angle is chosen to achieve optimal dE/dx resolution. Tracks outside the range of $0.65 < \theta < 2.5$ rad do not pass all nine superlayers, and hence have a lower number of hits deteriorating the dE/dx measurement. In addition both the polar angle and the momentum cut, affect the acceptance whereas the variation of the lower momentum cut is a dominating effect.
The systematic uncertainty on the momentum cut was estimated to ± 0.1 GeV and for the θ window to ± 0.05 rad. The changes are applied in the data, in the Monte Carlo and in the NLO calculation used for the extrapolation. The effect of these changes on the resulting charm cross section amounts to $-10\,\%$ to $+5\,\%$.

Selection of the Signal and Background Sample

The matching quality is improved by reducing the distance of closest approach between condensate and track by 3 cm. The change of the resulting semileptonic charm cross section is less than 1 %.
The uncertainty on the isolation cut on the calorimeter surface is estimated to be ± 5 cm. The resulting change of the cross section is between $+2.5$ and $-6.0\,\%$.

Corrections to dE/dx

A modified θ and dE/dx dependent space charge correction is used. No correction is applied for $dE/dx = 1.0$ mip and the usual correction for electron tracks with $dE/dx = 1.4$ mips. The values for $1.0 < dE/dx < 1.4$ mips are obtained via linear interpolation. The effect on the resulting electron signal is negligible.

Electron Background

The quality of the conversion finding is varied by changing the quantity D by ± 3. This results in a variation of the semileptonic charm cross section between $-1\,\%$ and $+3\,\%$.
Recent measurements of the beauty cross section at HERA exist. The H1 results exceed the predicted cross section from NLO calculations by a factor of two, whereas the ZEUS results show

agreement within large errors with the predictions from a LO Monte Carlo [Ad99C, Wi99B]. The uncertainty on the beauty background is estimated to $\pm 50\,\%$, resulting in a variation of the cross section by $\pm 3\,\%$.
The uncertainty on the background from Dalitz decays of π^0s, which are estimated from the track multiplicities in the data, is $\pm 30\,\%$. This results in a variation of the cross section by $\pm 4\,\%$.

Extraction of the Signal

A variation of the dE/dx cut value changes the statistical error as well as the purity of the electron signal (see Section 6.4, Figure 6.19). The uncertainty on the dE/dx cut value is estimated to be ± 0.05 mip. The resulting variation of the cross section is between $+1\,\%$ and $-2.5\,\%$.

Estimation of Background from Anti-protons

To estimate the systematic uncertainty due to the different fractions of anti-protons in the background and signal samples, Monte Carlo data is studied. Since the energy loss in Monte Carlo does not describe the data well, the dE/dx distributions in data were optimized by using data. It should be noted that the simulation even after this optimization is not perfect and only serves as a method to estimate the systematic error. The energy loss of electrons in data is well known from the clean conversion sample. Comparing data and Monte Carlo, the dE/dx in the simulation is off by about $+15\,\%$ with respect to the pion peak position. Hence the peak position of the electron dE/dx distribution was shifted by $-15\,\%$ in the Monte Carlo to describe the data. The entire analysis procedure is then performed with a sample of inclusive DIS Monte Carlo. The dE/dx in Monte Carlo is measured in FADC counts, because no normalization to minimum ionizing pions is performed. A lower dE/dx cut at 64 FADC counts, which refers to 45.8 % of the electron signal in the same way as in data, is applied (see Section 7.3). The resulting dE/dx distributions for the signal and the background samples, as well as the resulting

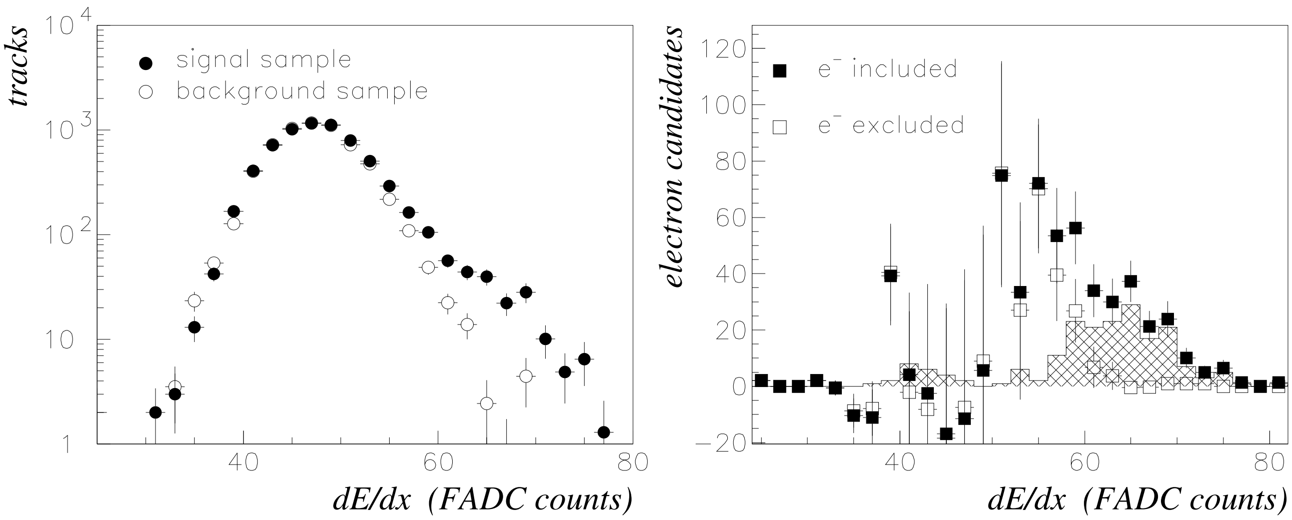

Figure 7.4: *The dE/dx distribution of signal and background sample as obtained from a sample of inclusive DIS Monte Carlo is shown in the left plot. The right plot shows the resulting electron signal after statistical subtraction, with and without electrons. The shaded histogram shows the pure electron distribution.*

electron signal after subtraction are shown in Figure 7.4. The subtraction is performed twice, once including the electron tracks and once without the electron tracks. The two resulting distributions are shown in the right plot of Figure 7.4. Also shown is the pure electron signal as a shaded histogram. The inclusive electron signal obtained from the subtraction procedure (solid squares) describes the pure electron signal quite well above the dE/dx cut value. For lower dE/dx values the contribution from hadrons, which are mainly anti-protons (see Figure 6.15) becomes significant. The ratio of the background from non-electron tracks to the signal above the dE/dx cut value is 2.0 %. The different fraction of electrons in the signal sample in Monte Carlo compared to data is taken into account. The background from non-electron tracks depends strongly on the dE/dx cut value chosen and on the anti-proton fraction in the signal sample. A variation of the dE/dx cut value by ± 2 FADC counts and a change of the anti-proton fraction by 50 % and 200 % results in a background contribution of between 0 and 8 %. Hence the systematic error on the inclusive electron signal is estimated to be -8 %. Since about 50 % of the tracks in the inclusive signal are tracks from semileptonic charm decays (see Section 6.4.1), the systematic error on the charm cross section is therefore about -16 %. However, the error varies with the different background fractions of electrons from non-charm decays in the inclusive signal.

7.2.2 Systematic Checks Performed on the DIS Selection

Only a few checks have been performed on the DIS selection, since the effect of those is only a minor contribution to the overall systematic error in comparison to the checks on the charm selection. Further studies concerning the effect of systematic uncertainties on the inclusive F_2 measurement can be found in [Def99, Fri99]. The following checks were performed in order to study the DIS event selection uncertainties:

- The cut on y_{JB} is removed. This allows to study the simulation of the hadronic final state and the description of noise in the uranium calorimeter.
- In order to study possible background from photoproduction events as well as the simulation of the hadronic final state, the $(E - p_z)$ cut is changed by ± 2 GeV.
- The cut on the energy of the scattered DIS positron is varied by ± 1.0 GeV. This estimates the uncertainty in the reconstruction and simulation of the energy measured in the SRTD, the presampler and the calorimeter.

The systematic effect of each of the checks is less than ± 2 %. An additional uncertainty arises from the overall normalization due to the error on the luminosity measurement of ± 1.65 %.

7.2.3 Theory Related Systematic Uncertainties

The Charm Quark Mass

For the Monte Carlo generation a charm quark mass of $m_c = 1.5$ GeV was used in RAPGAP. This value is also used for the acceptance corrections calculated with the HVQDIS program and the unfolding of the $F_2^{c\bar{c}}$. The influence of the charm mass is studied by allowing it to vary by ± 0.2 GeV in the HVQDIS calculations and the unfolding procedure.

The Branching Ratio $c \to e\nu X$

The overall effective branching ratio for the decay $c \to e\nu X$ represents another uncertainty in the calculation of the charm cross section and therefore in the extraction of the structure function $F_2^{c\bar{c}}$. As discussed in Section 2.2.4, the spectator model is a reasonable assumption to describe semileptonic decays of heavy hadrons, but fails for the description of hadronic decays. The overall branching ratio for the decay $c \to e\nu X$ therefore depends of the exact composition of different hadrons. Using spin counting and isospin symmetry the expected production ratio of $D^{\pm} : D^0 : D^{*\pm} : D^{*0}$ is $1 : 1 : 3 : 3$, which is approximately the branching fraction used by RAPGAP to simulate the production of charmed mesons in deep-inelastic ep scattering events (see Section 4.1.1). In addition RAPGAP uses the explicit branching ratios for the dominating decays of the charmed mesons as taken from the PDG [Cas99]. Those branching ratios not yet measured are estimated, but are only for a minor fraction of the decays. Since the resulting inclusive branching ratio for the semileptonic decay of 9.5 % in RAPGAP is found to be in agreement with the measurements performed at e^+e^- collider experiments, no systematic error is applied to account for the hadron composition in e^+e^- and ep scattering events.

The inclusive semileptonic branching ratio measured by the ARGUS collaboration is $B(c \to l^+) = 0.095 \pm 0.009$, where the lepton is either a muon or an electron [Alb92]. A more recent measurement, made by the OPAL collaboration, yields the same branching ratio into leptons, $B(c \to l\nu X) = 0.095 \pm 0.006^{+0.007}_{-0.006}$, and in addition quotes $B(c \to e\nu X) = 0.103 \pm 0.009^{+0.009}_{-0.008}$ for the semileptonic charm decay into electrons only [Abb99].

For the extraction of the charm cross section the branching ratio of $BR(c \to e\nu X) = 0.095$ is used. In addition to the 9 % error given by the measurement of $c \to e\nu X$ itself, another 10 % error accounts for the difference between the $B(c \to e\nu X)$ and $B(c \to l\nu X)$ ratios. This results in a total error of $\pm$ 13 % due to the uncertainties in the branching ratio.

	$1 < Q^2 < 1000$ GeV^2	$10 < Q^2 < 200$ GeV^2
$n_{sg}(dE/dx > 1.4\,\text{mips})$	4828	3597
$n_{bg}(dE/dx > 1.4\,\text{mips})$	1246	880
$n_{sg}(0.8 < dE/dx < 1.1\,\text{mips})$	140733	94803
$n_{bg}(0.8 < dE/dx < 1.1\,\text{mips})$	144361	97719
$n_{electron\ signal}(dE/dx > 1.4\,\text{mips})$	3613 ± 78	2743 ± 64
$n_{electron\ signal}$	7888 ± 171	5989 ± 139
$n_{conversions}$	3079 ± 100	2334 ± 87
n_{Dalitz}	648	435
$n_{semileptonic\ b\ decay}$	255	188
$n_{semileptonic\ c\ decay\ candidates}$	3906 ± 199	3032 ± 164
$\varepsilon_{event\ selection}$	35.1%	68.2%
$\varepsilon_{track\ finding}$	61.5%	57.7%
$\sigma_{measured}$	$532 \pm 27\,^{+40}_{-96}$ pb	$226 \pm 12\,^{+14}_{-34}$ pb
σ_{NLO}	558^{+89}_{-80} pb	206^{+27}_{-22} pb

Table 7.1: *Numbers used to calculate the cross sections in a limited kinematic range.*

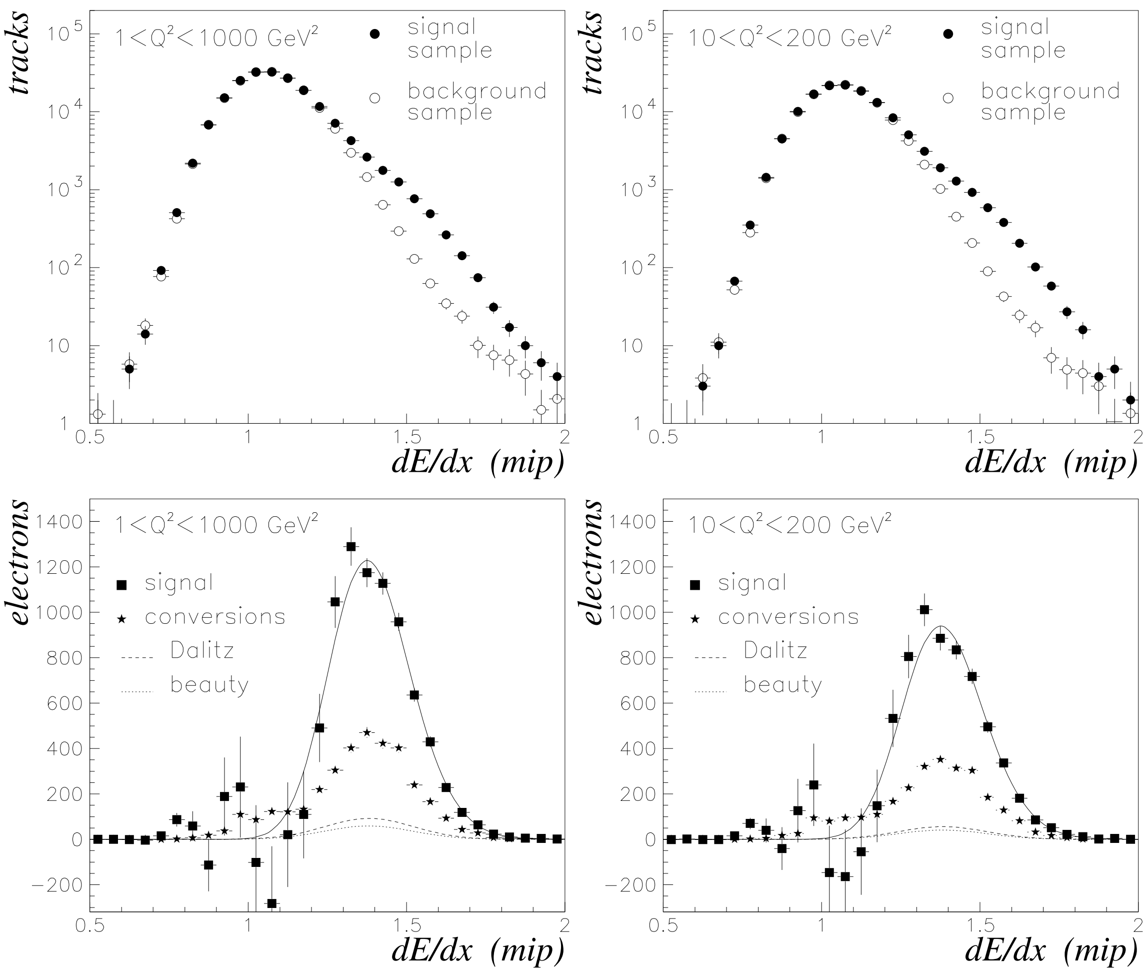

Figure 7.5: *The upper two plots show the signal and the background sample for the two kinematic regions, $1 < Q^2 < 1000\,GeV^2$ and $10 < Q^2 < 200\,GeV^2$. The lower plots show the resulting electron signal after the statistical subtraction. The contributions from the different classes of background electrons are also shown.*

7.3 Cross Section in a Limited Kinematic Range

The cross section for charm production with semileptonic decays of the kind $\bar{c} \to e^- \bar{\nu}_e X$ in NC deep-inelastic ep scattering events, $\sigma(e^+p \to e^+e^-X)$, can be calculated in the following way,

$$\sigma(e^+p \to e^+\ e^-\ X) = \frac{N_{e^-}(1.2 < p < 5.0\,\mathrm{GeV}, 0.65 < \theta < 2.5\,\mathrm{rad})}{\varepsilon_{event\ selection}\ \varepsilon_{track\ finding}\ \mathcal{L}}\ . \tag{7.3}$$

N_{e^-} is the number of electron candidates found that originate from semileptonic charm decays. The kinematic region of the electrons is limited to the acceptance window in momentum and polar angle, $1.2 < p < 5.0\,\mathrm{GeV}$ and $0.65 < \theta < 2.5\,\mathrm{rad}$. $\varepsilon_{event\ selection}$ and $\varepsilon_{track\ finding}$ are the event selection and track finding efficiencies, respectively. $\mathcal{L}$ denotes the total integrated luminosity, which amounts to $34.04\,\mathrm{pb}^{-1}$. The cross section is extracted in two kinematic regions, $1 < Q^2 < 1000\,\mathrm{GeV}^2$ and $10 < Q^2 < 200\,\mathrm{GeV}^2$, with $0.03 < y < 0.7$ for both regions.
The dE/dx distributions of the signal and the background samples for the two kinematic regions are shown in the upper two plots in Figure 7.5. The lower two plots show the resulting electron signal after the statistical subtraction. A clear signal is obtained for both regions. The fractions of background electrons from the different sources are shown.

A detailed list of all necessary numbers which are needed to calculate the cross section in the two kinematic regions is given in Table 7.1. $n_{sg}(dE/dx > 1.4)$ and $n_{bg}(dE/dx > 1.4)$ are the number of tracks with $dE/dx > 1.4$ in the signal and background samples, respectively. The next two numbers are used for the normalization of the background sample to the signal sample. The normalization factor for the background sample is calculated as $\alpha = n_{sg}(0.8 < dE/dx < 1.1)/n_{bg}(0.8 < dE/dx < 1.1)$. All numbers concerning the background sample are determined for the integrated reweighted histograms. The original background histogram taken from the preselected DIS sample contains about 172,000 tracks, and is the same for the determination of the cross sections, the differential cross sections and the (x, Q^2) bins shown in the sections below.
The number of electron tracks in the inclusive electron signal $n_{electron\ signal}(dE/dx > 1.4\,\text{mips})$ is obtained according to Equation 6.4. The acceptance of the signal region for $dE/dx > 1.4$ mips amounts to 45.8 %, as obtained from the Landau-like fit to a clean sample of conversion electrons. Hence dividing $n_{electron\ signal}(dE/dx > 1.4\,\text{mips})$ by the acceptance yields the total number of electron candidates in the inclusive electron signal, $n_{electron\ signal}$.
In order to obtain the number of electron candidates coming from semileptonic charm decay, $n_{semileptonic\ c\ decay\ electrons}$, the background electrons must be subtracted. $n_{conversions}$ gives the number of electrons from photon conversions, already corrected for efficiency. n_{Dalitz} is the number of electrons from Dalitz decays of π^0s and $n_{semileptonic\ b\ decay}$ is the background from electrons that stem from beauty decays (see Section 6.4.1).
Also given in Table 7.1 is the theoretical prediction for the cross section as calculated at NLO with the HVQDIS program. They are obtained using the GRV model for the proton parton density function (GRVHO94 [Glü95]). The charm mass was set to $m_c = 1.5$ GeV and the renormalization and factorization scales were set to, $\mu_F^2 = \mu_R^2 = \mu^2 = Q^2 + 4m_c^2$. The Peterson fragmentation function was used with $\varepsilon_Q = 0.035$ and the overall cross section was fixed by using a branching ratio for the semileptonic decay of the charmed hadrons of $BR = 9.5\,\%$. Unless otherwise stated these parameters are used below for calculations made with the HVQDIS program. The measured cross sections and the theoretical predictions agree within errors. The first error on the measured cross section corresponds to the statistical error, and the second two errors to the systematic uncertainties. The error on the calculated cross section refers to a variation of the charm mass by ± 0.2 GeV. The additional error of 13 % from the uncertainty in the branching ratio is not taken into account.

7.4 Differential Cross Sections

Differential cross sections are extracted in the kinematic region, $1 < Q^2 < 1000\,\text{GeV}^2$ and $0.03 < y < 0.7$. The signal sample tracks are binned according to p_t and η of the track and W, x and Q^2 of the event.
The inclusive electron signals obtained for the different bins can be found in Appendix B Figures B.1 to B.5. The background contribution to the inclusive electron signal in each of the bins is shown in Figure 7.6. The major contribution comes from photon conversions. The fraction stays almost stable with W, Q^2 and x of the event, but clearly depends on the track quantities p_t and η. Towards high p_t the contribution from conversion electrons decreases (see Figure 7.6 d), due to the low momentum spectrum of these electrons in combination with their polar angular distribution (see Figure 6.24). The conversion fraction increases towards shallow angles, as can be seen in Figure 7.6 e). This is expected, since more inactive material has to be traversed by the photons (see Section 6.4.1).

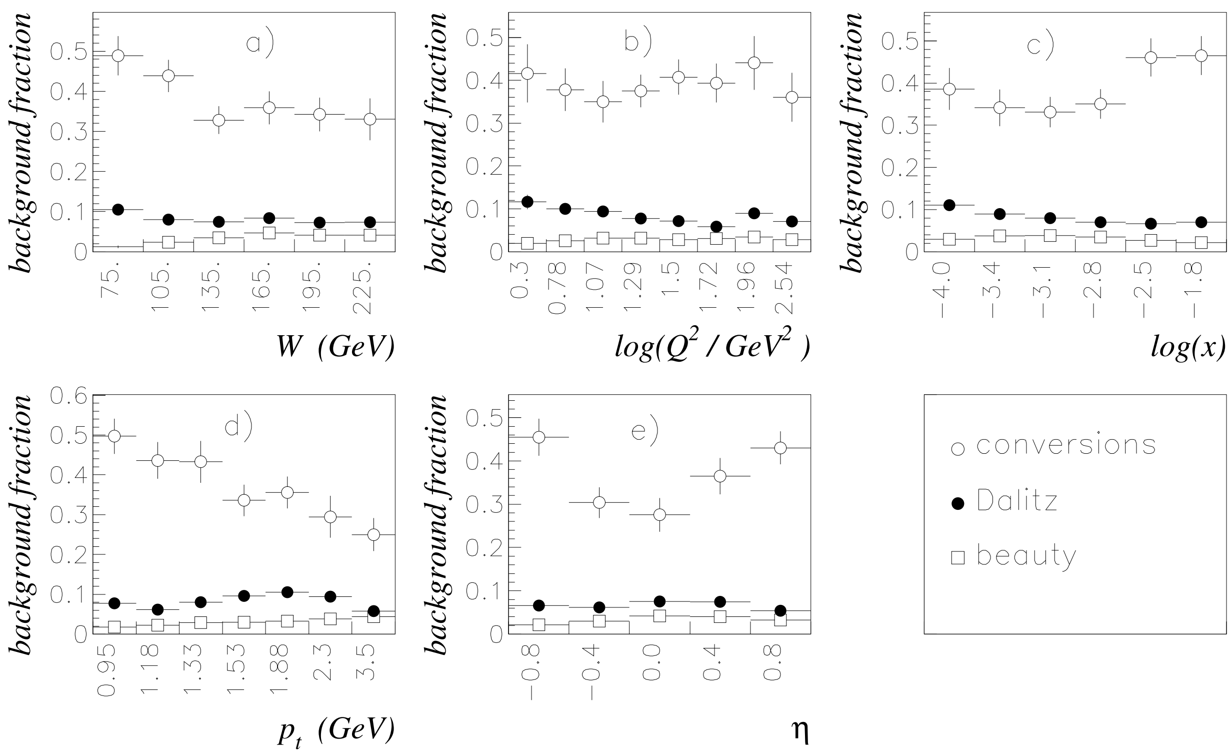

Figure 7.6: *Background electron contribution to the inclusive electron signal from conversion electrons (open dots), Dalitz decays of π^0s (solid dots) and beauty decays (open squares) in W (a), $\log(Q^2)$ (b), $\log(x)$ (c), p_t (d) and η (e) bins.*

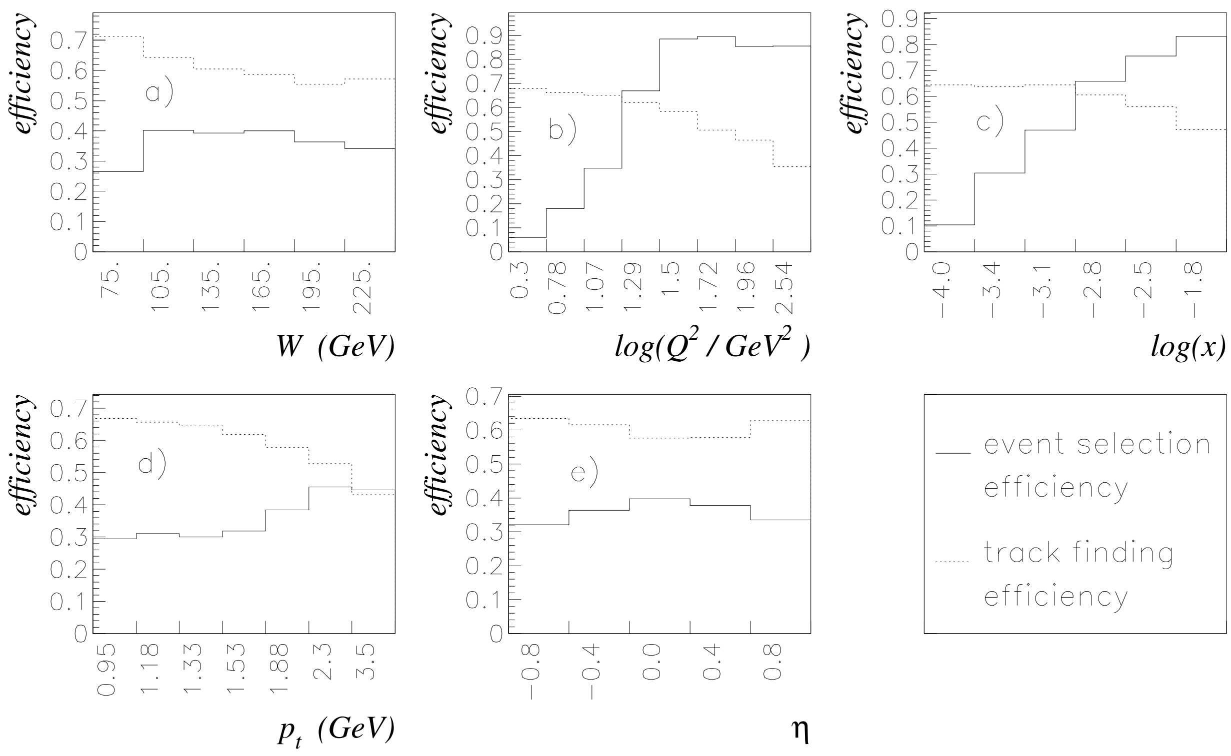

Figure 7.7: *The event selection and track finding efficiencies in W (a), $\log(Q^2)$ (b), $\log(x)$ (c), p_t (d) and η (e) bins.*

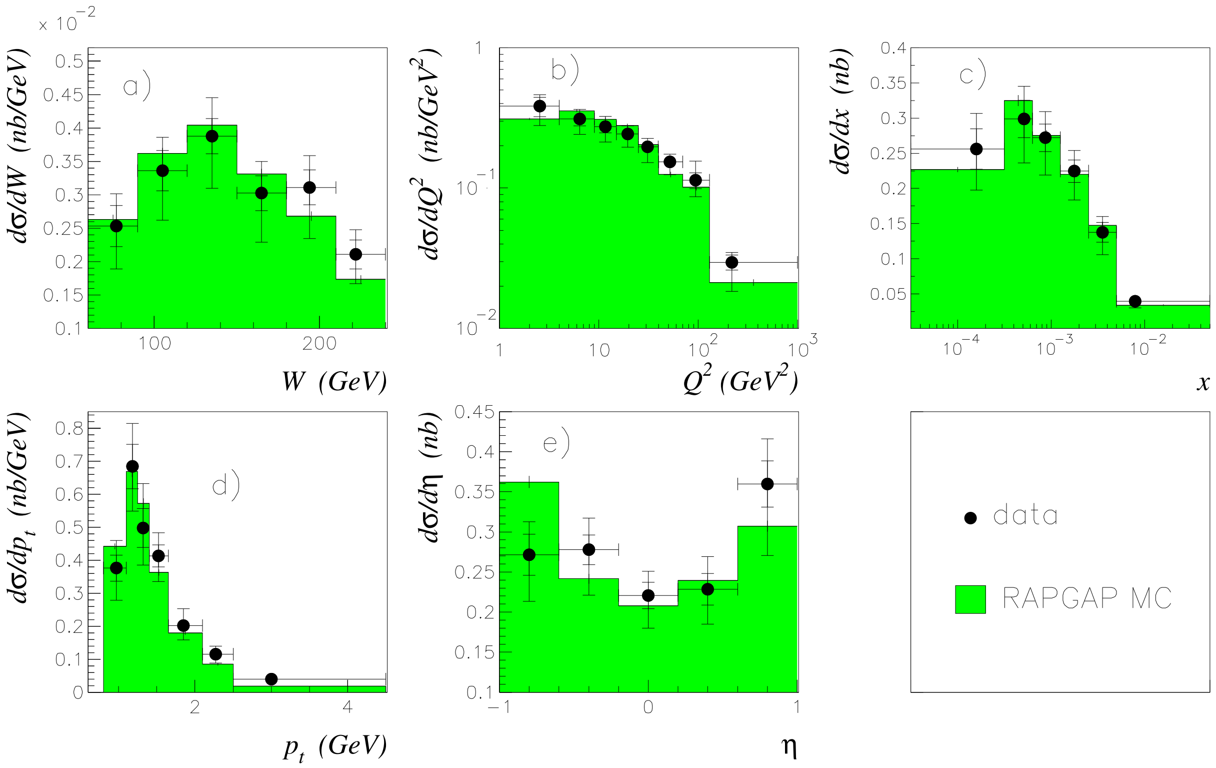

Figure 7.8: *The differential cross sections versus W (a),* $\log(Q^2)$ *(b),* $\log(x)$ *(c),* p_t *(d) and* η*. The data (solid dots) are compared to the distribution obtained from the RAPGAP charm Monte Carlo sample. The Monte Carlo distributions are normalized to the data.*

The contribution of electrons from Dalitz decays of π^0s to the inclusive electron signal fluctuates around 8 %. As expected, the background from beauty decays increases towards high Q^2 and high W of the event (see the beauty discussion in Section 6.4.1). Due to the higher mass of the beauty quarks compared to the charm mass, the electrons from semileptonic beauty decays have a higher transverse momentum. This shows up in the increasing fraction of background from beauty decays towards higher p_t bins in Figure 7.6 d).
The event selection and track finding efficiencies in the different bins are shown in Figure 7.7. Due to the prescale factor of 100 on the low-Q^2 third level trigger for about 70 % of the running period, the event selection efficiency (solid line) is low in the low-Q^2 and low-x region. For the other kinematic regions the event selection efficiency stays fairly constant with respect to the different bins.
The track finding efficiency depends on the track multiplicity of the event, which mainly effects the efficiency of the matching and of the isolation cut on the calorimeter surface. A clear tendency is visible in Figure 7.7 b), where the track finding efficiency decreases towards high Q^2. High-Q^2 events have higher multiplicity. Hence the isolation cut is more stringent and the matching quality deteriorates, decreasing also the E_{EMC}/E_{tot} cut efficiency. The same effect is observed for the track finding efficiency as a function of x and W (see Figures 7.7 a) and c). The track finding efficiency in the p_t and η bins exhibits mainly the effect of the isolation cut. This cut is less stringent at shallow angles due to the geometry and therefore the efficiency increases slightly in that region. The same effect shows up versus the p_t bins. The higher the p_t of a track the more centralized it is in η.

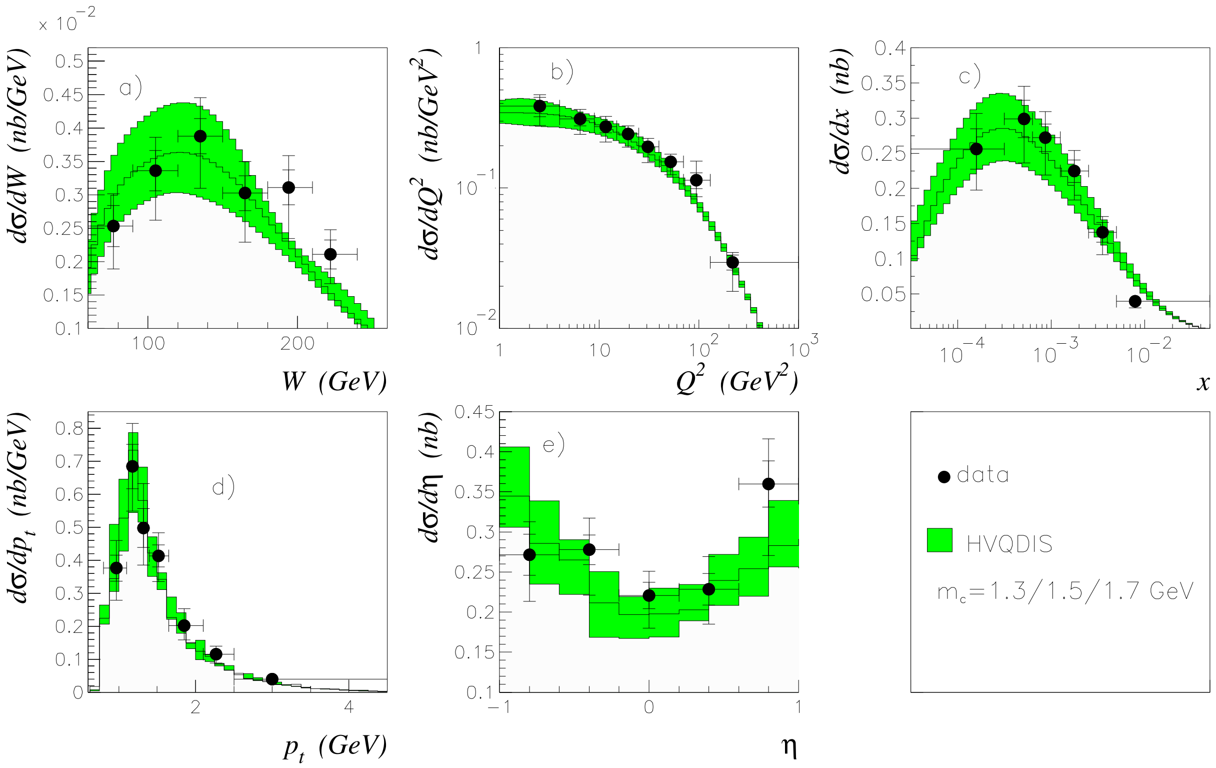

Figure 7.9: *The differential cross sections versus W (a), $\log(Q^2)$ (b), $\log(x)$ (c), p_t (d) and η. The data (solid dots) are compared to the distribution obtained from the HVQDIS program, calculated for different charm masses.*

The resulting differential cross sections are compared to the ones obtained from the RAPGAP charm Monte Carlo sample, shown in Figure 7.8. The Monte Carlo is normalized to the data, and therefore only the shape is to be compared. The Q^2 (b) and x (c) distributions show good agreement. The measured cross section shows the tendency to be above the prediction from Monte Carlo in the high-Q^2 region. The measured differential cross section in W (a) is in reasonable agreement with the Monte Carlo prediction. Figure 7.8 d) and e) show the differential cross section in p_t and η of the electron. The agreement in p_t is reasonable, but shows some excess of the data for high p_t tracks. For η some disagreement is observed in the backward region. The measured cross section drops, whereas the Monte Carlo predicts a rise of the cross section. However, the overall agreement is reasonable within errors.

The measured differential cross sections are also compared with the theoretical predictions for the differential cross sections as calculated at NLO with the HVQDIS program (see Section 4.2.1). The distributions shown in Figure 7.9 are obtained using the same parameters as for the calculation of the total cross section in Section 7.3. The agreement of the W, Q^2 and x distributions is fairly good. The same tendency of the data to be above the theoretical prediction in the high-Q^2 region is observed. The measured cross section in p_t and η are reasonably described by the NLO prediction.

bin number	y range	Q^2 range [GeV^2]
1	0.03 - 0.15	1-4
2	0.15 - 0.70	1-4
3	0.03 - 0.12	4-9
4	0.12 - 0.30	4-9
5	0.30 - 0.70	4-9
6	0.04 - 0.14	9-15
7	0.14 - 0.27	9-15
8	0.27 - 0.70	9-15
9	0.03 - 0.11	15-25
10	0.11 - 0.30	15-25
11	0.30 - 0.70	15-25
12	0.03 - 0.11	25-40
13	0.11 - 0.30	25-40
14	0.30 - 0.70	25-40
15	0.06 - 0.20	40-70
16	0.20 - 0.70	40-70
17	0.06 - 0.20	70-130
18	0.20 - 0.70	70-130
19	0.06 - 0.30	130-1000
20	0.30 - 0.70	130-1000

Table 7.2: *Bin borders in x and Q^2.*

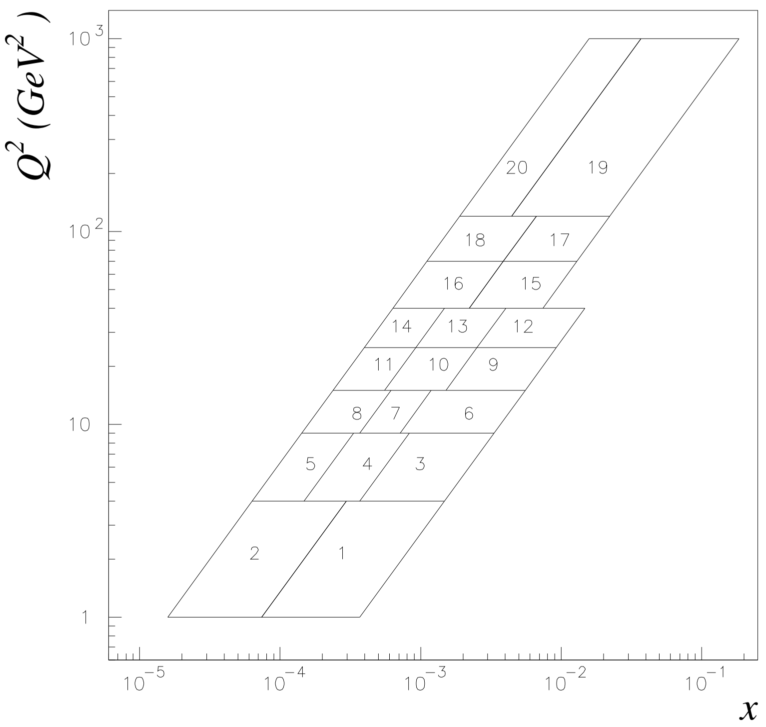

Figure 7.10: *The bins used to extract $F_2^{c\bar{c}}$ shown on the (x, Q^2) plane. The numbers indicate the bin number.*

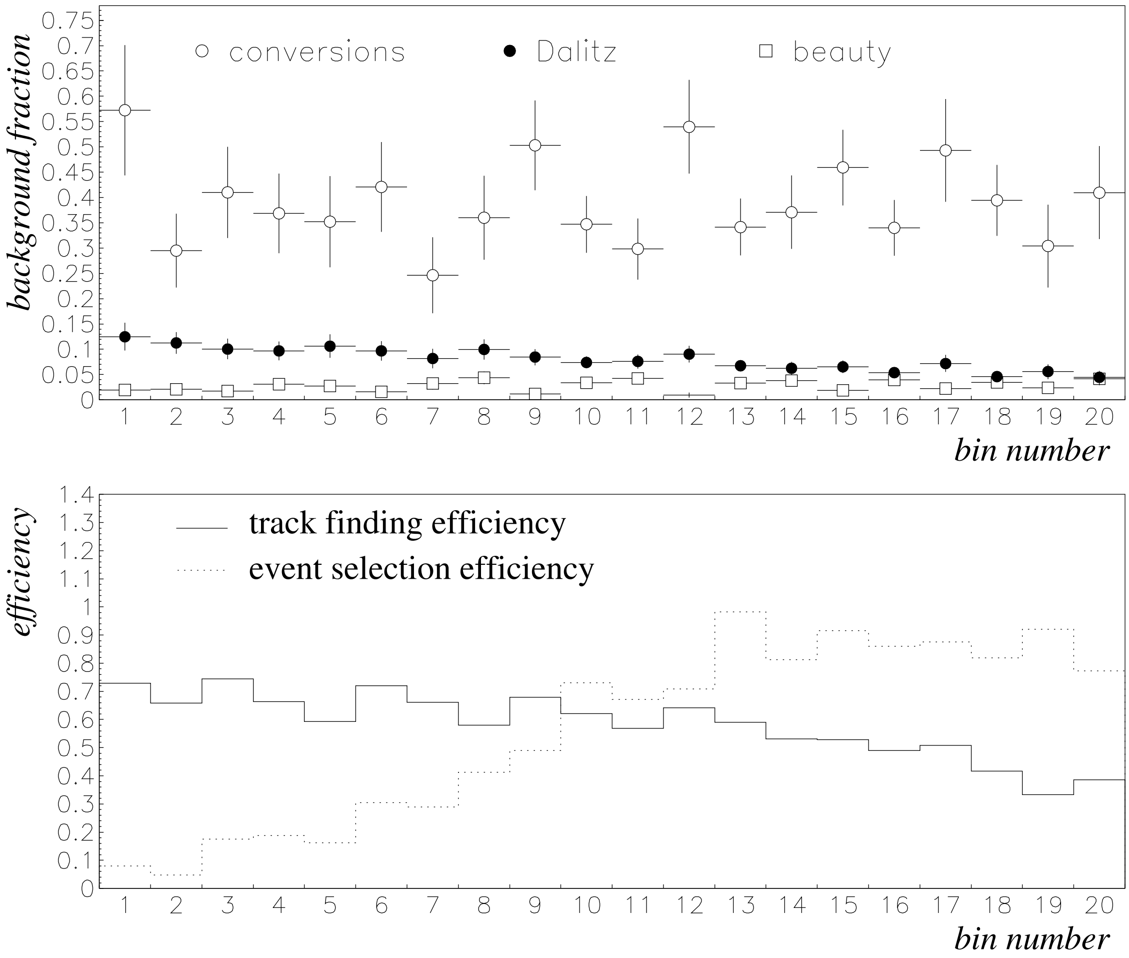

Figure 7.11: *The upper plot shows the contribution from the different electron background sources for each (x, Q^2) bin. The lower plot shows the event selection and track finding efficiency for each bin.*

7.5 Extraction of $F_2^{c\bar{c}}$

This section describes the unfolding procedure which is used to obtain $F_2^{c\bar{c}}$, the charm contribution to the proton structure function. The first two sections explain the binning in (x, Q^2) and how to extrapolate from the limited acceptance of the electrons from semileptonic decays to the full p and θ range. The third section describes the unfolding method and presents the resulting $F_2^{c\bar{c}}$. In the fourth section the systematic uncertainties in the different (x, Q^2) bins are discussed. The last section compares the results from the semileptonic decay analysis with those obtained from the D^* decay channel.

7.5.1 Binning in x and Q^2

In order to obtain the measured cross section in (x, Q^2) bins, the signal sample is binned according to Table 7.2. The bin size is optimized such that the number of electrons is roughly the same in each bin. Figure 7.10 shows the definition of the bins in the (x, Q^2) plane. The numbers indicate the bin number.

To obtain the electron signal for every bin the statistical subtraction procedure is performed in each bin. The dE/dx distribution for the signal and background sample in each (x, Q^2) bin can be found in Appendix C Figure C.1. Figure 7.12 shows the resulting inclusive electron signals.

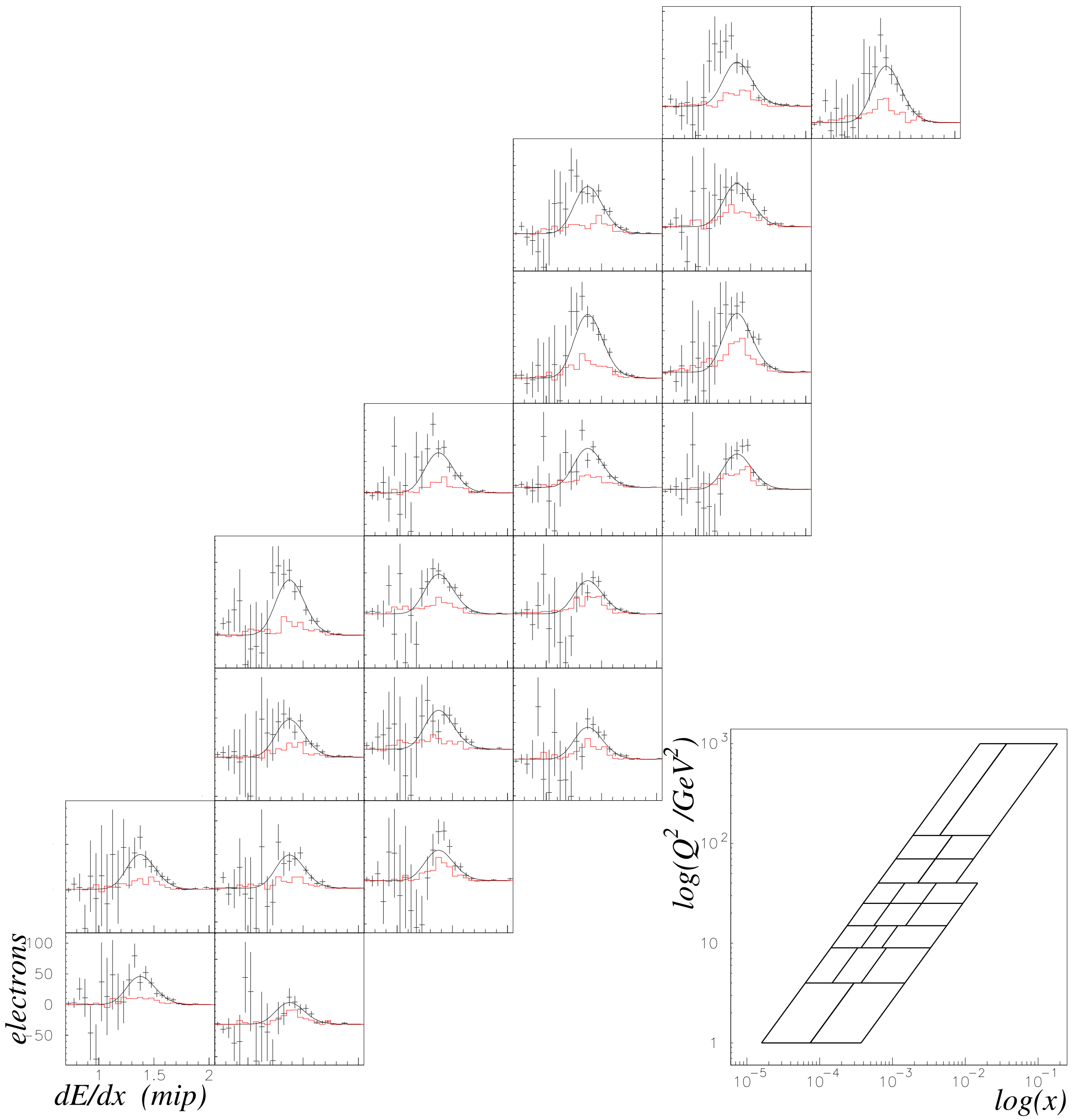

Figure 7.12: *The inclusive electron signal in (x, Q^2) bins. The background contribution from electrons from photon conversions is also shown. The lower right plot shows the bins in the (x, Q^2) plane.*

The background from electrons from photon conversions is also shown. A clear electron signal is obtained for each bin.

The contribution from the different electron background sources is shown in the upper plot of Figure 7.11. The contribution from the conversion electrons varies between 30 % and 50 %. In the low-Q^2 bins there is a tendency for the conversion background to be higher in the high-y bins.

The background from Dalitz decays of π^0s decreases towards higher Q^2 values as already observed in Figure 7.6 for the differential cross section in Q^2. The background from beauty decays rises towards higher values of y and it also rises towards higher Q^2 values.

The lower plot in Figure 7.11 shows the efficiencies for the different bins. The event selection

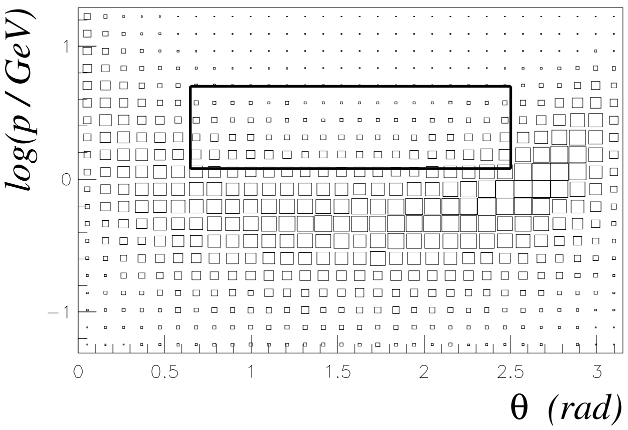

Figure 7.13: *The* $\log(p)$ *and* θ *distribution of electrons from semileptonic charm decays, calculated at NLO with the HVQDIS program,* $10 < Q^2 < 100\,GeV^2$ *and* $0.04 < y < 0.7$. *The acceptance region for the measurement is indicated by the solid lines.*

efficiency increases towards high Q^2 values and reaches about 80 %. The track finding efficiency drops towards high-y values within one Q^2 bin. The overall efficiency for the track finding varies between 70 % in the low-Q^2 region and 40 % in the high-Q^2 region.

7.5.2 Extrapolation of the Cross Section in p and θ

For the extraction of the charm contribution to the proton structure function, $F_2^{c\bar{c}}$, the total charm cross section is needed. Thus the measured cross section in the limited p and θ region must be extrapolated to the full phase space.
Figure 7.13 shows the polar angle versus the momentum of the electrons from semileptonic charm decays as calculated with the HVQDIS program. The black lines indicate the acceptance region. The lower momentum cut of 1.2 GeV cuts away most of the signal. Only about 10 % of all electrons are within the acceptance region for the overall kinematic range. The acceptance varies strongly with the kinematic region. Figure 7.14 shows the θ versus $\log(p)$ distribution for each (x, Q^2) bin. Towards higher Q^2 values the momentum of the electrons increases and more electrons are within the acceptance region, indicated by the solid lines. In the lower plot the acceptance for each bin is given.
The acceptance varies between 5 % and 25 %. Hence the measured cross section must be extrapolated by a factor 20 to 4, depending on the kinematic bin. The comparison between the measured and calculated differential cross sections for the limited acceptance region showed reasonable agreement. Using the results from HVQDIS program for the unfolding assumes that outside the acceptance region the data is described by the calculation.

7.5.3 Unfolding Procedure

The charm contribution, $F_2^{c\bar{c}}$, to the proton structure function F_2, is related to the double differential charm cross section by Equation 2.12 in Section 2.2.2. The contribution from $F_L^{c\bar{c}}$ to the cross section is estimated from NLO theoretical predictions [Rie95]. It is less than 1 % for

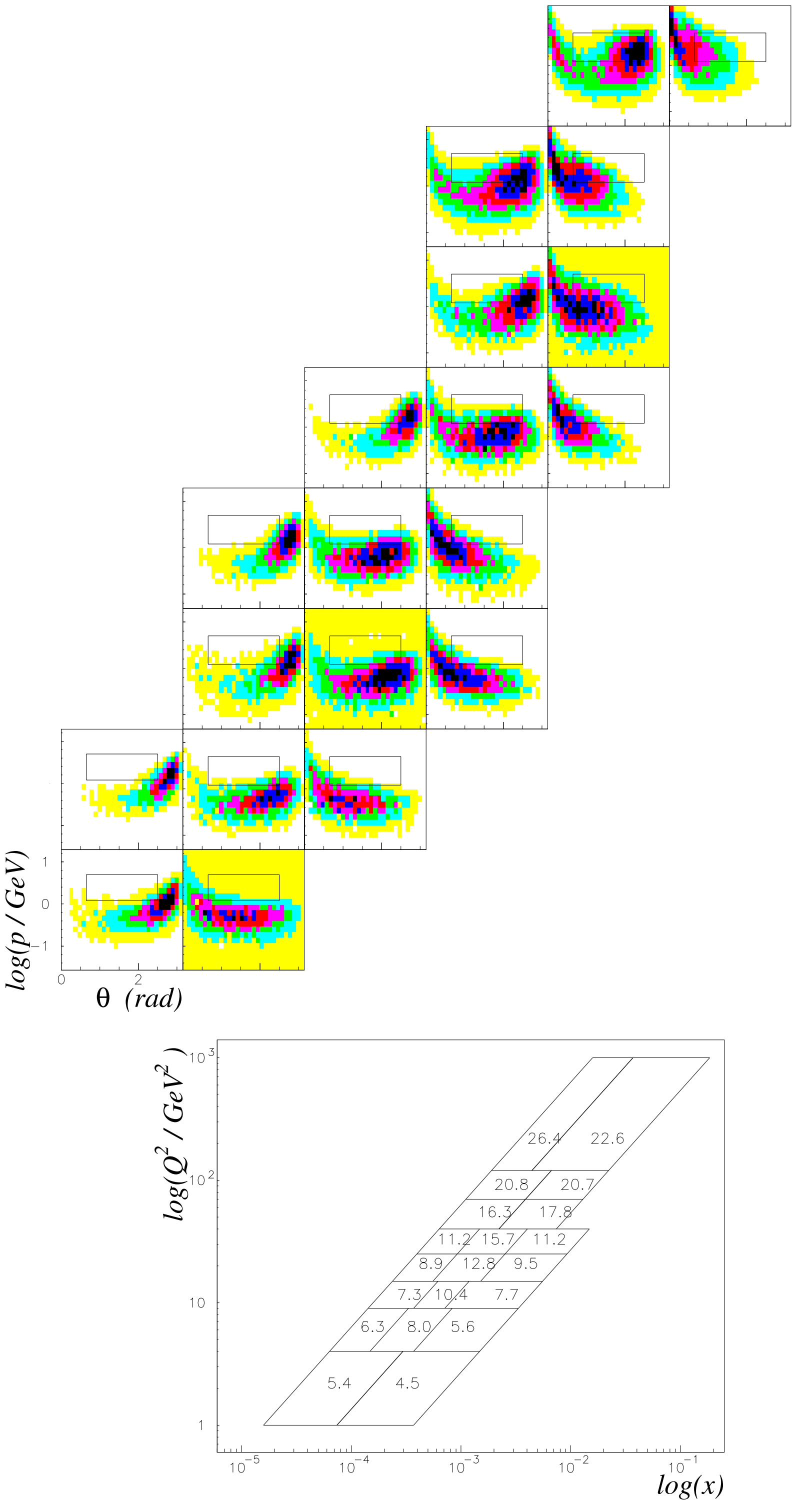

Figure 7.14: *θ versus $\log(p)$ for electrons from semileptonic decays in the different (x, Q^2) bins. Calculated at NLO with the HVQDIS program. The numbers in the different bins in the lower plot are the acceptances for each bin given in %.*

most of the kinematic region, and reaches up to 5 % at high y values. For the unfolding procedure any contribution from $F_L^{c\bar{c}}$ to the charm cross section can therefore be neglected. Within these approximations the following relation between the double differential cross section and $F_2^{c\bar{c}}$ is obtained:

$$\frac{d^2\sigma^{c\bar{c}}}{dxdQ^2} = \frac{2\pi\alpha^2}{xQ^4}(1+(1-y)^2)F_2^{c\bar{c}}(x,Q^2)\ . \tag{7.4}$$

To obtain the charm cross section, $\sigma^{c\bar{c}}$, the measured cross section has to be extrapolated to the full p and θ range as discussed above. Assuming a branching ratio of $BR(c \to e\nu X) = 9.5\,\%$ for the semileptonic decay of charmed hadrons into electrons, the total charm cross section in the respective kinematic region may be extrapolated.
The measured $F_2^{c\bar{c}}$ can be unfolded in the following way:

$$F^{c\bar{c}}_{2,measured}(x_i,Q_i^2) = \frac{\sigma^{bin\ i}_{measured}(e^+p \to e^+e^-X)}{\sigma^{bin\ i}_{theoretical}(e^+p \to e^+e^-X)} F^{c\bar{c}}_{2,theoretical}(x_i,Q_i^2)\ , \tag{7.5}$$

where x_i,Q_i^2 is the center of gravity of the bin i. The cross section, $\sigma^{bin\ i}_{measured}(e^+p \to e^+e^-X)$, is measured in the limited momentum and polar angular range of the electrons and it is not corrected back to the full charm cross section. The theoretical cross section is also obtained for the semileptonic decay into electrons in the limited phase space using the HVQDIS program at NLO. Hence the extrapolation factors are not directly used for the unfolding procedure, and are implicitly assumed to be correct. To calculate the cross sections with the HVQDIS program, the branching ratio of $BR(c \to e^-\nu X) = 9.5\,\%$ is used for the overall normalization of the charm cross section. The theoretical value of the structure function, $F^{c\bar{c}}_{2,theoretical}$, is calculated from NLO coefficient functions as implemented in [Rie95]. The same set of parameters is used for this calculation as for the HVQDIS calculations.

7.5.4 $F_2^{c\bar{c}}$ Results

Figure 7.15 shows the measured $F_2^{c\bar{c}}$ as a function of x at the different Q^2 values. The solid line is the theoretical prediction, as used for the unfolding procedure. The dotted lines indicate the effect of the variation of the charm mass by $\pm\,0.2$ GeV. The inner error bars refer to the statistical error only, and the outer ones to the combined statistical and systematic error, which are added in quadrature. The scale is the same for all plots. The impact of the different systematic uncertainties on the systematic error will be discussed in more detail in the next section. The dashed line shows the theoretical prediction for $F_2^{c\bar{c}}$ using the CTEQ parameterization (CTEQ4M) for the parton density functions instead of the GRV model. In the kinematic region of this analysis the theoretical $F_2^{c\bar{c}}$ varies by up to 10 % when changing to a different parton density function. Overall a good agreement between the measured $F_2^{c\bar{c}}$ values and the theoretical prediction is observed. The values for the measured data points and the full error can be found in Appendix C, Table C.1.
The structure function, $F_2^{c\bar{c}}$, rises towards low values of x. The rise becomes steeper with increasing Q^2. This behaviour shows the direct dependency of the charm production process on the gluon density of the proton. Figure 2.6 in Section 2.1.6 shows the same behaviour of the gluon density as a function of x for different Q^2 values. The data seem to favour a steeper rise than the theoretical prediction, but still agree within errors. In the highest Q^2 bin the data are systematically above the prediction. This behaviour will be further investigated in the next section.
Figure 7.16 shows the measured $F_2^{c\bar{c}}$ versus Q^2 at different values of x. To obtain the measured $F_2^{c\bar{c}}$ values at the fixed x values, the unfolding procedure (Equation 7.5) was repeated with slightly shifted x values. The solid lines correspond to the theoretical prediction and the dotted lines to the uncertainty due to the charm mass. The $F_2^{c\bar{c}}$ values are scaled by 4^i, where i corresponds to the value of x_i. Except for the highest Q^2 bin, the agreement between the data

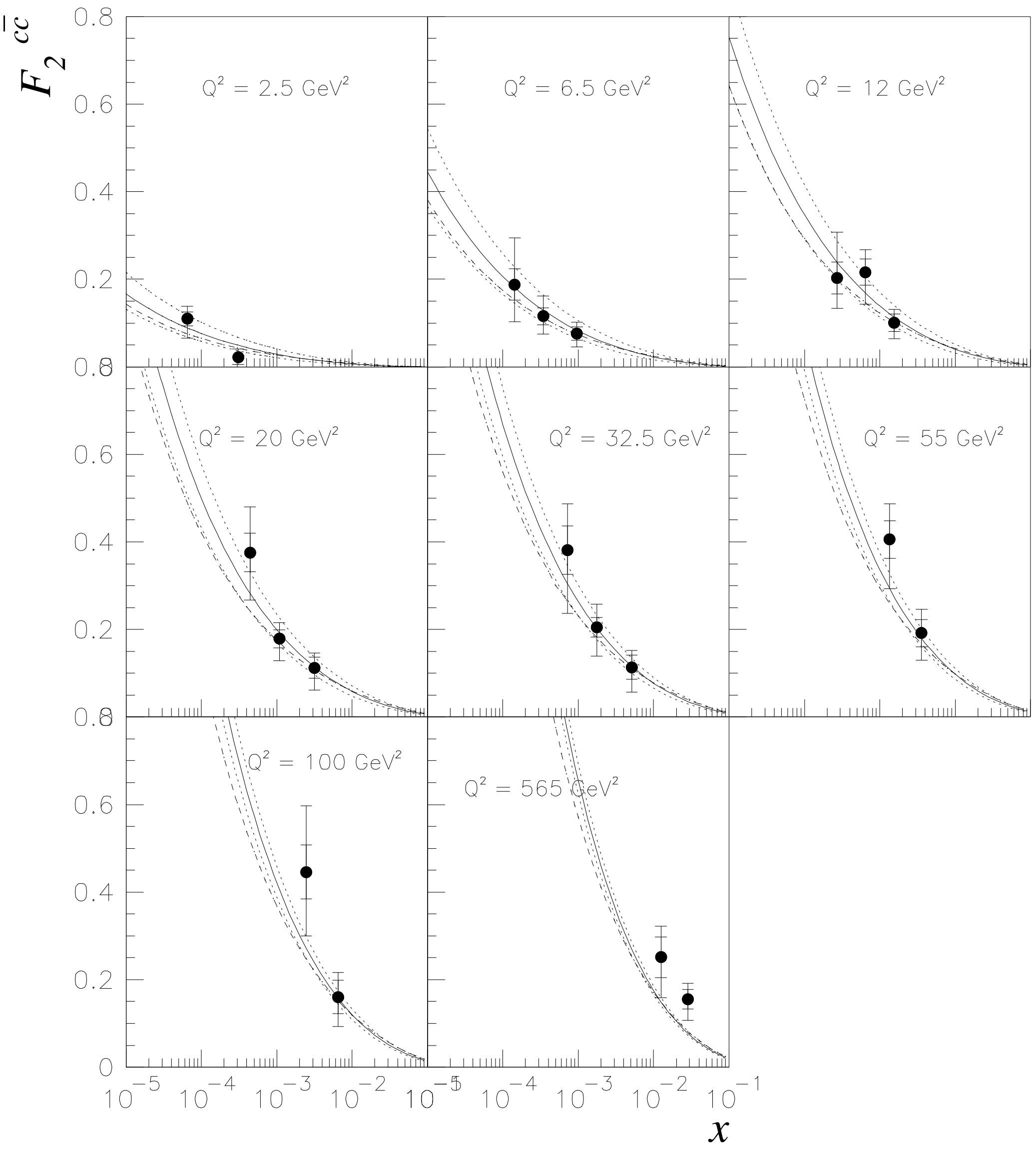

Figure 7.15: $F_2^{c\bar{c}}$ *as a function of* x *for different values of* Q^2. *The solid line is the theoretical prediction which was used as input for the unfolding procedure [Rie95]. The charm mass was set to* $1.5\,GeV$ *and for the parton density function the GRV parameterization was used. The dotted lines indicate the uncertainty due to a variation of the charm mass by* $\pm 0.2\,GeV$. *The dashed line corresponds to the theoretical prediction using the CTEQ4M parameterization for the parton density function and a charm mass of* $1.5\,GeV$.

and the theoretical prediction is good. Violation of scaling with Q^2 of the measured charm structure functions can be seen.

To show the charm contribution to the inclusive proton structure function F_2 the ratio of $F_2^{c\bar{c}}$ to F_2 is calculated. The F_2 values are taken from the ZEUS NLO QCD fit to F_2 as described in [Br99A]. Figure 7.17 shows the ratio $F_2^{c\bar{c}}/F_2$ as a function of x for different Q^2 values. The curves correspond to the ZEUS NLO QCD fits. The solid line uses 1.25 GeV as value for the charm mass. To be in agreement with the measured data points, the $F_2^{c\bar{c}}$ values are unfolded

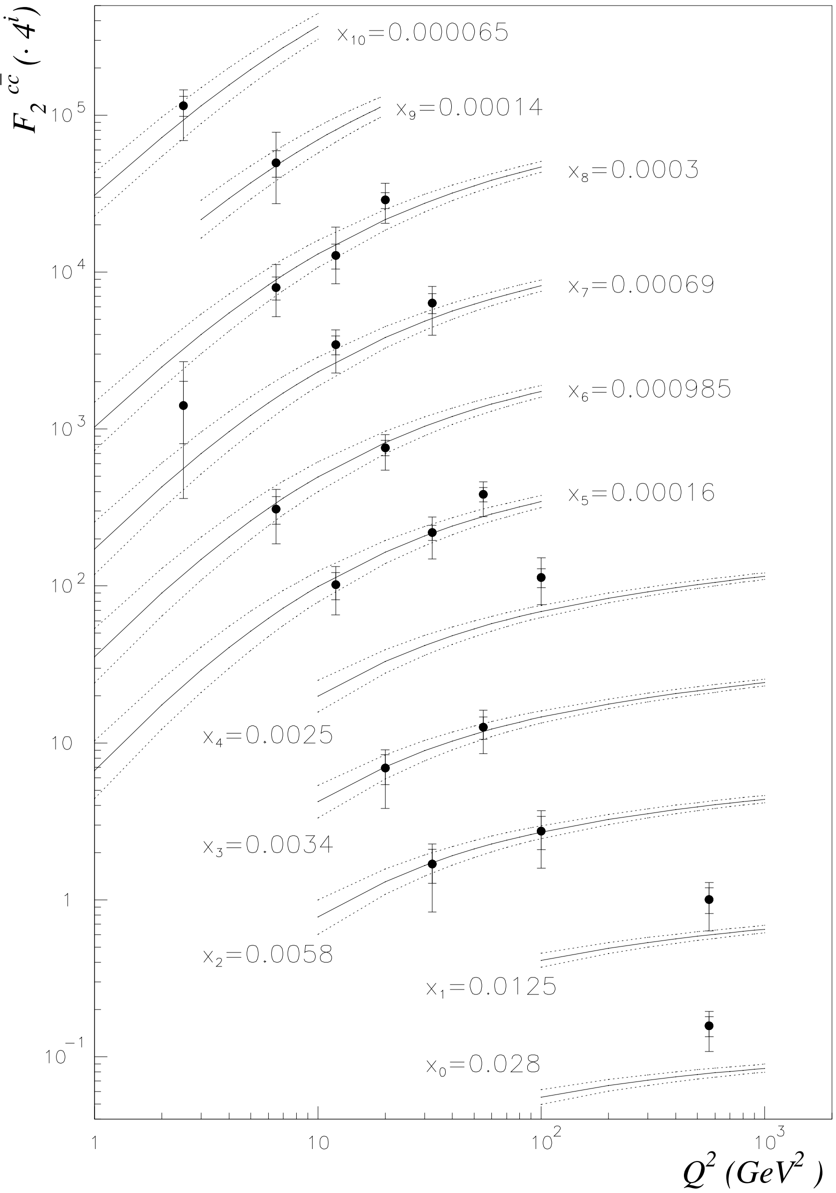

Figure 7.16: *$F_2^{c\bar{c}}$ as a function of Q^2 for fixed x values. For clarity of presentation, the $F_2^{c\bar{c}}$ values have been scaled by 4^i, where $i = 0, 1, ..., 10$ corresponds to the different x_i values. The solid line is the theoretical prediction which was used as input for the unfolding procedure [Rie95]. The charm mass was set to $1.5\,GeV$ and for the parton density function the GRV parameterization was used. The dotted lines indicate the uncertainty due to a variation of the charm mass by $\pm\,0.2\,GeV$.*

using a charm mass of $m_c = 1.25$ GeV. The dotted lines correspond to a charm mass variation between $m_c = 1.1$ and $m_c = 1.4$ GeV. It can be seen that the charm contribution to the inclusive proton structure function increases towards low x. In the low-Q^2 region $F_2^{c\bar{c}}$ contributes about 10 %. The fraction $F_2^{c\bar{c}}/F_2$ increases towards high Q^2 values, and reaches 30 % at Q^2 of 565 GeV^2.

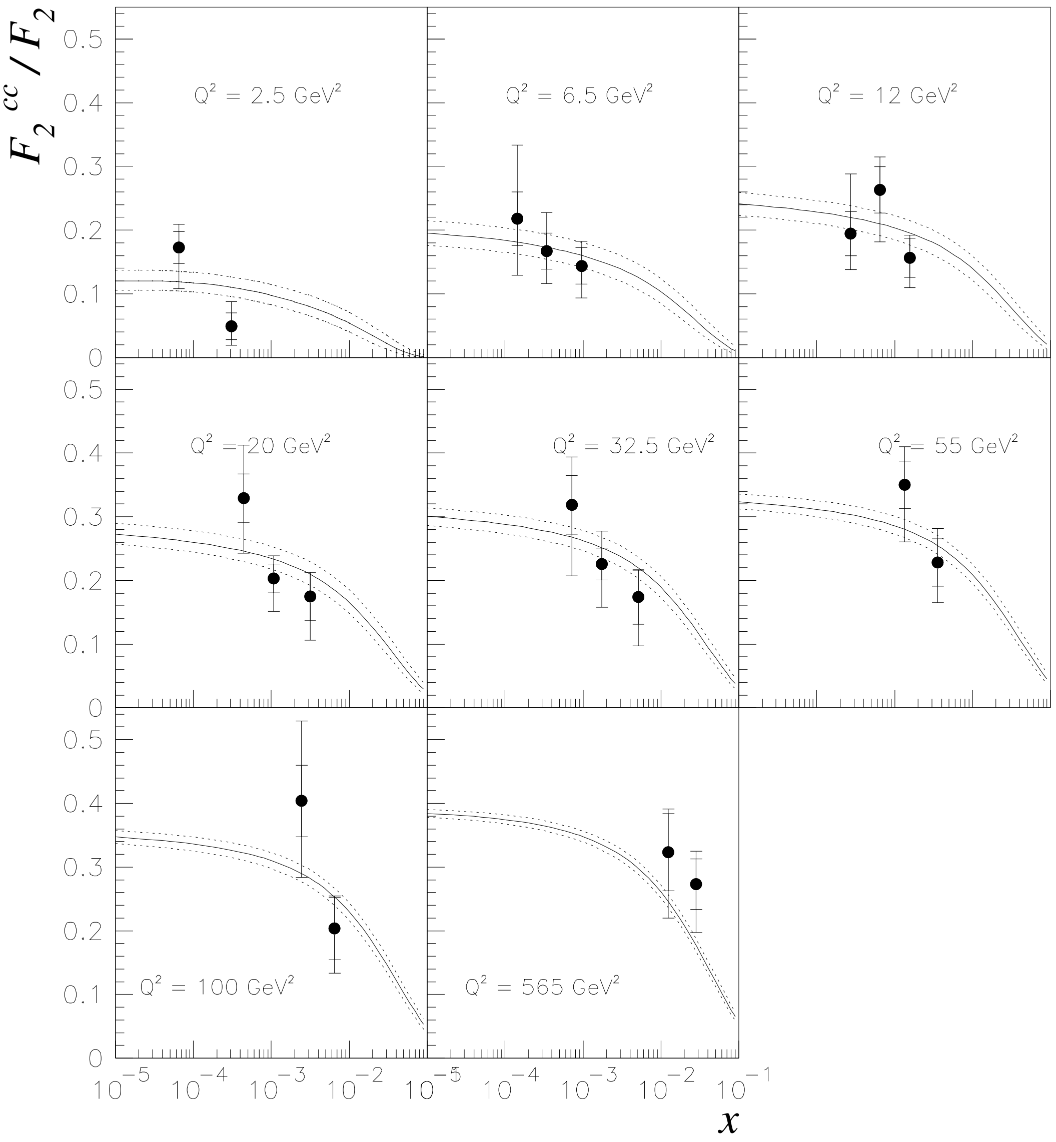

Figure 7.17: *The ratio of $F_2^{c\bar{c}}$ to F_2 as a function of x at different Q^2 values. The F_2 values are obtained from the ZEUS NLO QCD fit to F_2 as described in [Br99A]. The curves correspond to the ZEUS NLO QCD fits. The solid line is obtained using a charm mass of* 1.25 GeV, *the dotted line correspond to $m_c = 1.1$ and $m_c = 1.4\,GeV$.*

7.5.5 Systematic Effects in (x, Q^2) Bins

The contribution to the systematic error of the different systematic uncertainties is shown in Figure 7.19. The bin number corresponds to the (x, Q^2) bin as defined in Table 7.2.

The dominating uncertainty originates from the variation of the dE/dx cut value. This is caused by the fluctuations of the dE/dx distribution of the electron signal after the statistical subtraction. The measured $F_2^{c\bar{c}}$ values are shifted by up to 20 %. The effect of this dE/dx cut variation on the overall signal for the cross section measurement is below 2 % due to the cleaner signal. Another significant contribution stems from the variation of the momentum range. The

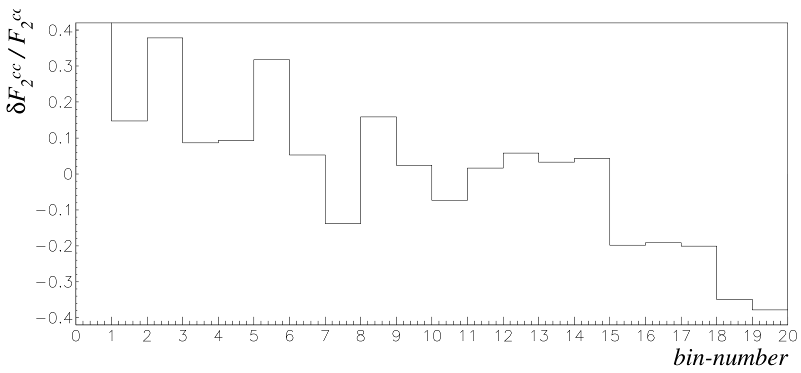

Figure 7.18: *The variation of the measured $F_2^{c\bar{c}}$ values, using the background sample corresponding to the kinematic bin instead of the overall background sample.*

lower bins, where the extrapolation factors are large, are particularly sensitive to this variation. The measured $F_2^{c\bar{c}}$ values are above the theoretical prediction in the high-Q^2 range. The same effect is observed for the differential cross section as a function of Q^2. In addition the $F_2^{c\bar{c}}$ values measured in the high-y region tend to be systematically higher than the prediction from theory. A likely reason for these effects is the different distribution of tracks due to the event kinematics. The number of tracks per event is high for high-y events, and decreases towards low y. In addition there is a Q^2 dependence, such that the number of tracks per event rises with increasing Q^2. The multiplicity distribution for events, which have at least one signal sample track, can be found in Appendix C Figure C.2 for the different (x, Q^2) bins. Also shown is the multiplicity distribution for the background sample events, which is the same for each bin. Assuming the isolation correction of dE/dx obtained for the overall y and Q^2 range is not perfect, the results may be systematically shifted, due to the different multiplicity distributions of the signal and background samples.
To have better agreement of the multiplicity distribution between signal and background sample events, the background sample tracks should only be taken from the corresponding kinematic bin. Due to the smaller statistics of the background sample, the quality of the resulting electron signal decreases (see Appendix C, Figure C.3). Figure 7.18 shows the shift of the $F_2^{c\bar{c}}$ values, when only tracks from the corresponding bin are taken for the background sample instead of using all tracks. A tendency is visible of the $F_2^{c\bar{c}}$ values to shift towards lower values in the high-Q^2 and high-y bins. However, since the signals obtained with the smaller bin-by-bin background samples show large statistical fluctuations, this additional uncertainty is not added to the systematic errors.

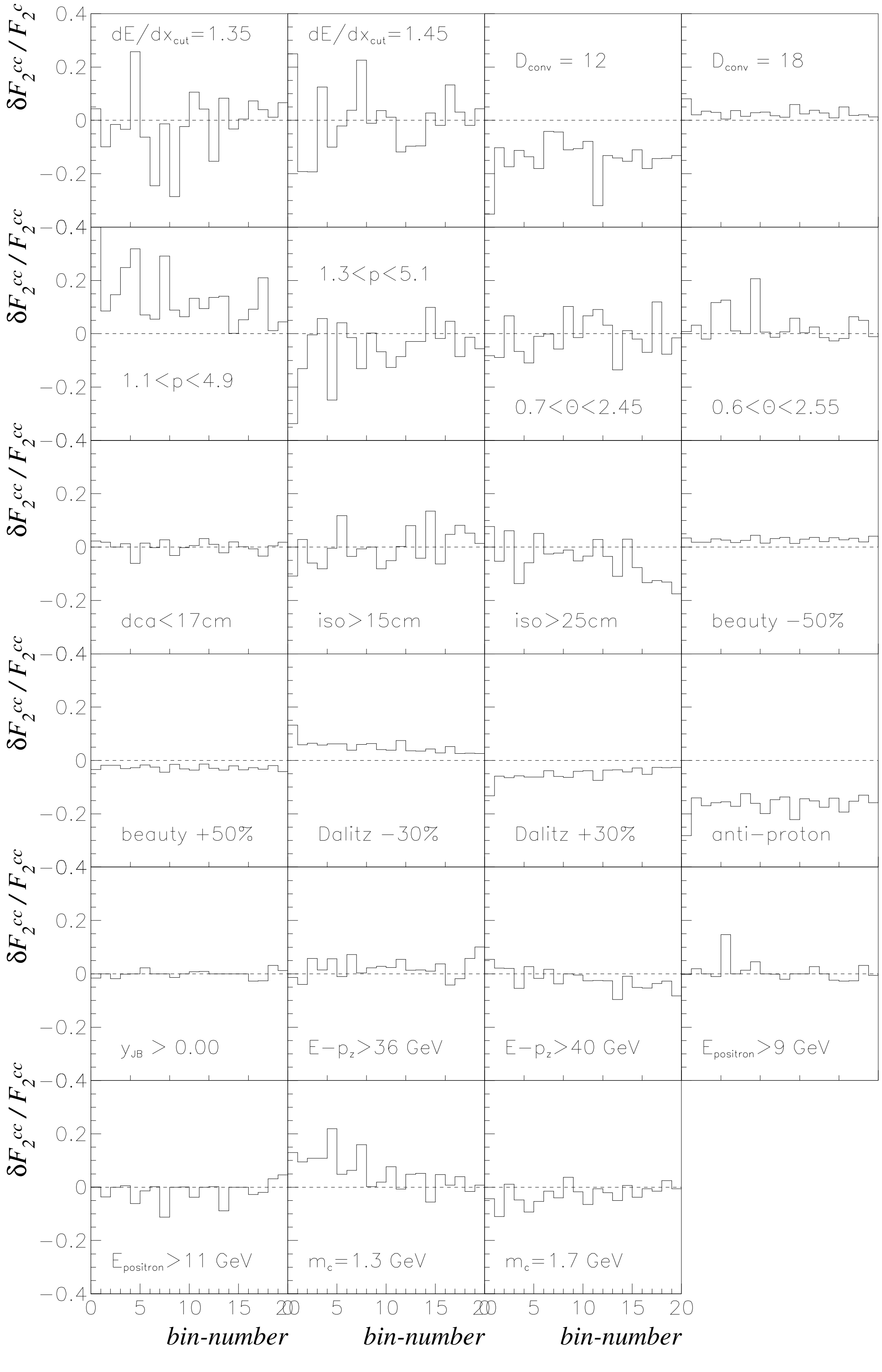

Figure 7.19: *The individual systematic errors in (x, Q^2) bins.*

7.5.6 Comparison with D^* Results

Finally the measured $F_2^{c\bar{c}}$ values are compared to those obtained via the D^* decay channel [Br00A]. The D^* analysis method is described in more detail in Section 6.1.

The results from the $(K\pi\pi_s)$ and the $(K\pi\pi\pi\pi_s)$ channel were combined in the bins common to both analyses. Figure 7.20 shows the resulting $F_2^{c\bar{c}}$ values from the D^* decay channel in the common Q^2 bins with the semileptonic charm analysis. The Q^2 values for the D^* channel are given in parentheses. For the unfolding of $F_2^{c\bar{c}}$ from the D^* channel, a charm mass of $m_c = 1.4\,\mathrm{GeV}$ was used as theoretical input for the unfolding procedure. The agreement between the two independent decay channels is good.

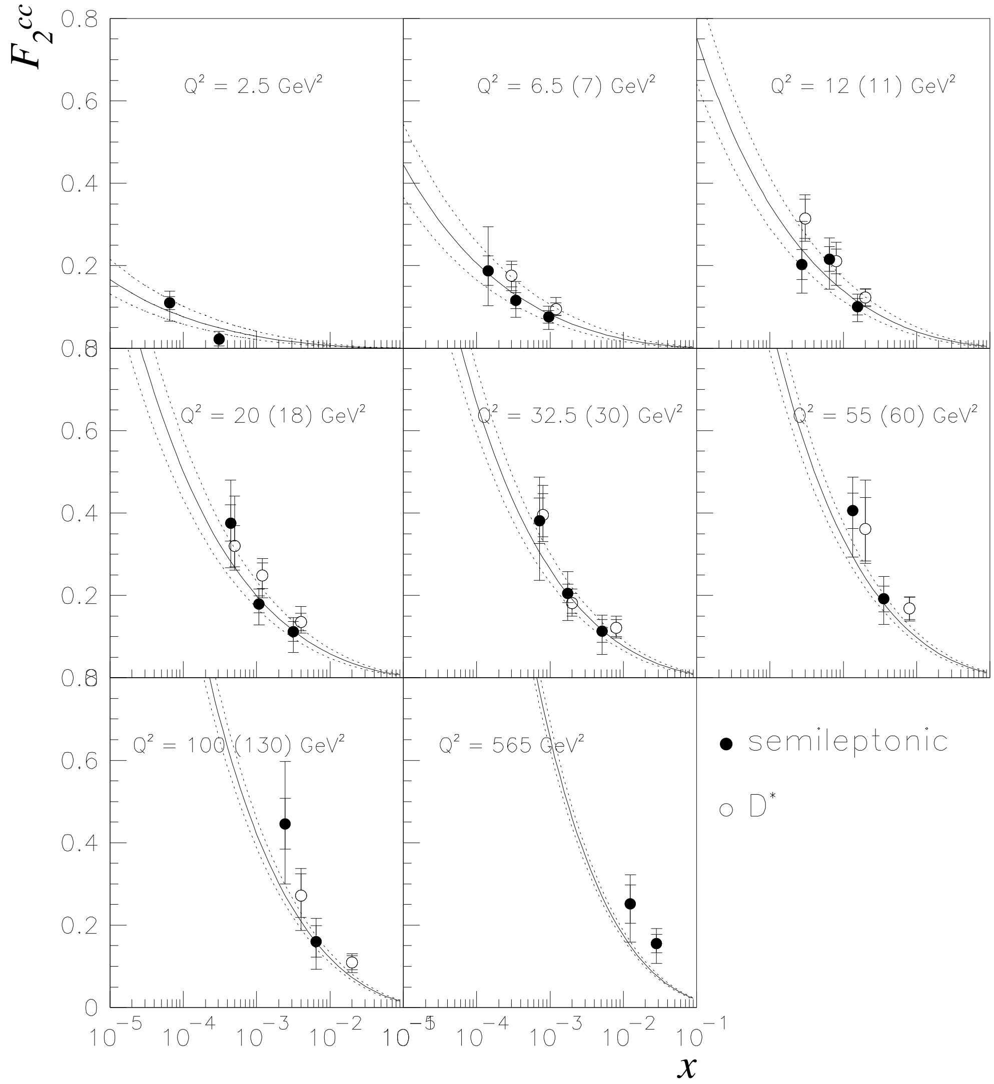

Figure 7.20: *The measured $F_2^{c\bar{c}}$ values as a function of x in different Q^2 bins. The curves correspond to the theoretical prediction calculated with $m_c = 1.5\,GeV$ (solid line) and $m_c = 1.5 \pm 0.2\,GeV$ (dotted lines). Also shown are the results from the D^* decay channel, which were obtained using $m_c = 1.4\,GeV$ for the unfolding procedure. The different Q^2 values for the D^* decay channel are given in parentheses.*

The semileptonic channel has the advantage of the higher branching ratio. Considering the smaller overall acceptance of between 5 % to 25 % compared to 25 − 65 % in case of the $(K\pi\pi_s)$ channel, the effective gain in statistics is about a factor five. This decreases further due to the method itself, mainly the dE/dx cut, which reduces the signal by another 50 %. The remaining advantage of the higher statistics for the semileptonic decay channel suffers from the large systematic uncertainties, which are about two times higher than the statistical error. Due to the clean signature of the D^* decays the systematic uncertainties in that channel are smaller, and are of the same order as the statistical errors.
Both methods used the NLO calculation performed with the HVQDIS program for the extrapolation to the full charm cross section. However, in case of the D^* decay channel a modified version was used. The differential cross sections for $D^{*\pm}$ production as a function of $\eta(D^*)$ and $x(D^*)$ showed significant disagreement with the theoretical prediction from the HVQDIS program. $x(D^*)$ is the fractional momentum of the D^* in the $\gamma\, p$ center-of-mass frame, $x(D^*) = 2|\vec{p}^*(D^*)|/W$, where $\vec{p}^*(D^*)$ is the D^* momentum in the $\gamma\, p$ center-of-mass frame. The calculations showed a shift with respect to the data to larger $x(D^*)$ values and an excess of the data in the forward η region when compared to the calculations [Br00A]. This effect was presumed to be a result of the use of the Peterson fragmentation function. No interactions between the colour charges of the c quark and the proton remnant are taken into account, which is called 'beam-drag effect' [Br00A,Nor99]. To account for these fragmentation effects, RAPGAP charm quark distributions were reweighted to match the charm quark distributions as calculated with HVQDIS. Hence the resulting HVQDIS distribution used the simulation of the fragmentation as implemented in RAPGAP, which includes parton shower evolution. The resulting differential cross sections gave a better description of the data, and were used for the extrapolation to the full charm cross section.
The differential cross section in η of the electrons from semileptonic charm decays also shows a tendency to be above the HVQDIS prediction in the forward region, but it is an insignificant effect, and hence no further corrections have been applied.

7.6 Summary of Results

In this chapter the results obtained for the cross sections, differential cross sections and $F_2^{c\bar{c}}$ are presented. The cross sections are found to agree in absolute value and in shape with the theoretical predictions from NLO QCD calculations for charm production, which are based on the boson-gluon-fusion process with three flavours of massless light quarks. The measured charm contribution to the proton structure function $F_2^{c\bar{c}}$ rises towards low values of x, whereas the rise becomes steeper with increasing Q^2. This shows the direct correlation of charm production with the gluon density of the proton due to the boson-gluon-fusion process being the predominant production mechanism. The agreement of the measurement with the theoretical predictions confirms the factorization theorem, whereby the same gluon density of the proton describes the inclusive F_2 and the charm production in DIS events (see Section 2.2.2).
The semileptonic decay analysis also shows good agreement with the measurement performed by ZEUS using the D^* channel. The agreement of the results shows the reliability of this completely independent decay channel.
However, the method is dominated by systematic uncertainties. One of the dominating systematic effects, the variation of the dE/dx cut, depends on the statistics of the signal. Hence, the measurement could be improved in the future with more luminosity. A systematic shift of the data with respect to the theoretical prediction in the high Q^2 and high y region is found. This may be attributed to the multiplicity dependence of dE/dx. The obtained correction function

is obtained for the overall sample. Due to limited statistics it is not possible to obtain different correction functions for the different kinematic regions separately. An increase in luminosity would allow to improve this correction procedure and thereby improving the results.

Chapter 8

Summary and Conclusions

In this thesis a measurement of charm production in deep-inelastic ep scattering events has been presented. Differential cross sections and $F_2^{c\bar{c}}$, the charm contribution to the proton structure function, were calculated. The data was taken with the ZEUS detector during 1996/97 and amounts to an integrated luminosity of $34.04\,\mathrm{pb}^{-1}$.

The reconstruction and selection of the DIS events followed the standard procedures, which have also been used in inclusive F_2 analyses. The selection of events with charm production was made using the semileptonic decay of charmed hadrons into electrons. An inclusive electron signal was obtained using the energy loss (dE/dx) information measured with the central tracking detector (CTD). Special emphasis was put on the understanding of dE/dx. After several corrections had been applied during reconstruction a dependency of the energy loss on the polar angle of the track and on the track multiplicity was observed. Correction functions for these two effects were obtained from the data. For $p_{track} > 1.2\,\mathrm{GeV}$ the measured energy loss dE/dx allowed electrons to be distinguished from hadrons. Due to most tracks being hadronic a statistical subtraction procedure, using the information of calorimeter clusters matched to the tracks, was performed to obtain an electron signal.

Only the charm decay into electrons, $\bar{c} \to e^- \bar{\nu}_e X$ was analysed. The analysis method is not applicable to the decay into positrons, due to the different hadron compositions of the two samples which were used for the statistical subtraction.

The obtained electron signal consisted of only about 50 % electrons from semileptonic charm decays. Almost 40 % of the signal arose from photon conversions, $\gamma \to e^+e^-$. Due to their decay signature, they can be identified effectively using a topological conversion finder. Further background of about 8 % came from Dalitz decays of π^0 mesons. Their contribution to the electron signal was estimated from track multiplicities in data. The third source of background electrons was beauty decays. Using Monte Carlo data they were estimated to contribute about 4 % to the overall signal.

Cross sections for charm production with semileptonic decays of the charm quarks were measured in the two kinematic ranges $1 < Q^2 < 1000\,\mathrm{GeV}^2$ and $10 < Q^2 < 200\,\mathrm{GeV}^2$ with $0.03 < y < 0.7$ for both regions. The results of $532 \pm 27^{+40}_{-96}\,\mathrm{pb}$ and $226 \pm 12^{+14}_{-34}\,\mathrm{pb}$ agree within errors with theoretical predictions from NLO calculations. The acceptance of the electrons was limited to $1.2 < p_{electron} < 5.0\,\mathrm{GeV}$ and $0.65 < \theta_{electron} < 2.5\,\mathrm{rad}$.

Differential cross sections as a function of W, Q^2, x, $p_{t\ electron}$ and $\eta_{electron}$ were presented. The agreement within errors with theoretical predictions from NLO calculations was reasonable.

The charm contribution to the proton structure function $F_2^{c\bar{c}}$ was calculated, and was presented as a function of x at different Q^2 values, as well as a function of Q^2 at different x values. The measurement agreed within errors with theoretical predictions and with the measurement made by ZEUS using the D meson decay channel. The ratio of $F_2^{c\bar{c}}$ to F_2 as a function of x was presented. The F_2 values were obtained from a ZEUS NLO QCD fit. The charm contribution to the inclusive proton structure function rises towards low x and high Q^2 and can be as high as 30 %. The overall agreement between the measurement and the predictions from NLO calculations provides a consistency test of perturbative QCD and demonstrates the universality of the gluon density of the proton.

The agreement of the results from the semileptonic decay analysis with those obtained from the D meson decay channel, using the same data set, demonstrates the reliability of this completely independent and different method. The statistics of the semileptonic decay channel are better than in case of the D meson decays. However, the semileptonic analysis suffers from large systematic errors. These are mainly caused by the limited acceptance of the electrons and fluctuations of the electron dE/dx distribution. A systematic shift is observed in the high-Q^2 region. This may be attributed to the dE/dx correction for the multiplicity dependence.

With the increased luminosity expected after the HERA upgrade, it should be possible to reduce the systematic uncertainties thanks to the better statistics which will be available to obtain the correction functions. In addition an extension of the kinematic range, for instance towards higher Q^2 values, should be possible. Already during 1998 a new DIS trigger was developed to select semileptonic charm decay events. This improved in particular the low-Q^2 region, which suffered from the prescale on the inclusive DIS trigger during 1996/97.

Another future prospect could be the measurement of beauty production in DIS events. Beauty decays were treated as background in this analysis, but contribute about 4 % to the inclusive signal. A beauty measurement has been already performed in the photoproduction region, for $Q^2 \approx 0\,\mathrm{GeV}^2$ [Wi99A, Wi99B], using the same electron identification method as in this thesis. If one measures differential cross sections as a function of the transverse momentum of the electrons relative to a jet axis, it is possible to separate beauty and lighter quark decays. Beauty decays are expected to produce electrons with higher transverse momentum relative to the jet due to the larger mass.

Thus this thesis presented an alternative charm measurement, which was found to yield compatible results to the D^* method. Furthermore the kinematic range is extendable with increasing luminosity in the future, and the same method may be used to measure beauty cross sections.

Appendix A

QED Calculation for Pair Production by Tsai

The cross section for photons with momentum k producing an electron with momentum $p_{e^-} = x \cdot k$ and a positron with momentum $p_{e^+} = k - p_{e^-}$ is given by:

$$\begin{aligned}
\frac{d\sigma}{dp} &= \frac{\alpha r_0^2}{k}\left(\left[\frac{4}{3}x^2 - \frac{4}{3}x + 1\right]\left[Z^2(\Phi_1 - \frac{4}{3}\ln Z - 4f) + Z(\Psi_1 - \frac{8}{3}\ln Z)\right]\right) \\
&\quad -\frac{2}{3}\frac{\alpha r_0^2}{k}x(1-x)\left[Z^2(\Phi_1 - \Phi_2) + Z(\Psi_1 - \Psi_2)\right] \ , \qquad \text{(A.1)}
\end{aligned}$$

$$\begin{aligned}
Z &: \text{atomic number, } Z \geq 5 \ , \\
\alpha &: \text{fine structure constant} \ , \\
r_0 &: \text{classical electron radius} \ , \\
\Phi_1(\gamma) &= 20.863 - 2\ln\left[1 + (0.55846\gamma)^2\right] - 4[1 - 0.6e^{-0.9\gamma} - 0.4e^{-1.5\gamma}] \ , \\
\Phi_2(\gamma) &= \Phi_1(\gamma) - \frac{2}{3}(1 + 6.5\gamma + 6\gamma^2)^{-1} \ , \\
\Psi_1(\epsilon) &= 28.340 - 2\ln\left[1 + (3.621\epsilon)^2\right] - 4[1 - 0.7e^{-8\epsilon} - 0.3e^{-29.2\epsilon}] \ , \\
\Psi_2(\epsilon) &= \Psi_1(\epsilon) - \frac{2}{3}(1 + 40\epsilon + 400\epsilon^2)^{-1} \ , \\
f(z) &= z\sum_{n=1}^{\infty}\frac{1}{n(n^2+z)} \approx 1.202z - 1.0369z^2 + 1.008\frac{z^3}{1+z} \ , \\
\gamma &= \frac{100 m_e k}{E_{e^-}E_{e^+}Z^{1/3}} \ , \\
\epsilon &= \frac{100 m_e k}{E_{e^-}E_{e^+}Z^{2/3}} \ , \\
z &= \left(\frac{Z}{137}\right)^2 \ .
\end{aligned}$$

Appendix B

Signals for Differential Cross Sections

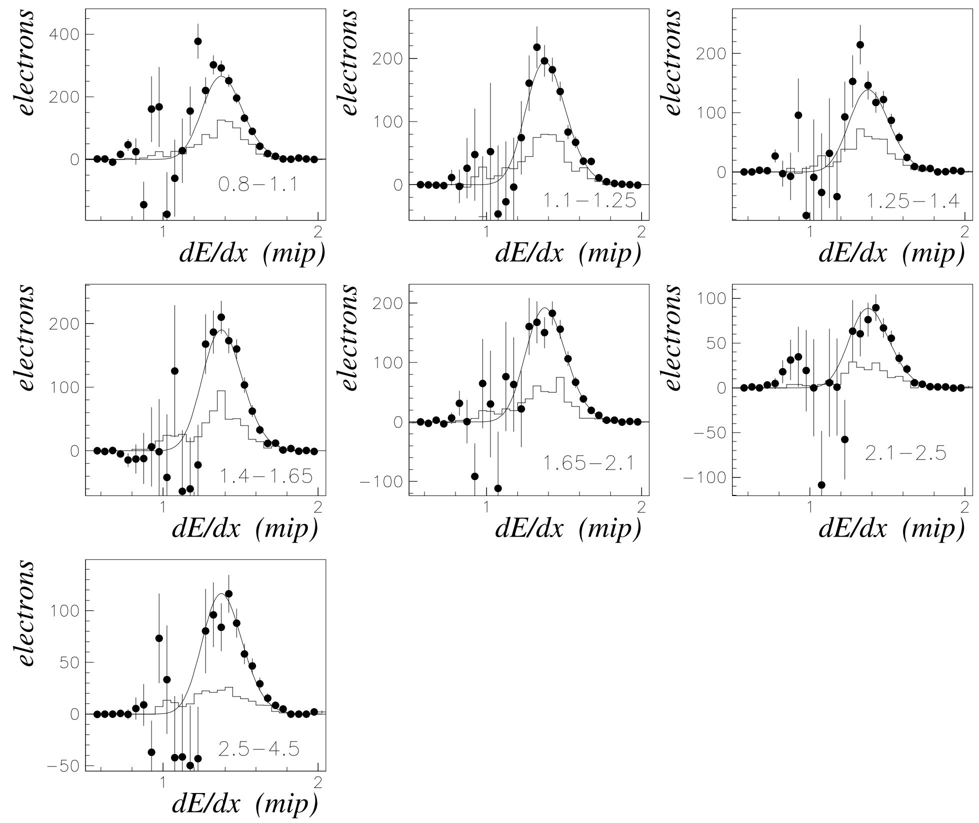

Figure B.1: *The inclusive electron signal in bins of p_t. The bin range in GeV is given in each plot. The background from electrons from photon conversions is also shown.*

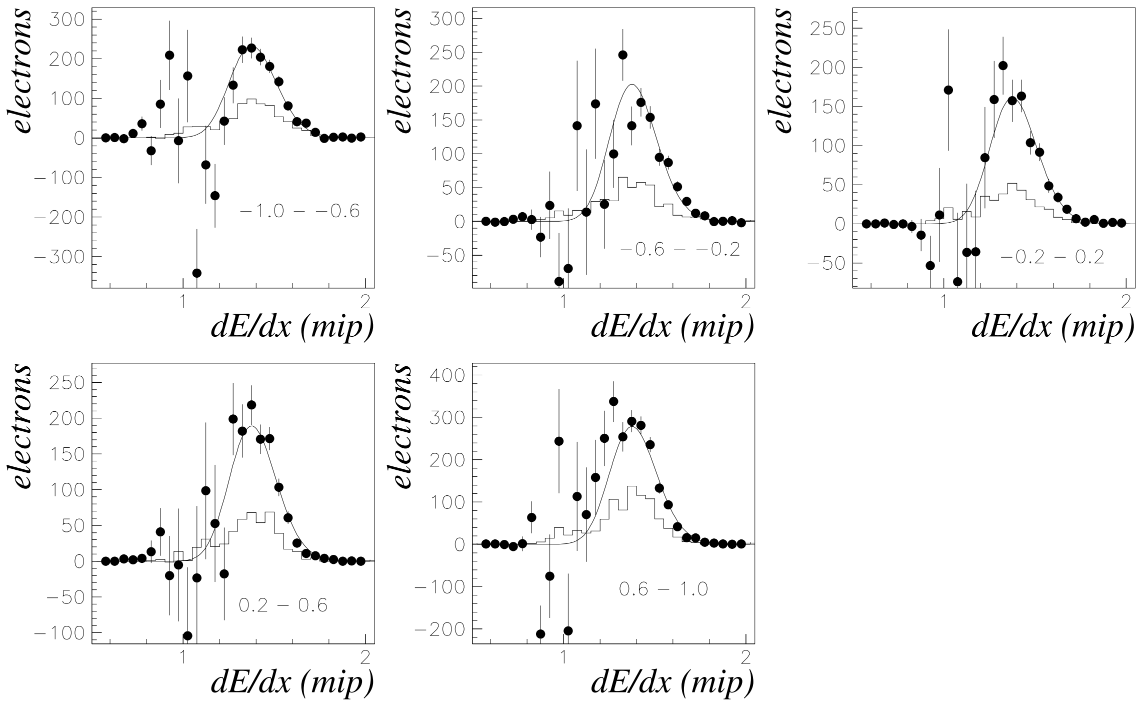

Figure B.2: *The inclusive electron signal in bins of* η*. The bin range is given in each plot. The background from electrons from photon conversions is also shown.*

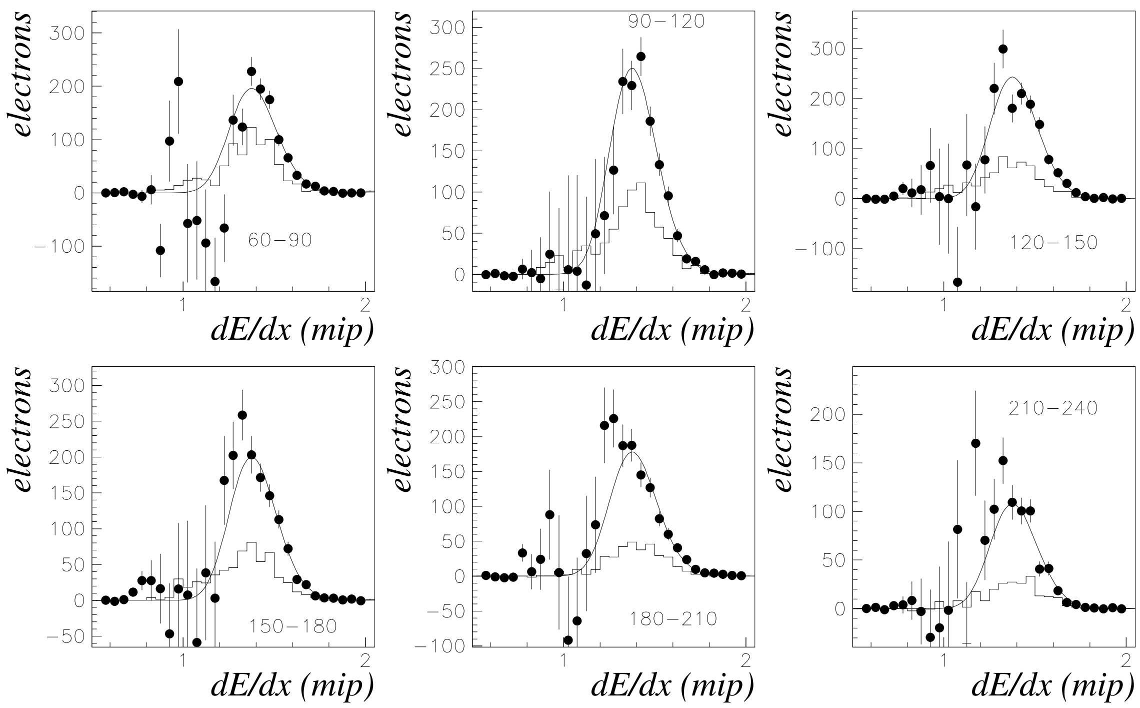

Figure B.3: *The inclusive electron signal in bins of* W*. The bin range in* GeV *is given in each plot. The background from electrons from photon conversions is also shown.*

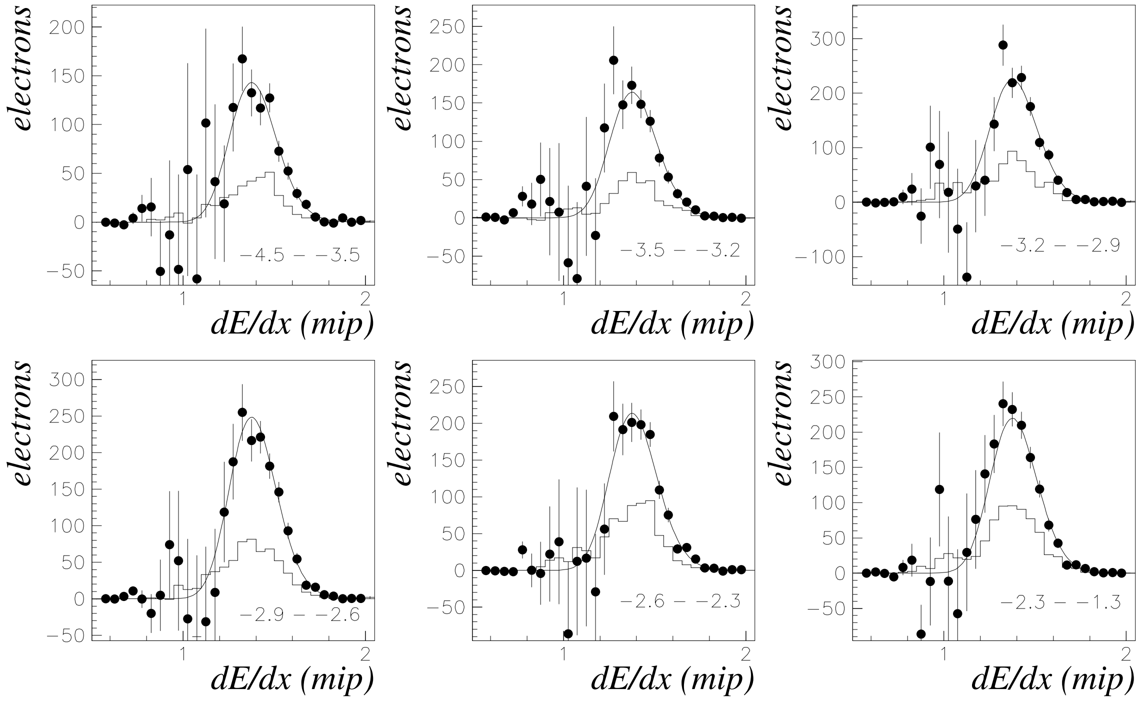

Figure B.4: *The inclusive electron signal in bins of x. The bin range in $\log(x)$ is given in each plot. The background from electrons from photon conversions is also shown.*

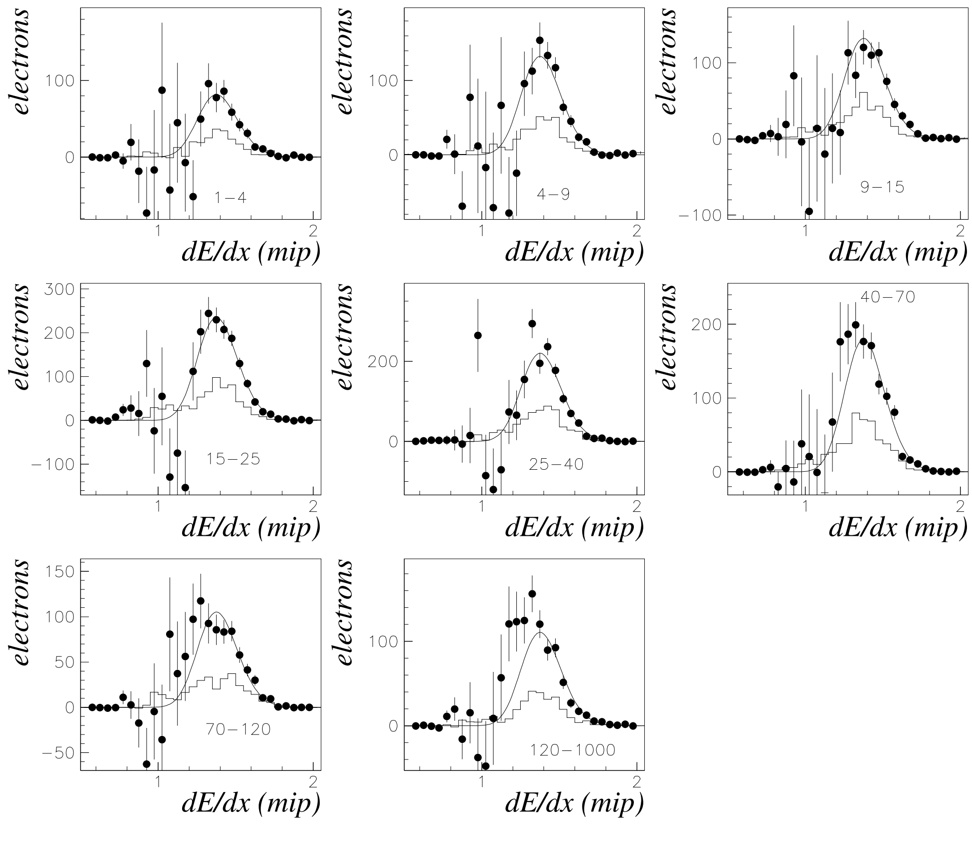

Figure B.5: *The inclusive electron signal in bins of Q^2. The bin range in GeV^2 is given in each plot. The background from electrons from photon conversions is also shown.*

Appendix C

Binning in (x, Q^2)

bin number	$Q^2/\,\mathrm{GeV}^2$	x	$F_2^{c\bar{c}}(x,Q^2)$
1	2.5	$3.1 \cdot 10^{-4}$	$0.021 \pm 0.009^{+0.019}_{-0.016}$
2	2.5	$6.5 \cdot 10^{-5}$	$0.110 \pm 0.016^{+0.028}_{-0.044}$
3	6.5	$9.6 \cdot 10^{-4}$	$0.076 \pm 0.015^{+0.026}_{-0.030}$
4	6.5	$3.4 \cdot 10^{-4}$	$0.115 \pm 0.019^{+0.046}_{-0.040}$
5	6.5	$1.4 \cdot 10^{-4}$	$0.188 \pm 0.036^{+0.106}_{-0.085}$
6	12.0	$1.6 \cdot 10^{-3}$	$0.101 \pm 0.020^{+0.030}_{-0.036}$
7	12.0	$6.5 \cdot 10^{-4}$	$0.216 \pm 0.030^{+0.052}_{-0.074}$
8	12.0	$2.7 \cdot 10^{-4}$	$0.203 \pm 0.036^{+0.104}_{-0.070}$
9	20.0	$3.2 \cdot 10^{-3}$	$0.112 \pm 0.024^{+0.034}_{-0.050}$
10	20.0	$1.1 \cdot 10^{-3}$	$0.178 \pm 0.020^{+0.038}_{-0.050}$
11	20.0	$4.4 \cdot 10^{-4}$	$0.376 \pm 0.044^{+0.104}_{-0.108}$
12	32.5	$5.1 \cdot 10^{-3}$	$0.114 \pm 0.028^{+0.039}_{-0.057}$
13	32.5	$1.8 \cdot 10^{-3}$	$0.205 \pm 0.023^{+0.052}_{-0.066}$
14	32.5	$7.2 \cdot 10^{-4}$	$0.381 \pm 0.055^{+0.106}_{-0.144}$
15	55.0	$3.6 \cdot 10^{-3}$	$0.191 \pm 0.031^{+0.055}_{-0.061}$
16	55.0	$1.4 \cdot 10^{-3}$	$0.405 \pm 0.043^{+0.082}_{-0.112}$
17	100.0	$6.5 \cdot 10^{-3}$	$0.161 \pm 0.038^{+0.056}_{-0.067}$
18	100.0	$2.5 \cdot 10^{-3}$	$0.446 \pm 0.062^{+0.152}_{-0.146}$
19	565.0	$2.8 \cdot 10^{-2}$	$0.155 \pm 0.022^{+0.037}_{-0.049}$
20	565.0	$1.2 \cdot 10^{-2}$	$0.251 \pm 0.047^{+0.071}_{-0.093}$

Table C.1: *The measured $F_2^{c\bar{c}}$ values. The first error corresponds to the statistical error, the second to the systematic error.*

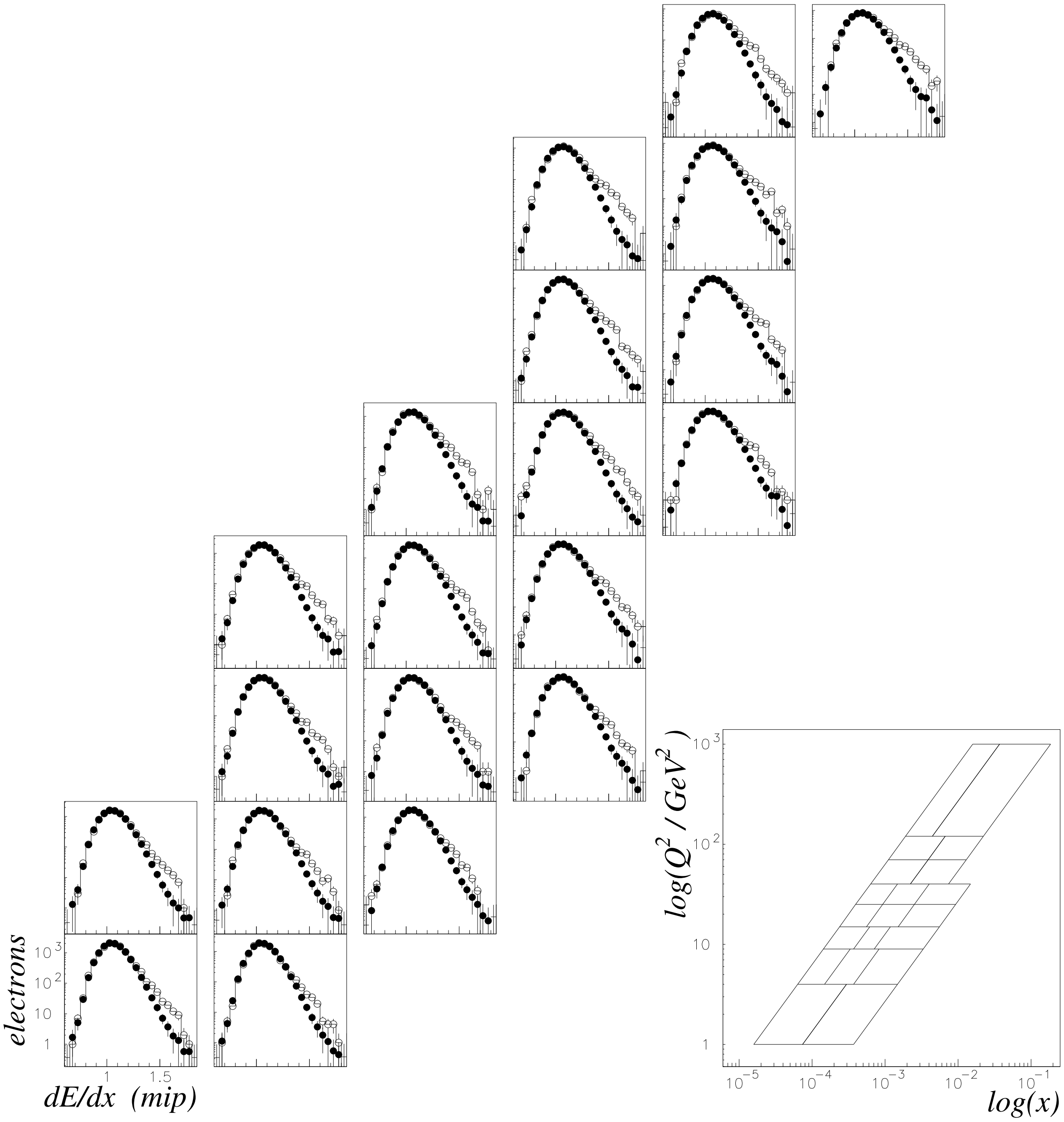

Figure C.1: *The dE/dx distribution of the signal (open dots) and the background (solid dots) sample in (x, Q^2) bins.*

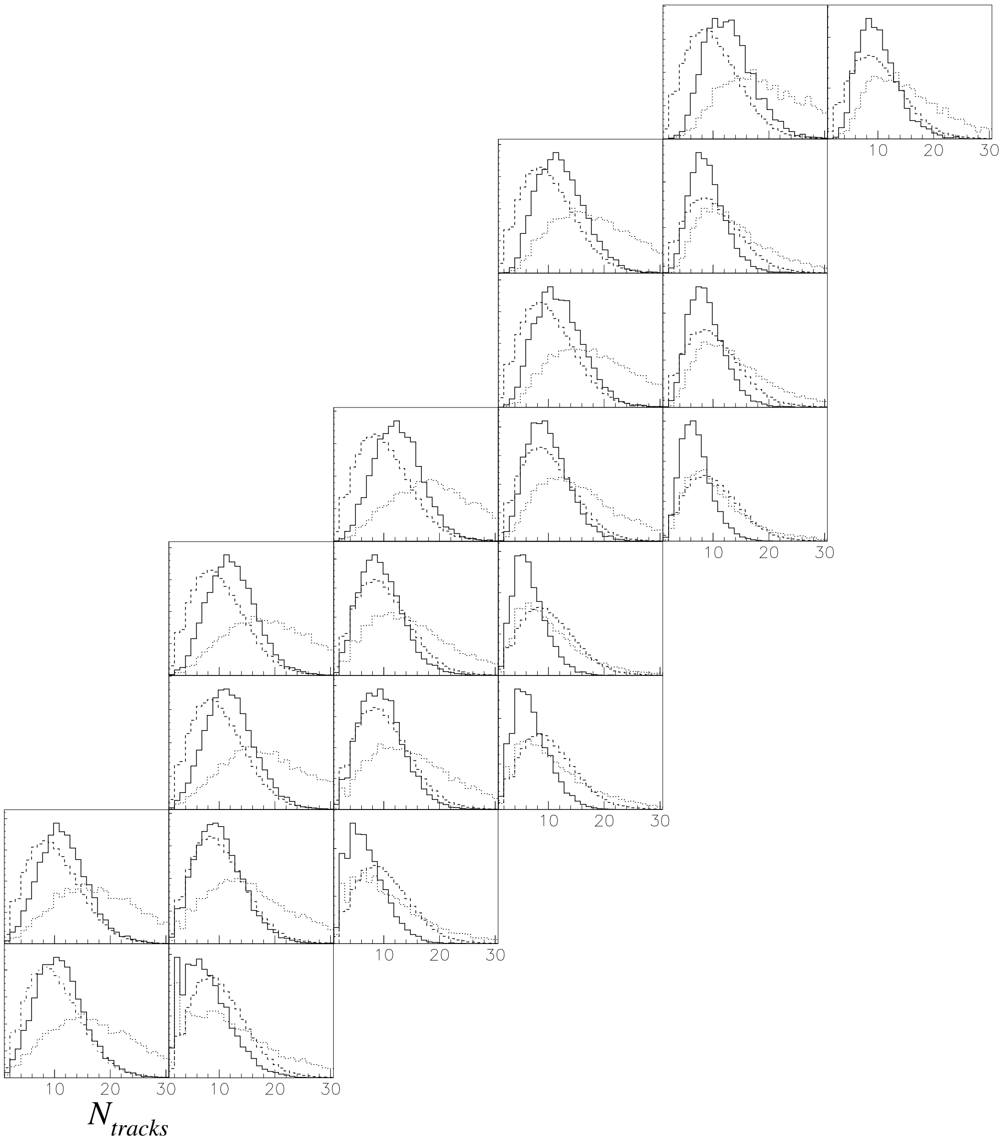

Figure C.2: *The number of all tracks (dotted line) and vertex tracks (solid line) per event in (x, Q^2) bins. The event has to have at least one track which fullfils the requirements of the signal sample. Also shown is the number of vertex tracks for events of the background sample, which is the same for all bins (dashed line).*

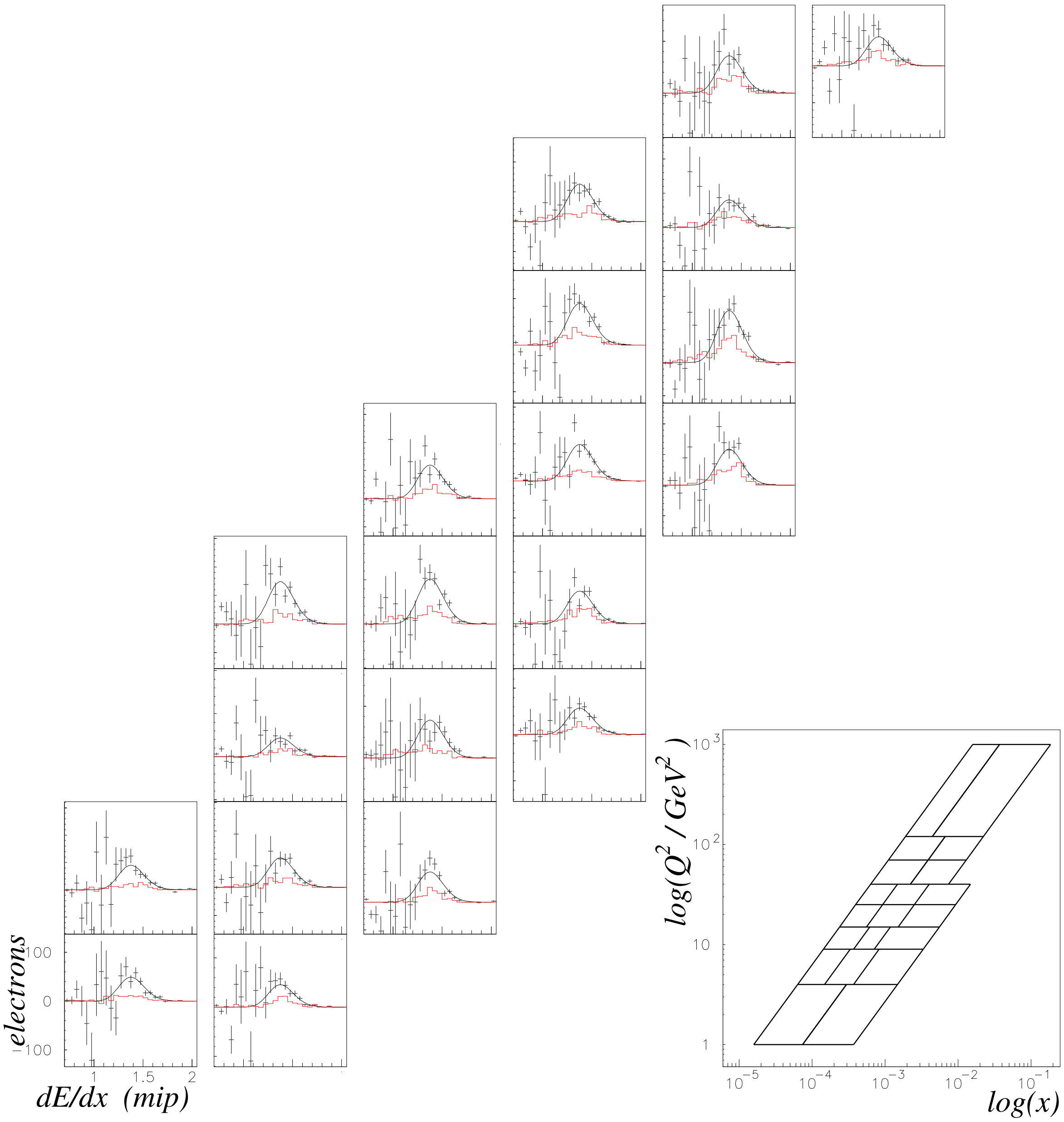

Figure C.3: *Electron signals in (x, Q^2) bins, obtained using the tracks for the background sample from the corresponding kinematic bin only, instead of using the overall background sample.*

Bibliography

[Aba95] D0 collaboration, S. Abachi et al., Phys. Rev. Lett. **74** (1995) 2632

[Abb99] OPAL Collaboration, G. Abbiendi et al., Eur. Phys. J. **C8** (1999) 573

[Abe95] CDF collaboration, F. Abe et al., Phys. Rev. Lett. **74** (1995) 2626

[Abr95] H. Abramowicz, A. Caldwell and R. Sinkus, NIM A 365 (1995) 508

[Ack98] OPAL Collaboration, K. Ackerstaff et al., Eur. Phys. J. **C1** (1998) 439

[Adl96] H1 Collaboration, C. Adloff et al., Z. Phys. **C72** (1996) 593

[Ad99A] H1 Collaboration, C. Adloff et al., Nucl. Phys. **B545** (1999) 21

[Ad99B] H1 Collaboration, C. Adloff et al., Eur. Phys. J. **C10** (1999) 373

[Ad99C] H1 Collaboration, C. Adloff et al., Phys. Lett. **B467** (1999) 156

[Ake95] OPAL Collaboration, R. Akers et al., Z. Phys. **C67** (1995) 27

[Alb91] ARGUS Collaboration, H. Albrecht et al., Z. Phys. **C52** (1991) 353

[Alb92] ARGUS Collaboration, H. Albrecht et al., Phys. Lett. **B278** (1992) 202

[Alt77] G. Altarelli and G. Parisi, Nucl. Phys. **B126** (1977) 298

[Aub74] J. J. Aubert et al., Phys. Rev. Lett. **33** (1974) 1404

[Aug74] J. E. Augustin et al., Phys. Rev. Lett. **33** (1974) 1406

[Bia96] S. Bianco, hep-ph/9602008 (1996)

[Big95] I.I. Bigi, hep-ph/9508408 (1995)

[Bjo69] J. D. Bjorken, Phys. Rev. **179** (1969) 1547

[Blo69] E. D. Bloom et al., Phys. Rev. Lett. **23** (1969) 930

[Bor88] CLEO Collaboration, D. Bortoletto et al., Phys. Rev. **D37** (1988) 1719

[Br97A] ZEUS Collaboration, J. Breitweg et al., Phys. Lett. **B407** (1997) 402

[Br97B] ZEUS Collaboration, J. Breitweg et al., DESY-PRC 97/01, (1997)

[Br98A] ZEUS Collaboration, J. Breitweg et al., ZEUS Note 98-046, (1998)

[Br99A] ZEUS Collaboration, J. Breitweg et al., Eur. Phys. J. **C7** (1999) 609

[Br99B] ZEUS Collaboration, J. Breitweg et al., Eur. Phys. J. **C6** (1999) 603

[Br99C] ZEUS Collaboration, J. Breitweg et al., Eur. Phys. J. **C6** (1999) 67

[Br00A] ZEUS Collaboration, J. Breitweg et al., Eur. Phys. J. **C12** (2000) 35

[Br00B] ZEUS Collaboration, J. Breitweg et al., (paper in preparation)

[Bru89] R. Brun et al., *GEANT3*, CERN DD/EE/81-1, (1989)

[Buz97] M. Buza, Y. Matiounine, J. Smith and W.L. van Neerven, Phys. Lett. **B411** (1997) 211

[Ca97A] M. Cacciari et al., Phys. Rev. **D55** (1997) 2736

[Ca97B] M. Cacciari and M. Greco, Phys. Rev. **D55** (1997) 7134

[Cas99] C. Caso et al, The European Physical Journal C3 (1998) 1 and 1999 off-year partial update for the 2000 edition available on the PDG WWW pages (URL: http://pdg.lbl.gov/)

[Cat95] C. Catterall, *Measurement of Charged Particles from the Hadronic Final State of Electron-Proton Deep Inelastic Scattering at a Centre of Mass Energy of 296 GeV*, Ph.D. thesis, Univ. College London (1995)

[Col85] J. C. Collins, Nucl. Phys. **B261** (1985) 104

[Def99] R. Deffner, *Measurement of the Proton Structure Function F_2 at HERA using the 1996 and 1997 ZEUS Data*, Ph.D. thesis, Univ. of Bonn (1999)

[Der93] ZEUS Collaboration, M. Derrick et al., *The ZEUS Detector*, Status Report 1993

[Dep99] O. Deppe, *Measurement of $D^{*\pm}$ Electroproduction at HERA*, Ph.D. thesis, Univ. of Hamburg (1999)

[Dok77] Y. L. Dokshitzer, Sov. Phys. JETP **46** (1977) 641

[Ell96] R.K. Ellis, W.J. Stirling and B.R. Webber, *QCD and collider physics*, (Cambridge University Press, 1996)

[Fri99] U. Fricke, *Precision Measurement of the Proton Structure Function F_2 at Low Q^2 and Very Low x at HERA*, Ph.D. thesis, Univ. of Hamburg (1999)

[Gel64] M. Gell-Mann, Phys. Lett. **8** (1964) 214

[Gla70] S. L. Glashow, J. Iliopoulos and L. Maiani, Phys. Rev. **D2** (1970) 1285

[Glü92] M. Glück, E. Reya and A. Vogt, Z. Phys. **C53** (1992) 127

[Glü95] M. Glück, E. Reya and A. Vogt, Z. Phys. **C67** (1995) 433

[Gri72] V. N. Gribov and L. N. Lipatov, Sov. J. Nucl. Phys. **15** (1972) 438

[Hal84] F. Halzen and A.D. Martin, *Quarks & Leptons*, (John Wiley & Sons, New York, 1984)

[Har96] B. W. Harris, J. Smith and R. Vogt, Nucl. Phys. **B461** (1996) 181

[Ha98A] B. W. Harris and J. Smith, Phys. Rev. **D57** (1998) 2806

[Ha98B] G.F. Hartner, ZEUS-Note 98-058, (1998)

[Hal99] R. Hall-Wilton, N. McCubbin, P. Nylander, M. Sutton and M. Wing, ZEUS-Note 99-024, (1999)

[Har99] B.W. Harris, E. Laenen, S. Moch and J. Smith, Monte Carlo generators for HERA physics 464-473, DESY-PROC-1999-02

[Heb99] K. Hebbel, ZEUS Note 99-036, (1999)

[Her77] S. W. Herb et al., Phys. Rev. Lett. **39** (1977) 252

[Ing91] G. Ingelman, L. Jönsson and M. Nyberg, DESY HERA Workshop, Vol 1, 353 (1991)

[Ing96] G. Ingelman and M. Thunman, Z. Phys. **C73** (1997) 505

[Ing97] G. Ingelman, A. Edin and J. Rathsman, Comp. Phys. Comm. **101** (1997) 108

[Jac79] F. Jacquet and A. Blondel, *Proceedings of the study of an ep facility for Europe*, DESY 79/48 (1979), 391

[Jon92] P. de Jong, ZEUS-Note 92-019, (1992)

[Jun95] H. Jung, Comp. Phys. Comm. **86** (1995) 147

[Kiw92] A. Kwiatkowski, H. Spiesberger and H.J. Mohring, Comp. Phys. Comm. **69** (1992) 155

[Köp94] L. Köpke and R. van Woudenberg, ZEUS-Note 94-016, (1994)

[Lai97] H. L. Lai et al. Phys. Rev. **D55** (1997) 1280

[Leo92] W. R. Leo, *Techniques for Nuclear and Particle Physics Expriments*, Springer-Verlag, Berlin, 2nd edition (1992)

[Mar92] G. Marchesini, B.R. Webber, G. Abbiendi, I.G. Knowles, M.H. Seymour and L. Stanco, Comp. Phys. Comm. **67** (1992) 465

[Mar94] A. D. Martin, R. G. Roberts, W. J. Stirling, Phys. Rev. **D50** (1994) 6734

[Nor99] E. Norrbin and T. Sjöstrand, hep-ph/9905493 (1999)

[Pan68] W. Panofski, in Proceedings of the International Conference in High Energy Physics, (Vienna, Austria, 1968)

[Pet83] C. Peterson et al., Phys. Rev. **D27** (1983) 105

[Plo93] H. Plothow-Besch, Comp. Phys. Comm. **75** (1993) 396

[Qua96] A. Quadt, *Measurement and QCD Analysis of the Proton Structure Function F_2 from the 1994 HERA Data Using the ZEUS Detector*, Ph.D. thesis, Univ. of Oxford (1996)

[Qua98] ZEUS Collaboration, J. Breitweg et al., ZEUS Note 98-036, (1998) [Rie95] S. Riemersma, J. Smith and W.L. van Neerven, Phys. Lett. **B347** (1995) 143

[Sch91] G. A. Schuler and H. Spiesberger, DESY HERA Workshop, Vol 3, 1419-1432 (1991)

[Sin97] R. Sinkus and T. Voss, NIM A 391 (1997) 360

[Sjö94] T. Sjöstrand, Comp. Phys. Comm **82** (1994) 74

[Tsa74] Y.-S. Tsai, Rev. Mod. Phys. **46** (1974) 815
Y.-S. Tsai, Rev. Mod. Phys. **49** (1977) 421

[Tun97] Wu-Ki Tung, hep-ph/9706480 (1997)

[Ver98] W. Verkerke, *Measurement of Charm Production in Deep Inelastic Scattering*, Ph.D. thesis, Univ. of Amsterdam (1998)

[Wi99A] M. Wing, *The Study of Heavy Quark Production in High E_T Photoproduction at HERA using the ZEUS detector*, Ph.D. thesis, Univ. College London (1999)

[Wi99B] M. Wing (for the ZEUS collaboration), DIS99 conference, Berlin, hep-ex/9905051

[Wou95] R. van Woudenberg, *Study of charm production at HERA using the ZEUS detector*, Ph.D. thesis, Univ. of Amsterdam (1995)

[Zwe64] G. Zweig, CERN-8192/TH (1964) 401
G. Zweig, CERN-8419/TH (1964) 402

Acknowledgments

Many people contributed to the development of this thesis, to whom I would like to say ‘thank you’ at this point.
First of all I would like to thank Prof. Robert Klanner and Prof. Erich Lohrmann for offering me the opportunity to start my Ph.D. in the ZEUS collaboration. Thanks to Lothar Bauerdick for his supervision during the three years and many lively and fruitful discussions. Thanks to Wolfram Zeuner for his straightforward and clear way of discussing physics and to Leonid Gladilin for working through the analysis, thereby always giving me new things to work on.
A special thanks to Wouter Verkerke for help and support, as well as encouragement and for showing me Amsterdam. Thanks to Sven Schagen, for having been very patient during the last few months, when I had no time to work on the analysis. I wish to encourage him in his future physics analyses !
I enjoyed very much the friendly working atmosphere within the ZEUS collaboration. Many people helped me with this work and more importantly helped me to enjoy life beyond physics. Special thanks go to Dominik Dannheim, Rolf Deffner, Olaf Deppe, Kai Desler, Joachim Flammer, Ulrich Fricke, Elke Gminder, Florian Göbel, Sonja Hillert, Stephan Hurling, Dorian Kcira, Amaya Lopez-Duran-Viani, Bruce Mellado, Margherita Milite, Teresa Monteiro, Matthias Moritz, Ignacio Redondo, Olaf Ruske, Dorothea Samtleben, Michael Sievers, Stefan Steinbeck, Stefan Stonjek, Enrico Tassi and the CAL-team.
Thanks to Ulrike Wollmer for making life at DESY much happier and for lots of laughs in Italy. Thanks to Adrian Fox-Murphy who volunteered to proof-read the whole thesis.
Special thanks to Renate Mohr, who accompanied my ‘physics career’ from the very beginning, always finding time to motivate and help sort out problems - ‘Wir haben’s geschafft !’.
Thanks to all my friends outside DESY - two and four-legged - for showing me the enjoyable part of life outside physics. Thanks to my parents for all the support they gave me. And finally a special thanks to Mark for his patience during the last months and always having been there for me to cheer me up and to motivate me.